Title

Semi-Empirical Characterization of Ground Motions Including Source, Path and Nonlinear Site Effects

Permalink

https://escholarship.org/uc/item/1jb3q3rc

Author

Seyhan, Emel

Publication Date

2013

Peer reviewed|Thesis/dissertation

UNIVERSITY OF CALIFORNIA

Los Angeles

Semi-Empirical Characterization of Ground Motions Including
Source, Path and Nonlinear Site Effects

A dissertation submitted in partial satisfaction of the requirements for the degree
of Doctor of Philosophy in
Civil Engineering

by

Emel Seyhan

2013

ABSTRACT OF THE DISSERTATION

Semi-Empirical Characterization of Ground Motions Including

Source, Path and Nonlinear Site Effects

by

Emel Seyhan

Doctor of Philosophy in Civil Engineering

University of California, Los Angeles, 2013

Professor Jonathan P. Stewart, Chair

The objective of this thesis is to improve the physical understanding of earthquake ground motion characteristics related to source, path and nonlinear site effects and our ability to model those effects with engineering models. This was achieved through four research studies consisting of: (1) calibrating broadband simulation procedures to remove previously recognized sources of bias in distance attenuation and standard deviation; (2) enhancing a site database used for assigning site parameters to ground motion recordings, particularly with regard to the level of rigor and transparency with which the database is populated; (3) leveraging a state-of-

the-art ground motion database and recent simulation-based studies to develop a nonlinear site amplification model suitable for use in ground motion predictions equations (GMPEs) and relatively simplified building code applications; and (4) developing GMPEs that provides mean and standard deviation of ground motion intensity measures in active crustal regions.

The high-frequency component of the simulation procedure considered in this study combines deterministic Fourier amplitude spectra (dependent on source, path, and site models) with random phase. Significantly too-fast distance attenuation bias identified in prior work has been removed by increasing the quality factor (Q). We introduced random site-to-site variations to Fourier amplitudes using a log-normal standard deviation ranging from 0.45 for M < 7 to zero for **M**8 to achieve dispersion terms that are more compatible with those from empirical models but remain lower at large distances (e.g., > 100 km).

Site database work was performed within the context of the NGA-West 2 project. Starting with the site database from original (2008) NGA project (last edited in 2006), we provided site classifications for 2538 new sites and re-classifications of previous sites. The principal site parameter is the time-averaged shear wave velocity in the upper 30 m (V_{s30}), which is characterized using measurements where available, and proxy-based relationships otherwise. We improved the documentation and consistency of site descriptors used as proxies for the estimation of V_{s30}, developed evidence-based protocols for V_{s30} estimation from available proxies, and augmented estimates of various basin depth parameters.

Site factors typically have a small-strain site amplification that captures impedance and resonance effects coupled with nonlinear components. Site factors in current NEHRP *Provisions*

are empirically-derived at relatively small ground motion levels and feature simulation-based nonlinearity. We show that current NEHRP site factors have discrepancies with respect to the site terms in the original NGA GMPEs both in the linear site amplification (especially for Classes B, C, D, and E) and the degree of nonlinearity (Classes C and D). We analyzed the NGA-West 2 dataset and simulation-based models for site amplification to develop a new model. The model has linear and nonlinear additive components. The linear component is fully empirical, being derived from worldwide ground motion data (regional effects were examined but found to not be sufficiently important to be included in the model). The model features linear V_{s30}-scaling in a log-log sense below a corner velocity (V_c), and no V_{s30}-scaling for velocities faster than V_c. The nonlinear component is developed from consideration of empirical data analysis and simulation results within a consistent context. The resulting nonlinearity operates principally at short periods and soft soils. This model is suitable for use as a site term in GMPEs and was applied to develop a proposal for updating the NEHRP site factors. The recommended factors remove a discrepancy between the reference condition used in the site factors and the national seismic hazard maps published by USGS.

We have developed empirical equations for predicting the average horizontal component of earthquake ground motions from active crustal region earthquakes worldwide. The equations build upon a previous ground-motion model by Boore and Atkinson in 2008. Significant new features of the proposed GMPEs include: modified site terms; a modified magnitude scaling function that produces a higher degree of saturation at large magnitude for high-frequency ground motions; region-specific apparent anelastic attenuation term; basin depth correction factors that are centered on the average level of basin amplification

conditional on V_{s30}; standard deviation terms that depend on M for between-event standard deviations and M-, R_{jb}- and V_{s30}-dependent within-event standard deviations. The resulting equations are applicable for events over a magnitude range of 3 to 8.5 for strike-slip or reverse-slip events (**M**3 to 8 for normal slip events), distance range up to 400 km, and site conditions ranging from V_{s30} = 150 to 1500 m/s. The equations are useful for prediction of the ground-motion intensity measures (*IMs*) PGA, PGV, and PSA at periods T = 0 to 10 sec.

The dissertation of Emel Seyhan is approved.

_____
Scott Brandenberg

_____
Jian Zhang

_____
Hongquan Xu

_____
Robert W. Graves

_____
Jonathan Stewart, Committee Chair

To my beloved family...

TABLE OF CONTENTS

LIST OF FIGURES

xiii

LIST OF TABLES

ACKNOWLEDGEMENTS

I am very grateful for my four years at UCLA. Apart from major efforts of myself, the accomplishments and success of the four projects depend largely on the encouragement and guidelines of many others. Without them, this dissertation would not have been possible. I take this opportunity to express my gratitude to my advisor Dr. Jonathan P. Stewart, *the Chair of Civil and Environmental Engineering at UCLA*, who continually encouraged, supported and guided me during the journey of my dissertation. I cannot thank him enough for his tremendous support and help. Besides of my advisor, I would like to thank the rest of my thesis committee: Dr. Scott J. Brandenberg, Dr. Jian Zhang, Dr. Hongquan Xu and Dr. Robert W. Graves, for their insightful comments, and hard questions. I also would like to express my deepest appreciation to Dr. Yousef Bozorgnia, *the Executive Director of PEER*, who convincingly conveyed a spirit of mentorship and support in regard to research. Furthermore, I am extremely indebted to Dr. Robert W. Graves who kindly shared the information and provided me with incredible support and knowledge. My special gratitude and thanks to my colleague Dr. Lisa M. Star who supported me from the beginning. Furthermore, I would like to express my gratitude

VITA

2003-2008	B.S., Geological Engineering Middle East Technical University Ankara, Turkey
2004-2007	Minor Degree in Geotechnical Engineering Middle East Technical University Ankara, Turkey
2009-2010	M.S., Geotechnical Engineering University of California, Los Angeles Los Angeles, California
2009-2013	Research Assistant Department of Civil and Environmental Engineering University of California, Los Angeles Los Angeles, California
2012	Teaching Assistant Department of Civil and Environmental Engineering University of California, Los Angeles Los Angeles, California
2013	Special Reader Department of Civil and Environmental Engineering University of California, Los Angeles Los Angeles, California

PUBLICATIONS AND PRESENTATION

Seyhan E., Star L.M., Graves R.W., Stewart J.P., (2010), " Calibration of Simulated Motions from Spontaneous Rupture Models Relative to NGA Ground Motion Prediction Equations" Seismological Society of America (SSA) Annual Meeting, **April 21-23, 2010**, Portland, Oregon, Abstract 10-507, pp. 321, ***Oral Presentation by Emel Seyhan.***

Seyhan E., Star L.M., Graves R.W., Stewart J.P., (2010), "Comparison of Recorded and Simulated Ground Motions", Pasific Earthquake Engineering Research Center (PEER), *Quake Summit 2010 : NEES / PEER Joint Annual Meeting,* **October 8-9, 2010**, San Francisco, CA, Abstract.

Stewart J.P., **Seyhan E.**, Graves R.W., (2011), "Engineering Perspective on Validation and Calibration of Physics-based Ground Motion Simulations" *Seismological Society of America (SSA) Annual Meeting,* **April 13-15, 2011,** Memphis, Tennessee, Abstract, pp. 281-282.

Stewart J.P., **Seyhan E.,** and Graves R.W., (2011). " Calibration of Semi-Stochastic Procedure for Simulating High Frequency Ground Motions", **PEER Report 2011/09**, *Pacific Earthquake Engineering Research Center*, UC Berkeley.

Graves R.W., **Seyhan E.**, Stewart J.P., (2011),"Broadband Ground Motion Simulations for a Kinematic Variation of the Mw 7.8 ShakeOut Rupture", *American Geophysicial Union (AGU), Fall Meeting 2011*, **December 5-9, 2011**, San Francisco, CA, Abstract.

Seyhan E., Stewart J.P., Graves R.W., (2012) "Calibration of a Semi-Stochastic Procedure for Simulating High Frequency Ground Motions" **Earthquake Spectra (in-press)**.

Seyhan, E., Stewart, J.P., (2012). "Site Response in NEHRP Provisions and NGA Models", State of Art and Practice in Geotechnical Engineering, ASCE *GeoCongress 2012*, Oakland, California, **March 25-29, 2012**, Abstract, pp. 359-379

Stewart J.P., **Seyhan E.,** Boore D.M., Campbell K.W., Erdik M., Silva W.J., Di Alessandro C., and Bozorgnia Y., (2012) "Site Effects in Parametric Ground Motion Models for the GEM-PEER Global GMPEs"*15th World Conference on Earthquake Engineering,* Lisbon, Portugal, **September 24-28, 2012**, Abstract, Paper No: 2554

Ancheta T.D., Darragh R.B., Stewart J.P., **Seyhan E.**, Silva W.J., Chiou B.S.J., Wooddell K.E., Graves R.W., Kottke A.R., Boore D.M., Kishida T., and Donahue J.L., (2013). "PEER NGA-West2 Database "*PEER Report 2013/03*, *Pacific Earthquake Engineering Research Center*, UC Berkeley.

Ancheta, T., Darragh, R., Stewart, J., Silva, W., Chiou, B., Bozorgnia, Y., **Seyhan, E.**, Kishida, T., Wooddell, K, Kottke, A., Boore, D., (2013), " PEER NGA-West2 Database: A Database of Ground Motions Recordings from Shallow Crustal Earthquakes in Active Tectonic Regimes ",*Seismological Society of America (SSA) Annual Meeting*, **April 17-19, 2013**, Salt Lake City, Utah

Boore, D. M., Stewart, J. P., **Seyhan, E.**, Atkinson, G. M., (2013), "Ground Motion

Prediction Equations for RotD50 Horizontal Component for Active Crustal Regions"
Seismological Society of America (SSA) Annual Meeting, **April 17-19, 2013**, Salt Lake City, Utah, ***Oral Presentation by Emel Seyhan.***

Boore D.M., Stewart J..P, **Seyhan E.**, and Atkinson G.M., (2013). "NGA-West2 Equations for Predicting Response Spectral Accelerations for Shallow Crustal Earthquakes" ***PEER Report 2013/05***, *Pacific Earthquake Engineering Research Center*, UC Berkeley.

Stewart J.P., and **Seyhan E.,** (2013). "Semi-Empirical Nonlinear Site Amplification and its Application in NEHRP Site Factors" PEER Report 2013/13, *Pacific Earthquake Engineering Research Center*, UC Berkeley. (available in **Summer 2013**)

1   INTRODUCTION

1.1   GENERAL

For many decades, the inadequacy in understanding of seismic performance of man-made structures during earthquakes has been attributed to great loss of life and property. Earthquake engineering researchers and practitioners have been seeking effective ways to better meet the needs of society. Accurate ground motion characterization is vital to all seismic design. The strong ground motions caused by an earthquake may be characterized by earthquake ground motion Intensity Measures (IMs). To estimate IMs - such as spectral acceleration and duration - Ground Motion Prediction Equations (GMPEs) are used. GMPEs are used in seismic hazard applications to specify the expected levels of shaking as a function of predictor variables such as earthquake magnitude and distance. GMPEs account for the source, path and site effects. For a given moment magnitude, site-to-source distance and site parameter gathered from a processed dataset of recordings within specific tectonic regimes, GMPEs can provide estimates of median motion predictions of IMs with their associated uncertainties. For engineering applications, a potential alternative to GMPEs is the use of ground motions computed using seismological simulation techniques, especially for scenarios with a scarcity of data such as large magnitude shallow crustal earthquakes (e.g., $M_w \geq 5$).

This research involves four multi-disciplinary projects related to improving ground motion characterization. The first project investigates the suitability of the ground motions generated through calibrated simulation procedure for engineering application for loss estimation. The second project develops an enhanced site database to be used in the analysis of model development. Third project utilizes this database and develops improved insight into empirical site amplification factors for shallow crustal earthquakes in active tectonic regions, which is formulated into revisions to the National Earthquake Hazards Reduction Program (NEHRP) Provisions. Revisions to the NEHRP site factors have substantial and far-reaching impact on seismic design for buildings, bridge, and other structures. Closely related to third project, a fourth work utilizes the site amplification model acquired in the second project and develops a Next Generation Attenuation (NGA) GMPE (Boore et al., 2013; BEA13) which is applicable to active crustal regions (ACRs) worldwide. These projects have been outlined in Sections 1.3, 1.4 and 1.5, and explained in greater detail in Chapter 2 and Chapter 3 to 6, respectively.

1.2   OVERVIEW OF GROUND MOTIONS

Strong ground motion refers to strong shaking that is associated with a sudden release of energy due to a fault rupture often well below the surface of the earth. Ground motions for the most important interest for engineering design purposes and hazard assessments happen to be at close distance (≤ around 40 km) and large magnitudes (≥ around 5). Although, the limitation in the available data regarding shallow earthquakes in active crustal regions in this magnitude-distance range is improved in the number of recordings by earthquakes such as **M**7.62 Chi-Chi, Taiwan (1999), **M**7.90 Wenchuan, China (2008), **M**7.0 Darfield, New Zealand (2010) and **M**7.20

El Mayor-Cucapah, Mexico (2010), there is still scarcity of data. For cases where recorded strong ground motions for characterization are limited in distribution and size, synthetic ground motions can be good supplements for analysis of a wide spectrum of source and site characterization. Similar to GMPEs, synthetic ground motions also account for characteristics of seismic source, path and local soil conditions. The validations and implementations of synthetic ground motions need to be evaluated by engineers for engineering design purposes.

1.3 CALIBRATION OF GROUND MOTION SIMULATIONS

The first research study, titled "Calibration of Semi-Stochastic Procedure for Simulating High Frequency Ground Motions," is performed by using a simulation procedure that combines physics based deterministic modeling of source, path, and site effects at low frequencies with semi-stochastic procedures at high frequencies. Such procedures are referred to as hybrid broadband simulations. Broadband simulation procedures have the potential to play a significant role in the engineering characterization of seismic ground motion, especially for conditions poorly represented in ground motion databases. The high-frequency procedure considered in Chapter 2 combines a deterministic Fourier amplitude spectrum that is a function of closed-form source, path, and site models with a random phase.

Previous analysis of the simulation procedure in the ShakeOut exercise (Star et al., 2010) - a rupture scenario earthquake with a M_w 7.8 event on the southernmost 300 km of the San Andreas Fault (Graves et al., 2010) - demonstrated faster distance attenuation and lower intra-event dispersion of high-frequency ground motions than in empirical ground motion equations. The current research investigates how to remove these biases by increasing quality factor (Q)

and introducing random site-to-site variations to the Fourier amplitudes produced by the high frequency (semi-stochastic) component of the hybrid procedure. The findings from this research- that will be discussed in greater detail in Chapter 2 - illustrate that when implemented in a repeat of broadband simulations for the ShakeOut event, the calibrated high-frequency procedure reduces the distance attenuation bias although the low dispersion misfit remains as a result of issues with the source model for this event. This research study is completed to date, is published as a PEER report in 2011/09 and is accepted (in press) as a journal paper in Earthquake Spectra. This work is performed in collaboration with Robert Graves, PhD, from USGS.

1.4 EVALUATION OF NONLINEAR SITE AMPLIFICATION FACTORS

The objective of this work is to support the development of improved models for site response in NGA-West-2 project and to build consensus toward updated site factors in the NEHRP Provisions. This research addresses several important issues in earthquake engineering focusing on the evaluation of soil amplification factors in NGA models versus NEHRP site factors.

The characteristics of ground motions such as amplitude, frequency content and duration can be affected by local site conditions. Relevant site conditions include the soil layering, material properties, and surface topography. Since 1820's the influences of local geologic and site conditions on the intensity of ground shaking and damage have been recognized. MacMurdo (1824) and Mallet (1862) noted the effect of local geologic conditions on structural damage. Then, Wood (1908) and Reid (1910) showed that the intensity of ground motions in the 1906 San Francisco earthquake relates to local geologic and site conditions.

4

Gutenberg (1927) developed site-dependent amplification factors from different subsurface conditions from recordings at sites. For many years, it has been well recognized that site effects, i.e. site amplification factors, establish an important part of characterization of ground motions, thus, play important role in engineering practices since they may amplify or deamplify the motions before reaching the surface of the ground or the basement of the man-made structure.

Site effects can be evaluated using theoretical and empirical procedures. Theoretical procedures typically represent the layering as one-dimensional and simulate the soil properties elastically (for small strain problems) or with non-linear relationships (for large strain problems). Empirical methods utilize recorded ground motions to infer site effects. These procedures seek to remove source and path effects using various techniques, so that the effects of site condition on the ground motions can be identified. These topics along with source and path effects are explored in Chapter 3 up to Chapter 7.

Site effects are represented in GMPEs by site terms that provide broad, averaged estimates of site amplification for generalized descriptions of site condition (e.g., rock vs. soil). Some of the ways that site conditions are represented in generalized site amplification models include surface geology, near-surface shear wave velocity and geotechnical data.

Shear-wave velocity, V_s, is an important parameter for evaluating dynamic behavior of soil in the shallow subsurface. The ratio of 30 m to shear wave travel time through the upper 30 m of the site is referred to as V_{s30}. Most modern site factors utilize V_{s30} as the descriptor of site condition. In Chapter 3, I present some of the arguments for and against the use of V_{s30} a proxy of site condition for defining ground motion amplification factors. This research study is

completed to date, is released as a PEER report in 2013 and produced a conference paper and a keynote in GeoCongress in 2012.

The site amplification work consists of several tasks such as:

Task 1 - Direct Site Factors Comparisons: Here I compare NEHRP site factors to site factors in four modern GMPEs produced in the NGA project in 2008. The objective is to evaluate differences in median amplification levels at various rock ground motion levels and also differences in the nonlinearity of site amplification. This task is completed, is published as the keynote in GeoCongress in 2012. It is presented in Chapter 3.

Task 2 - Development of Site Database: The original NGA project produced databases of ground motions, earthquake source attributes, and site condition. The last updates to these databases are from 2006. Task 2 in my work consists of updating the site database, and is being performed collaboratively with broader efforts by others to update the source and ground motion databases. Significant additions to the dataset since 2006 come from the 2008 Wenchuan (China) earthquake, 2009 L'Aquila (Italy) earthquake, 2007 Kashiwazaki (Japan) earthquake, and 2010 Sierra El Mayor (Mexico) earthquake. My work on the site database involved (1) providing site classifications for 2538 new sites added to the main flatfile in the NGA-West 2 project; (2) updating the site database to include V_{s30} values based on newly available measurements; (3) improving the documentation and consistency of site descriptors used as proxies for the estimation of V_{s30} such as new techniques by Boore (2004), Boore et al. (2011), Chiou and Youngs (2008a), Matsuoka et al. (2006), Wald and Allen (2007), Wills and Gutierrez (2008), Yong et al. (2012), both for sites in the previous site database and newly added sites; (4) developing evidence-based protocols for V_{s30} estimation from available proxies;

and (5) updating estimates of basin depth parameters $Z_{1.0}$ and $Z_{2.5}$ for both existing and new sites (primarily California and Japan). It is completed, published as a PEER report and NGA-West 2 site database spreadsheet in 2013/03. This task is presented in Chapter 4.

Task 3 – Semi-Empirical site amplification studies: The database compiled in Task 2 was utilized to evaluate site amplification using various approaches that will be described in Chapters 3 to 6. The purpose of this work is two-fold. The first objective is to use the newly generated database, which is unprecedented in scope and size, to explore fundamental factors in site amplification including: (1) the degree of nonlinearity in site factors (i.e., their dependence on the strength of the input) for short and long period *IMs* and for soft and stiff site conditions (represented by V_{s30}); (2) scaling of site factors with V_{s30} at weak motion levels (linear site response); and (3) scaling of site factors regionally. The second objective of this work is to utilize the lessons learned about site amplification in this work and previous work to better understand the reasons for misfits between contemporary site factors and the NEHRP site factors, which date from the early 1990s. This improved understanding is essential to support proposed revisions to building code provisions.

Task 4 – Develop Recommendations: Task 4 includes the development of new NEHRP site factors and checking the impact of the change with hazard calculations for selected locations and return periods (e.g., Goulet and Stewart, 2009). The proposed modifications in NEHRP site factors will have substantial and far-reaching impact on seismic design for buildings, bridge, and other structures. Tasks 3 and 4 will be published as a PEER report in Summer 2013.

1.5   DEVELOPMENT OF GROUND MOTION PREDICTION EQUATIONS

This research study, closely related to the study in Section 1.4, is performed by utilizing the strong-ground motion database developed in the NGA-West 2 project whose site database is presented in Chapter 3, using the site amplification model as its site term that is presented in Chapter 5, and investigating secondary descriptor variables such as source depth, basin depth etc. and improvements to the previous version of the NGA GMPE of Boore and Atkinson (2008) (BA08) that is explained in more details in Chapter 6. The main objective of this work is to develop an improved and up to date GMPE for shallow crustal earthquakes in ACRs worldwide which is used in seismic hazard applications to specify the expected levels of shaking as a function of predictor variables such as earthquake magnitude and distance. The applicability of this particular GMPE involves the prediction of horizontal-component peak ground acceleration (PGA), peak ground velocity (PGV) and response spectra (PSA, the 5% damped pseudo response spectral acceleration), for earthquakes of M_w 3.0 to 8.5, at distances from 0 to 400 km, at sites having V_{s30} in the range from 150m/s to 1500 m/s, for periods between 0.01 s and 10 s. It also considers regional variability in source, path and site, and selected secondary source and site effects, but it does not address near fault effects such as directivity effects.

Early GMPEs were very simple equations giving peak ground acceleration as a function of magnitude and epicentral distance (e.g., Douglas, 2003). Over the time, the GMPEs have become more sophisticated and complex as the strong ground motion datasets and the associated metadata of source and site conditions have grown. This also serves well for the resolving power of empirical regression techniques. Although these were inevitable, it is still

important to keep the GMPE models as simple as possible which are able to capture the median predictions of the ground motion with its associated dispersions.

In this research, I present the three-phase model building process, constraining some variables based on an initial analysis of the data (Phase I), performing two-stage regressions to define some of the model coefficients (Phase II) and refining of the model based on examinations of residuals (defined by the difference, in natural log units, between the observed and predicted amplitude of motion) of the regression against secondary predictor variables that are available as part of the NGA-West 2 metadata (Phase III). The secondary parameters involve event specific regions, the depth to the top of fault rupture, the depth to basement rock and so on. Phase II comprises two-stage regressions for the base-case model based on a simple functional form. I intentionally leave the details on Phase II of this study out of this dissertation due to the fact that it was performed by one of the collaborators of this research (i.e. David M. Boore). This work is performed in collaboration with David M. Boore, PhD, from USGS and Gail Atkinson, PhD, from WU, Ontario. This work is completed to date and is published as a PEER report in 2013/05.

1.6   ORGANIZATION OF THIS DISSERTATION

This dissertation describes four multi-disciplinary projects as outlined in Sections 1.3 to 1.5. The first project on the simulation work is presented in Chapter 2. The second project is described in details in Chapter 4. It explains the steps in developing the NGA-West 2 site database (Task 2 in Section 1.4). Chapter 3 and 5 present the third project about the work on discrepancies between the original NGA site factors and the NEHRP site factors (Task 1 in Section 1.4). . and

on the semi-empirical nonlinear site amplification and its application in proposed NEHRP site factors (Task 3 and 4 in Section 1.4). The fourth project, the development of GMPE and the equations for the model of predicting response spectral accelerations for shallow crustal earthquakes, is presented in Chapter 6. Chapter 7 describes the research findings and future studies on the projects.

2 CALIBRATION OF SEMI-STOCHASTIC PROCEDURE FOR SIMULATING HIGH FREQUENCY GROUND MOTIONS

2.1 INTRODUCTION

Broadband simulation procedures have the potential to play a significant role in the engineering characterization of seismic ground motion, especially for conditions poorly represented in ground motion databases. For example, the database used in the Next Generation Attenuation (NGA) project included earthquake magnitudes up to M_w 7.9, but relatively sparse recordings at moderate to close distance (< 40 km) for M_w > 7.6 (Chiou et al., 2008). Ground motion hazard for sites in the vicinity of the San Andreas fault is often controlled by earthquake magnitudes near 8.0 (e.g., Harmsen and Frankel, 2001), and hence there is a significant practical need for ground motion prediction tools that can operate beyond the limits of the database. Broadband simulations therefore have the potential to help solve two important problems: (1) provide simulated motions to help constrain semi-empirical ground motion prediction equations (GMPEs) beyond the data limits; and (2) provide realistic waveforms for use in response history analyses for conditions not represented in empirical databases.

Ground motion simulation procedures vary in their methodology and sophistication, but all compute in some manner source processes, path effects, and local site response. Deterministic procedures utilize rigorous seismological models of source, path, and site response without introducing a stochastic element. Such procedures are typically useful only at frequencies below about 1 Hz (e.g., Frankel, 1993; Sato et al., 1999; Stidham et al., 1999; Xu et al., 2003; Day et al. 2008; Olsen et al., 2008, 2009). Higher frequency seismic waveforms are difficult to reproduce deterministically, in part because source radiation and wave propagation become increasingly incoherent at high frequencies (e.g., Liu and Helmberger, 1985; Sato and Fehler, 1998; Hartzell et al., 1999). Motions lacking coherency are by definition stochastic; accordingly, a separate family of non-deterministic simulation procedures has been used for many years which employ stochastic components (referred to here as "semi-stochastic"; Boore, 1983; Silva and Darragh, 1995; Beresnev and Atkinson, 1997; Atkinson et al, 2009; Ameri et al., 2009) or which are more fully stochastic (e.g., non-stationary models of Conte and Peng, 1997; Rezaeian and Der Kiureghian, 2008).

Hybrid ground motion simulations leverage the strengths of deterministic procedures at low frequencies and stochastic or semi-stochastic procedures at higher frequencies to produce broadband waveforms. Hartzell et al. (1999), Liu et al (2006), Graves and Pitarka (2010), and Mena et al. (2010) review past hybrid methods and the latter two references present recent developments in two alternative hybrid procedures. Most modern broadband procedures use analytical Green's functions to model low frequency path effects, including the effects of sedimentary basins. Current procedures are differentiated principally in the following respects:

12

The source description for low frequency simulations is described kinematically (including spatially variable slip distributions, rise times, and rupture velocities) or is represented through spontaneous dynamic processes (which prescribe initial fault stresses and constitutive relations for shear failure criteria). In some cases, the development of kinematic models is guided by results of dynamic rupture simulations (Guatteri et al., 2004; Schmedes et al., 2010), so the outcomes of the different modeling procedures can be similar. The kinematic approach is used by Zeng et al (1994), Liu et al. (2006), Frankel (2009), and Graves and Pitarka (2010). A combination of kinematic and dynamic rupture modeling was considered by Hartzell et al. (2005) and Mena et al. (2010). The dynamic rupture approach is used by Ripperger et al. (2008), Pulido and Dalguer (2009) and Olsen et al. (2008, 2009).

High frequency source and path effects are simulated semi-stochastically (as described further below) or deterministic methods are applied in which random processes are introduced through the source description or path operators. The semi-stochastic approach prescribes the Fourier amplitude using a deterministic mean combined with random frequency-to-frequency perturbations, whereas the phase is stochastic (e.g., Hartzell et al., 1999, 2005; Frankel, 2009; Graves and Pitarka, 2010). Mai et al. (2010), Mena et al. (2010) introduce stochasticity through scattering operators within the analytical Green's functions, which requires tuning of scattering parameters and inherently takes high frequency incoherence as predominantly path-induced. Zeng et al (1994) and Liu et al. (2006) introduce stochasticity via the source, which is defined to very short length scales (on the order of 100 m or less) with random distributions of slip, rise times, and rupture velocities.

13

Because ground motion simulation involves complex numerical models with significant potential for coding errors, simulation results should be verified by comparing outcomes (at low frequencies) from independent computational platforms for a common set of source and path conditions (Bielak et al., 2010). Such verification is an essential first step towards the establishment of simulation procedures as a potentially reliable engineering tool. Following verification, there is a need for careful validation and calibration of simulation results relative to ground motion data or data-driven empirical models. The lack of engineering application of broadband simulations in the western U.S. to date reflects, in part, validation and calibration that has not adequately convinced engineers of the reliability of simulation tools. In general, the following procedures have been used for validation/calibration:

Waveform comparisons using earthquake data: Simulated waveforms for a particular earthquake event are compared to recordings (e.g., Zeng et al., 1994; Stidham et al., 1999; Hartzell et al., 2005; Liu et al., 2006; Graves and Pitarka, 2010; Mai et al, 2010). In most cases these comparisons are qualitative but quantitative comparison schemes have also recently been proposed (e.g., Olsen and Mayhew, 2010). This is the most common validation technique in previous research. Typically, velocity or displacement histories are used for these comparisons, thereby emphasizing low frequency ground motions relatively unaffected by stochastic processes. Problems with this approach are, (1) often the same recordings used to invert the source function are then used to demonstrate the efficacy of the simulation code, which makes good matches probable but less meaningful, and (2) high frequency components are often not considered.

Ground motion intensity measures comparison using earthquake data: Intensity measures (IMs) such as peak velocity or spectral quantities are calculated for simulated motions from an event and compared (as a function of distance or frequency) to IMs from recordings (e.g., Silva et al., 1999; Hartzell et al., 1999, 2005; Liu et al., 2006; Graves and Pitarka, 2010; Mai et al., 2010). If a suitable number of recordings are available, both bias and dispersion of simulated motions can be compared to those from recordings. One drawback of this approach is that recordings are generally not available for the types of earthquakes for which simulations are most valuable (i.e., large magnitude). In addition, the circular reasoning associated with use of an inverted source function with recordings from that same event (as described above) diminishes the value of these comparisons.

Ground motion IM comparison using prediction equations: Ground motions are simulated for hypothetical events and *IMs* are compared to predictions from semi-empirical Ground Motion Prediction Equations (GMPEs). This approach enables relatively robust evaluations of distance scaling, site response, and standard deviation terms (e.g., Star et al., 2011) or subsets of these (Frankel, 2009). Parameters in the simulation code can be calibrated to match GMPE trends; for example, Mena et al. (2010) calibrate the number of scatterers to achieve desired median levels of high frequency motions in their hybrid procedure.

Most of the procedures described above validate simulations in the sense that computed motions (or their *IMs*) are simply checked against data or GMPEs, although we expect that some process of parameter adjustment (i.e., informal calibration) has typically been undertaken to fit simulation results to data in a generalized sense. Relatively formal calibration involves adjusting model parameters to achieve specified attributes in simulated motions. In

15

this paper, as a first step of the calibration process, we describe calibration of selected high-frequency components of the broadband simulation procedure of Graves and Pitarka (2010). The calibration seeks to remove too-fast distance attenuation in simulated motions and too-low standard deviation terms. These problems with broadband simulated motions have been identified in previous work by Star et al. (2011) using motions from a ShakeOut (southern San Andreas fault) earthquake (e.g., Graves et al., 2008 and Porter et al., 2011). Calibration of low frequency components is not undertaken in the current work.

Following this introduction, we briefly review the hybrid broadband simulation methodology that is the subject of this work, with an emphasis on the high frequency (semi-stochastic) component. We then describe a series of hypothetical events for which high frequency ground motions are simulated (we do not include low frequency components). Using the ShakeOut rupture scenario (Graves et al., 2011), we demonstrate that the short period IMs of ground motions generated using the high frequency simulation procedure are similar to broadband motions with respect to their distance attenuation and dispersion. We then calibrate the simulation procedure by, (1) modifying the quality factor (Q) to remove distance attenuation bias relative to NGA GMPEs, and (2) adding dispersion to match intra-event standard deviations in GMPEs. We conclude by repeating the ShakeOut broadband simulations with the modified hybrid procedure.

2.2   UTILIZED SIMULATION METHODOLOGY

We utilize the hybrid broadband simulation methodology of Graves and Pitarka (2010), which is briefly described here. This method was selected from among several hybrid simulation procedures principally on the basis of its utilization in high-profile scenario earthquake and loss estimation studies (e.g., Aagaard et al., 2008; Graves et al., 2011). The Graves and Pitarka (2010) procedure consists of a low frequency component that utilizes a kinematic source model and analytical Green's functions for path effects.

The high frequency portion of the model is adapted from the classical point source simulation procedure of Boore (1983), later adapted to finite sources by Frankel (1995). The source and path components for a finite fault are summed as follows to construct the Fourier spectrum for a given site:

$$A(f) = \sum_{i=1}^{N} \sum_{j=1}^{M} C_{ij} \bar{S}_i(f) G_{ij}(f) P(f) \tag{2.1}$$

The fault is discretized into i=1 to N sub-faults, each with its own prescribed slip δ_i. Seismic waves can travel from the source along j=1 to M ray paths (e.g., two are used by Graves and Pitarka, 2010; direct and Moho-reflected). The source spectrum for sub-fault i and ray path j includes (1) a frequency-independent term (C_{ij}) that accounts for radiation pattern as well as shear wave velocity and mass density of rock at the sub-fault and (2) a frequency-dependent term $S_i(f)$ that describes the seismic radiation from sub-fault i. As shown schematically in Figure 2.1, the source acceleration spectrum $C_{ij}S_i(f)$ is broad banded with an ascending branch that scales with the square of frequency and a flat branch for frequencies beyond the corner frequency f_{ci}. $S_i(f)$ includes the shaping factor introduced by Frankel (1995), which scales

17

the subfault corner frequency to that of the mainshock and ensures the total moment of the

summed subfaults is the same as the mainshock moment.
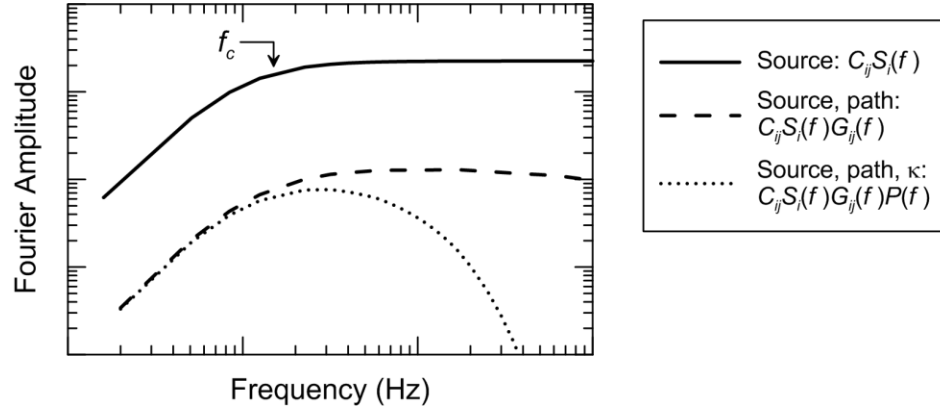
Figure 2.1. **Schematic illustration of source term, path operator, and effect of κ_o on Fourier amplitude spectrum.**

The path parameter $G_{ij}(f)$ is calculated as:

$$G_{ij}(f) = \frac{I_i(f)}{R_{ij}} \exp\left[-\pi f \sum_{k=1}^{L_j} \frac{\Delta t_{kj}}{Q_k(f)} \right] \tag{2.2}$$

where R_{ij} represents ray path distance from sub-fault i to the site along path j (i.e. path length),

$I_i(f)$ represents impedance effects calculated using quarter wavelength theory (Boore and

Joyner, 1997) that uses a crustal velocity model specified across k=1 to L_j layers having thickness

Δz_k, shear wave velocity V_{sk}, and whole path attenuation term Q_k. Many methods used *1/R* (*R* is

the distance from source to site) to approximate the distance attenuation (geometric

spreading) of high frequency body waves (Boore, 1983). Clearly this does not apply for longer

periods or situations where surface waves become more important, and more recent

applications utilize a geometric spreading term of the form *1/R$_x$*, where x can be a function of

distance and frequency to account for these complexities (e.g., Atkinson et al, 2009). In Eqn. (2.2), $1/R_{ij}$ corresponds to 1/path length, which is close to $1/R$ for a direct ray path. For a reflected ray path, the value of $1/R_{ij}$ is reduced due to the longer ray path. However, the full response at a particular site represents a summation over multiple ray paths, which can add constructively when several rays arrive at the site at approximately the same time. Assuming sufficient rays are considered, this approach naturally incorporates velocity model specific variations in geometric spreading due to crustal reflections and development of surface waves (Graves and Pitarka, 2010). The term Δt_{kj} represents the travel time of the given ray through layer k. In the limiting case of vertically propagating waves, Δt_{kj} is equal to its minimum value of $\Delta z_k / (V_s)_k$, although generally it is significantly larger than this due to non-vertical incidence. As shown in Figure 1, the path term $G_{ij}(f)$ reduces ground motions relative to the source spectrum, with the amount of reduction increasing with frequency.

Figure 2.2 shows location-specific and generic crustal velocity models. The Northridge model utilized by Graves and Pitarka (2010) ranges from 3.8 km/s at 31 km depth to 0.45 km/s at the surface with a V_{s30} = 865 m/s. The path attenuation term depends on the shear wave velocity of each layer and frequency as follows:

$$Q_z(f) = Q_0 f^x = \left[a + bV_{s,z} \right] f^x \tag{2.3}$$

where a, b, and x are empirical parameters generally taken as 25, 34, and 0.6 to 0.8, respectively (e.g., Aagaard et al., 2008; Graves and Pitarka, 2010). In Figure 2.3 we compare the Q implied by Eqn. (2.3) with Q models for California in the literature (Raoof et al., 1999; Fatehi and Herrmann, 2008). The mathematical description of distance attenuation typically includes geometric spreading terms and whole path attenuation related to Q. While the geometric

spreading terms in the work that produced the *Q* models in Figure 2.3 is not identical to that in Eqn. (2.2), the comparison nonetheless indicates that the overall levels of *Q* implied by Eqn. (2.3) with the aforementioned empirical parameters are comparable to those obtained by other researchers. Also shown in Figure 2.3 is a modest revision to the *Q* model that is developed subsequently in this paper.
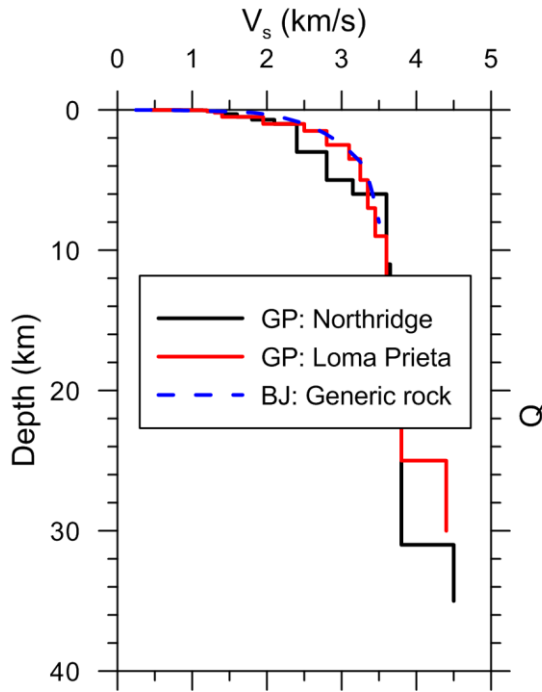
Figure 2.2. Crustal velocity models used by Graves and Pitarka (2010) for verifications of Northridge and Loma Prieta data and generic rock profile of Boore and Joyner (1997).
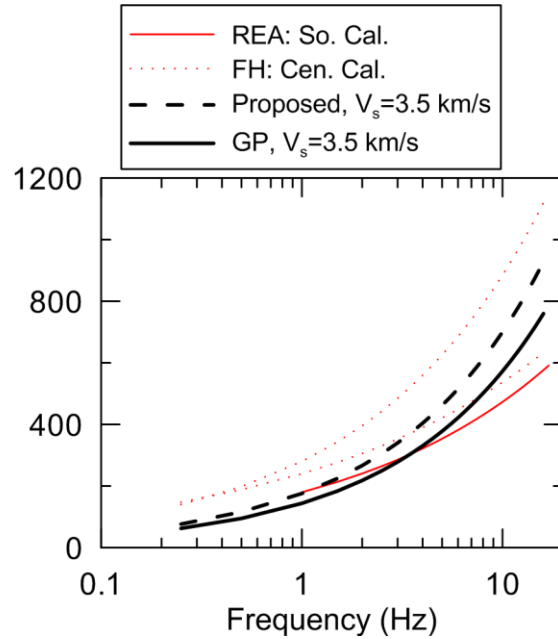
Figure 2.3. Crustal Q models from Raoof et al. (1999) and Fatehi and Hermann (2008) compared with default model from Graves and Pitarka (2010) and proposed adjustment (this study).

The term *P(f)* in Eqn. (2.1) models high frequency decay using the empirical κ_o parameter (Anderson and Hough, 1984):

$$P(f) = \exp(-\pi \kappa_0 f) \tag{2.4}$$

which is independent of distance in this formulation. Campbell (2009) presents typical values of κ_o, which was taken as 0.04 sec by Graves et al. (2011). The effect of κ_o on the Fourier spectrum is shown in Figure 2.1.

Each element of the high frequency simulation procedure described to this point is theoretically-based and deterministic, in the sense that specified equations are used to represent modeled phenomena. However, there are stochastic elements to the simulations that affect the Fourier amplitude and phase, including: (1) random frequency-to-frequency perturbations added to the smooth target spectrum shown in Figure 2.1 using the procedure of Boore (1983) and (2) spatially variable slip among the subfaults (described further below). Following the formulation of Boore (1983), the stochastic elements are introduced to the subfault source term $S_i(f)$ by first specifying a windowed time sequence of band-limited random white Gaussian noise with zero expected mean and variance chosen to give unit acceleration spectral amplitude on the average, which is then multiplied by the smooth target spectrum. In addition, the response for each subfault is delayed in time to account for rupture propagation across the fault and the travel time of the given ray.

Figure 2.4 shows an example of high- and low-frequency waveforms along with Fourier and response spectra from the broadband ShakeOut simulations of Graves et al. (2011). The final simulated waveform is obtained by combining the low and high frequency results using a set of matched Butterworth filters that do not alter the phase of the response and sum to unity at all frequencies. These filters have already been applied to the high- and low-frequency motions plotted in Figure 2.4, with the crossover of the filters occurring at 1 Hz. Waveforms and spectra from the combined motions are also shown in Figure 2.4. While an individual motion

may show a peak or valley near the matching frequency of 1.0 Hz (as well as at other frequencies), Graves and Pitarka (2010) show that when many motions are examined in an average sense, there are no systematic trends in the level of the simulated spectra near the matching frequency.
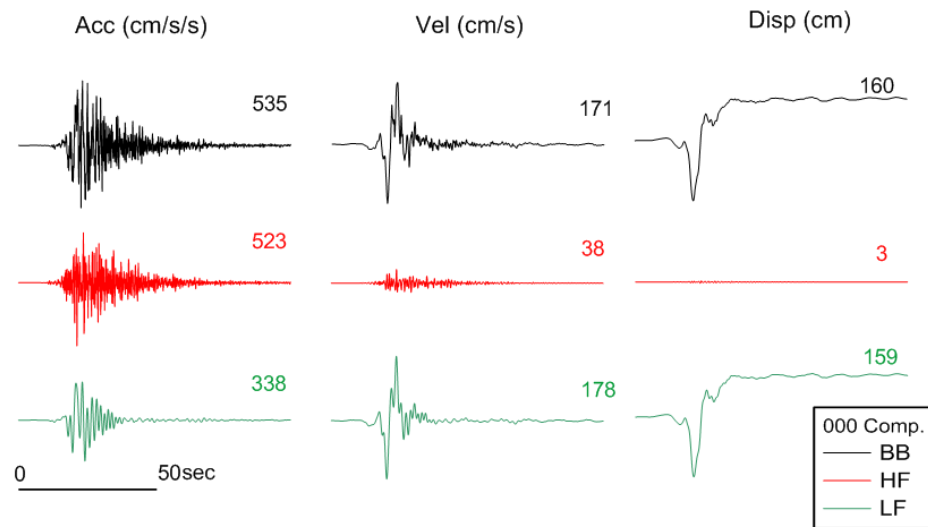
Figure 2.4(a)   **Acceleration, velocity, and displacement histories generated for M_w 7.8 ShakeOut event at site HLN, which is about 5 km from the San Andreas fault in the San Bernardino region. Results from the high frequency (HF) and low frequency (LF) simulations are shown along with the full broadband (BB) motion.**
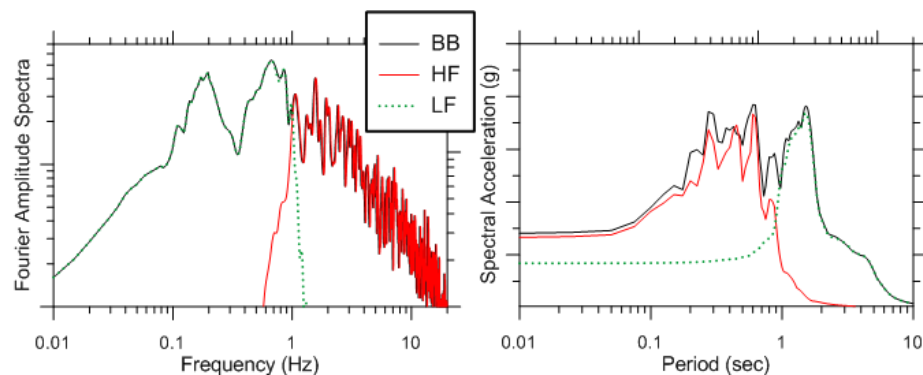
Figure 2.4(b)   **Fourier amplitude spectra and 5% damped response spectra of BB, HF, and LF acceleration histories from Figure 2.4(a).**

2.3 HIGH FREQUENCY SIMULATIONS FOR PARAMETER CALIBRATION

2.3.1 Conditions Considered

The simulated events are strike-slip earthquakes at four magnitudes (5.0, 6.5, 7.25, 8.0). As shown in Figure 2.5, there are two events per magnitude having different slip distributions (but the same moment). The faults are vertically dipping and the rupture is bilateral with the epicenter at the middle of the fault. Additional details on the simulated fault ruptures are given in Table 2.1. The use of the Frankel (1995) shaping filter ensures the simulation results are relatively insensitive to subfault dimension (Boore, 2009), thus the choice of specific subfault size is based primarily on computationally efficiency. The spatial variability of slip incorporates randomness and spatial correlation as described in Graves and Pitarka (2010). The level of slip randomness and spatial correlation affects ground motion dispersion; for the present application it was set at the levels described in Graves and Pitarka (2010), which is less smooth than the source models used in some previous applications such as ShakeOut (Graves et al., 2011).
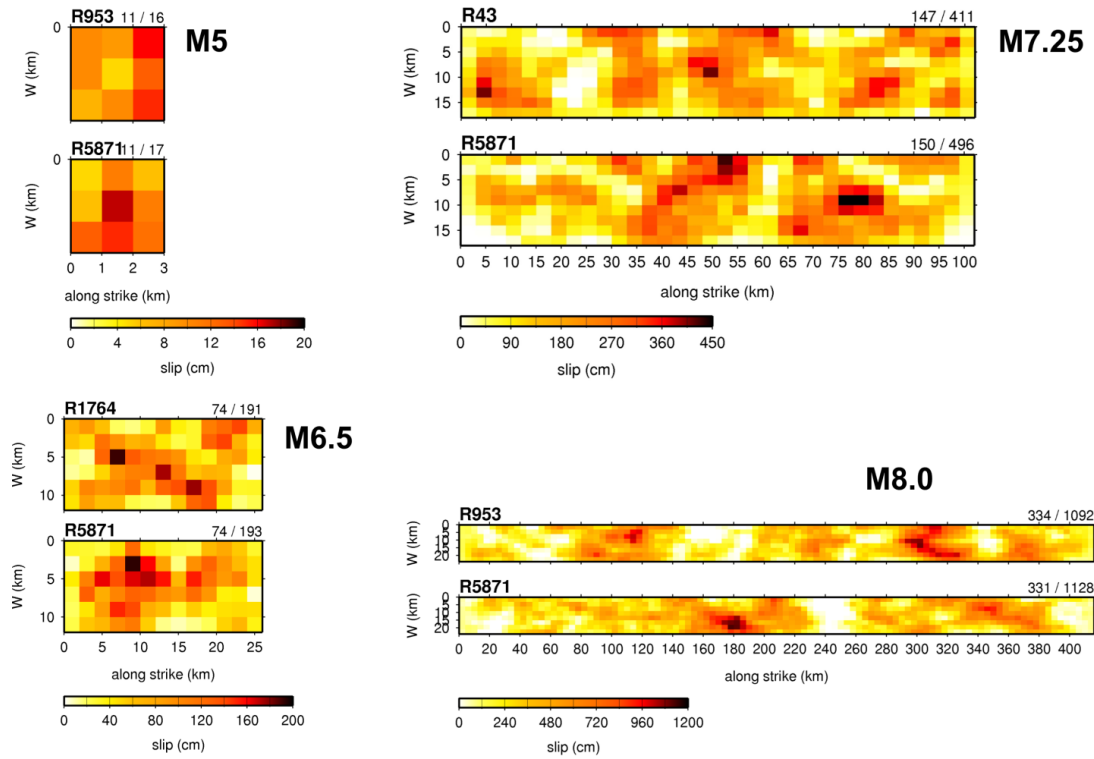
Figure 2.5. Slip models for M_w 5, 6.5, 7.25 and 8 scenario earthquakes (from left to right). Average and maximum values of the slip are shown on the top right of each model.

Table 2.1. Attributes of simulated events for high frequency ground motion simulations.

M_w	Length (km)	Width (km)	Top Depth (km)	Subfault Size (km x km)
5.0	3	3	10	1 x 1
6.5	26	12	0	2 x 2
7.25	102	18	0	3 x 2
8.0	416	24	0	4 x 3

The locations of simulated motions relative to the source faults are shown in Figure 2.6.

Each array has recordings on lines radiating out from the fault. On each radiating line there are

18 stations at the following distances from the surface projection of the fault: 1.0, 1.5, 2.0, 3.0,

5.0, 7.0, 10, 15, 20, 30, 50, 70, 100, 120, 140, 160, 180, 200 km.
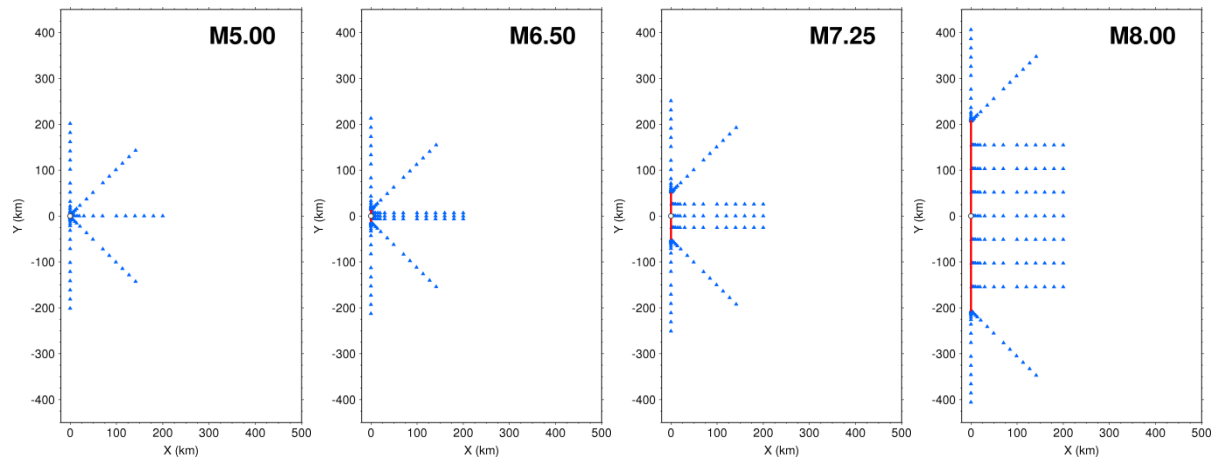
Figure 2.6. Station arrays for the four simulated strike-slip earthquakes. Red line indicates the fault.

2.3.2 Comparison of Motions from High Frequency and Broadband Simulations

The high frequency simulation procedure utilized for the strike slip earthquakes depicted in Figures 2.5 and 2.6 is first applied to the ShakeOut source model (Graves et al., 2011) to investigate the relationship between short-period *IMs* from high frequency and broadband simulations. The Graves et al. (2011) source model no longer reflects current recommendations regarding source heterogeneity (it has less), but this approach is used here because the ShakeOut simulations associated with that source model are a familiar point of reference. Figure 2.7 shows the variation of PGA and 0.1, 0.3, 1 sec pseudo spectral accelerations (5% damping) with distance from the broadband simulations along with medians (μ) and medians $\pm$ two log standard deviations for data within distance bins. The binned quantities are also shown for the high frequency simulations. The median and dispersion trends from the two data sets are similar, indicating that the high frequency component of the simulation procedure has a dominant effect on each of the considered high frequency intensity measures (PGA and spectral

ordinates at periods < 1.0 sec). This finding supports focusing the calibration process on the

high-frequency component of the simulation procedure to remove biases in simulated short

period *IMs*.
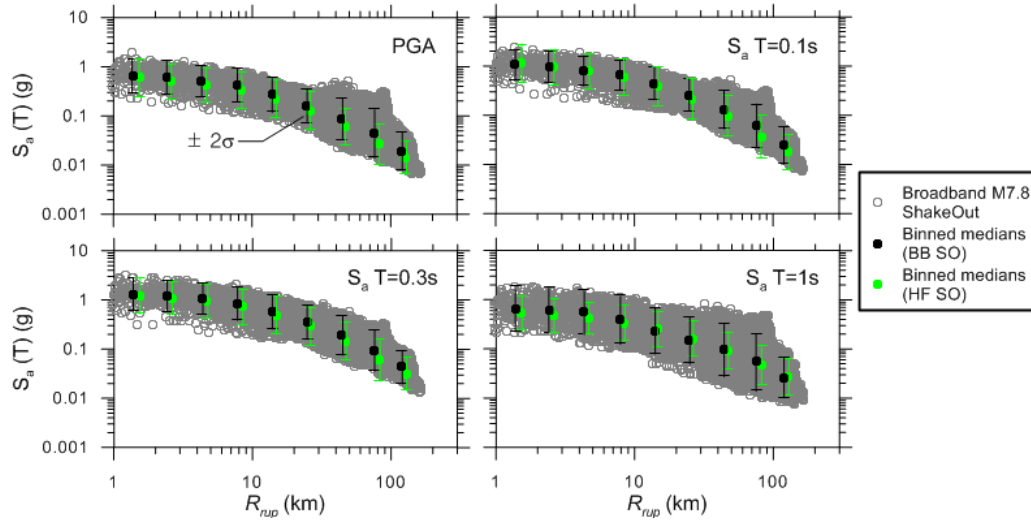
Figure 2.7.   **PGA and spectral accelerations from ShakeOut simulation using full broadband (BB) waveforms and high-frequency waveforms. Site conditions in the two simulations are not identical, being location-specific according to a basin model for BB and set to a common crustal profile for HF.**

Star et al. (2011) found that high frequency *IMs* from the ShakeOut broadband

simulations attenuated faster with distance than suggested by the NGA GMPEs. This was found

by calculating residuals between each simulated motion (treated like data) and the median

model prediction from a GMPE as follows:

$$R_i(T) = \ln\left(S_a(T)\right)_{sim,i} - \ln\left(S_a(T)\right)_{GMPE,i} \tag{2.5}$$

where index *i* refers to a particular location where ground motions were simulated

(latitude and longitude), $S_a(T)_{sim,i}$ refers to the 5% damped spectral acceleration of the

simulated motion for oscillator period *T* at location *i*, $S_a(T)_{GMPE,i}$ refers to the median spectral

acceleration for location *i* predicted by a GMPE considering the earthquake magnitude, site-source distance, and site condition (different for a given site in the BB and HF simulations), and R_i is the residual in natural logarithmic units. Residuals were calculated relative to the Abrahamson and Silva (2008), Boore and Atkinson (2008), Campbell and Bozorgnia (2008), and Chiou and Youngs (2008) GMPEs (referred to subsequently as AS, BA, CB, and CY).

Star et al. (2011) found residuals $R_i(T)$ to have a statistically significant slope with respect to rupture distance (R_{rup}) for the ShakeOut event for response spectral accelerations at periods under 5 sec. Using both the high-frequency and broadband simulations, we calculate median values of $R_i(T)$ within distance bins:

$$\bar{R}_k(T) = median \left[R_i(T) \right]_{i=1..N_k} \tag{2.6}$$

where *k* is an index for a particular distance bin having N_k simulated motions. Distance attenuation trends are investigated by plotting $\bar{R}_k(T)$ for the two sets of simulations (broadband and high frequency only). As shown in Figure 2.8 for the 0.3 sec spectral acceleration and the BA GMPE, the slopes are similar for the broadband and high frequency simulations. Similar results are obtained at other periods (Stewart et al., 2011). These results verify that the high frequency simulations reproduce the trends from broadband simulations that we seek to adjust through calibration. We undertake this in the following section.
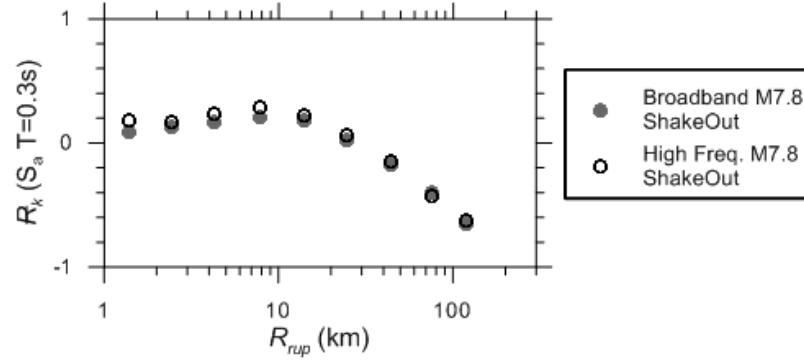
Figure 2.8.   Median residuals of simulated motions (0.3 s S_a) for M_w 7.8 ShakeOut event from broadband procedure and its high-frequency component. The similarity of the slope of residuals with distance demonstrates that the high frequency component of the simulation procedure is responsible for the distance attenuation trend. Residuals calculated with respect to Boore and Atkinson, 2008 (BA) GMPE.

2.4   SIMULATION CALIBRATION

2.4.1 Calibration Procedure for Distance Attenuation

Input parameters required to perform broadband simulations using the hybrid procedure of Graves and Pitarka (2010) include those for the kinematic rupture model (fault dimensions, slip distribution, rise time, rupture velocity, etc.), additional parameters for the high frequency source spectrum [c_0 (used for corner frequency), stress parameter σ_p, sub-fault dimension dl], and those related to analysis of Green's functions (crustal velocity profile, Q model, number of ray paths, geometric spreading).

All of these parameters are potential candidates for model calibration. To address the too-fast distance attenuation problem, we choose to focus on the number of ray paths, which is an attempt to account for changes in geometric spreading, and the Q model. We recognize that a variable exponent on the R_{ij} term in Eqn. (2.2) (to capture geometric spreading effects) could also be used to modify distance attenuation. Our approach was selected both because it is

28

more convenient to implement and because the observed distance attenuation misfits occur beyond about 20-50 km (geometric spreading dominates distance attenuation at closer distances, where the trends are unbiased). The original ShakeOut simulations used only two rays for the high-frequency modeling: direct and Moho-reflected (Graves et al., 2011). Within about 100 km of the fault, these two rays are dominant; however, at further distances, additional ray paths including multiple surface and Moho-reflected phases, as well as other super-critically crustal reflected phases, can become important. At large source to site distance, many rays may need to be considered to obtain the full response, although the dominant high-frequency phases are surface and Moho-reflected rays (e.g., Ou and Herrmann, 1990). For our calibration experiments, we have utilized a total of four rays. In addition to the direct and Moho-reflected rays, we also consider 1) a ray initially traveling upward from the source, reflecting at the surface and traveling down to the Moho, then reflecting back to the site and 2) another ray initially traveling down from the source to the Moho, reflecting back up to the surface, reflecting back down to the Moho, then reflecting back to the site. Sensitivity tests using combinations up to a total of 10 rays indicated that the distance attenuation between 100 to 200 km was not strongly affected when more than four rays were used.

We use the crustal velocity profile of Boore and Joyner (1997), which is modified to have a V_{s30} of 1100 m/s (Figure 2.2). This site condition was selected so that the simulations are consistent with the hard rock site condition of the NGA GMPEs, effectively removing nonlinear site amplification effects from the analysis. Source-related parameters will shift up or down the Fourier amplitude spectrum or portions thereof, but will generally not significantly affect the variation of ground motion with distance. We adjusted Q through parameter a (Eqn. 2.2), which

was a = 25 in the reference broadband simulations. We did not perform a formal optimization exercise, but found through trial and error that $a \approx$ 55-60 (we use 57) with four rays effectively removes distance attenuation bias, which we demonstrate below. Increasing Q in this manner decreases material damping in the crust, hence decreasing the attenuation of ground motion. The effect of the increased number of ray paths was modest by comparison.

The effects of the modifications are demonstrated in Figure 2.9(a) where simulated spectral accelerations for the M_w 7.25 event are shown for the original (low) and proposed (high) Q. The Q increase raises spectral accelerations noticeably for rupture distance R_{rup} > ~50 km (e.g., by approximately 50% at 100 km). Figure 2.9(b) shows spectral acceleration residuals calculated using Eqn. (2.5), which fluctuate with R_{rup} but increase markedly at high Q for R_{rup} > 50 km.
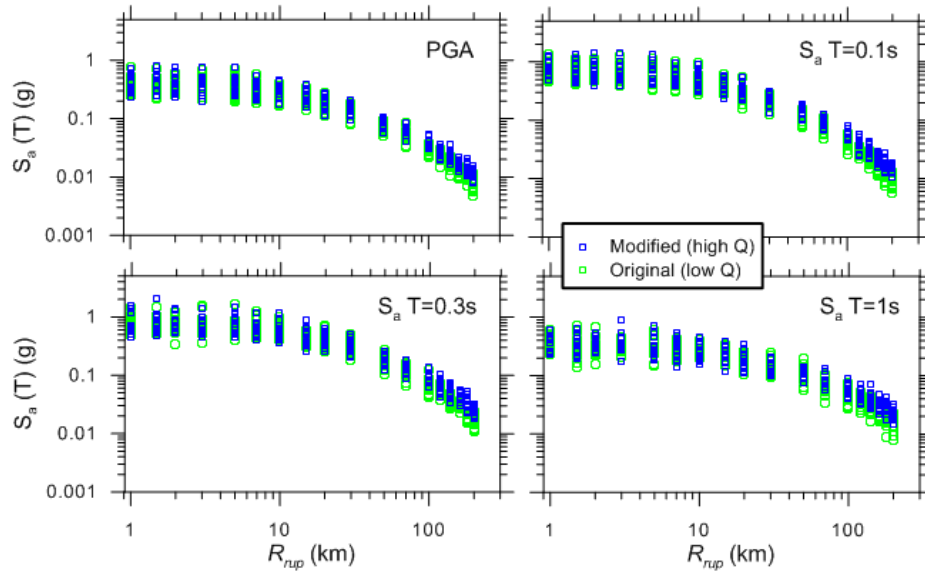
Figure 2.9(a)   Spectral accelerations for original (low Q, 2 rays) and modified (high Q, 4 rays) high frequency simulations of M_w 7.25 strike-slip earthquake.
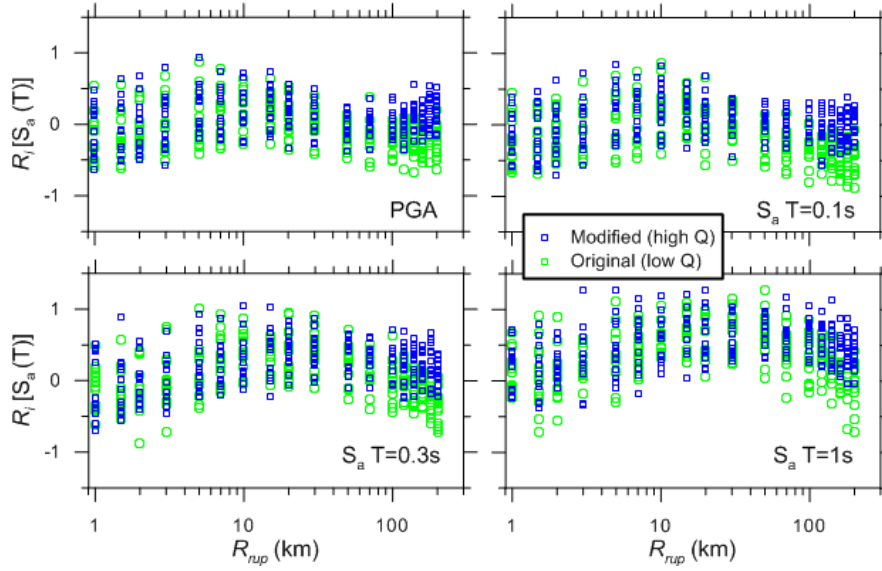
Figure 2.9(b)   Spectral acceleration residuals from simulated motions from Figure 2.9(a) relative to BA GMPE.

The simulation results can be more easily visualized using median residuals ($\bar{R}_k(T)$ per Eqn. 2.6) as shown in Figure 2.10. The figure shows median residuals for all four GMPEs using the proposed (high) Q and one reference set of residuals (using BA) for low Q. Note that the AS and CB residuals have a relatively strong negative trend at large distance because the GMPE slope (in log-log space) is effectively constant with respect to distance beyond the near-fault region, whereas the data falls off relatively rapidly for R_{rup} > ~50 km as a result of the Q effect (shown in Figure 2.10 as a downward slope in the residuals). The BA and CY GMPEs have a distance-dependent slope that better accommodates this trend in the ground motions.
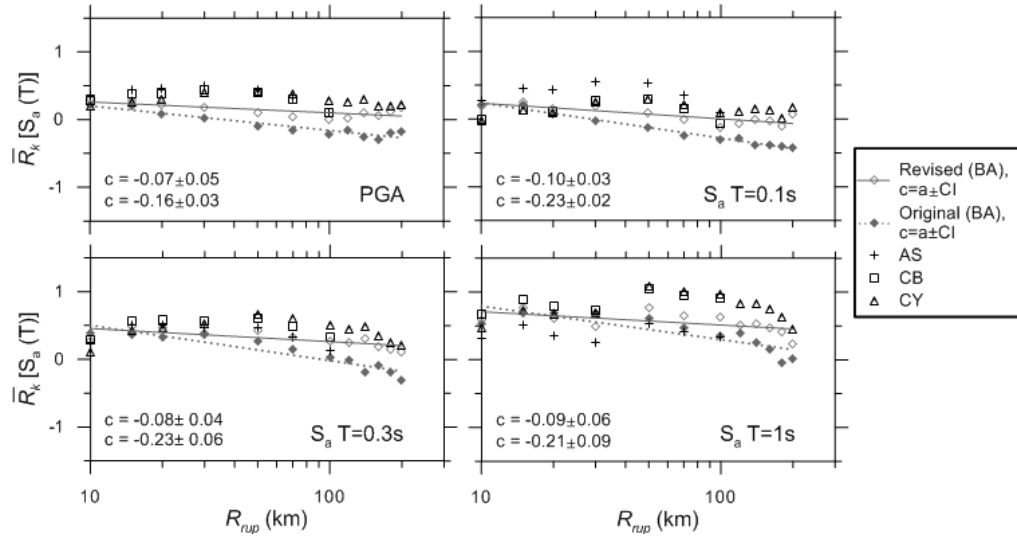
Figure 2.10. Median residuals for modified (high Q, 4 rays) high frequency simulations of M_w 7.25 strike-slip earthquake (AS, BA, CB, CY GMPEs). Also shown are results for original (low Q, 2 rays) high frequency simulation procedure (BA GMPE only). Fit lines with slope care shown for BA; the slope is within its confidence interval and hence not significantly different from zero for the modified simulations. The slopes are significant for the original simulation procedure.

The extent to which the data demonstrate distance-attenuation bias can be concisely represented by the slope of the median residuals in Figure 2.10. This slope (denoted as c) is established by least-squares linear regression, as illustrated for BA in Figure 2.10. The fit is taken from 10 - 200 km distance for BA and CY but only from 10 - 100 km for AS and CB due to their restrictive distance attenuation function described above. Figure 2.11 shows slopes averaged across the four GMPEs as a function of period for the original and proposed Q values. The slopes are markedly negative for the original Q, slightly negative for the modified Q for M_w 5 and 6.5, and near zero for the modified Q for M_w 7.25 and 8. We judge this lack of trend for the larger simulated magnitudes to indicate the level of Q modification is adequate. Further increases of Q could have removed the bias at lower magnitudes, but at the expense of too-

slow distance attenuation for large magnitude. Since the value of simulations is principally at larger magnitudes where recordings are sparse, we chose to optimize the fit for those larger magnitudes.
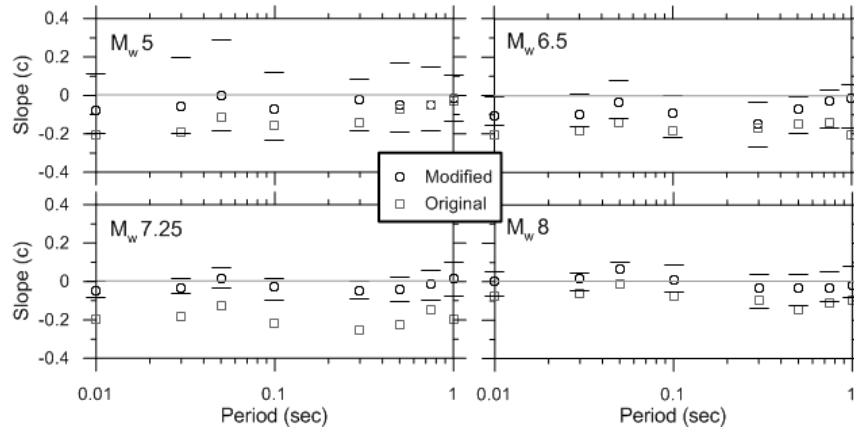
Figure 2.11. **Slope parameter c (non-zero slope indicates misfit from GMPE) as function of spectral period for original (low Q, 2 rays) simulations and proposed modification (high Q, 4 rays). Values plotted are the averages across the four GMPE using 10-200 km for BA and CY and 10-100 km for AS and CB. Solid lines indicate range of slope parameter across GMPEs for the modified case.**

We checked our results for *Q* modification using the Northridge rock crustal velocity profile shown in Figure 2.2, which has V_{s30} = 865 m/s (compare to V_{s30}= 1100 m/s in the generic rock profile). The changed crustal velocities affect the ground motions but do not appreciably change distance attenuation trends (or their sensitivity to *Q*).

2.4.2 Calibration Procedure for Intra-Event Dispersion

To address the too-low intra-event dispersion, we began by randomizing crustal velocities relative to the Boore and Joyner (1997) model, which also affects *Q* values through Eqn. (2.2). While this approach has a physical basis, it only produces a modest increase in the dispersion of the simulated motions since the Fourier phase at high frequencies is already fully random and

33

the impact of randomizing path-related parameters (which affect Fourier amplitude) are smoothed out due to the use of quarter-wavelength impedance functions (Boore and Joyner, 1997). An alternative approach is to simply randomize Fourier amplitudes directly. In doing so, we do not specifically attribute the individual contributions of the variations to source, path or site effects, but rather we are designing a modification to the modeling algorithm that represents the combination of all these factors. The randomization takes the Fourier amplitude from Eqn. (2.1) (after conversion to natural log units) as a median of a normal distribution (denoted $A(f)$). Modifications are calculated as:

$$A_r(f) = A(f)\exp(\varepsilon\sigma_A) \tag{2.7}$$

where $A_r(f)$ denotes the randomized Fourier amplitude, σ_a is a frequency-independent log-normal standard deviation optimized in the present work, and ε is selected using a random number generator that produces realizations according to the standard normal distribution (mean of zero, standard deviation of one). This randomization assumes perfect correlation between frequencies and no correlation between simulations at different locations, which causes the adjusted Fourier spectrum per Eqn. (2.7) to shift up or down uniformly. We recognize that this is not strictly correct. Fourier amplitudes for a single site at neighboring frequencies exhibit only modest correlation (Ancheta et al., 2011), not the perfect correlation assumed here. For site locations separated by 100s of meters, spatial correlations are practically negligible at high frequency (Ancheta et al., 2011), which is consistent with the lack of correlation taken here.

Figure 2.12 shows intra-event dispersion for rock site conditions (V_{s30} = 1100 m/s) from the NGA GMPEs as a function of period along with the dispersion from the non-randomized and

randomized simulation procedures. All simulations utilized fault slip randomness and spatial correlation as described in Graves and Pitarka (2010) along with the modified path parameters described above (high Q, 4 ray paths). The non-randomized simulations produce dispersions significantly lower than those from GMPEs, except at M_w 8. The dispersion matches shown in Figure 2.12 were achieved with a Fourier amplitude randomization of $\sigma_A = 0.45$ (natural log units) for the M_w 5 and 6.5 simulations, $\sigma_A = 0.35$ for the M_w 7.25 simulation, and $\sigma_A = 0$ (no randomization) for the M_w 8 simulations. The reason for the magnitude-dependent σ_A is that slip randomization significantly affects ground motion dispersion when the fault dimensions are comparable or larger than the spatial extent of the stations used in computing the residuals. To reinforce this point, simulations were performed for the M_w 8 event using a smoothed slip model (derived by scaling the standard deviation of slip variations by a factor of 0.65, which is comparable to that used in ShakeOut); as shown in Figure 2.12, the intra-event dispersion from those simulations is markedly reduced.
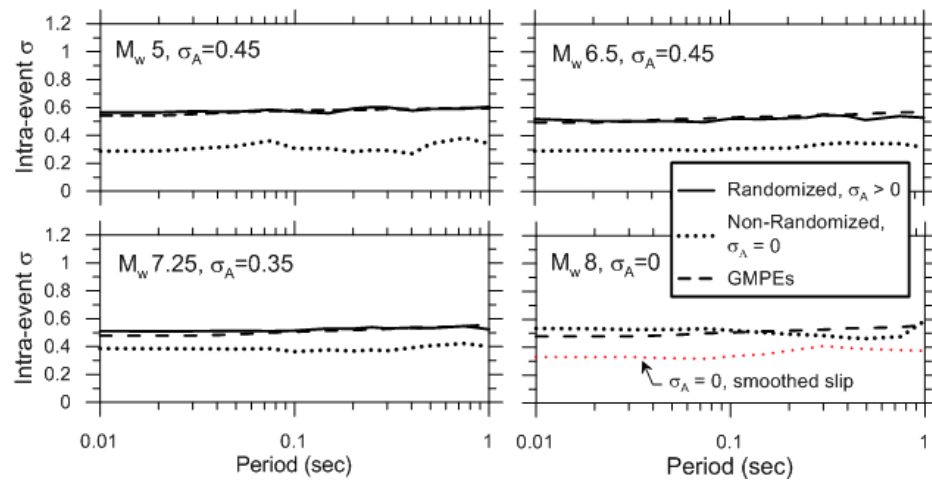
Figure 2.12. Intra-event standard deviation σ for original (low Q, 2 rays) simulations and proposed modification (high Q, 4 rays) with magnitude-dependent randomization. All standard deviation terms plotted are the averages across the four NGA GMPEs.

The variation of dispersion with distance is shown in Figure 2.13 for the M_w 6.5, 7.25, and 8 simulations. Results are shown with and without Fourier amplitude randomization. Simulations without randomization ($\sigma_A = 0$) show a dispersion decay with distance, whereas the introduction of Fourier amplitude randomization markedly reduces the distance trend. We interpret these trends as indicating that (1) randomization of the fault slip function introduces high dispersion near the fault but relatively low dispersion at greater distance (i.e., for rupture distances larger than the source dimension) that is significantly below empirical dispersion estimates and (2) randomization of Fourier amplitudes modestly affects near fault dispersion but significantly affects dispersion at large distances. For the M_w 6.5 and 7.25 simulations, the overall dispersion levels with the proposed Fourier amplitude randomization are compatible with empirical estimates across the distance range considered. For the M_w 8 simulations, the near-source dispersion levels match empirical estimates without Fourier amplitude randomization but fall below empirical estimates beyond about 10 - 20 km. We have chosen to not randomize these simulations.

A potential refinement of our methodology that was not pursued would be to make σ_A both magnitude and distance-dependent. In future research, an increase of σ_A with distance could be implemented to remove the distance trends in Figure 2.13(c).
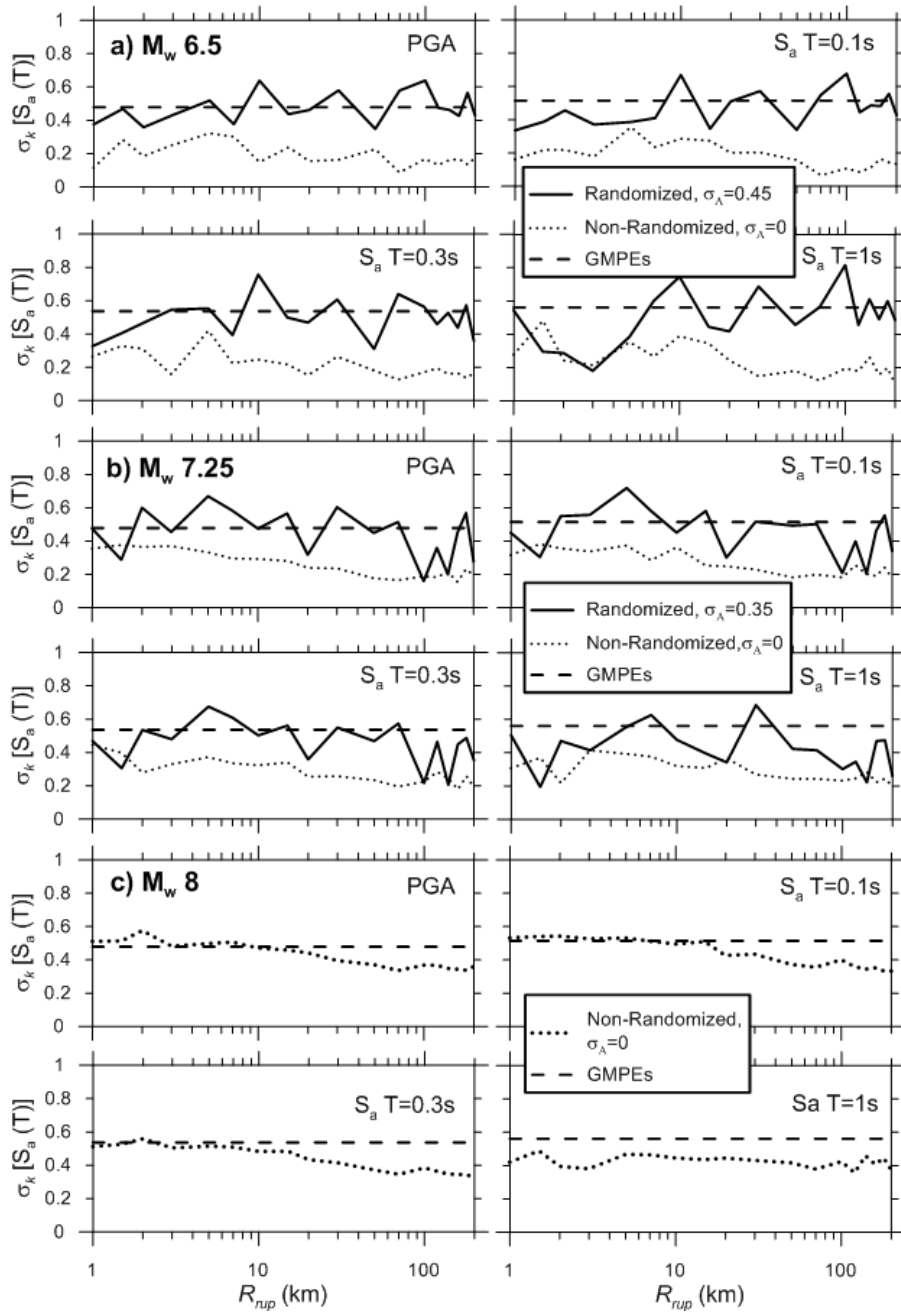
Figure 2.13. Variation with distance of intra-event standard deviation of modified simulations (high Q, 4 rays) relative to BA GMPE before and after randomization of Fourier amplitudes for (a) M_w 6.5, (b) M_w 7.25 and (c) M_w 8 strike slip earthquake. Intra event standard deviation terms plotted for GMPEs are the averages across the four NGA GMPEs.

37

2.5   VERIFICATION OF PERFORMANCE IN BROADBAND SIMULATIONS

The calibration process described in previous sections operated on the high frequency component of the simulation procedure. Here we verify that the modified high frequency procedure generates satisfactory results when implemented in the full hybrid broadband methodology. This is done using broadband simulations of the ShakeOut event. The ShakeOut simulations were repeated using a revised source model reflecting the more heterogeneous slip distribution produced by the Graves and Pitarka (2010) method as well as the increased Q and the use of four ray paths instead of two. Because the magnitude is near 8, the Fourier amplitudes were not randomized ($\sigma_A = 0$).
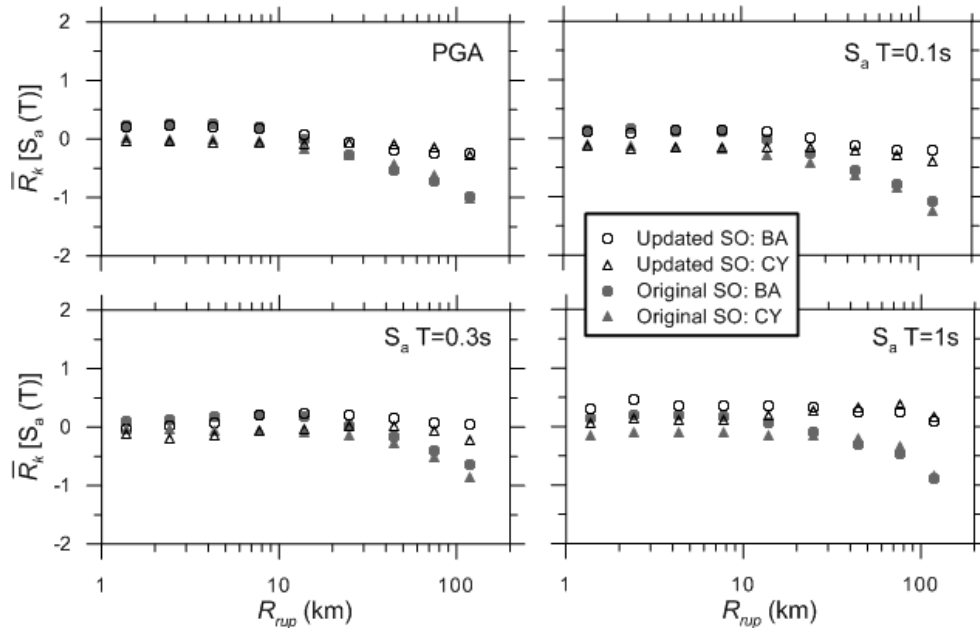
Figure 2.14.   Median residuals relative to BA and CY GMPEs within distance bins for updated and original (a) ShakeOut simulations and (b) Intra-event standard deviation of original and updated ShakeOut simulations compared to GMPEs.

38

Residuals for both the original and updated ShakeOut simulations were calculated relative to the NGA GMPEs using Eqn. (2.5) and median residuals $[\bar{R}_k(T)]$ were calculated within distance bins using Eqn. (2.6). In Figure 2.14, those median residuals are plotted versus R_{rup} for the various intensity measures. The distance attenuation bias from the original ShakeOut simulations has been significantly reduced for the BA and CY GMPEs. Substantial misfit remains (not shown in Figure 2.14) for AS and CB as a result of their distance attenuation functions, as described earlier (i.e., Figure 2.10). At a distance of 100 km, the difference between the original and updated median residuals for BA and CY is an increase of approximately 0.65 (in ln units), which nearly doubles predicted ground motions at this distance.

To facilitate comparisons to GMPE intra-event dispersions, we evaluate period-dependent intra-event dispersions that represent average values for R_{rup} < 10 km and R_{rup} > 100 km. These dispersions are calculated as:

$$Var(R) = \frac{\sum_{k=1}^{N_{bins}} \sum_{i=1}^{N_k} \left(R_i - \bar{R}_k\right)^2}{\sum_{k=1}^{N_{bins}} N_k - N_{bins}}$$

$$\sigma = \sqrt{Var(R)}$$

(2.8)

where N_{bins} is the number of distance bins within the respective distance ranges (four for R_{rup} < 10 km; one for R_{rup} > 100 km) and N_k is the number of simulated motions in bin k. By subtracting distance-bin medians $\bar{R}_k$ in the variance calculation, bias in the distance attenuation is not mapped into the dispersion calculation. The subtraction of N_{bins} in the denominator

reflects the number of degrees of freedom in the variance calculation (since separate means are calculated for each bin).

Figure 2.15 presents results of the above calculation, in which σ terms are computed using Eqn. (2.8) for all four NGA GMPEs and then averaged. The average intra-event standard deviation terms from the GMPEs are also shown. At close distances, the updated ShakeOut dispersions are slightly lower than those from GMPEs, especially between 0.1 and 1.0 sec. At greater distances, the misfit is greater, which is expected due to the lack of Fourier amplitude randomization for this magnitude, as described in the previous section. Stewart et al. (2011) show that if Fourier amplitude randomization at the level of σ_A = 0.35 is added to the high frequency simulated motions; near-source dispersion becomes slightly over-estimated while dispersion at far distances from the source remains under-estimated. Hence, it does not appear that Fourier amplitude randomization alone can achieve dispersion levels compatible with GMPEs over a wide distance range.
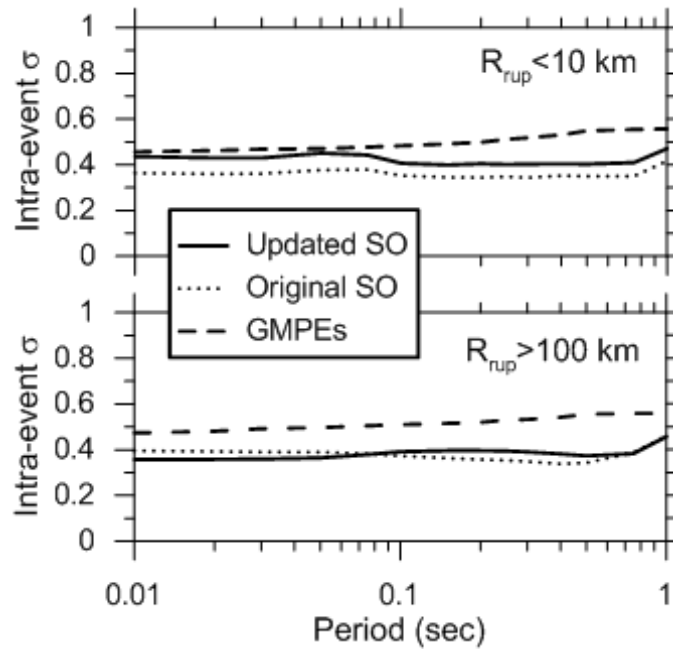
Figure 2.15. Intra event standard deviation for the updated and original ShakeOut simulations for near- and far-field distance bins. All standard deviation terms plotted are the averages across the four NGA GMPEs. The updated ShakeOut simulations have no Fourier amplitude randomization.

2.6 INTERPRETATION AND CONCLUSIONS

Broadband ground motion simulation procedures typically utilize physics-based modeling of source and path effects at low frequencies coupled with semi-stochastic procedures at high frequencies. Previous validation of the hybrid procedure of Graves and Pitarka (2010), which was used with some modification in the ShakeOut exercise and other earthquake scenario studies, demonstrated faster distance attenuation and lower dispersion of high-frequency ground motions than in empirical ground motion equations (Star et al., 2011).

As discussed by Star et al. (2011), when comparing attributes of simulated motions to GMPEs, one must consider whether a misfit indicates a deficiency with the simulations, the GMPEs, or both. The critical aspect is the degree to which the effect under consideration is well

constrained in the empirical model. This is reflected to some extent by the consistency of GMPEs, which in turn relates to the sophistication of the GMPE functional forms (admittedly subjective) but also to the amount of data available to constrain those portions of the empirical models. With regard to the distance attenuation discrepancy, attenuation of high-frequency *IMs* in the NGA models is well constrained up to approximately 100 km for magnitudes between approximately 5.5 and 7.5 and the various models are reasonably consistent (Abrahamson et al. 2008). While the available data are sparse at the large magnitudes associated with the ShakeOut event, the potential for a large shift in distance attenuation rates from M_w 7.5 to 7.8 is low. Accordingly, we judge the deficiency in this case to lie mostly with the simulation. A similar rationale can be applied to the standard deviation terms. This motivates the work presented in this article, in which we seek to calibrate high frequency components of the Graves and Pitarka (2010) simulation procedure to remove the too-fast distance attenuation and the too-low intra-event dispersion.

The high-frequency component of the simulation procedure combines a deterministic Fourier amplitude spectrum that is a function of closed-form source, path, and site models with a random phase. We increase the crustal Q term to reduce the distance attenuation bias. This is done by increasing parameter a in the frequency-independent portion of the Q model (Eqn. 2.2) from 25 to 57. Both the original and adjusted Q models are within the range provided by previous studies of Q using California earthquakes (Figure 2.3).

We introduce random site-to-site variations to the Fourier amplitudes using a magnitude dependent log-normal standard deviation (0.45 for $M_w \leq 6.5$, 0.35 for M_w 7.25, 0 for M_w 8). In general, this raises the intra-event standard deviations of response spectral

accelerations to levels consistent with NGA GMPEs in terms of both their overall level and their variation with period. For the M_w 8 simulations, dispersions from the simulated motions fall-off with distance and are well below those from GMPEs beyond about 10 - 20 km.

3   SITE RESPONSE IN NEHRP PROVISIONS AND NGA MODELS

3.1   INTRODUCTION

Site factors are used to modify ground motions from a reference rock site condition to reflect the influence of geologic conditions at the site of interest. Site factors typically have a small-strain site amplification (linear) that captures impedance and resonance effects coupled with nonlinear components. They express the effects of shallow site conditions on various ground motion *IMs* as a function of V_{s30}. The parameter V_{s30} represents the average shear wave velocity of a site in the upper 30 m, and is computed as the ratio of 30 m to shear wave travel time through the upper 30 m of the site. The parameter V_{s30} is an index of velocity profile and used as a key parameter for general site classifications.

     The work presented in this chapter represents the results of collaborative work involving the Task 8 working group of the NGA-West 2 project. The results given here have been previously presented by Seyhan and Stewart (2012).

3.2 SITE EFFECTS IN NEHRP PROVISIONS

Site factors in the NEHRP Provisions, which are used in building codes worldwide and also in financial loss modeling for insurance applications, are based on site categories derived from V_{s30}. The NEHRP Provisions and Commentary (BSSC 2003) provide the documentation from which seismic provisions in building codes are periodically updated (every four years, last update in 2009). One important aspect of the NEHRP Provisions and Commentary is the specification of design-basis ground motions, which are derived for rock site conditions at 0.2 sec and 1.0 sec period from probabilistic seismic hazard analysis (PSHA) and then modified by site factors. The PSHA-based rock site ground motions used in building codes are mapped by the U.S. Geological Survey (USGS) (http://earthquake.usgs.gov/hazards/). In the 2008 version of the maps, the reference site condition is specified as V_{s30} = 760 m/sec, where V_{s30} is the average shear wave velocity computed as the ratio of 30 m to shear wave travel time through the upper 30 m of the site.

As shown in Table., NEHRP site factors are based on site classes derived from V_{s30}. An exception to the V_{s30} criteria is made for soft clays (defined as having undrained shear strength < 24 kPa, plasticity index > 0.20, and water content > 0.40), for which Class E is assigned if the thickness of soft clay exceeds 3 m regardless of V_{s30}. The site factors are intended to modify ground motion relative to the reference condition used in development of the PSHA maps, which is at the boundary between Classes B and C (V_{s30} = 760 m/sec).

Table.3.1.   Site Classes in NEHRP Provisions (Martin 1994).

NEHRP Category	Description	Mean Shear Wave Velocity to 30 m
A	Hard rock	> 1500 m/s
B	Firm to hard rock	760 - 1500 m/s
C	Dense soil, soft rock	360 - 760 m/s
D	Stiff soil	180 - 360 m/s
E	Soft clays	<180 m/s
F	Special study soils, e.g., liquefiable soils, sensitive clays, organic soils, soft clays > 36 m thick	

Figure 3.1 presents the short- and long-period NEHRP site factors (BSSC 2003) F_a and F_v, which depend on both site class and intensity of motion on reference rock. The ground motion parameters for the reference site condition used with site factors are: (1) S_s - the pseudo spectral acceleration (PSA) at 0.2 sec (used with F_a); and (2) S_1 – pseudo spectral acceleration (PSA) at 1 sec (used with F_v).
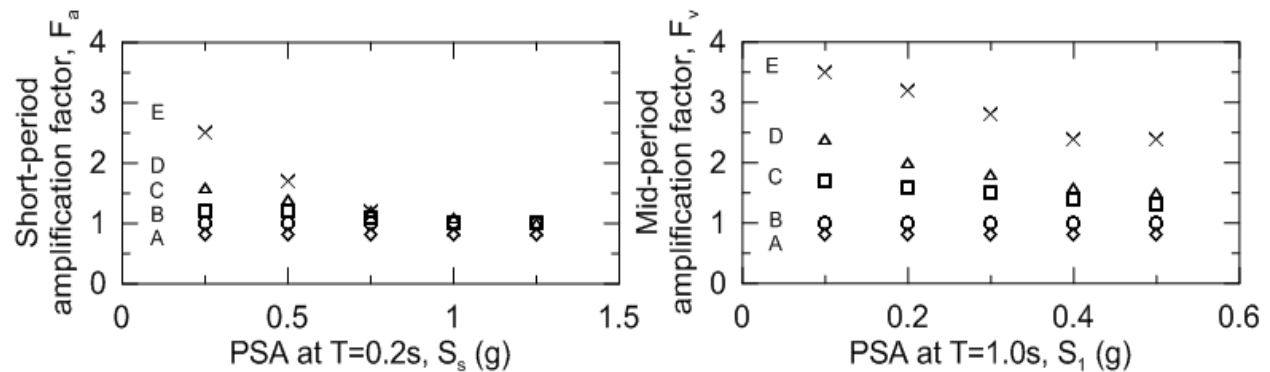
Figure 3.1.   Site factors F_a and F_v in NEHRP Provisions (BSSC 2003).

46

Some physical processes underlying the trends in the NEHRP site factors shown in Figure 3.1 are as follows:

(1) Site factors decrease with increasing V_{s30}. This effect is related to the impedance contrast between the shallow soil sediments and the underlying stiffer sediments and rock. Slow velocities in shallow sediments will amplify weak- to moderate-amplitude input motions, especially near the fundamental frequency of the soil column.

(2) Site factors decrease with increasing S_s or S_1 and the rate of decrease is fastest for soft soils. As ground motion amplitude increases, the shear strains in the soil increase, causing increased hysteretic damping in the soil. The increased damping dissipates energy and reduces ground motion levels. Because softer sediments develop larger strains than stiffer sediments, this effect is most pronounced for Class E and is less significant for stiffer sites.

(3) Site factor F_a (short periods) decreases more rapidly with increasing S_s than does F_v with S_1. The damping effect described in (2) acts on each cycle of ground motion. High-frequency ground motions will have larger fractions of wavelengths within the soil column than low-frequency motions. Because the soil has more opportunity to influence high-frequency motions, it produces greater nonlinearity.

Site factors can be developed using theoretical and empirical approaches. Existing NEHRP site factors were developed empirically for relatively low input rock ground motions (peak accelerations or S_l near 0.1g) and have levels of nonlinearity derived from simulations. Additional details on the development of NEHRP factors utilizing empirical and theoretical methods are given in the following sections. Justification for the use of V_{s30} as a site parameter is beyond the scope of this thesis, but is discussed elsewhere, including Stewart et al. (2001).

3.2.1 Empirical Basis for Weak Motion NEHRP Site Factors

The empirical basis for the relatively weak motion NEHRP site factors was developed by Borcherdt (1994b), Borcherdt and Glassmoyer (1994), and Joyner et al. (1994), who examined ground motions from the 1989 Loma Prieta earthquake recorded on a variety of site conditions varying from soft clay to rock in the San Francisco Bay Area. Site conditions at recording sites were generally characterized using bore-hole seismic-velocity measurements. A reference site approach was used in which Fourier spectral ratios were calculated for pairs of stations in which one is on soil and one is on reference rock. Figure 3.2 shows a map of the rock and soil sites considered by Borcherdt and Glassmoyer (1994) (BG94). For a particular period T and rock-soil site pair, the site factor determined by this method is:

$$F(T) = \frac{FA_{Vs30}(T)}{FA_{ref}(T)} \tag{3.1}$$

where $FA_{Vs30}(T)$ is the Fourier amplitude at period T from a recording on a site condition with velocity V_{s30}, and $FA_{ref}(T)$ is a recording from a neighboring rock site that is taken as the reference ($V_{s30} > 760$ m/sec). Fourier amplitude spectral ratios were computed at frequency intervals of 1/40.96 sec in the frequency domain. Period-specific spectral ratios calculated from Eqn. (3.1) were averaged across a short period band (0.1–0.5 sec) and mid-period band (0.4–2.0 sec) to estimate F_a and F_v for each rock-soil pair. Resultant empirical estimates of F_a and F_v and the corresponding regression lines are presented in BG94 and have been reproduced in Figure 3.3. The reference rock motions used by BG94 have bedrock peak ground accelerations that range from 0.075 to 0.11g, with an average of about 0.1g.
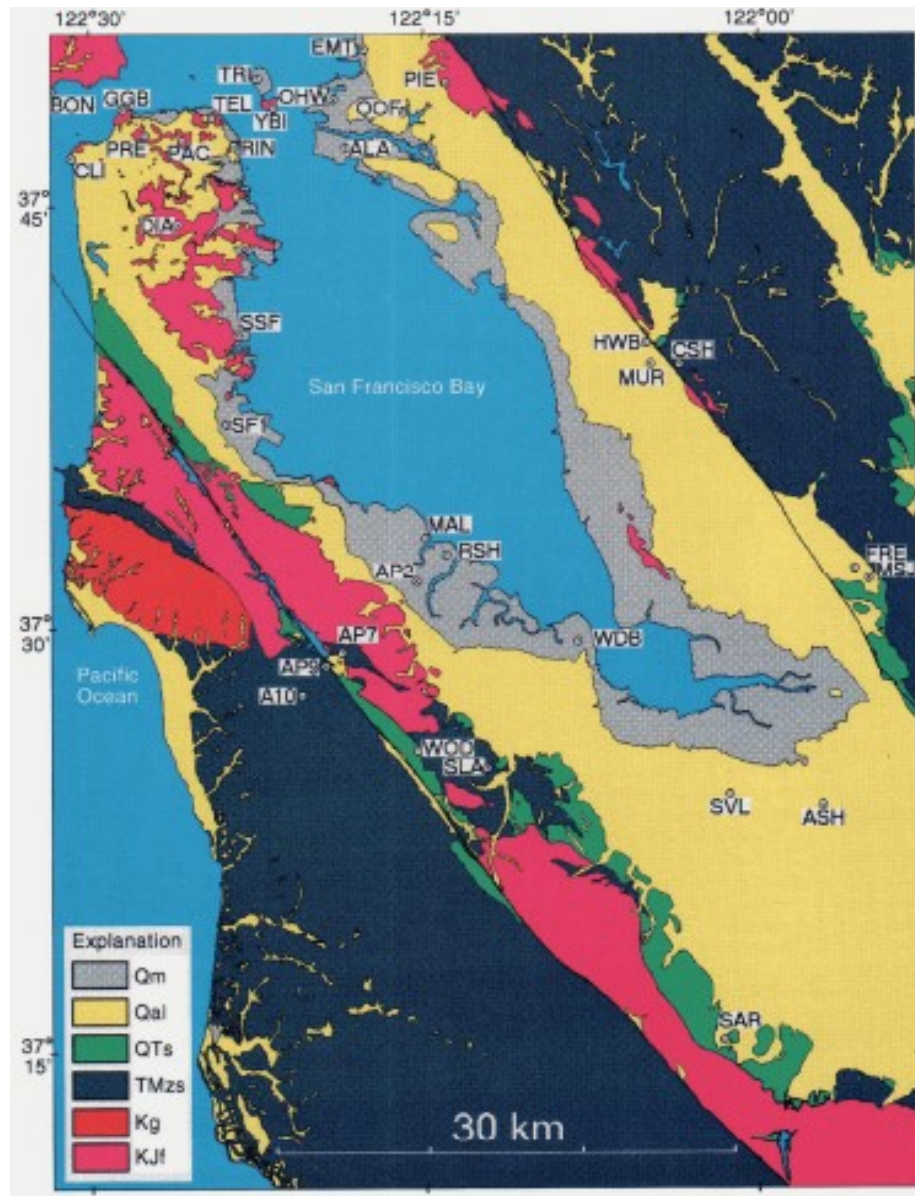
Figure 3.2. **Map of San Francisco Bay region, showing locations of 34 of 37 free-field stations that recorded 1989 Loma Prieta earthquake and generalized geologic units. KJf corresponds to Franciscan formation bedrock of Cretaceous and Jurassic age that was taken as reference rock. Borcherdt and Glassmoyer (1994).**

Figure 3.3 shows the F_a and F_v factors produced by BG for each station pair plotted as a function of V_{s30} along with regression lines, 95% confidence intervals for the ordinate to the true population regression line, and the limits for two standard deviations of the estimate. The

49

relatively narrow confidence intervals indicate that the scaling of the site terms with V_{s30} is statistically significant, but it is apparent from the trends in Figure 3.3 that the scaling is more pronounced at mid periods than at short periods. This is thought to occur because most soil sites have fundamental vibration periods within the mid-period band, producing stronger site effects in that period range than at shorter periods.
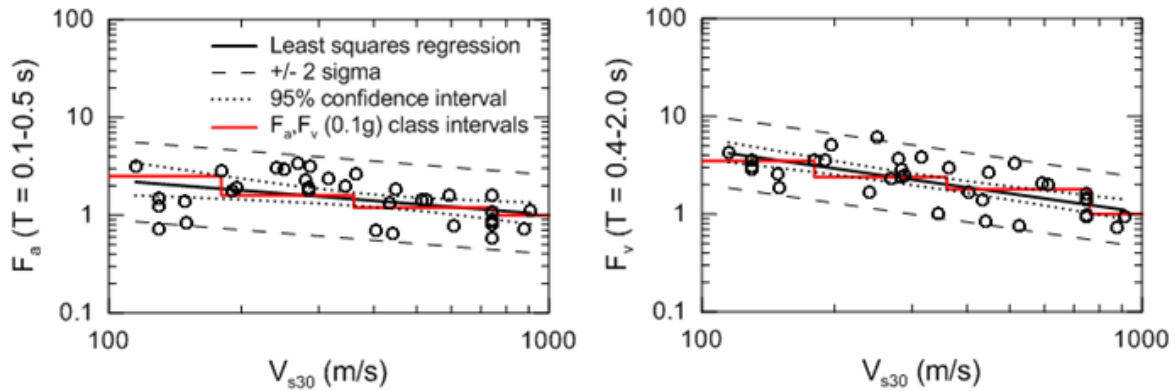
Figure 3.3. Site factors F_a and F_v evaluated from reference site approach from recordings of 1989 Loma Prieta earthquake as function of V_{s30} (data from Borcherdt, 1994b). The reference motion amplitude for the data is $PGA_r = 0.1g$. Red stepped lines correspond to site factors in site class intervals.

The reference sites used by BG94 correspond to a competent rock site condition, which in the San Francisco Bay Area corresponds specifically to Franciscan formation bedrock of Cretaceous and Jurassic age. The average values of V_{s30} among the reference sites is approximately 795 m/sec, but the linear trend line through the data in Figure 3.3 reaches unity at V_{s30} = 1050 m/sec. Hence, the linear trend line produces non-unity amplification levels at the contemporary reference condition of V_{s30} = 760 m/sec (B-C boundary).

In Figure 3.3 the red stepped lines correspond to F_a and F_v values in use since publication of the 1994 NEHRP *Provisions* (BSSC, 1995). As shown in Figure 3.3, the NEHRP F_a

and F_v factors are generally consistent with the trend of the regression lines. The stepped site factors in Figure 3.3 are slightly different from those presented by Borcherdt (1994b), which match the lines at V_{s30} = 150, 270, 560, and 1050 m/sec. The modifications in NEHRP factors relative to Borcherdt (1994b) are in (1) the velocity boundaries, the final values of which were selected in committee; and (2) the amplification levels for particular categories (e.g., F_a for E) that were increased by committee consensus (details in Dobry et al., 2000). As seen from Figure 3.3, the NEHRP factors match the regression lines at V_{s30} = 120, 290, 600; and 1050 m/sec (for F_a) and at 160, 290, 450, and 1050 m/sec (for F_v).

With regard to the V_{s30} = 1050 m/sec reference condition provided by Borcherdt (1994b) and adopted for the 1994 NEHRP *Provisions*, it is useful to recall the national ground motion maps with which the NEHRP site factors were originally applied. As described by Algermissen and Perkins (1976), the GMPE used at that time was a model for rock conditions by Schnabel and Seed (1973), which was used directly for peak acceleration in the western U.S. (non-subduction regions) and with some modification for other conditions (i.e., other regions and longer periods, as described by Algermissen and Perkins (1976). The rock site conditions represented by the GMPE are poorly defined, although many of the motions used in GMPE development are from soil sites and were deconvolved to rock using wave propagation analysis (Schnabel et al. 1971). The rock conditions used in the deconvolution appear to have been hard (V_s = 2400 m/sec), whereas the motions from rock sites were associated with much softer geologic conditions. Considering that the rock GMPE represents the average of these conditions, the 1994 national maps likely applied for firm rock conditions. Therefore, we postulate that general compatibility existed between those maps and the NEHRP site factors,

51

which in equation form are referenced to firm rock (V_{s30} = 1050 m/sec). By the time of the 1996

national maps (Frankel et al. 1996) as adopted by BSSC (1998), the reference condition used for

the PSHA calculations was clearly defined as V_{s30} = 760 m/sec (e.g., Frankel et al., 1996, p5 &

17), but the incompatibility with the reference condition for site factors was either not

recognized or not considered to be significant. This condition has remained to the present time.

3.2.2 Theoretical Basis for Nonlinearity in NEHRP Site Factors

Theoretical ground response analyses generally model the stratigraphy as one-dimensional (1D)

and simulate the nonlinear soil behavior using equivalent-linear or nonlinear methods. Site

factors can be evaluated from ground response analysis using the ratio of response spectra at

the top of the soil column to that of the outcropping base motion. Some key issues in the

utilization of ground response analysis to develop site factors are: (1) the shear wave velocity

profiles utilized in the analysis should be representative of the region where the site factors will

be applied; (2) the selected modulus reduction and damping (MRD) curves should be

appropriate for the predominant soil types; and (3) input motions should have appropriate

amplitude and frequency content for the seismicity of the region. Similar considerations apply

for nonlinear ground response analysis.

Borcherdt (1994b) and Dobry et al. (2000) described the process by which the ground

response analysis results from equivalent linear and nonlinear methods were used to

supplement the weak motion amplification levels depicted in Figure 3.3. Suites of profiles were

analyzed by Seed et al. (1994) and Dobry et al. (1994) for Classes C-E using measured velocity

profiles from sites in California and Mexico City. The empirical amplification values shown in

Figure 3.4 were found to be in good agreement with those derived independently by Seed et al. (1994), those computed parametrically by Dobry et al. (1994) at input ground motion levels near 0.1g, and response spectral ratios computed by Joyner et al. (1994). Hence, the modeling results were used to extrapolate the inferred amplification factors to higher input peak acceleration levels of 0.2, 0.3, and 0.4g. Borcherdt (1994b) and Dobry et al. (2000) describe how the computed site factors were expressed in a linear form in log-log space as shown in Figure 3.4 and given by the following expressions:

$$F_a = \left(\frac{V_{ref}}{V_{s30}} \right)^{m_a}$$

(3.2)

$$F_v = \left(\frac{V_{ref}}{V_{s30}} \right)^{m_v}$$

(3.3)

where V_{ref} = 1050 m/sec and m_a and m_v are fit coefficients that vary with input motion amplitude to capture trends in the simulations with the results shown in the legend of Figure 3.4 (Borcherdt 1994b; Dobry et al. 2000). The black line in Figure 3.4 applies to PGA_r = 0.1g. For PGA_r > 0.1g the amplification levels decrease in accordance with the simulation results, with the amount of decrease being greatest at low V_{s30}. Note from Figure 3.4 that these expressions for site factors are referenced to a common V_{s30} = 1050 m/sec. For the NEHRP site factors (Figure 3.1), the input motion ground motion amplitude was re-expressed as S_s and S_1 in lieu of PGA according to S_s = 2.5 PGA and S_1 = PGA.
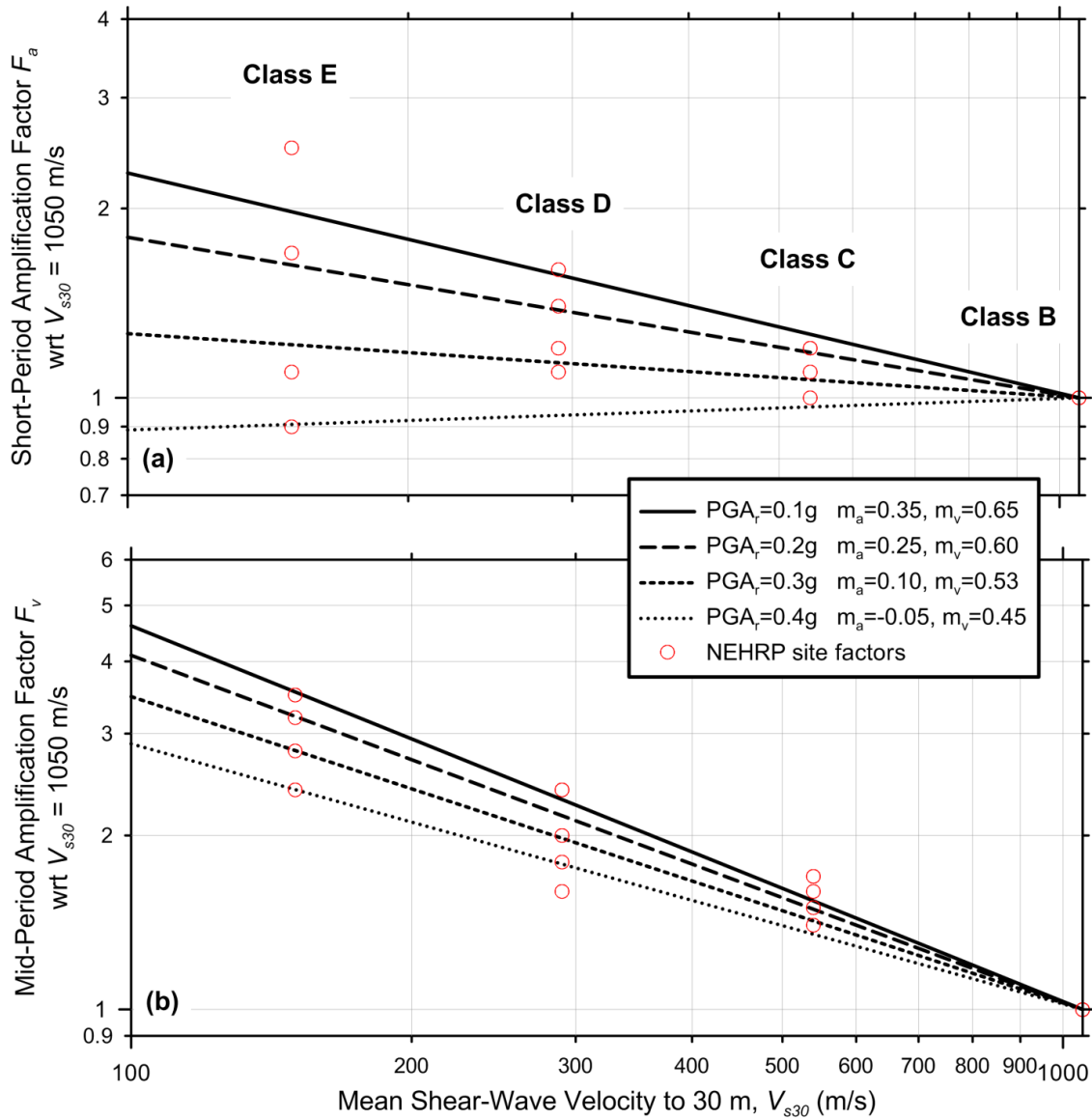
Figure 3.4. (a) Short-period F_a ;and (b) mid-period F_v amplification factors. Parameters m_a and m_v are slopes of the amplification factors with V_{s30} in log-log space; PGA_r corresponds to the input ground motion level on rock in units of g (Dobry et al. 2000). Reported slopes from Borcherdt (1994a, b).

Figure 3.4 also shows the NEHRP site factors plotted at the V_{s30} values for which category-based site factors were originally developed by Borcherdt (1994b), as explained previously. The NEHPR factors have some discrepancies from the regression lines, especially for

F_a in Category E and F_v in Categories C-D. As mentioned previously, those discrepancies arose from committee decisions.

3.3 BASIS OF SITE FACTORS IN NGA RELATIONS

The 2008 version of the Next Generation Attenuation (NGA) project produced GMPEs for shallow crustal earthquakes in active tectonic regions (Power et al. 2008). GMPEs were developed by five teams consisting of Abrahamson and Silva (2008), Boore and Atkinson (2008), Campbell and Bozorgnia (2008), Chiou and Youngs (2008), and Idriss (2008). For ease of use, the abbreviations of AS08, BA08, CB08, CY08, and I08 are applied. The models are based on analyses of the PEER-NGA empirical strong ground motion database, which contains 3551 recordings from 173 earthquakes (Chiou et al. 2008).

The NGA models are semi-empirical equations for peak ground acceleration (PGA), peak ground velocity (PGV) and 5% damped elastic pseudo-acceleration spectra (PSA) for periods up to 10 sec. These ground motion prediction equations (GMPEs) have a typical form of:

$$\ln Y = f_1(M) + f_2(R) + f_3(F) + f_4(HW) + f_5(S) + \varepsilon_T \tag{3.4}$$

where Y is the median geometric mean ground motion *IM*, f_i are functions of magnitude (*M*), source-to-site distance (*R*), style of faulting (*F*), hanging-wall effects (*HW*), and site conditions (*S*). Parameter ε_T is a random error term with a mean of zero and a total aleatory standard deviation given by

$$\sigma_T = \sqrt{\sigma^2 + \tau^2} \tag{3.5}$$

where σ is the standard deviation of the within-event residuals, and τ is the standard deviation of the between-event residuals.

The site factors in the NGA GMPEs express the effect of shallow site conditions on various ground motion *IMs* as a function of V_{s30}, and in the case of the AS08, CB08, and CY08 relations, a basin depth term as well. Different NGA developers used different methods to obtain site factors. AS08 and CB08 set coefficients describing the linear site response empirically and constrain the nonlinearity in site response based on simulations by Walling et al. (2008) (WEA08). BA08 and CY08 fit the coefficients for both the linear and nonlinear components of their site amplification model empirically.

When site amplification factors are developed empirically, the process can be described as a non-reference site approach. In contrast with the reference site approach utilized by BG94, the non-reference site approach compares IMs from recordings (*IM_{rec}*) to median predictions from a GMPE for a reference site condition [$S_a{}^r(T)_{GMPE}$] as follows:

$$F(T) = \frac{\left(S_a{}^{rec}(T) \right)}{\left(S_a{}^r(T)_{GMPE} \right)} \tag{3.6}$$

Note that this approach does not require a reference site recording, hence a much larger set of ground motions can be used to develop site amplification levels, the median of which is taken as the site factor. In natural log units, $\ln F(T)$ can be viewed as the data residual relative to the rock GMPE:

$$\ln F(T) = \ln\left(S_a^{rec}(T) \right) - \ln\left(S_a^r(T)_{GMPE} \right) \tag{3.7}$$

The site factors are generally evaluated during the development of the GMPE in such a way as to minimize residuals.

As noted previously, the AS08 and CB08 GMPEs utilize site amplification models whose nonlinear component is set from the results of 1D ground response analyses. The ground response analyses and model building process are described in WEA08. The ground response analyses used an equivalent-linear analysis method with random vibration theory as implemented in the program RASCALS (Silva and Lee 1987). The velocity profiles were taken from a proprietary database maintained by $\underline{P}$acific $\underline{E}$ngineering and $\underline{A}$nalysis (PEA) for active tectonic regions. The $\underline{m}$odulus $\underline{r}$eduction and $\underline{d}$amping (MRD) curves were taken from judgment-driven relations known as the Peninsular Range curves. For each soil profile, amplification factors were computed for input rock PGA values ranging from 0.001 to 1.5g. For each case, the amplification with respect to V_{s30} = 1100 m/sec was computed. Example site factors for V_{s30} = 270 m/sec and 560 m/sec, obtained at T = 0.2 sec from this process, are plotted against PGA for V_{s30} = 1100 m/sec m/sec (i.e., PGA1100) in Figure 3.5. Additional calculations were performed using MRD curves from EPRI (1993), with otherwise identical conditions. Models developed from those results are unpublished but were provided by Walling (*personal communication*, 2011).
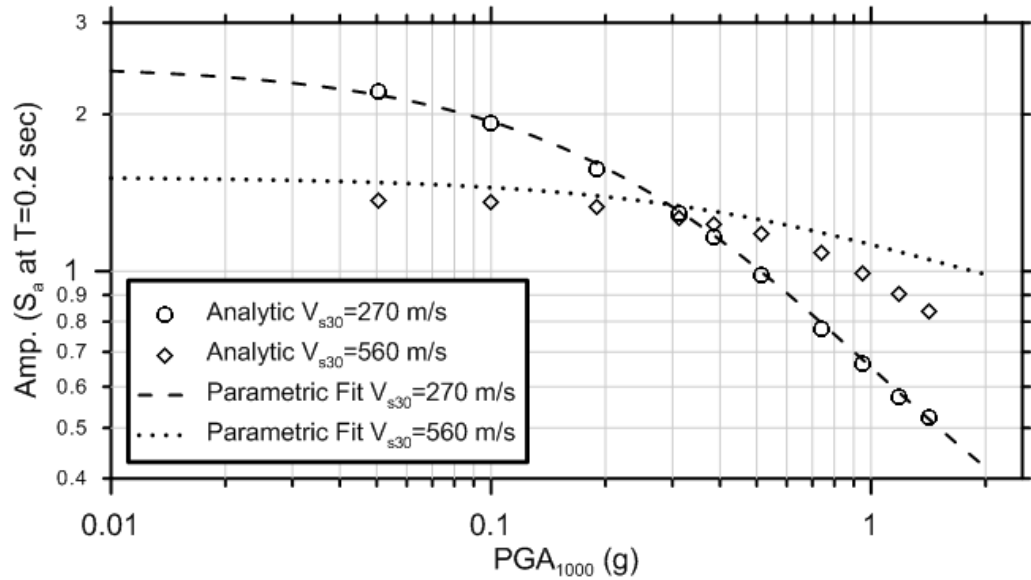
Figure 3.5. Examples of the site factors computed by WEA08 and parametric fits to the analysis results. Adapted from WEA08.

3.4 COMPARISON OF NEHRP AND NGA SITE FACTORS

3.4.1 Site Factors Comparison

In this Section, we compare the NEHRP site factors with NGA site factors derived from the four 2008 NGA GMPEs having site terms. The objective is to identify discrepancies, with specific attention paid to evaluating differences in median amplification at low levels of rock ground motion, as well as possible differences in the nonlinearity of site amplification. In this chapter, when we refer to NGA GMPEs, we mean the 2008 version, not those associated with the NGA-West 2 project.

The NGA relations use different functional forms for the site terms. The reference rock ground motion amplitude parameter used to drive nonlinearity in the models is taken as PGA for AS08, BA08, and CB08 and as spectral acceleration at the period of interest for CY08. Site terms F_x (V_{s30}, A_x) are assumed to be log normally distributed and depend on A_x, the ground

58

motion amplitude for a reference site condition having a particular $V_{s30} = x$. Reference motion amplitude A_x is a median PGA for AS08, BA08, and CB08, and an event-term adjusted median S_a at the period of interest for CY08. The event term (η_i) is approximately the median residual for well recorded events and is formally evaluated from random effects regression procedures (Abrahamson and Youngs, 1992). To summarize, input parameters for the site amplification models are:

NEHRP: V_{s30}, S_s, S_1

AS08: V_{s30}, Median PGA_{1100} (PGA for V_{s30}=1100 m/sec)

BA08: V_{s30}, Median PGA_{760} (PGA for V_{s30}=760 m/sec)

CB08: V_{s30}, Median PGA_{1100} (PGA for V_{s30}=1100 m/sec)

CY08: V_{s30}, Median + η_i $(S_a)_{1130}$ (S_a for V_{s30}=1130 m/sec)

Note that the reference motions are defined for different reference rock site conditions in the GMPEs.

To facilitate comparisons between the NGA and NEHRP site factors, we compute site terms relative to the $V_{s30} = 760$ m/sec reference condition used in the national PSHA maps published by USGS. This condition is selected because the NEHRP factors are used to modify ground motions for site conditions that differ from the $V_{s30} = 760$ m/sec reference. The NGA site factors are calculated relative to this reference condition as:

$$\ln\left(F_{760}(V_{s30}, A_x)\right) = \ln\left(F_x(V_{s30}, A_x)\right) - \ln\left(F_x(760, A_x)\right)$$

Or

$$F_{760}(V_{s30}, A_x) = \frac{F_x(V_{s30}, A_x)}{F_x(760, A_x)} \tag{3.8}$$

We define the reference site motion amplitude as A_x = median PGA for V_{s30} = 760 m/sec, which is denoted PGA_r in the following text. Site factors are evaluated for PGA_r = 0.01–0.9g. The CY08 site term uses S_a at the period of interest instead of using the median PGA. For this model, reference motion amplitude is estimated from PGA_r as:

$$S_a\left(T=0.2\sec\right)\approx 2.3PGA_r \qquad S_a\left(T=1.0\sec\right)\approx 0.7PGA_r \tag{3.9}$$

The factors of 2.3 and 0.7 in Eqn. (3.9) are based on differences in the median spectral ordinates (e.g., 0.2 sec S_a versus PGA) from the origional (2008) NGA (i.e. NGA-West 1) GMPEs for rock site conditions and typical ranges of M_w (6–8) and distance (< 30 km) that control seismic hazard. These values are updated from 2.5 and 1.0 in the original NEHRP factors. The factor S_a (1.0 sec)/PGA is significantly dependent on magnitude, and the value of 0.7 corresponds approximately to **M**7.0. Huang et al. (2010) use a procedure similar to that described above-instead of calculating the site term directly, they apply the NGA GMPEs for a range of magnitudes, distances, and other parameters to compute median S_a for selected V_{s30} values. They take the ratio of median S_a at V_{s30} to median S_a at 760 m/sec as a period-dependent site factor. Huang et al. (2010) average these values across three GMPEs (i.e., BA08, CB08 and CY08) and across period ranges to develop recommendations for F_a and F_v site factors.

We use the NGA-West 1 site models at representative V_{s30} values for each NEHRP category. The representative velocities are evaluated from medians within the various classes B-E using the site database compiled for the NGA-West 2 project (Ancheta et al., 2013). That database contains 1144 California and international sites with measured V_{s30} values derived from profiles 30 m or greater in depth, which are distributed as shown in Figure 3.6. The

median V_{s30} values for each site class are indicated in Figure 3.6. More detailed histograms within the relatively well populated C and D classes are given in Figure 3.7. The representative category velocities given in Figure 3.6 are generally similar to those used by Borcherdt (1994b) to set the empirical site factors (i.e., 155 versus 150 m/sec for E; 266 versus 290 m/sec for D; 489 versus 540 m/sec for C; 913 versus 1050 m/sec for B) and the geometric means of the boundary end points (254 m/sec for D; 523 m/sec for C; 1070 m/sec for B).
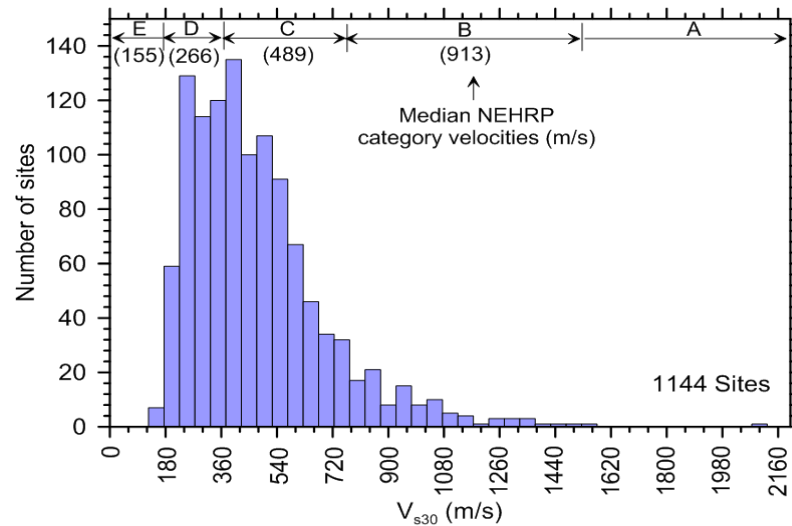
Figure 3.6.   **Histogram of measured V$_{s30}$ values for strong motion sites used in this study.**
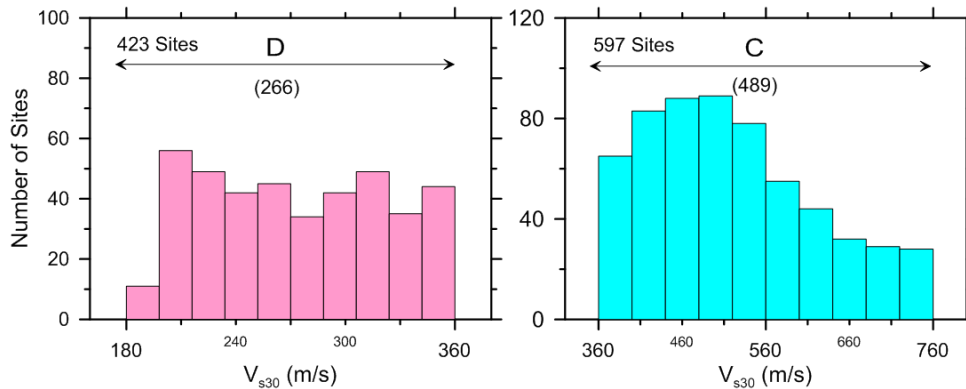
Figure 3.7.   **Histogram of V$_{s30}$ values within Site Classes C-D.**

61

Figure 3.8 compares the discrete published NEHRP site factors (black solid symbols) with NGA-West 1 site amplification terms computed for median spectral accelerations across the period range for F_a (T = 0.1–0.5 sec) and F_v (T = 0.4–2.0 sec) relative to V_{s30} = 760 m/sec. Adjustments to the NEHRP factors are also shown in Figure 3.8 (black open symbols), which are discussed further below. Also shown for comparison are site amplification factors from Huang et al. (2010) for Classes D and E (results for comparable V_{s30} values are not available for other site classes). Note the Huang et al. (2010) factors plotted in Figure 3.8 are averaged from their values for specific spectral periods within the respective period ranges for F_a (0.1–0.5 sec) and F_v (0.4–2.0 sec). Because the reference rock amplitudes used by Huang et al. (2010) are 0.2 sec and 1.0 sec S_a, we convert to PGA_r using S_a/PGA_r ratios in Equation (3.9), which are compatible with the magnitude and distance range selected by Huang et al. (2010).

The spread of NGA-West 1 site factors in Figure 3.8 reflects epistemic uncertainty, which is relatively large for Class E and modest elsewhere. We judged differences in NGA and NEHRP site factors to be significant when they clearly exceed the epistemic uncertainty for a given site class. In Classes C-D, NEHRP and NGA factors have different slopes for F_v, indicating different levels of nonlinearity. This issue is discussed further in the following section. In Classes C and D, NEHRP and NGA site factors are in reasonable agreement for F_a. In Classes B and E, NEHRP site factors are larger than NGA factors for F_a and F_v. The NEHRP C and D factors for F_v are also larger than NGA factors for weak motions (i.e., PGA_r = 0.1g). The trends shown in Figure 3.8 are not changed appreciably if the V_{s30} values used to compute the NGA site factors are changed to the values selected by Borcherdt (1994b) of 150, 290, 540, and 1050 m/sec. The Huang et al. (2010) site factors are generally similar to the NGA factors shown in Figure 3.8 for Classes D and

E (and hence they also have similar discrepancies relative to NEHRP). The modest differences between our site factors and those of Huang et al. (2010) likely result from variability in the S_a/PGA_r ratios used to correct the abscissa, the use of different averaging procedures (i.e., different numbers of averaged spectral periods within F_a and F_v period bands) and other details. Huang et al. (2010) also report similar discrepancies between their site factors and NEHRP factors (e.g., their Figure 2).
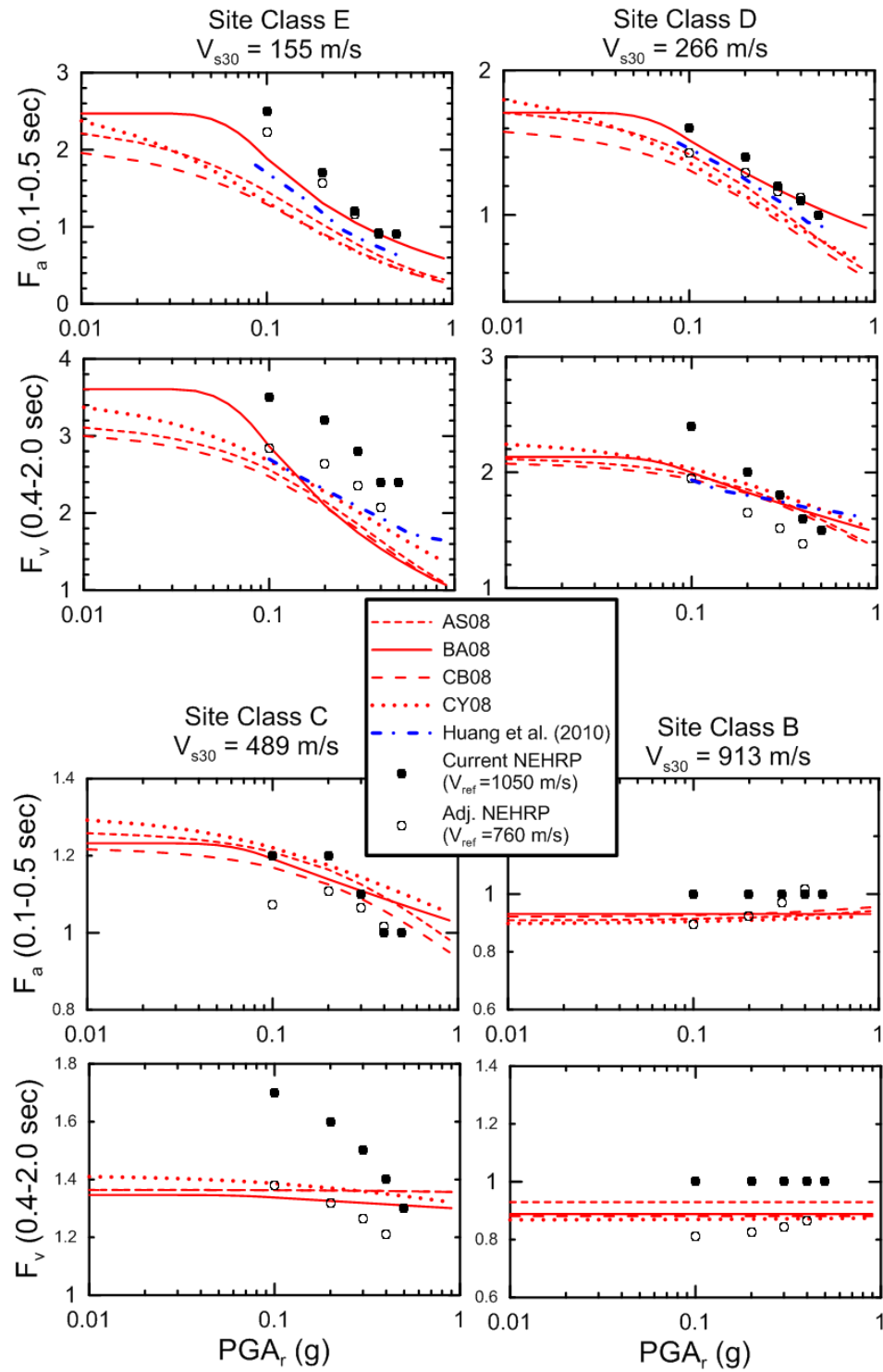
Figure 3.8. Comparison of original and adjusted NEHRP site factors to site factors from NGA relationships averaged across corresponding period ranges (0.1–0.5 sec for F_a; 0.4–2.0 sec for F_v).

As mentioned previously, adjusted NEHRP factors are also shown in Figure 3.9. The adjustment is computed to re-normalize the NEHRP factors from a reference velocity of 1050 m/sec to 760 m/sec as follows:

$$F_a^N = F_a \left(\frac{V_{ref}}{760} \right)^{-m_a} , \; F_v^N = F_v \left(\frac{V_{ref}}{760} \right)^{-m_v} \tag{3.10}$$

where superscript 'N' indicates re-normalization, F_a and F_v are the original, published NEHRP factors, V_{ref} = 1050 m/sec per Borcherdt (1994b) and Dobry et al. (2000), and m_a and m_v are taken from Dobry et al. (2000) (shown in Figure 3.4). No adjustments are made at PGA_r = 0.5g due to a lack of published m_a and m_v values in Figure 3.4.

Shown with the open black symbols in Figure 3.8, the re-normalized NEHRP site factors are generally in better agreement with NGA site factors. The re-normalization essentially removes all misfits for Class D; misfits for other classes remain but are generally reduced. We wish to emphasize that the 'adjusted' NEHRP factors in Figure 3.8 are not proposed for adoption in NEHRP, but are presented to demonstrate the reduction in site factors discrepancies that is possible through the use of a consistent reference rock condition (in this case, V_{s30} = 760 m/sec).

The variation of amplification factors with V_{s30} is also investigated to isolate the V_{s30} dependence of the amplification factors from the dependence on PGA_r. Figure 3.9 plots F_a and F_v from NEHRP and NGA (based on median spectral accelerations across the period range for T = 0.1–0.5 sec for F_a; T = 0.4–2.0 sec for F_v) versus V_{s30} for PGA_r = 0.01g, 0.1g, 0.3g, and 0.5g. The original and adjusted NEHRP factors are plotted at the category-averaged V_{s30} values of 155 m/sec, 266 m/sec, 489 m/sec, and 913 m/sec, corresponding to categories E, D, C, and B,

respectively. The PGA_r values used in Figure 3.9, when modified to S_s and S_1 per Eqn. (3.9), do not perfectly coincide with the tabulated NEHRP factors. Accordingly, we have interpolated as needed to produce the points in Figure 3.9. The results indicate consistent slopes of the F_a and F_v versus V_{s30} relations for PGA_r = 0.01g and 0.1g. This indicates that the scaling of site factors with V_{s30} in the original BG94 and Borcherdt (1994b) relations is robust (i.e., similar V_{s30}-scaling is present in the NGA site terms). The offset between the NEHRP and NGA factors is partly due to the 1050 m/sec reference condition in the NEHRP factors. For larger PGA_r values, significant differences in site factors occur for V_{s30} < ~500 m/sec, which encompasses conditions at most soil sites. Those differences arise principally from different levels of nonlinearity, which is addressed further in the following section.
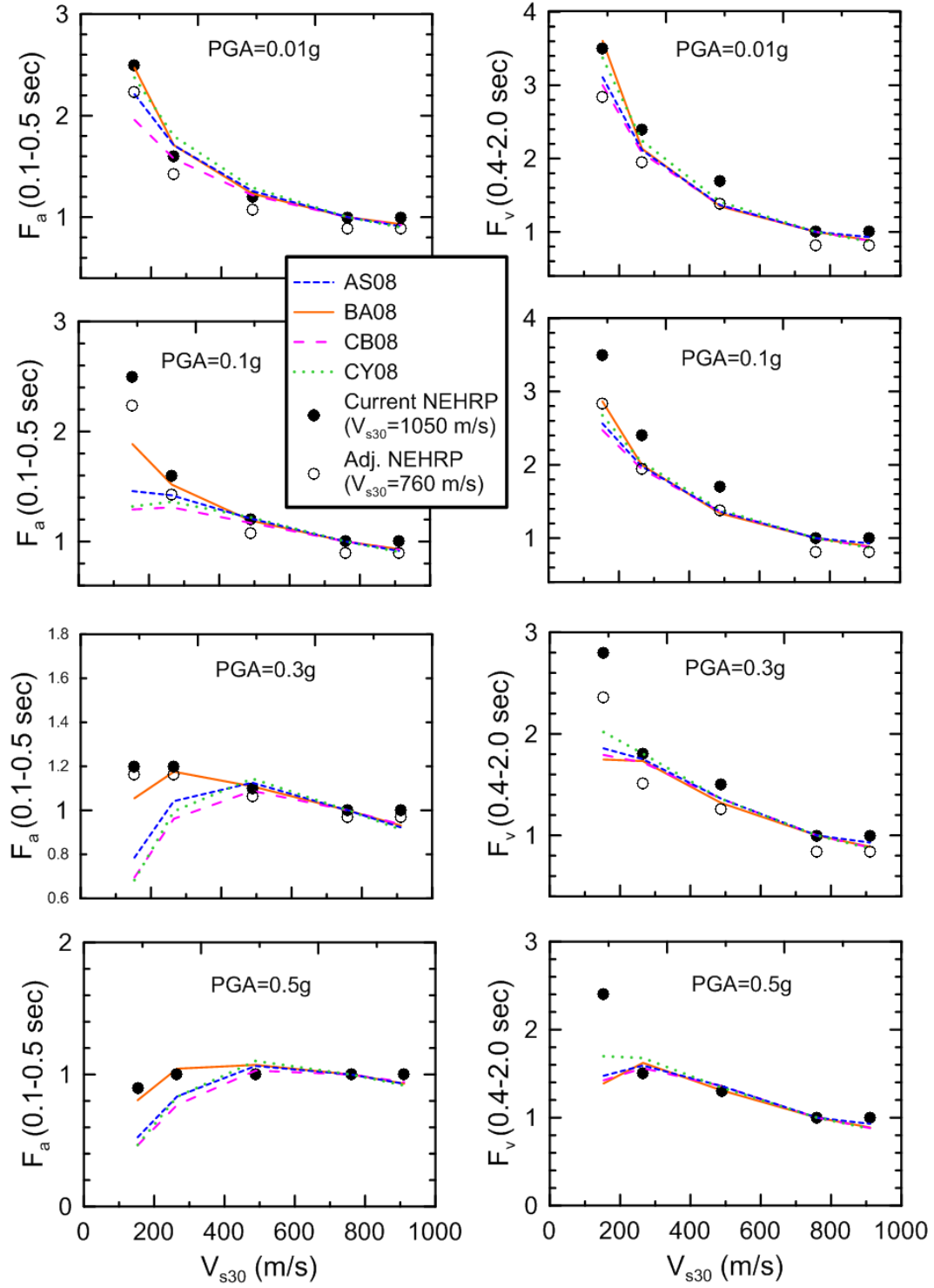
Figure 3.9. Variation of site amplification with V$_{s30}$.

3.4.2 Evaluation of Nonlinearity in Simulation-Based Site Factors

Figure 3.10 compares the results of analytical studies presented by Dobry et al. (2000) (Figure 3.4) with the site factors derived from more comprehensive equivalent-linear analyses by WEA08, in which the "Peninsular Range" modulus reduction and damping (MRD) curves (i.e., PEN model) were used. Results are shown for the short-period band amplification factor, F_a (0.2 sec) and mid-period band amplification factor, F_v (1.0 sec). The important conclusions to draw from this comparison relate to the relative slopes of the WEA08 and Dobry et al. (2000) relations (not necessarily the vertical position of the curves). For instance, whereas the slopes for V_{s30} = 270 m/sec are similar, the slopes for faster velocities are flatter in the more recent work.

Figure 3.11 illustrates the same type of comparison, but the results derived from the PEN model by WEA08 are replaced with similar results provided by Walling (*personal communication*, 2011) that are derived from more nonlinear MRD curves from EPRI (1993). Using this soil model, the F_a slopes are steeper than those from Dobry et al. (2000). For F_v, the slopes are comparable at V_{s30} = 270 m/sec; the Walling slopes are flatter for faster velocities.
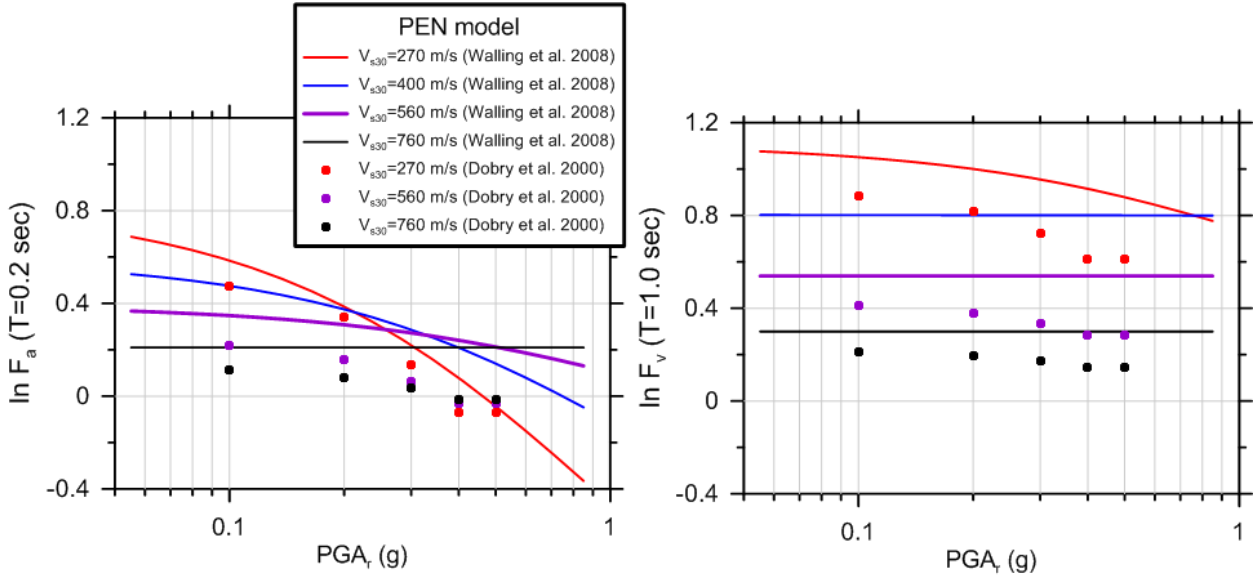
Figure 3.10. Comparison of short-period F$_a$ (0.2 sec) and mid-period F$_v$ (1.0 sec) amplification factors between Dobry et al. (2000) and WEA08 (PEN model). Results show flatter nonlinear relationship in the WEA08 model for V_{s30} > 270 m/sec.
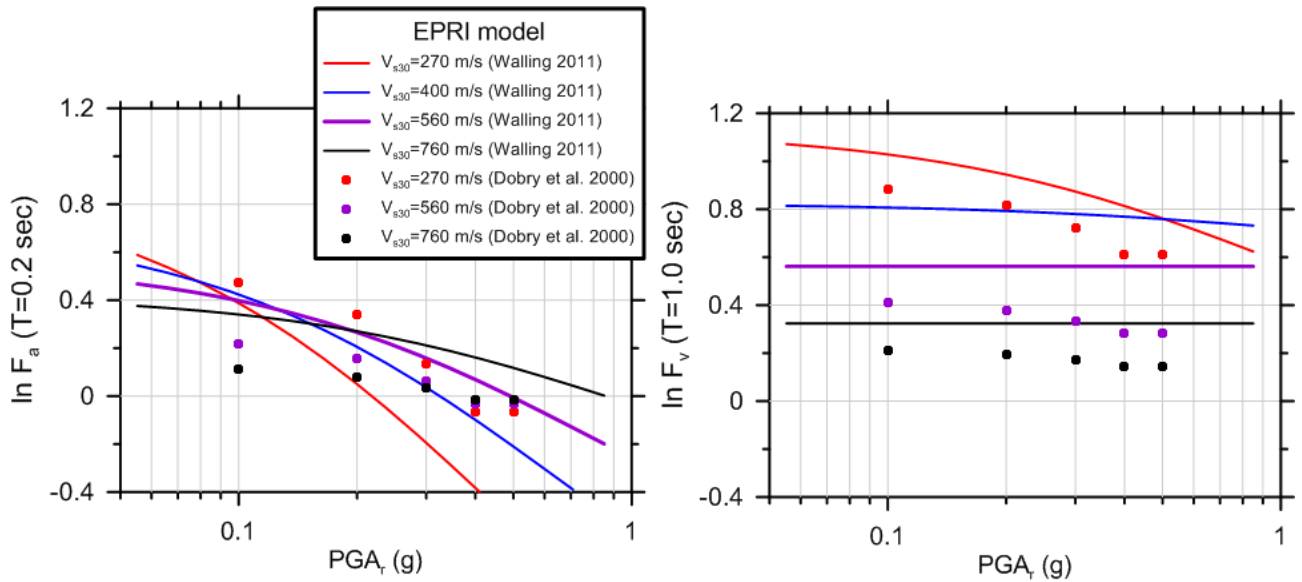
Figure 3.11. Comparison of short-period F$_a$ (0.2 sec) and mid-period F$_v$ (1.0 sec) amplification factors between Dobry et al. (2000) and Walling (personal communication, 2011) (EPRI model).

The principal factor responsible for the varying levels of nonlinearity is different MRD models used in the ground response simulations. The Dobry et al. (2000) site factors are based on simulations by Seed et al. (1994) and Dobry et al. (1994), both of which used MRD curves from Vucetic and Dobry (1991) (i.e., VD91) for cohesive soils. For sands, Seed et al. (1994) used MRD curves from Seed et al. (1984) (i.e., S84) while Dobry et al. (1994) used the VD91 MRD curve for $PI = 0$. Figure 3.12 compares the PEN curves from WEA08 with the aforementioned curves that provide the basis for the Dobry et al. (2000) site factors. The PEN curves are more linear than VD91 MRD at $PI = 0$and the Seed et al. (1984) MR curves, although the VD91 $PI = 50$ MRD curves are similar to PEN. Accordingly, the generally high nonlinearity in the MRD curves used in the studies behind the Dobry et al. (2000) amplification factors explains the relatively nonlinear site amplification terms.

The varying levels of nonlinearity in amplification factors derived from the PEN and EPRI MRD curves reflects epistemic uncertainty, in the sense that we lack knowledge regarding which set of MRD curves are most "correct" for ground response calculations. Given that the simulation results from WEA08 and Walling (*personal communication*, 2011) to some extent bracket the Dobry et al. (2000) curves (at least for F_a), we cannot conclude that the nonlinearity present in the NEHRP provisions is invalid on this basis.

However, nonlinearity from theoretical simulations can be checked against empirical data. Kwok and Stewart (2006) compared recorded ground motion recordings from various site conditions in California to predictions from rock GMPEs modified by theoretically-based site factors very similar to those of WEA08. Residuals were calculated in a manner similar to Eqn. (3.7), but with the rock GMPE median modified with the theoretical site factor and event term

η. An example result is shown in Figure 3.13, which shows no trend in residuals versus PGA_r, indicating that the nonlinearity in the theoretical site factors captures the data trends. This comparison provides support for the more linear recent amplification factors presented by WEA08 and used in several of the NGA site terms.
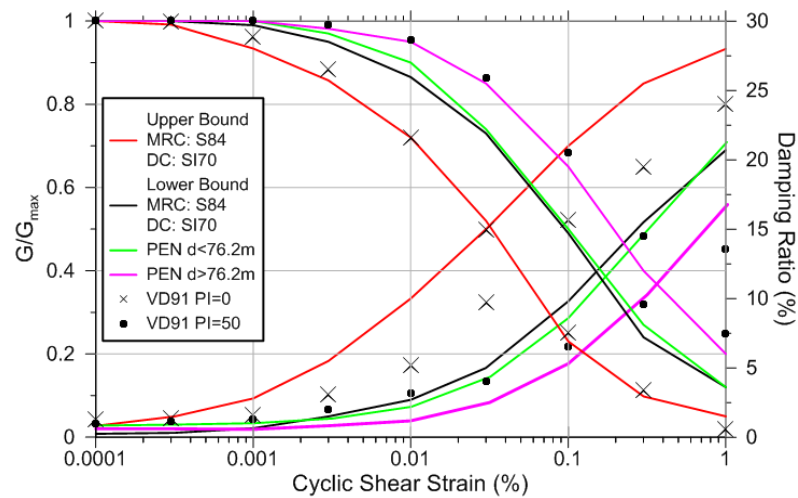
Figure 3.12.   **Comparison of modulus reduction and damping curves from Dobry et al. (1994), Seed et al. (1984), and WEA08 (PEN model). S84 means Seed et al. (1984), SI70 represents Seed and Idriss (1970), and VS91 comes from Vucetic and Dobry (1991).**

3.5   CONCLUSIONS

The NGA and NEHRP site factors are consistent in certain respects (e.g., the scaling of linear site amplification with V_{s30}), but have discrepancies in linear site amplification (applicable for rock PGA ≤ 0.1g) for site Classes B to E and in the levels of nonlinearity for Classes C and D. The amount of these discrepancies ranges from up to 50% for Class E to amounts ranging from about 0 to 20% for Classes B-D. Previous work has identified similar discrepancies in NEHRP and NGA site factors (Huang et al. 2010), but the discrepancies were not clearly associated with

differences in linear site amplification levels and nonlinearities. Such associations are useful to understand causes of misfits and to formulate possible future updates to NEHRP factors.

A major cause of the weak motion amplification misfit is that the NEHRP factors are normalized relative to a reference site condition of V_{ref} = 1050 m/sec (i.e., the equations behind the tabulated factors reach unity at this velocity), whereas their current application is relative to V_{s30} = 760 m/sec. When re-normalized to V_{s30} = 760 m/sec, the NEHRP factors are much closer to NGA factors (especially for Class D), although misfits remain for Classes B, C, and E.

We find that the nonlinearity in F_a and F_v from recent simulation-based work (WEA08) is smaller than the nonlinearity in the NEHRP factors (Dobry et al. 2000). Those reduced levels of nonlinearity are consistent with trends from empirical ground motion data.

Figure 3.13. Trend of residuals with *PHA*$_r$ (from Kwok and Stewart, 2006).

4   DEVELOPMENT OF SITE DATABASE

4.1   OBJECTIVES OF SITE DATABASE DEVELOPMENT

The latest PEER NGA site database, Version 23, was completed in 2006 as part of the NGA-West

1 project as described by Chiou et al. (2008) and in particular Appendix B of Chiou et al. (2008),

which provides definitions for the site classifications that were used. These include the

Geomatrix 3-letter site classification, NEHRP site classification (BSSC 1994), and several others.

The project also supported various investigations to systematically fill in available site

information, with an emphasis on ultimately selecting V_{s30} values for sites with recordings. The

current database project significantly expands and continues these efforts.

      The work presented in this chapter represents the results of collaborative work

involving myself and Prof. Stewart along with Robert W. Graves from Task 8 group and the

following additional project researchers: Timothy D. Ancheta (PEER), Walter J. Silva and Robert

Darragh (Pacific Engineering and Analysis, PEA), and Brian Chiou (Caltrans). Our role was

principally to enhance the NGA-West 2 site database. The results given here have been

previously presented in Chapter 3 of a report by Ancheta et al. (2013).

The objectives of the work described in this chapter were as follows: (1) provide site classifications for 2538 new sites added to the main flatfile in the NGA-West 2 project; (2) update the site database to include V_{s30} values based on newly available measurements; (3) improve the documentation and consistency of site descriptors used as proxies for the estimation of V_{s30}, both for sites in the previous site database and newly added sites; (4) develop evidence-based protocols for V_{s30} estimation from available proxies; and (5) update and augment estimates of basin depth parameters $z_{1.0}$ and $z_{2.5}$ for both existing and new sites (primarily California and Japan).

With respect to objectives (1), (2), (3), and (5) new information was compiled for addition to the site database. This information was provided/developed by a number of sources. Relative to the Version 23 database, substantial amounts of new V_{s30} data are available for Japan, Taiwan, California, Turkey, New Zealand, and Italy, most of which is from web sites or archival literature. Pacific Engineering and Analysis provided proxies for a number of sites that recorded new earthquakes. University of California, Los Angeles (UCLA) researchers gathered most of the new information on proxies, with assistance from Chris Wills and Carlos Gutierrez (California Geological Survey), and Dave Wald, Vince Quitoriano, and Alan Yong (USGS). Robert Graves, Albert Kottke, and Paul Spudich worked with the database team to compile updated basin depth parameters for southern California and the San Francisco Bay Area, and to obtain basin depth parameters for sites in Japan. The newly added information includes: V_{s30} values from measurements (see Section 4.3); velocity profile numbers and depths (principally in California, from PEA); various proxies including ground slopes, surface geology, Geomatrix 3rd letter classifications, and geomorphologic site classifications (see Section 4.4); and basin depths

74

(see Section 4.6). Site parameters have been subject to peer reviews with extensive discussion to resolve technical issues and establish consensus-based protocols.

4.2 PREVIOUS AND CURRENT SITE DATABASE

In general, the site database contains metadata on conditions at the sites of strong-motion stations that have contributed data to the flatfile. The Version 23 site database from 2006 has 1611 worldwide stations that have recorded ground motions from shallow crustal earthquakes. The updated version of the site database for NGA-West2 has been expanded in two principal respects: (1) addition of new stations that had not produced usable recordings prior to the NGA-West2 project; and (2) incorporation of new site data for existing and new stations to provide more robust estimates of the site parameters used in GMPEs. Beyond the addition of these new data, the updated site database incorporates the results of a large amount of logistical book-keeping in regards to reconciling variations in stations names, station numbers, station locations, and other issues related to the 2006 site database, the current flatfile, and the current site database.

The total number of stations in the 2013 Version 32 site database is 4149. We have estimated or measured V_{s30} for all sites but Robic (Italy) and Rimforest, Lake Arrowhead (California), but only 1144 of those values (28%) are based on geophysical measurements with profile depths (z_p) ≥ 30 m. The most common site information for stations is GMX 3rd letter classifications, which are available for 3180 stations (77%) via assignments by Geomatrix, PEA, and UCLA. Only 484 (12%) have surface geology information (principally from California), mostly because geology look-ups are labor intensive in most regions worldwide because it is

performed using paper-based maps. The number of stations in the 2006 and current version of the site database for the five most populated regions are shown in Figure 4.1. The 2013 site database has a large increase in the number of stations from Japan. Other geographic regions contributing significant numbers of stations include western North America (mostly California), Taiwan, China, and Mediterranean regions.

As shown in Figure 4.1, there are a substantial number of new sites added in WNA, which are mostly from southern California and the San Francisco Bay Area. Among those new California sites, most of the V_{s30} values from measurements (164 sites) are based on data provided by Yong et al. (2013). The surface geologic information was provided by Carlos Gutierrez (personal communication, 2012) and includes geologic unit and ground slope at 3-arc-sec resolution. Ground slope was also provided by David Wald and Vince Quitoriano of USGS (personal communication, 2012) at 30-arc-sec resolution for use with the slope proxy of Wald and Allen (2007). Geomatrix 3rd letter site classifications were also developed for nearly all of the new California stations by PEA.
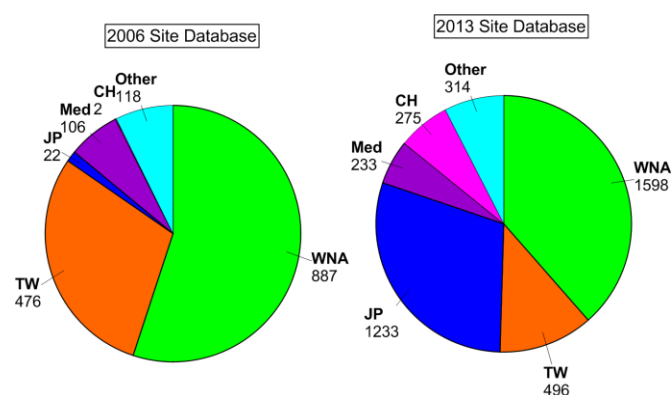
Figure 4.1. **Pie charts of station numbers in 2006 and 2013 site database for five main regions. CH:China, JP: Japan, Med: Mediterranean, TW: Taiwan, WNA: Western North America (i.e., mostly California).**

A substantial effort was made to assign Geomatrix 1st letter classifications, which are related to the structure type housing the instrument. Several additional 1st letter codes were added in this project to deal with unique structural types located in Italy. For example, 1st letter "P" is used for a massive 1−3 story castle.

For the newly added California sites, we looked up COSMOS site classification codes used by the four data providers SCSN\CIT, NCEDC\BDSN, CGS\CSMIP, and USGS\NSMP. These codes were correlated to GMX 1st letter by PEA as shown in the table below. In addition, GMX 3rd letter was developed from BDSN descriptions of surface geology. For example, for Black Diamond Mines Park near Antioch, California, the BDSN description is "Sand, the instruments are sited about 150 m into an old mine tunnel, there is about 100 m of over-burden composed on sandstone, shale and coal." Station descriptions give useful site and embedment information that allows GMPE developers to choose appropriate site conditions.

Table 4.1.   COSMOS codes for site classification and corresponding GMX 1st-letter code.

COSMOS Code	GMX 1st-letter	Description	Data Provider[1]
1	I	T-Hut	CGS, USGS
2	I	Armco	CGS, USGS
3	I,F	Sensors buried/set in ground (shallow, near surface). Also used by BDSN for US Array vault design described as: shallow burial at 2-5 ft, locations on rock are preferred.	All 4
4	A,B	Reference station (1-2 story, small, light building)	All 4
5	B,C,D,E	Base of building, larger than code 4.	All 4
10	G	Building Instrumentation	USGS
14	F	Tunnel	All 4
*		Unknown	CGS, USGS

[1] Data providers include: CGS, USGS, BDSN, CIT

4.3   Measured Velocity Profiles

4.3.1 Previous and New Data Sources

The V_s profiles used for the calculation of V_{s30} are derived from a variety of sources including: (1) for WNA, profiles are obtained from the PE&A profile database (664 profiles) and Yong et al. (2013) (191 profiles), which are a combination of surface wave, downhole, suspension logging, and other methods; (2) for Japan, profiles are obtained from http://www.kyoshin.bosai.go.jp/kyoshin/db/index_en.html?all, mostly from downhole methods; (3) for Taiwan, profiles are obtained from http://www.cwb.gov.tw/ which are mostly suspension logging profiles; (4) for China, values of V_{s30} are tabulated in an unpublished

document referred to as the "Yu and Silva report" and provided by Robert Darragh (personal communication, 2011), which are based mostly on downhole methods; (5) for Turkey, values of V_{s30} are tabulated by Sandikkaya et al. (2010) which are mostly derived from surface wave methods; and (6) for Italy, values of V_{s30} are tabulated by Scasserra et al. (2009) and http://itaca.mi.ingv.it/ItacaNet/, which are mostly derived from downhole, crosshole, and surface wave methods. All of the V_s profiles are available for independent review except for those in the PEA profile database, which is proprietary. As described in Chiou et al. (2008), the original sources for the PEA profiles are USGS, ROSRINE, CUREE, NCREE, Agbabian and Associates, Shannon and Wilson, Caltrans, and other organizations that have measured V_s profiles. While the V_s profiles from the PEA profile database were not available for the present work, V_{s30} values were provided by PEA staff along with PEA profile ID number and total profile depth. Many of these values were also used in Version 23 of the site database (Chiou et al. 2008).

Of the 1611 stations in the 2006 site database, 1604 had V_{s30} information (either measured or inferred) and 380 had V_{s30} values based on measurements from profiles at least 30 m in depth (23.5%). In the 2013 Version 32 site database, the number of V_{s30} values based on measurements with profile depths greater than 30 m has increased to 552 stations out of 4149 (13%). The distributions of measured and inferred V_{s30} values for the 2006 and 2013 site databases are shown in Figure 4.2. Note that most of the sites, and most of the measurements, are at soil sites. However, there are substantially more firm ground sites with V_{s30} values based on measurements in the 2013 version of the database (e.g., sites with $V_{s30} > 750$ m/sec number 46 in the 2006 database and 186 in 2013).
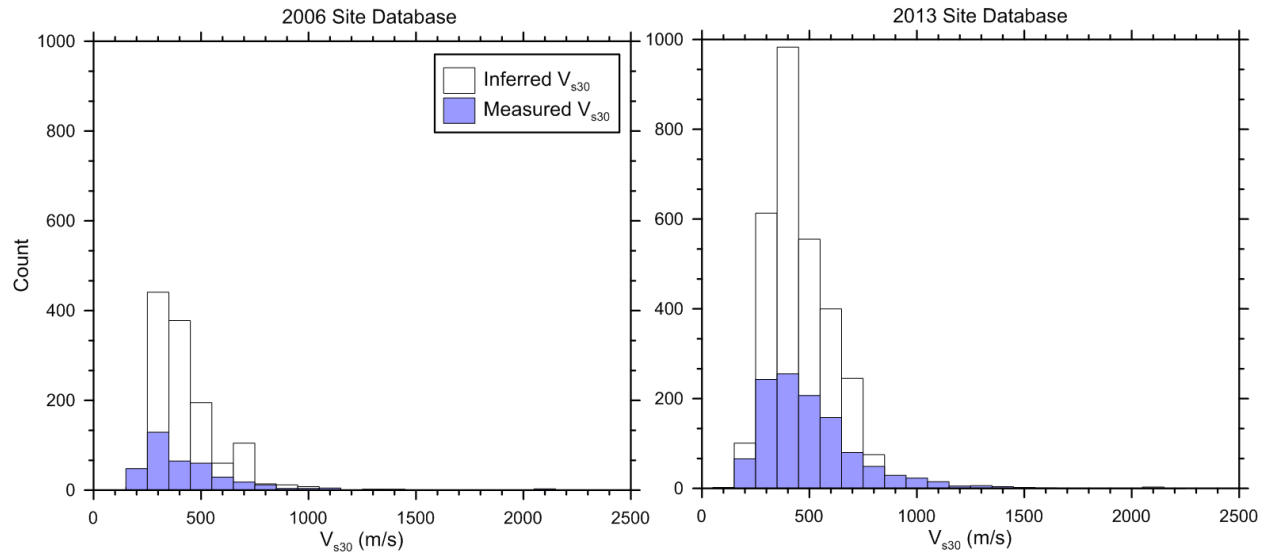
Figure 4.2. **Histograms of measured and inferred V$_{s30}$ at the recording station sites in both the 2006 and 2013 site databases.**

Figure 4.3 shows the distribution of all sites and sites with V_{s30} values based on measurements by region in the 2006 and 2013 versions of the site database. Comparing the 2006 and 2013 numbers, the number of sites has increased modestly in WNA (mostly California), Taiwan, and the Mediterranean regions, but has increased substantially in Japan and China. In the 2013 site database, the regions with the highest percentages of V_{s30} values based on measurements are Taiwan (53%) and Japan (34%). Note that this figure only includes sites as "measured" when the profile depth is 30 m or greater.

The data in Figure 4.3 are misleading in the sense that many strong-motion stations have available profiles with depths (z_p) less than 30 m, which are not included in those histograms. The distribution of z_p by region is shown in Figure 4.4. Most of the profiles shallower than 30 m are from Japan in the K-net array (Kinoshita 1998). It should be noted that not all profiles have known profile depths. For Japan, 96% of the 1085 sites with measurements have known profile depths, and most of those depths are 10-21 m. For Taiwan, 89% of the 300

80

sites with measurements have assigned profile depths, and most of those depths (231) are ≥ 30

m (77%). In California there are 442 sites with V_{s30} from measurements, 97% of which (430)

have known profile depths, and 350 of those depths have z_p ≥ 30 m. The following section

describes the estimation of V_{s30} from profiles with z_p < 30 m.
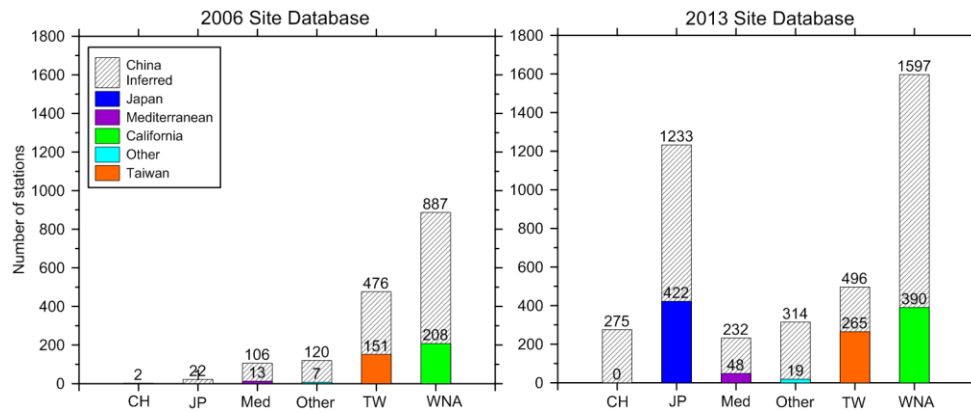
Figure 4.3. **Histograms for sites with measured V_s and profile depths > 30 m in the 2006 and 2013 site databases for five main regions and other regions.**
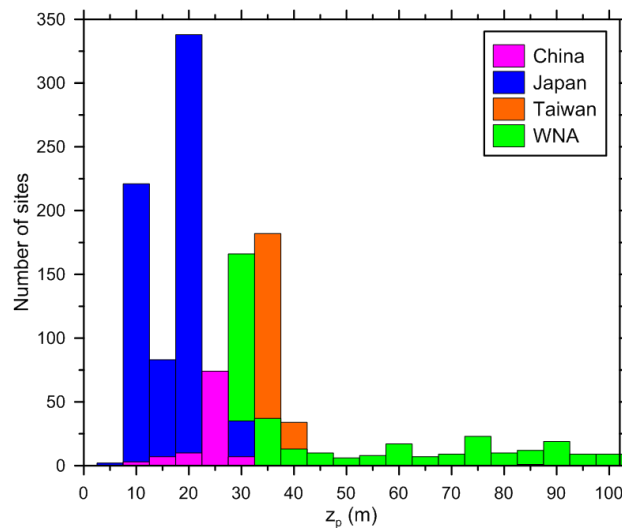
Figure 4.4. **Histogram of profile depth bins by region. Profile depths for Japan extend up to 365 m, but are concentrated at 100 m in the figure. Note that there is one station with z_p = 82 m in Japan.**

4.3.2 Computation of V_{s30}

When profile depths (z_p) are 30 m or more in depth, V_{s30} is computed as the ratio of 30 m to the shear-wave travel time through the upper 30 m of the site as follows:

$$V_{s30} = \frac{30}{\int_0^{30} \frac{dz}{V_s(z)}} \tag{4.1}$$

where the integral is evaluated in practice through summation across velocities taken as constant within depth intervals.

It is not unusual for shear-wave velocity measurements to extend to depths shallower than 30 m. In such cases, V_{s30} cannot be calculated directly, but the available geophysical data to profile depth z_p can be used to estimate V_{s30}. The average velocity to depth z_p, termed V_{sz}, is calculated similarly to V_{s30}:

$$V_{sz} = \frac{z_p}{\Delta t_z} \tag{4.2}$$

where z_p = profile depth and Δt_z = travel time for shear-waves from depth z_p to the ground surface, calculated as:

$$\Delta t_z = \int_0^{z_p} \frac{dz}{V_s(z)} \tag{4.3}$$

Using these variables, the procedures discussed in this section estimate V_{s30} from V_{sz} conditional on z_p.

The simplest method to estimate V_{s30} from V_{sz} for $z_p < 30$ m is to extend the lowermost velocity in the profile to 30 m (Boore 2004). This method was used in Version 23 of the site

database (Chiou et al. 2008). More generally, correlation relationships are used based on borehole measurements. Boore (2004) used profile data from 135 boreholes in California to develop V_{s30}-V_{sz} correlations. Kanno et al. (2006), Cauzzi and Faccioli (2008), Cadet and Duval (2009), and Boore et al. (2011) similarly utilized velocity profiles based on borehole measurements at 691 vertical array sites in Japan that are within the KiK-net network (Kinoshita 1998; Okada et al. 2004). The unpublished Yu and Silva report (R. Darragh, personal communication, 2011) derived a V_{s30}-V_{sz} correlation using 73 KiK-net stations with both measured V_{s30} and assigned Geomatrix 3rd letter. As described by Boore et al. (2011), the KiK-net sites are preferentially located on relatively hard rock geologic conditions, so V_{s30}-V_{sz} correlation relationships will reflect that type of geology.

An expression for relating V_{sz} to V_{s30} is:

$$\log\left(V_{s30}\right) = c_0 + c_1 \log\left(V_{sz}\right) + c_2 \left[\log\left(V_{sz}\right)\right]^2 \tag{4.4}$$

where c_0, c_1, and c_2 are regression coefficients that depend on profile depth z_p. Boore (2004) used a linear model (i.e., $c_2 = 0$) and provided coefficients for z_p from 10 to 29 m. Boore et al. (2011) find that the Boore (2004) model is appropriate for alluvial and soft rock sites outside of California, including the K-net sites in Japan (typically located on sediments in urban areas), Turkey, and sites in Europe. This is illustrated in Figure 4.5(b), which shows V_{s20} values for K-net sites that are similar to those for California sites. However, Boore et al. (2011) find the 2004 model biased for regions with stiffer rock site classifications and develop an alternative relationship using the second order polynomial form in Equation (4.4) for depths ranging from 5

to 29 m using the KiK-net data. Figure 4.5(a) illustrates this bias, by the shift towards faster V_{S20} values for KiK-net sites relative to K-net sites.

These differences in velocities are consistent with a statement by Okada et al. (2004) that K-net and KiK-net stations are predominantly located on soil and rock sites, respectively. The KiK-net stations in Japan are located on a nominally uniform grid, which means that a number of stations are in valleys in hilly terrain with shallow sediments over rock. California stations are predominately in urban areas, such as Los Angeles and San Francisco, which are located within broad areas of low topographic relief, underlain by sedimentary basins. Figure 3.6 shows histograms of topographic slopes for California strong-motion sites and Japan KiK-net sites. The slopes at the California borehole sites are systematically lower than those at the KiK-net sites in Japan, indicating the tendency for KiK-net stations to be preferentially sited on stiffer soils or rock.
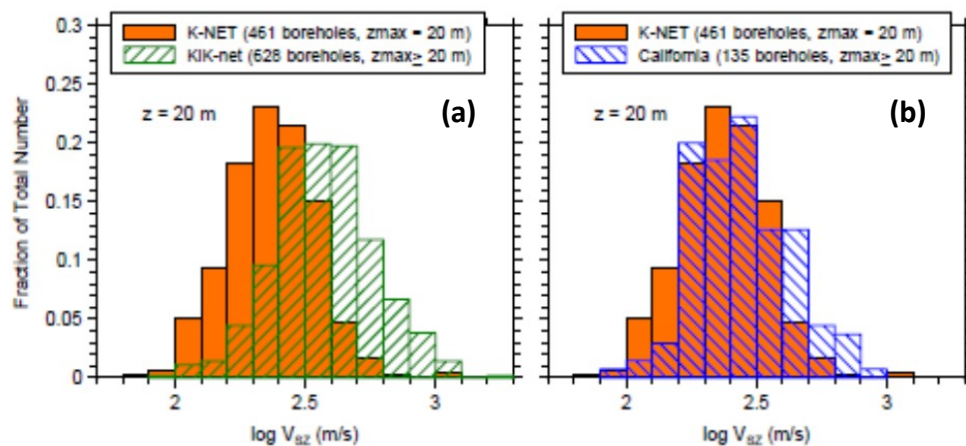
Figure 4.5. Histograms of log V_{s10} and log V_{s20} for shear-wave velocity models from K-net, KiK-net, and California, for $z_p = 20$ m (from Boore et al., 2011).
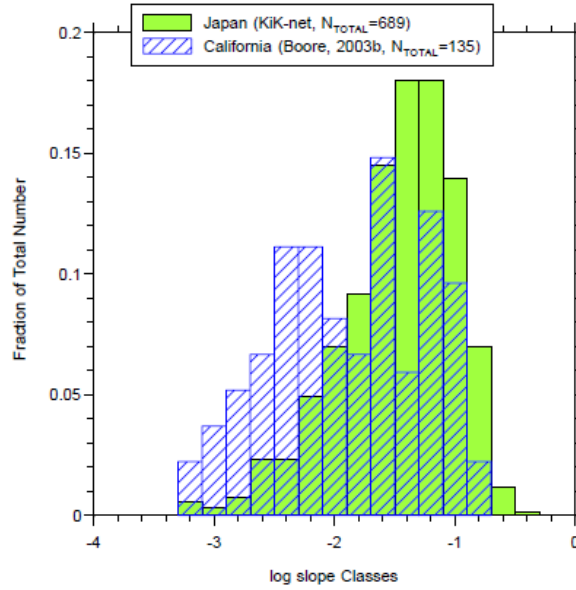
Figure 4.6. **Histogram of ground slopes at sites in California and Japan from which the velocity models were obtained (from Boore et al., 2011).**

Yu and Silva (R. Darragh, personal communication, 2011) identified bias in the Boore (2004) V_{s30}-V_{sz} correlations during a PEER study of V_s data from 147 sites in southwest China (SWC sites) that recorded the Wenchuan, China, earthquake. The bias (or regional dependence) was identified by calculating V_{s30} at the SWC sites by extending the lowermost velocity in the profile to 30 m (simple extrapolation) and then comparing those results to estimates from Boore (2004), from which an under-prediction bias of 0.139 (ln) was found for 32 sites with $z_p = $ 10–20 m. Elevation and terrain proxies for V_{s30} also had significant bias for those sites.

Yu and Silva then developed V_{s30}-V_{sz} correlation, intended for application at SWC sites that are generally stiffer than California, using data from seventy-three selected Kik-net sites having GMX 3rd letter classifications. They developed both linear (c_2=0) and parabolic equations. It was not possible for this relationship to be based on SWC data because very few of those

boreholes extend beyond 30 m. A linear relationship was recommended that is not conditioned on additional parameters such as GMX site codes. The aforementioned Boore et al. (2011) study includes many more KiK-net sites and does not use GMX 3rd letter classifications.

Figure 4.7 compares the V_{s30}-V_{sz} correlations from Boore et al. (2011) and Yu and Silva. The differences between the curves increase as z_p decreases, with the Yu and Silva model having a flatter gradient for z_p = 5 and 10 m (leading to higher V_{s30} estimates for lower V_{sz}; lower V_{s30} for high V_{sz}).The differences between the two curves are minor for V_{sz} > 250 m/sec, which is a common condition for SWC sites (the application region for Yu and Silva). Figure 3.8 compares the two correlations to KiK-net data for four values of z_p. As expected, the Boore et al. (2011) parabolic model generally provides a better fit, although the difference is most significant for V_{sz} < 200 m/sec.
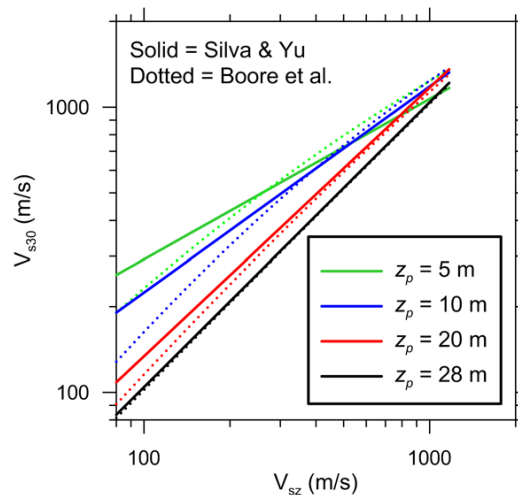
Figure 4.7.   **Comparison of V_{s30}-V_{sz} relationships developed by Yu and Silva and Boore et al. (2011) for four profile depths, z_p.**
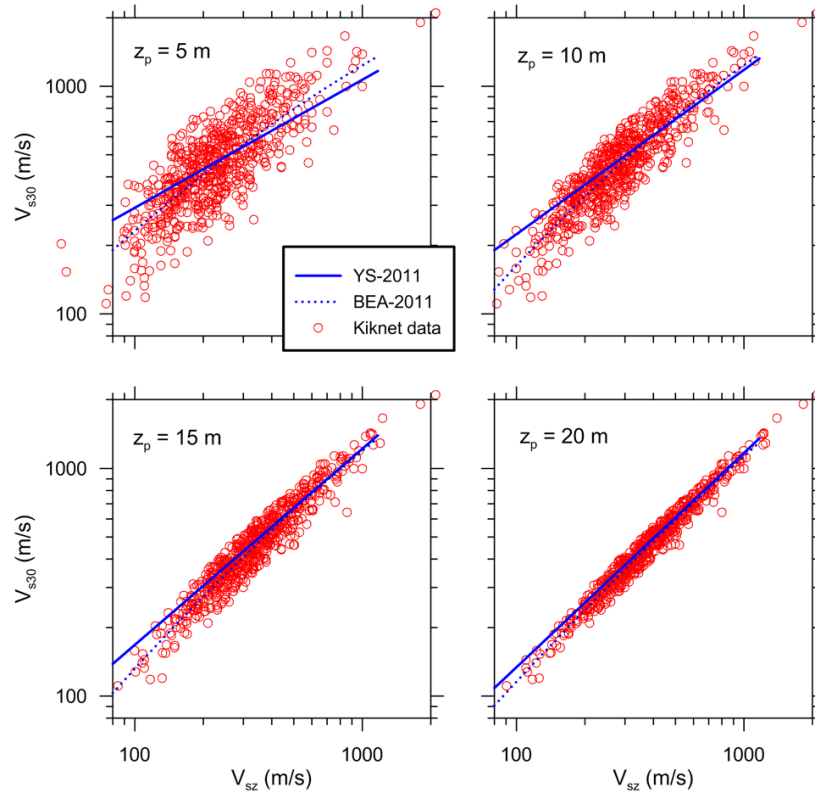
Figure 4.8. Comparison of V_{s30}-V_{sz} relationships developed by Yu and Silva and Boore et al. (2011) with KiK-net data for four profile depths, z_p

4.4 Proxy Based Estimation of V_{s30}

4.4.1 Description of the Methods

4.4.1.1 Methods based on Surface Geology or Geotechnical Conditions

Correlations have been developed to relate V_{s30} to surface geologic units and geotechnical site categories (the most widely used of which is the GMX 3rd letter). The California correlations described in this section both used V_{s30} values from the PEA profile database in their original development. Although the underlying databases were similar, the level of documentation of the correlations varies from well-documented in archival literature (these tend to be based on

87

surface geology) to relatively sparsely documented in principally grey literature (GMX, although

a brief summary is provided in Chiou et al. (2008).

Correlations utilizing surface geology are available for California and Italy. For such

correlations to be useful, variations of velocities within the broad geological categories typically

shown in geological maps (e.g., Quaternary alluvium, Qa) need to be captured. This can be

accomplished by either using relatively detailed categories, (e.g., separating thin and deep Qa),

region-specific categories (e.g., for alluvium in the Imperial Valley and Los Angeles basin), or

geologic information coupled with geomorphologic data (e.g., slope or other terrain

descriptors).

For California, V_{s30} statistics (medians and standard deviations) were compiled for

nineteen relatively detailed geological categories (including region-specific categories) by Wills

and Clahan (2006), which were used in the 2006 site database. Current recommendations are

to use the Wills and Clahan (2006) values for rock sites (i.e., Tertiary or older), and to use

relations based on ground slope at 3 arc sec resolution for Quaternary sediments (Wills and

Gutierrez 2008), as shown in Figure 4.9. The slope based values in Figure 4.9 are modified from

those published in Wills and Gutierrez (2008) by converting arithmetic means and standard

deviations to the median and standard deviation of a log-normal distribution (using Ang and

Tang, 1975). The alluvial ground slope correlation shows an increase of velocity with slope,

which follows expected trends, because flatter slopes tend to be in mid-basin areas having

relatively fine-grained alluvium with slower velocities. Figure 4.9 also shows that the standard

deviation of velocities decreases as V_{s30} decreases.

The applicability of the Wills and Clahan (2006) correlations to Italy was investigated by Scasserra et al. (2009), who found that the median velocities for Quaternary categories are unbiased relative to Italian data. For rock sites, the California categories were not descriptive of Italian geology, and distinct correlations therefore were developed for appropriate geologic rock categories.

The principal geotechnical site categorization scheme that has been used in previous ground motion studies (e.g., Chiou et al., 2008) and correlated to V_{s30} was proposed by the consulting firm Geomatrix (GMX) (D. Wells. personal communication, 2005). The GMX scheme has three letters, the last of which represents site condition. The GMX 3rd letter categories and the corresponding site conditions are shown in Table 4.2. The values of V_{s30} in Table 4.2 are based on the PEA profile database and were used in the 2006 site database as the basis for V_{s30} estimation when surface geological information was not available but Geomatrix 3rd letter classifications were available (Chiou et al 2008).
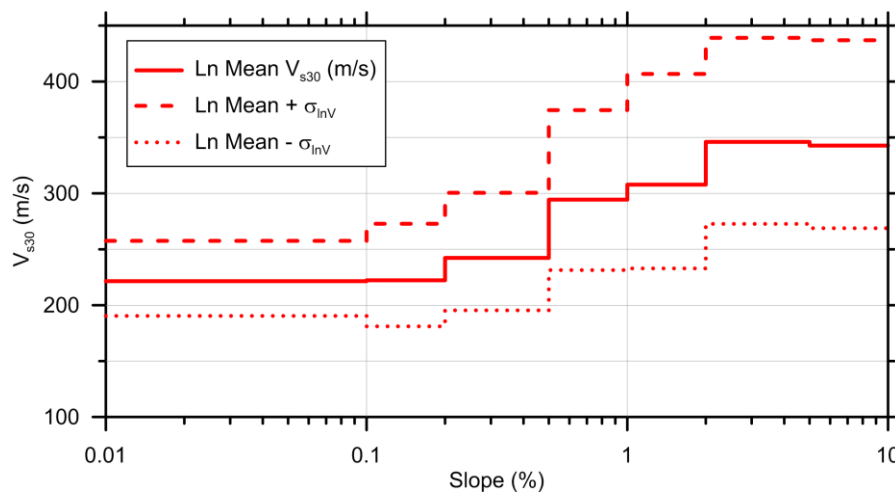
Figure 4.9. Variation of V_{s30} with ground slope within basins (adapted from Wills and Gutierrez, 2008). Slopes are based on digital ground elevation models at 3 arc sec resolution.

Table 4.2. Geomatrix 3rd letter site categories and recommended V$_{s30}$ and uncertainty (adapted from Chiou et al., 2008).

Geomatrix Third Letter	Description	Median V$_{s30}$ (m/s)	σ_{ln}	Mean V$_{s30}$ (m/s)	σ
A	Rock. Instrument on rock (V$_s$ > 600 mps) or <5m of soil over rock.	659.6	0.416	720.2	324.2
B	Shallow (stiff) soil. Instrument on/in soil profile up to 20m thick overlying rock.	424.8	0.431	464.3	211.0
C	Deep narrow soil. Instrument on/in soil profile at least 20m thick overlying rock, in a narrow canyon or valley no more than several km wide.	338.6	0.203	345.4	70.4
D	Deep broad soil. Instrument on/in soil profile at least 20m thick overlying rock, in a broad valley.	274.5	0.335	291.4	110.5
E	Soft deep soil. Instrument on/in deep soil profile with average V$_s$ < 150 mps.	191.3	0.29	199.4	61.4

4.4.1.2 Methods based on Ground Slope, Geomorphology, or Elevation

Correlations have been developed to link surface topographic features to V_{s30}. The most well-known of these correlations relate topographic slope to V_{s30} (Wald and Allen 2007; Allen and Wald 2009) for applications in active tectonic regions with shallow crustal earthquakes and stable continental regions. Techniques in which V_{s30} is estimated based on geomorphology-based categories have been presented by Yong et al. (2012) for California and Matsuoka et al. (2006) for Japan. Another technique that has been used locally for Taiwan stations correlates V_{s30} to elevation within Geomatrix categories (Chiou and Youngs, 2008a; updated in the present work).

Slope Model: The motivation behind development of the V_{s30}-slope correlation is that topographic data are globally available, and slope may be an indicator of near-surface

morphology and lithology (http://earthquake.usgs.gov/hazards/apps/V$_{s30}$/custom.php). Steep terrain is expected in mountains, indicating rock, whereas nearly flat slopes occur in basins, indicating soil. Transition zones would be expected to have moderate slopes involving weathered rock and potentially older sediments near basin boundaries. Wald and Allen (2007) developed a correlation between ground slope and measured V_{s30} using available regional data sets, including the PEA profile database for sites in California. Separate slope-V_{s30} correlations were developed for active and stable continental regions that indicate increasing V_{s30} with increasing topographic slope. Data exists for gradients < 7%, corresponding to a 4° slope. Equations relating V_{s30} to slope were not provided; rather, stepped relationships of slope tied to discrete velocity bands were provided. Elevation did not provide additional predictive power for V_{s30} beyond ground slope.

Terrain Model (California): The Yong et al. (2012) procedure for V_{s30} considers slope along with geomorphologic factors including convexity and texture. This technique utilizes the same globally available SRTM 30-arc-sec surface models employed by Wald and Allen (2007). Hence, for a given location (latitude, longitude), the slope parameters used in the two models should be identical. The convexity element of the classification scheme is intended to distinguish convex-upward topography (characteristic of lowland terraces and alluvial fans) from concave-downward topography (broad valleys and foothills). The texture elements distinguish relatively smooth terrain from terrain having pits and peaks. These textural descriptions should not be confused with soil texture (e.g., fine, course) used in some sediment classification schemes (e.g., Fumal and Tinsley, 1985).

Ground slope, convexity, and texture are jointly analyzed using an automated topography classification scheme by Iwahashi and Pike (2007) to segregate terrain types into sixteen categories, which are depicted in Figure 4.10. As one moves to the right in the matrix, ground slope is decreasing, whereas moving down in the matrix produces less convexity and smoother texture. We note that the classification scheme has relatively fine discretization of rock conditions (rock categories include 1−7, 9, 11, and 13) but limited discretization of soil (e.g., there is no category that would seem to encompass lacustrine or marine clays, which produce the largest site amplification).

Statistics on V_{s30} (median and standard deviation) are provided by Yong et al. (2012) for each of the categories using a California data set derived largely from values in the PEA profile database.

Terrain Model (Japan): Matsuoka et al. (2006) provide V_{s30} values for categories within the "Japan Engineering Geomorphologic Classification Map (JEGM)," which was released by Wakamatsu et al. (2005). The JEGM actually utilizes geomorphology, surface geology, slope angle, and relative relief to classify locations into geomorphologic units. The empirical correlations are based on shear-wave velocity profiles from 1937 sites. The categories and their median values of V_{s30} are indicated in Figure 4.11 (indicated as "AV_{S30}" in the figure). Categories 1−4 correspond approximately to rock conditions, 5−7 are transitional categories, and categories of 8 and above represent variable soil conditions. Matsuoka et al. (2006) provide intra-category regressions against elevation for categories 8−13, against slope for categories 3, 5, and 8−11, and against distance from hill for categories 8, 10, 13, 15, and 18−19. Maps of JEGM and associated values of V_{s30} have been prepared at 250-m grid-size resolution by

Wakamatsu and Matsuoka (2006) and at 1-km grid resolution by Matsuoka et al. (2006). This classification scheme was not included in the 2013 version of the site database, but is noted here for completeness.
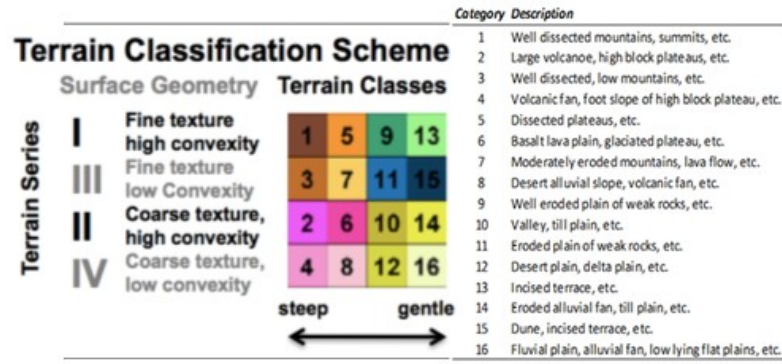
Figure 4.10.   Variation of slope, texture, and convexity with terrain categories of Yong et al. (2012).
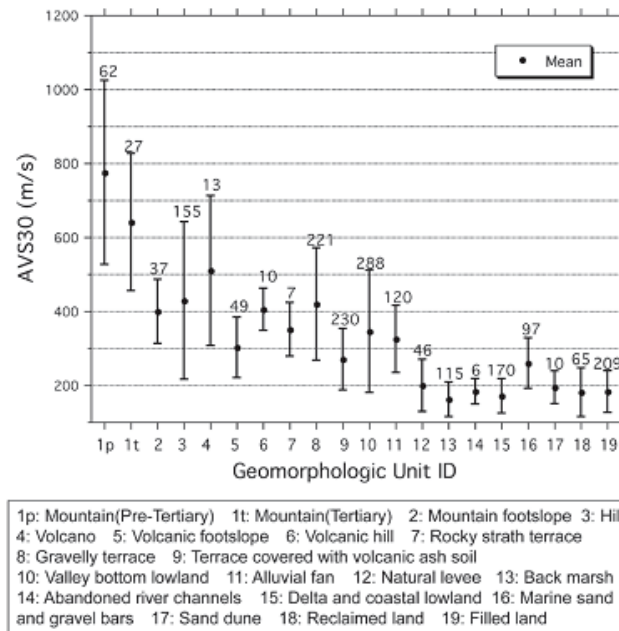
Figure 4.11.   Mean values of V_{s30} (indicated as "AV_{s30}") for geomorphologic categories in JEGM (from Matsuoka et al., 2006).

93

**Elevation Model (Taiwan):** Chiou and Youngs (2008a) present a model for V_{s30}

estimation based on both Geomatrix (GMX) 3rd letter categories (Table 4.2) and elevation that

is locally applicable in Taiwan. The model has been updated as part of the NGA-West 2 project

by B. Chiou (personal communication, 2012) using the Taiwan sites in the site database. The

model is based on the observation that elevation and geology are correlated in Taiwan due to

the tectonic setting (Lee et al. 2001), with higher elevations having stiffer materials in GMX soil

categories C and D. The analysis used 165 V_{s30} data points to estimate median values of V_{s30} for

GMX categories A, B, and E (for which no trends of V_{s30} with elevation were observed) and to

establish the following regression relation for GMX categories C and D:

$$\ln(V_{S30}) = \ln(\varphi_1) + \frac{\ln(\varphi_2) - \ln(\varphi_1)}{1 + e^{(\ln(\varphi_3) - \ln(Elv))/\varphi_4}}$$

(4.5)

The estimated coefficients are given in Table 4.3.

Table 4.3.   Coefficients for Taiwan-specific estimation of mean V_{s30} within GMX categories.

Category	ϕ_1	ϕ_2	ϕ_3	ϕ_4
A	683.9	-	-	-
B	559.6	-	-	-
C+D	225	513	31.4	0.476
E	204.2	-	-	-

4.4.2 Proxy Evaluations

4.4.2.1 California

It is clear that V_{s30} is most reliably obtained with high-quality geophysical measurements;

however, no consensus exists regarding how it should be estimated in the absence of such

measurements. In many cases, practical considerations dictate the choice of method to be

applied in a given area; for example, in the absence of geological maps, topography or terrain-based methods are the only viable option. However, when the available information does provide options (e.g., when both high-quality geological and topographic information are available), which method should be selected? Ideally this decision would be made on the basis of local or regional studies of the efficacy of these techniques to the region. We investigate the relative reliability of the techniques described above through comparative analysis against a California data set consisting of 475 V_{s30} values based on measurements. An earlier version of these analyses was presented by Stewart et al. (2012). The following section presents a similar analysis using data from Taiwan.

We utilize the California sites in the site database having V_{s30} from measurements and z_p > 20 m. For sites with z_p = 20–29 m, we compute time-averaged velocity to the profile depth (V_{sz}) and then use the Boore (2004) V_{sz} to V_{s30} extrapolation technique as described in Section 4.3.2.

We calculate V_{s30} residuals as follows:

$$R = \ln\left(V_{s30}\right)_{meas} - \ln\left(V_{s30}\right)_{proxy}$$

(4.6)

where $(V_{s30})_{meas}$ is a measured value and $(V_{s30})_{proxy}$ is estimated based on a correlation relationship. Note that by taking the natural log of the data, we assume the velocities to be log-normally distributed. Model bias can be estimated from the median of the residuals (μ_{lnV}). The standard deviation of residuals (σ_{lnV}) can be calculated for the entire set of residuals or sub-sets having certain conditions (e.g., sites within a particular category). The standard deviation term σ_{lnV} represents epistemic uncertainty on velocity, which should be considered in ground motion

estimation. Boore et al. (2011) describe procedures by which this uncertainty can be considered in ground motion evaluation from GMPEs.

Figure 4.12 presents histograms of residuals from the geology proxy of Wills and Clahan (2006) and Wills and Gutierrez (2008) (the latter of which uses geology in combination with ground slope for post-Tertiary sediments). We note that the standard deviation increases with age from approximately 0.28 for Quaternary to about 0.43 for Mesozoic bedrock units. When all data are combined together, the median is -0.06 and the standard deviation are 0.33.

Figure 4.13 presents histograms based on the Geomatrix 3rd letter (Chiou et al. 2008). The bias is modest (generally < 0.1) except for category A and E (rock and soft, deep soil in Table 3.2). Standard deviations range from approximately 0.2−0 3 for soils to about 0.4−0.5 for rock. When all data are combined together, the median is -0.08 and the standard deviation is 0.40.

Figure 4.14 presents V_{s30} data plotted versus slope along with the recommended ranges from Wald and Allen (2007). The proxy estimates reasonably well the data median for slopes under about 0.07 m/m and over-predicts approximately from 0.07−0.15 m/m. There are practically no data for steeper slopes. The overall median of residuals is -0.01 and the standard deviation is 0.45.
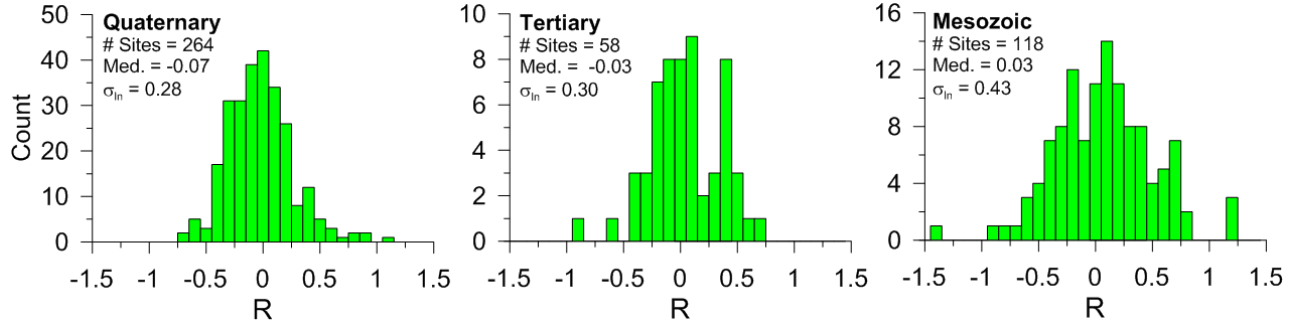
Figure 4.12. Residuals of V_{s30} from estimates based on the geology proxy using the methods of Wills and Gutierrez (2008) for alluvium and Wills and Clahan (2006) for all other conditions.
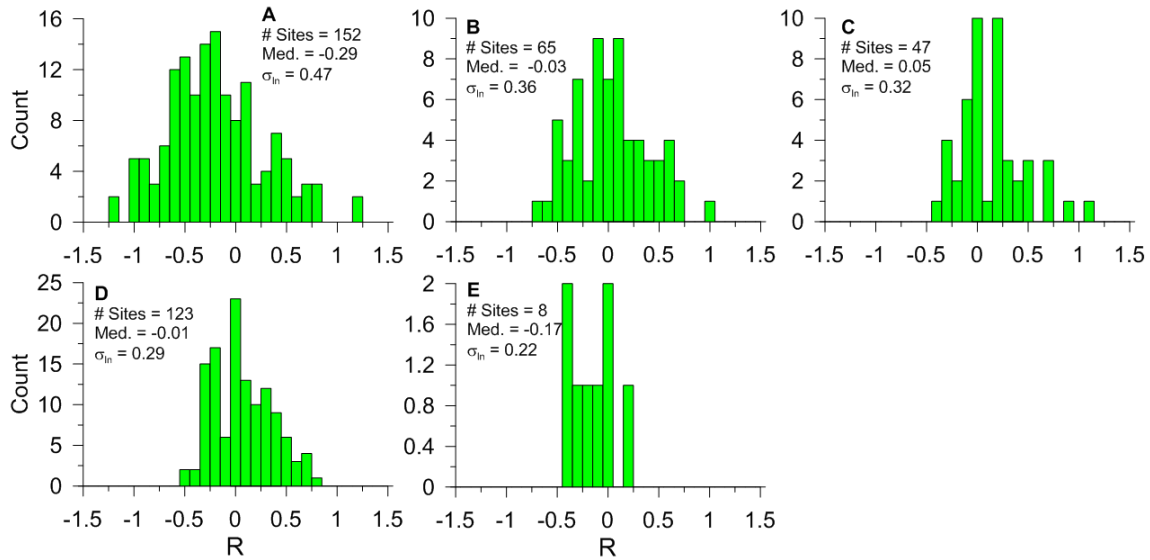
Figure 4.13. Residuals of V_{s30} from estimates based on the geotechnical proxy (Geomatrix 3rd letter) using the methods of Chiou et al. (2008). Based on V_{s30} measurements and V_{sz}-V_{s30} relations.
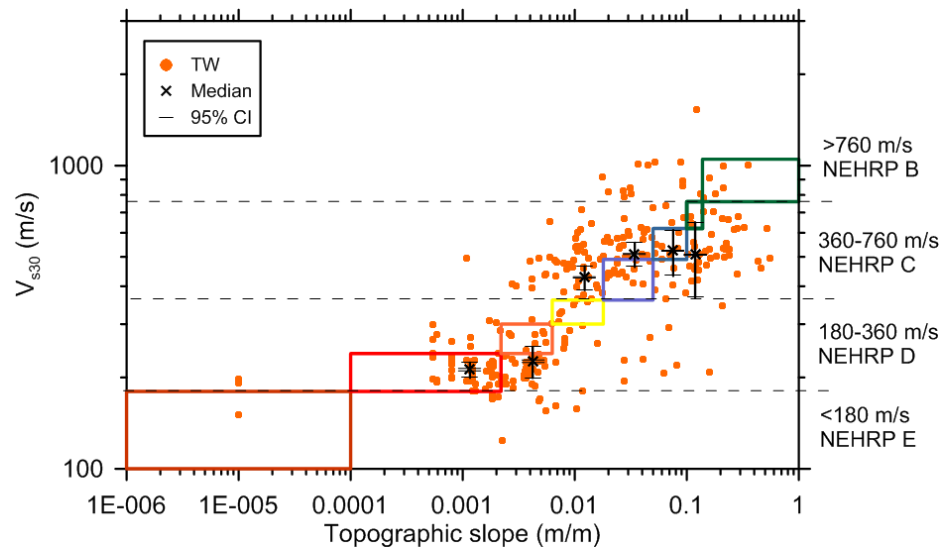
Figure 4.14. **V$_{s30}$ versus slope from California data and estimates from Wald and Allen (2007) for active tectonic regions. Color coded polygons correspond to slope ranges within NEHRP classes.**

Residuals for the terrain-based method were evaluated by using an updated terrain map relative to that used by Yong et al. (2012), although the data are not adequate to constrain statistically significant medians or standard deviations for most categories. Categories with results considered to be reliable are indicated in Table 4.4. There is relatively little bias except for category 1, and standard deviations range from about 0.2 for softer geology to 0.4–0.6 for rock categories. Looking across all categories, the median of residuals is -0.11 and the standard deviation is 0.42.

Table 4.4.   **Terrain-based categories by Yong et al. (2012) and corresponding V_{s30} and uncertainty.**

Category	Description	# V_{s30} meas.	μ_{lnV}	σ_{lnV}
1	Well dissected mountains, summits, etc.	39	-0.27	0.36
3	Well dissected, low mountains, etc.	49	-0.11	0.55
4	Volcanic fan, foot slope of high block plateau, etc.	40	0.13	0.47
7	Moderately eroded mountains, lava flow, etc.	44	-0.09	0.36
8	Desert alluvial slope, volcanic fan, etc.	47	-0.07	0.43
12	Desert plain, delta plain, etc.	21	-0.09	0.17
16	Fluvial plain, alluvial fan, low lying flat plains, etc.	33	-0.17	0.19

The relative efficacy of the different proxy-based estimation techniques can be judged on the basis of bias and standard deviation of residuals, as shown in Figure 4.15. Bias is generally small for the proxies investigated with the aforementioned exceptions. The standard deviation results were separated by categories when practical as indicated in Figure 4.15. For comparison, Figure 4.15 also shows an approximate standard deviation for measurements of V_{s30} at single sites with multiple V_s measurements (justification for the plotted value is given in Section 4.5.2.2). This value of σ_{lnV} reflects spatial variations in seismic velocities for modest separation distances between profiles (on the order of 10 m to several hundred meters) but similar geologic conditions. Significantly higher dispersion occurs when the site geology is heterogeneous and V_s measurements reflect significantly variable geologic conditions (e.g., both deep and shallow soil).

As expected, none of the estimation techniques are able to reproduce the low dispersions from measurement. We generally see lower dispersion for softer sites, represented by Quaternary geology, Geomatrix soil categories C-E, and terrain categories 12 and 16. Average dispersion levels (marked as the "overall" sigma in Figure 4.15) from the geology and

geotechnical schemes are similar, and are somewhat lower than those from geomorphic schemes.
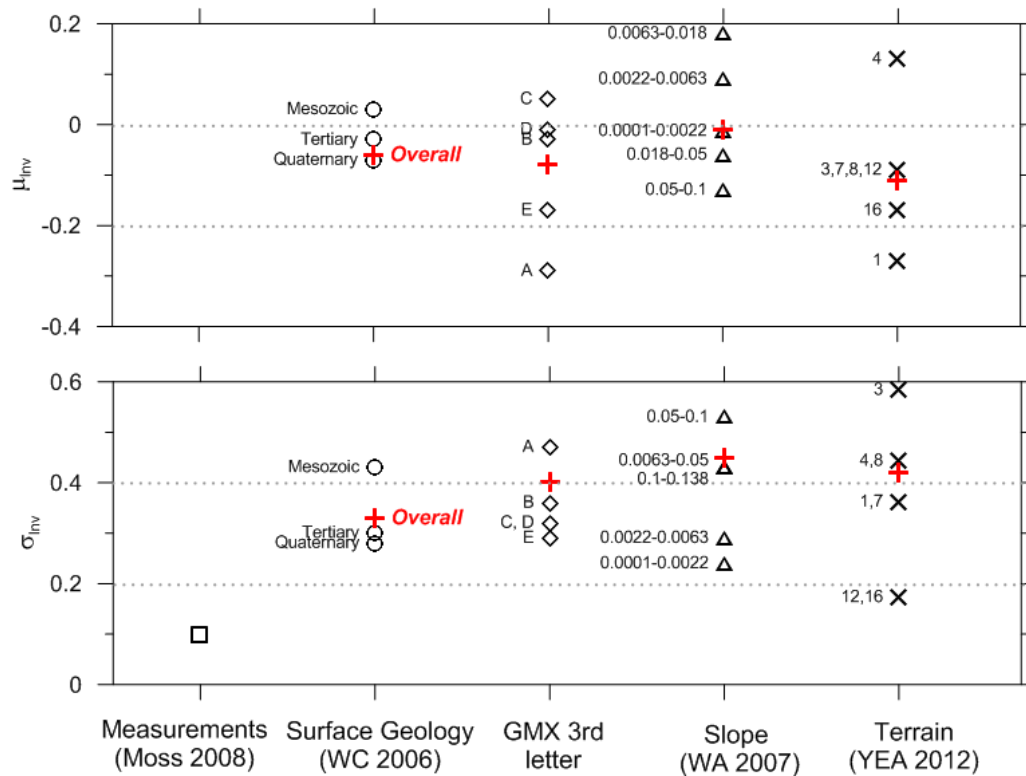
Figure 4.15. Median and dispersion of V_{s30} prediction residuals for California in natural log units based on the analyses in this study. Results for measurements are derived from data presented by Moss (2008) and Thompson et al. (2012), as discussed in Section 4.5.2.2. Explanation of codes: GMX: A-E, see Table 4.2. Slope: slope categories within various NEHRP classes. Terrain: numbered categories, see Figure 4.10. WC 2006 = Wills and Clahan (2006), WA 2007 = Wald and Allen (2007), YEA 2012 = Yong et al. (2012). Proxy aggregates are marked as "Overall".

4.4.2.2 Taiwan

This section presents proxy analysis for Taiwan using a database of 301 V_{s30} values based on profiles 20 m or greater in depth from the site database. The same procedures are used as in the previous section for California. Ongoing work performed in collaboration with Dr. Annie Kwok from National Taiwan University is developing geology-based proxy estimation

procedures for Taiwan, but these are not available at present. The proxies evaluated in this section are GMX 3rd letter, slope, terrain, and GMX 3rd letter combined with elevation. Note that the first and third of these proxy relationships were derived based on data from California, so some misfit for Taiwan is to be expected. The slope proxy is based on international data, whereas the GMX/elevation model is based on Taiwan data, and hence would be expected *a priori* to have the least bias.

Figure 4.16 presents histograms based on the Geomatrix 3rd letter for Taiwan where the bias is negligible except for category E. Standard deviations range from 0.2 for soft soils to about 0.4 for rock. When all data are combined together, the median is 0.15 and the standard deviation is 0.37.

Figure 4.17 presents V_{s30} data plotted versus slope along with the recommended ranges from Wald and Allen (2007). The proxy estimates reasonably well the data median for slopes under about 0.1 m/m, with over-prediction misfits for steeper slopes. There are practically no data for slopes steeper than approximately 0.3 m/m. The overall median of residuals is 0.07 and the standard deviation is 0.34.
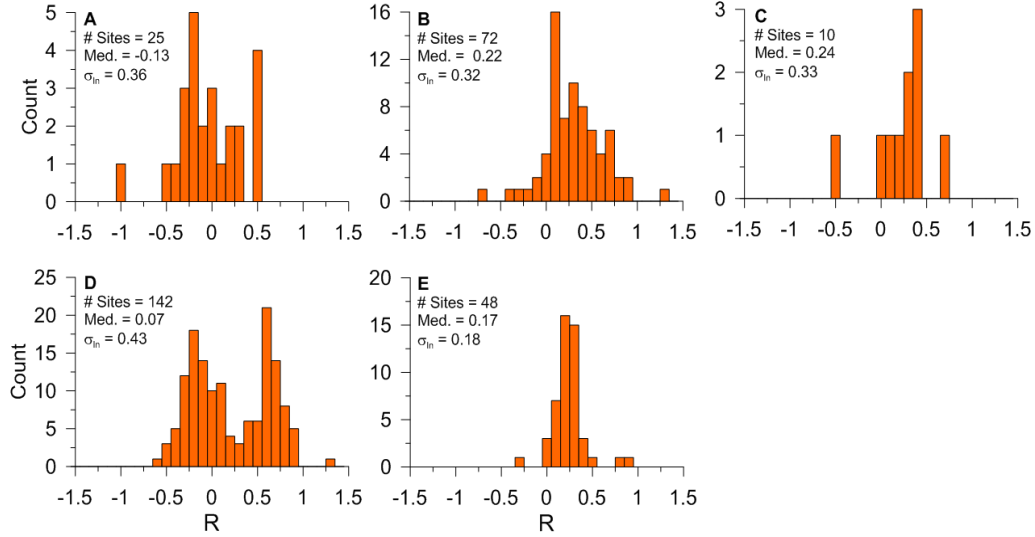
Figure 4.16. Residuals of V_{s30} from estimates based on the geotechnical proxy (Geomatrix 3rd letter) using the methods of Chiou et al. (2008). Based on V_{s30} measurements and V_{sz}-V_{s30} relations.
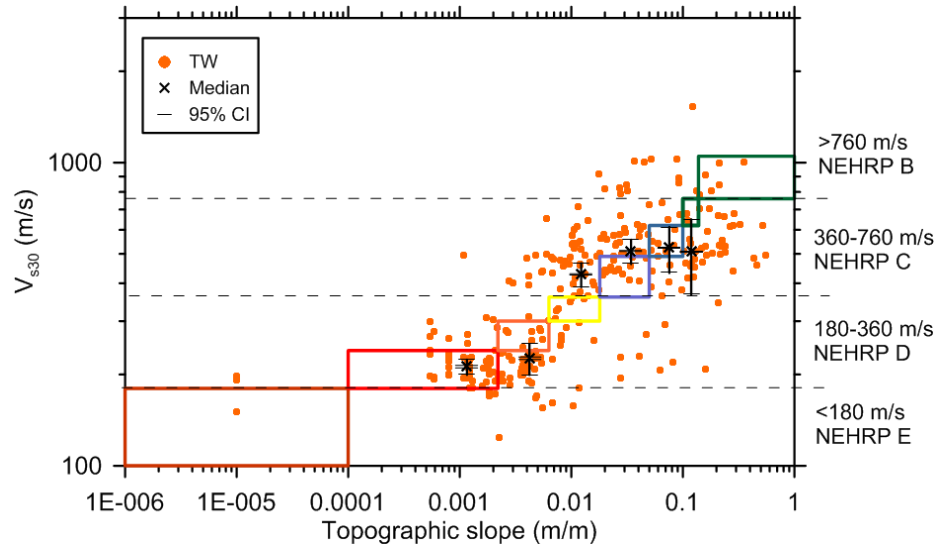
Figure 4.17. V_{s30} versus slope from California data and estimates from Wald and Allen (2007) for active tectonic regions. Color coded polygons correspond to slope ranges within NEHRP classes. TW = Taiwan.

Residuals for the terrain-based method were evaluated in categories for which statistically significant medians or standard deviations could be constrained (as was done for

102

the California data). Categories with results considered to be reliable are indicated in Table 4.5. There is relatively little bias except for category 15, and standard deviations range from about 0.2 for softer geology to 0.4–0.5 for harder rock categories. Looking across all categories, the median bias is -0.13 and the standard deviation is 0.42.

Table 4.5. Terrain-based categories by Yong et al. (2012) and corresponding V_{s30}.

Category	Description	# V_{s30} meas.	μ_{lnV}	σ_{lnV}
1	Well dissected mountains, summits, etc.	19	-0.02	0.28
3	Well dissected, low mountains, etc.	71	-0.01	0.38
7	Moderately eroded mountains, lava flow, etc.	41	0.24	0.49
8	Desert alluvial slope, volcanic fan, etc.	19	0.19	0.32
11	Eroded plain of weak rocks, etc.	29	0.01	0.37
15	Dune, incised terrace, etc.	16	-0.5	0.28
16	Fluvial plain, alluvial fan, low lying flat plains, etc.	49	-0.17	0.18

Figure 4.18(a) shows relationships between V_{s30} and elevation for GMX 3rd letter categories. Figure 4.18(b) shows results for categories C and D only along with the recommended relationship (updated from Chiou and Youngs, 2008a). The fitted line in red is computed using Eqn. (4.5). The fit matches the data well at low elevations ($\leq$ 20 m) but underestimates the increase in V_{s30} as elevation increases, causing bias for high elevations. Corresponding histograms of residuals within GMX categories are shown in Figure 4.19. Looking across all categories, the median bias is 0.02 and the standard deviation is 0.32.
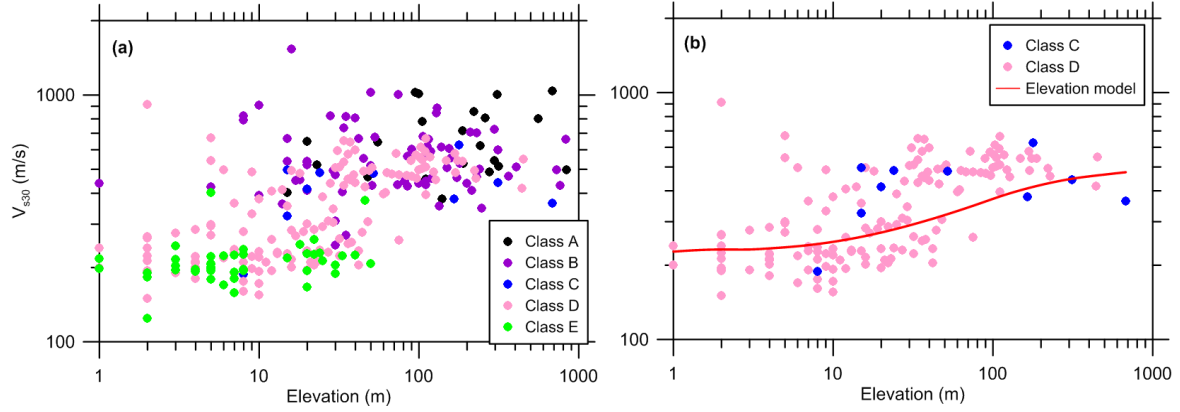
Figure 4.18. Variation of V_{s30} with elevation within GMX 3rd letter categories: (a) all categories; and (b) categories C and D and elevation-based model from Chiou (personal communication, 2012). The data set used for development of the proxy is not the same as that shown here.
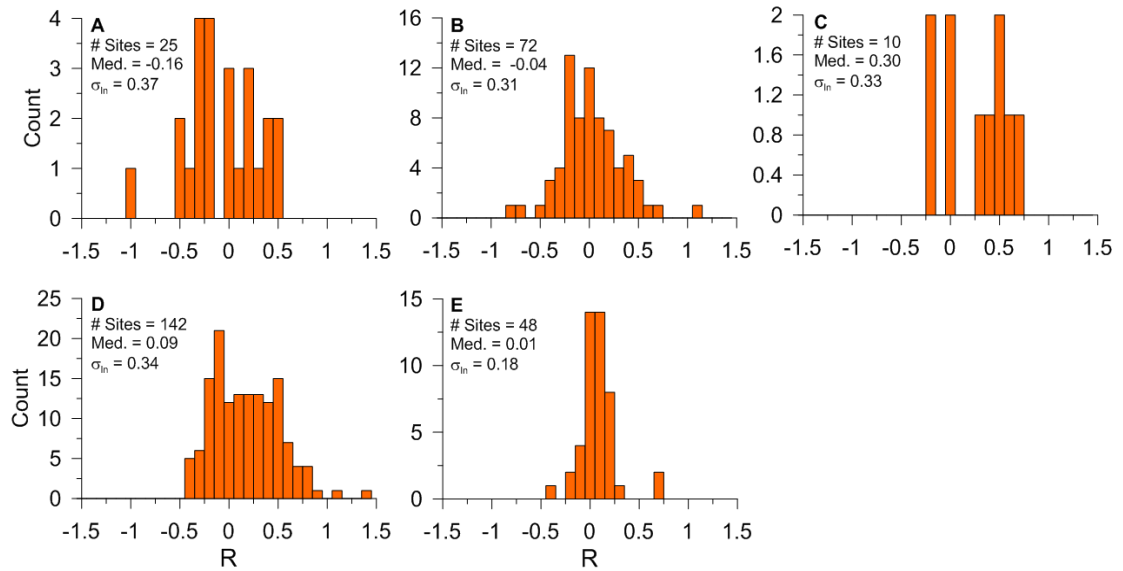
Figure 4.19. Residuals of V_{s30} from estimates based on elevation-based method within GMX 3rd letter categories using the methods of Chiou and Youngs (2008a). Based on V_{s30} measurements and V_{sz}-V_{s30} relations for Taiwan data.

The relative efficacy of the different proxy-based estimation techniques can be judged on the basis of bias and standard deviation of residuals, as shown in Figure 4.20. Bias is not

104

negligible, generally ranging from -0.2 to +0.2 without systematic trends for rock or soil sites. The standard deviation results were separated by categories when practical as indicated in Figure 4.20. We generally see lower dispersion for softer sites, such as Geomatrix category E and flat slopes. General dispersion levels provided by the four considered proxies are generally similar.
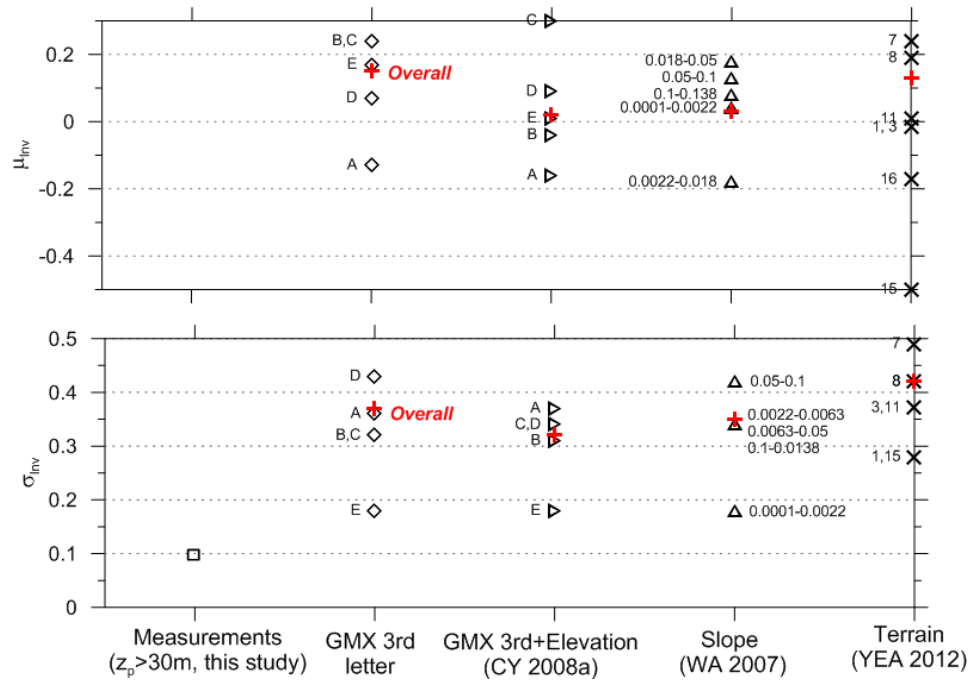
Figure 4.20. **Median and dispersion of V_{s30} prediction residuals for Taiwan in natural log units based on the analyses in this study. All explanations for abbreviations are the same as in Figure 4.15, except for CY 2008a= Chiou and Youngs (2008a). Proxy aggregates are marked as 'Overall'.**

4.4.2.3 Japan

In this section we present proxy analysis for Japan using a database of 751 V_{s30} values based on profiles 20 m or greater in depth from the site database. The proxies evaluated in this section are GMX 3rd letter, slope, terrain, and geomorphology-based categories. Note that the first and third of these proxy relationships were derived based on data from California, so some misfit

for Japan is to be expected, as occurred for Taiwan. The slope proxy is based on international data, whereas the geomorphology-based analysis is Japan-specific.

Figure 4.21 presents histograms based on the Geomatrix 3rd letter for Japan. The bias is negligible for categories B, C, and D, but significant for A and E. Similar biases were observed for California data. Standard deviations range from 0.20–0.30 for soft soils to about 0.4 for rock. When all data are combined together, the median is -0.14 and the standard deviation is 0.38.

The Japanese data set is different from other regions in that a relatively high percentage of V_{s30} values are derived from rock sites (GMX Category A). This occurs because the NIED ground motion network emphasized locating ground motion stations at rock sites. Figure 4.22 shows the mapped distribution of V_{s30} in Japan. The bias at rock sites that was observed in California and Japan motivated a suggested modification to the GMX A mean V_{s30} value, as described further in Section 4.4.2.4.
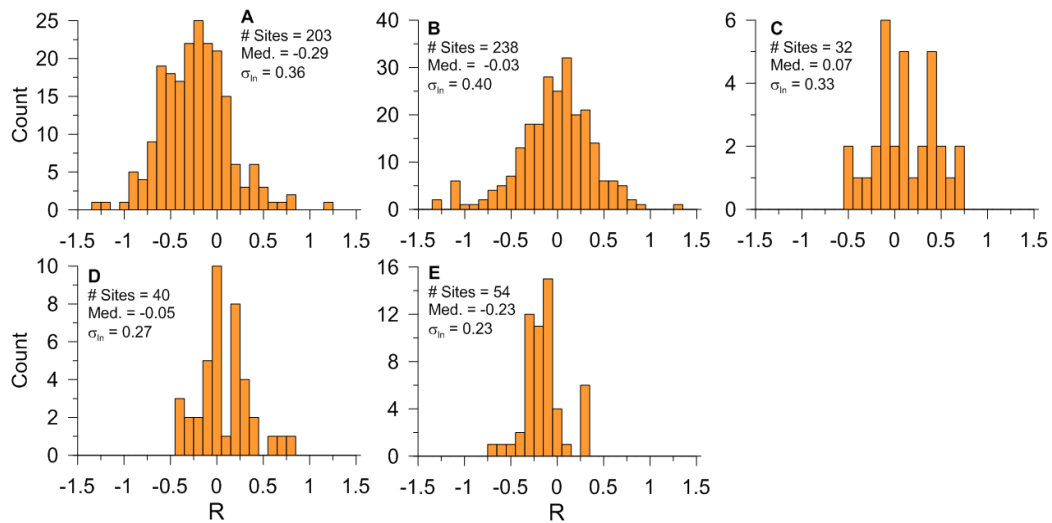
Figure 4.21. Residuals of V_{s30} from estimates based on the geotechnical proxy (Geomatrix 3rd letter) using the methods of Chiou et al. (2008). Based on V_{s30} measurements and V_{sz}-V_{s30} relations.
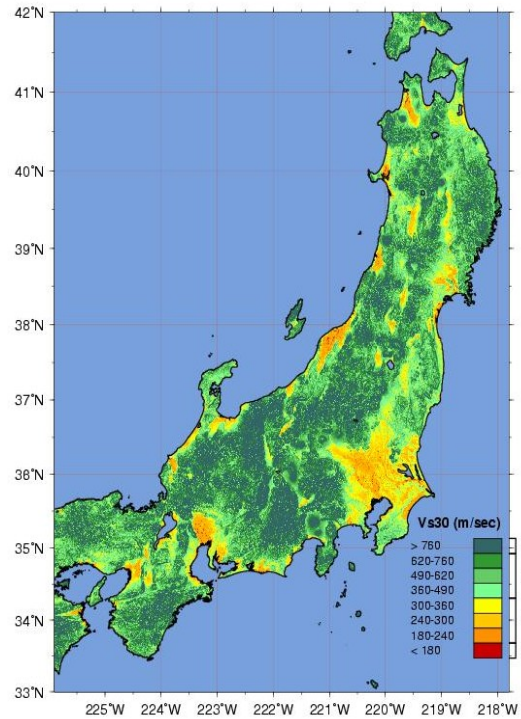
**Figure 4.22.   Distribution of V$_{s30}$ in Japan
(source: http://earthquake.usgs.gov/hazards/apps/vs30/predefined.php).**
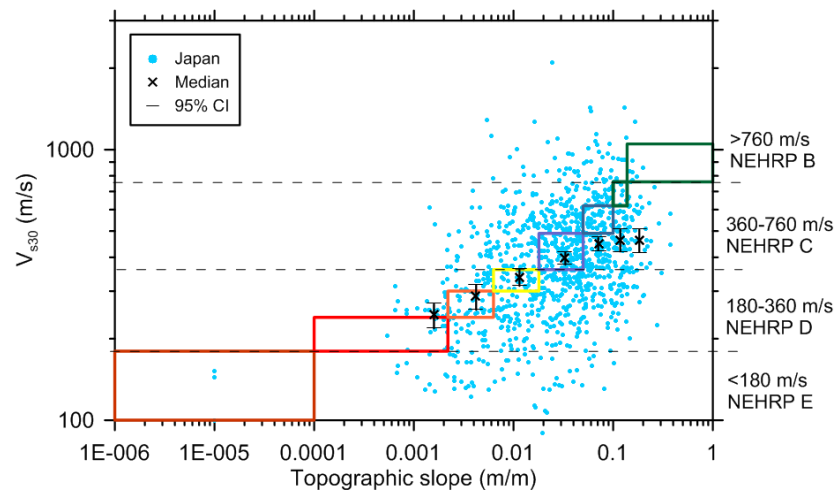
Figure 4.23.   V$_{s30}$ versus slope from Japan data and estimates from Wald and Allen (2007) for active tectonic regions. Color coded polygons correspond to slope ranges within NEHRP classes.

Figure 4.23 presents V_{s30} data plotted versus slope along with the recommended ranges from Wald and Allen (2007). The proxy performance is generally good for slopes between 0.004–0.04 m/m, with some under-prediction for slopes flatter that 0.004 m/m and over-prediction for slopes steeper than 0.04 m/m. The overall median of residuals is -0.12 and the standard deviation is 0.42.

Residuals for the terrain- and geomorphology based methods were evaluated in categories for which statistically significant medians or standard deviations could be constrained (as was done for the California data). Categories with results considered to be reliable are indicated in Table 4.6(a) and 4.6(b). The terrain-based proxy has significant negative bias for five of the eight categories. Looking across all categories, the median bias is -0.14 and the standard deviation is 0.43. The most populated Japan-specific geomorphic categories are shown in Table 3.6b. There are modest negative biases in categories 1 and 8, i.e, rock sites, whereas positive biases are found for categories 5, 13, 15 and 17, i.e., soft soils. Considering all categories, the median bias is -0.04 and the standard deviation is 0.42.

The relative efficacy of the different proxy-based estimation techniques can be judged on the basis of bias and standard deviation of residuals, as shown in Figure 4.24. Biases are generally negative for the GMX, slope, and terrain proxies, whereas geomorphology biases are positive. The standard deviation results were separated by categories when practical as indicated in Figure 4.24. As in other regions, we generally see lower dispersion for softer sites, such as Geomatrix category E and flat slopes. General dispersion levels provided by the four considered proxies are generally similar. Average dispersion levels (marked as the 'Overall'

sigma in Figure 4.24) are generally similar, although the Japan-specific geomorphology-based scheme is lowest.

Table 4.6(a).   Terrain-based categories by Yong et al. (2012) and V_{s30} bias and dispersion.

Category	Description	# V_{s30} meas.	μ_{lnV}	σ_{lnV}
1	Well dissected mountains, summits, etc.	297	-0.09	0.36
3	Well dissected, low mountains, etc.	188	-0.29	0.41
5	Dissected plateaus, etc.	108	0.00	0.44
7	Moderately eroded mountains, lava flow, etc.	227	-0.05	0.46
9	Well eroded plain of weak rocks, etc.	33	-0.45	0.36
11	Eroded plain of weak rocks, etc.	74	-0.13	0.41
15	Dune, incised terrace, etc.	69	-0.44	0.37
16	Fluvial plain, alluvial fan, low lying flat plains, etc.	20	-0.21	0.37

Table 4.6(b). Geomorphology-based categories Matsuoka et al. (2006) and corresponding V_{s30} bias and dispersion.

Category	Geomorphologic map unit	Description	# V_{s30} meas.	μ_{lnV}	σ_{lnV}
1	Mountain (Tertiary)	Steeply to very steeply sloping topography with highest elevation and relative relief within a grid cell of approximately more than 200 m. Moderately to severely dissected.	250	-0.39	0.38
3	Hill	Steeply to moderately sloping topography with higher elevation and relative relief within a grid cell of approximately 200 m or less. Moderately dissected.	87	0.03	0.40
5	Volcanic footslope	Gently sloping topography located around skirt of volcano including pyroclastic-, mud- and lava-flow fields, and volcanic fan produced by dissection of volcanic body. Slightly dissected.	21	0.15	0.26
8	Moderately eroded mountains, lava flow, etc.	Fluvial or marine terrace with flat surface and step-like form. Covered with subsurface deposits (gravel or sandy soils) of more than 5 m in thickness.	174	-0.12	0.34
9	Terrace covered with volcanic ash soil	Fluvial or marine terrace with flat surface and step-like form. Covered with cohesive volcanic ash soil of more than 5 m in thickness.	60	0.04	0.25
10	Valley bottom plain	Long and narrow lowland formed by river or stream between steep to extremely steep slopes of mountain, hill, volcano and terrace.	165	0.08	0.37
11	Alluvial fan	Semi-cone-like form comprised of coarse materials, which is formed at boundary between mountains and lowland. Slope gradient is more than 1/1000.	79	0.02	0.31
12	Natural levee	Slightly elevated area formed along the riverbank by fluvial deposition during floods.	16	-0.07	0.36
13	Back marsh	Swampy lowland formed behind natural levees and lowlands surrounded by mountains, hills and terraces.	41	0.21	0.47
15	Delta and coastal lowland	Delta: flat lowland formed at the river mouth by fluvial accumulation. Coastal lowland: flat lowland formed along shoreline by emergence of shallow submarine deposits, including discontinuous lowlands along sea- or lake- shore.	68	0.19	0.44
16	Marine sand and gravel bars	Slightly elevated topography formed along shoreline, comprised of sand and gravel, which was washed ashore by ocean wave and/or current action.	34	0.00	0.36
17	Sand dune	Wavy topography usually formed along shoreline or river, comprised of fine to moderately aeolian sand, generally overlies sandy lowland.	15	0.14	0.35
20	Filled land	Former water body such as sea, lake, lagoon, and river reclaimed as land by filling.	15	-0.04	0.35
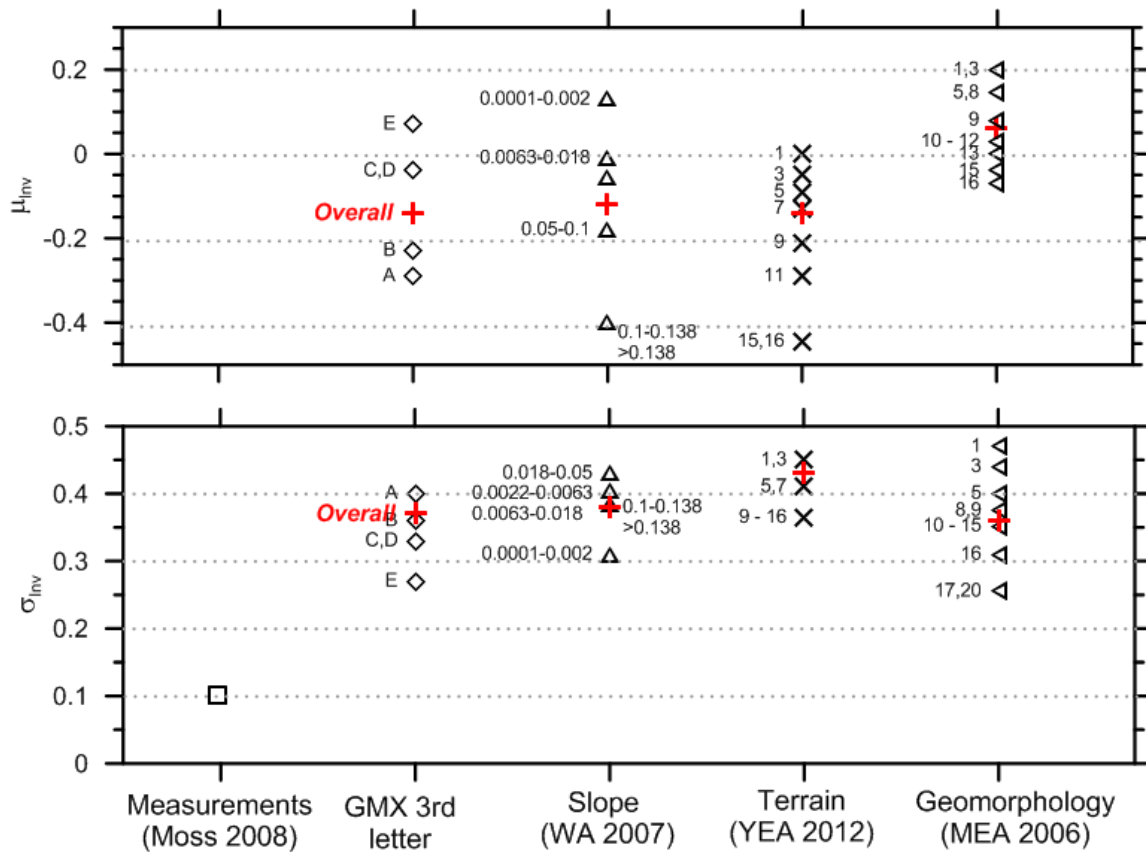
Figure 4.24. Median and dispersion of V_{s30} prediction residuals for Japan in natural log units based on the analyses in this study. Proxy aggregates are marked as 'Overall'.

4.4.3 Adjustments to Recommended V_{s30} values for GMX Classes A and E

As described in Section 4.4.1.1, the GMX 3rd letter proxy was originally derived from California data. The proxy analyses presented above have used a much larger California database as well as substantial additional data for other regions. In this subsection, we address bias in the values for Classes A and E that justify modification of the recommended values. Negative bias for Category A was observed in all three regions investigated (California, Taiwan, and Japan) by amounts ranging from -0.13 to -0.29. In Figure 4.25, we show a joint histogram across all three regions, which indicates a mean and median of 516 and 507 m/sec, respectively. For Class E,

the results are more mixed, with California and Japan showing relatively consistent biases of -0.17 and -0.23, whereas Taiwan is positively biased (0.17). We recommend the use of the combined data shown in Figure 4.25 with a mean and median 185 and 182 m/sec, respectively. We recommend updating the general GMX proxy-based estimation with these new values. Table 4.7 presents our recommended values for each GMX category.
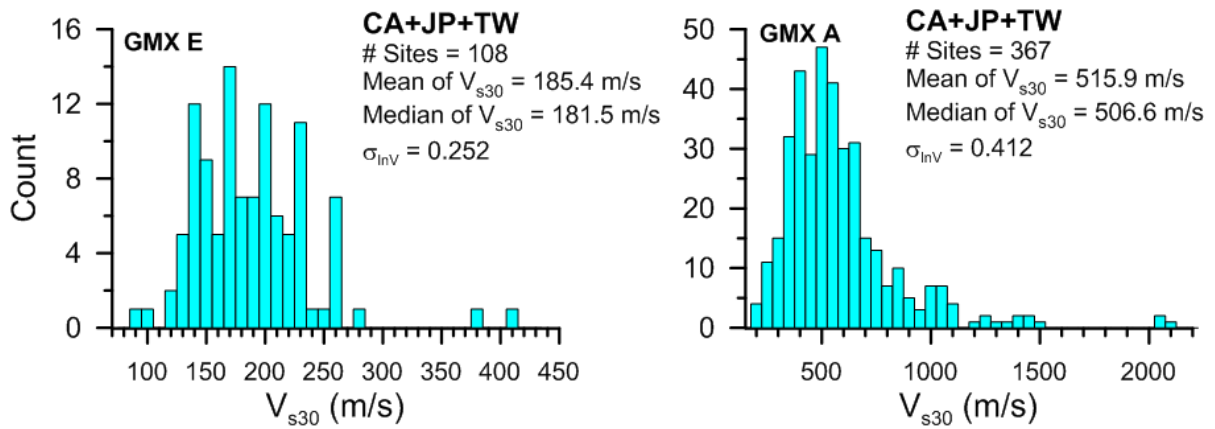
Figure 4.25. Histograms of V_{s30} from sites in California, Japan, and Taiwan for GMX categories A and E. Data utilized is from V_{s30} measurements (for profile depths greater than 20 m) and inferences of V_{s30} from V_{sz}-V_{s30} relations for shallower profiles.

Table 4.7. Recommended V_{s30} for GMX 3rd Letter categories. Values for A and E are modified from those in Chiou et al. (2008).

GMX 3rd letter	Median V_{s30} (m/s)	Mean V_{s30} (m/s)	σ_{lnV}
A	506.6	515.9	0.412
B	424.8	464.3	0.431
C	338.6	345.4	0.203
D	274.5	291.4	0.335
E	181.5	185.4	0.252

4.5 Selection of Preferred V_{s30} and Uncertainty

4.5.1 Method of Selecting Preferred V_{s30}

For purposes of comparison, the process by which "preferred" V_{s30} values were assigned from

available data in the 2006 site database are given below (Chiou et al. 2008).

(0) Assigned from measured velocity profile generally come from PEA profile database.

Only profiles with depths $z_p \geq 20$ m are considered with constant velocity extrapolation of the

deepest V_s measurement to 30 m. A velocity profile is assigned to a strong-motion site if the

separation distance is 300 m or less (Borcherdt, 2002).

(1) Inferred for California sites that recorded the Northridge earthquake from Borcherdt

and Fumal (2002) or from other California stations from Wills and Clahan (2006) based on

surface geology correlations.

(2) Inferred from GMX 3rd letter correlations (Section 4.4.1.1) except for Taiwan sites,

where the GMX/elevation procedure of Chiou and Youngs (2008a) was used (similar to that

described in 4.4.1.2).

(3) Inferred from V_s profiles with depth $z_p < 20$ m using constant velocity extrapolation

of the deepest V_s measurement to 30 m.

(4) Inferred from site categories by Spudich et al. (1997, 1999) and correlations to V_{s30}.

This code is specific to stations in extensional regions.

(5) Taken directly or inferred from maps of V_{s30} for Alaska based on VIC (Vibration

Instrument Ltd., Tokyo, Japan) high-frequency Rayleigh wave data (Martirosyan et al. 2002).

This code is specific to Alaska.

The numbers in the list above (0–5) correspond to codes in the 2006 Version 23 site database used to identify the source of V_{s30} information. The lowest value of the code have the highest preference for the assignment of V_{s30} (0 is most preferred; 5 is least preferred). The manner by which the codes were sequenced was expert judgment. There are prescribed levels of uncertainty associated with each code, as explained further in the next section.

In the current 2013 site database, the protocols have been updated as a result of the availability of additional proxies and the analysis of proxy performance presented in Section 4.4.2. The following codes are applied to V_{s30} measurements and estimates in the 2013 site database:

(0) Assign from measured velocity profile, $z_p \geq 30$ m using the data sources given in Section 4.3.1.

(1) Estimated from V_s profiles with depths $10 < z_p < 30$ m using region-dependent correlations with depth in Boore (2004) and Boore et al. (2011).

(2) (a) Infer from geology-based correlations calibrated for the region where the site is located and using detailed descriptions of geological categories (e.g., distinguishing Quaternary alluvium based on texture and/or age). These maps are typically digital   maps or paper maps 1:50,000 scale or smaller.

(b) Infer from geology-based correlations that do not meet the criteria of (2a) (e.g., lack of local calibration, relatively coarse geological mapping).

(3) (a) Infer from geotechnical correlations (GMX 3rd letter, etc.) within its calibration region (e.g., California).

114

(b) Inferred from generalized geotechnical correlations outside the calibration region.

(4) Infer from geomorphologic proxies described in Section 4.4.1.2, including models based on:

(a) GMX+Elevation (i.e., Taiwan only, Chiou, *personal communication*, 2012).

(b) Ground slope [i.e., Wald and Allen (2007)].

(c) Terrain-based categories (i.e., Yong et al., 2012).

(5) Infer from local V_s mapping (e.g., microzonation maps). Applicable in Alaska.

As before, the low codes corresponding to measurements (0 or 1) receive the highest priority for V_{s30} assignment. The proxy analysis from Section 4.4.2 does not clearly reject any particular proxy-based method for estimating V_{s30}, but does provide a basis for assigning relative weights to proxies based on the regional proxy aggregated mean and standard deviation of residuals ($\mu_{\ln V}$ and $\sigma_{\ln V}$, respectively). The relative weight is taken from the inverse of the residual sum of squares of the aggregated mean and standard deviation:

$$\text{Relative weight for selected proxy and region} \quad \frac{1}{\mu_{\ln V}^{2} + \sigma_{\ln V}^{2}} \tag{4.7}$$

The actual weight is computed from the relative weights through adjustment to ensure they sum to one. Table 4.8 shows the relative weights and computed proxy weights using this procedure. The computed weights apply only when all proxies are available. If only a subset of proxies is available, the weights are adjusted to sum to one for those proxies. For example, in California, if a site has geology (2a) and ground slope (4b), the weights are 0.67 and 0.33 for the

geology- and slope-based estimates of V_{s30}, respectively. The proxies listed in Table 4.8 are those that are available for the respective regions.

Table 4.8. **Relative proxy weights by region and applied weights for V_{s30} estimation when each proxy is available for a site.**

Region	Proxy	μ_{lnV}	σ_{lnV}	Rel. Wt. (Eq. 3.7)	Weight[1]
CA	Geology	-0.06	0.33	8.89	0.35
	GMX	-0.08	0.40	6.01	0.24
	Slope	-0.01	0.45	4.94	0.20
	Terrain	-0.11	0.42	5.31	0.21
Taiwan	GMX	0.15	0.37	6.27	0.21
	GMX+elev	0.02	0.32	9.73	0.33
	Slope	0.07	0.34	8.30	0.28
	Terrain	0.13	0.42	5.17	0.18
Japan	GMX	-0.14	0.38	6.10	0.28
	Geomorph.	-0.04	0.42	5.62	0.26
	Slope	-0.12	0.42	5.24	0.24
	Terrain	-0.14	0.43	4.89	0.22

[1] Weights in this column apply when all proxies available for a given site

4.5.2 Uncertainties of V_{s30}

The preferred V_{s30} value for the site is taken to represent the median estimate of V_{s30} or the mean estimate ln(V_{s30}). The assignment of epistemic uncertainty to V_{S30} is dependent on the estimation method and is expressed as a log standard deviation, σ_{lnV}. The manner by which this uncertainty was assigned in the 2006 database (for comparison purposes) and for the present database is described in the following sub-sections.

4.5.2.1 V_{s30} Uncertainty in Vol. 23 Site Database

In the 2006 Version 23 site database (Chiou et al. 2008), V_{s30} uncertainty was assigned for sites with and without measurements, based principally on the judgment of PEA and cluster analyses at a limited number of sites with multiple and closely-spaced V_s measurements at the time.

The estimate of V_{s30} uncertainty for sites with measured shear-wave velocities was based in part on the outcome of an analysis of variance of closely spaced V_{s30} measurements in the PEA profile database. The assigned uncertainty is a function of profile stiffness which was represented by NEHRP classification, as shown in Figure 4.26. As described in Chiou et al. (2008), data from a site in Gilroy, California (NEHRP D site) having sixteen nearby measurements of V_{S30} yielded a standard deviation of $\sigma_{\ln V} = 0.08$, so a value of 0.10 was used for D sites generally. Uncertainty values for other site classes were set based on similar cluster analyses and judgment of PEA, with the results given in Figure 4.26. The observations of increased uncertainty in V_s for rock sites as compared to soil sites noted by Schneider and Silva (1994) influenced this judgment, resulting in increased $\sigma_{\ln V}$ values of up to 0.3 for Class A sites.

The observed V_{s30} aleatory variability (within category randomness) within surface geological units (Table 2 of Chiou et al., 2008) formed the basis for the assigned epistemic variability in the V_{s30} values inferred from site geology (Figure 4.26). Similarly, Geomatrix or Spudich within category randomness (Table 3 of Chiou et al., 2008), along with judgment formed the basis of assigned epistemic variability for other cases shown in Figure 4.26.
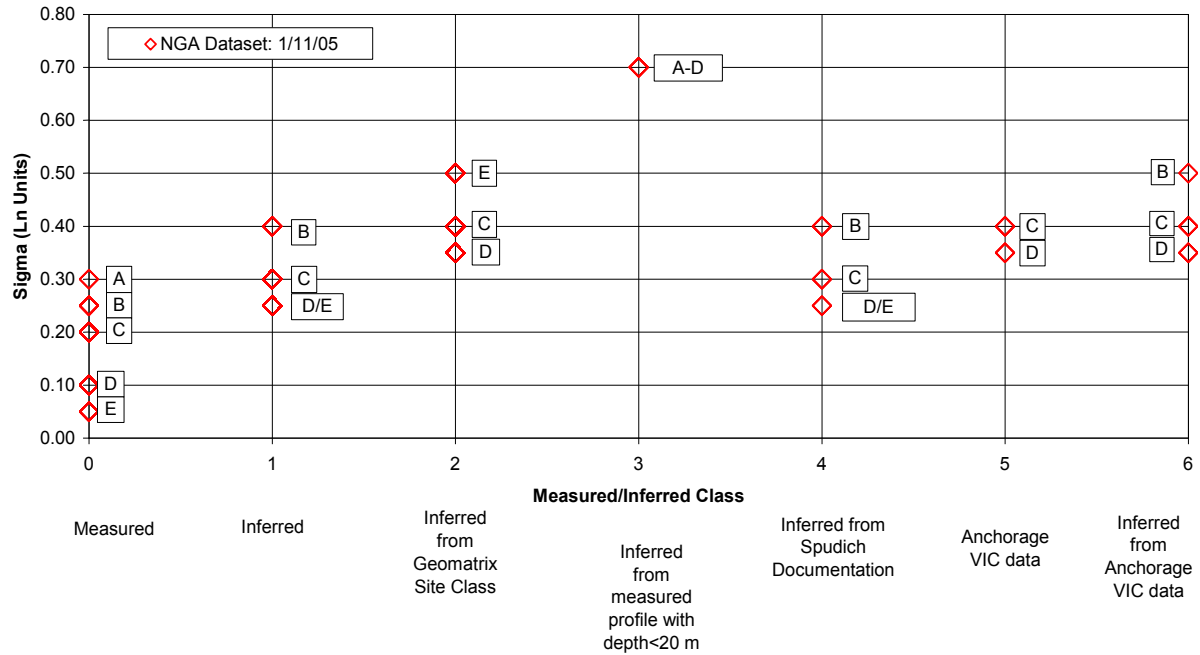
Figure 4.26.   Uncertainty of V_{s30} used in 2006 Version 23 site database (from Chiou et al., (2008).

4.5.2.2 V_{s30} Uncertainty in Present (2013) Site Database

For the current site database, we have re-visited the assignment of $\sigma_{\ln V}$ and attempted to increase the transparency by which the values are assigned, although some judgment is still applied.

(a) V_{s30} uncertainty for Code 0 sites

In the case of code 0 sites, we have re-examined the dispersion of V_{s30} measurements from single sites with multiple profiles. The profile data analyzed include six sites in California from Boore and Asten (2005), two sites in California from Brown et al. (2000), three sites explored with surface wave method by various researchers and reported by Moss (2008), and the DCPP site owned by Pacific Gas & Electric (PG&E, 2011). The profiles from this data set were

118

in some cases derived from combinations of surface wave (SW) and downhole (DH) methods, while in other cases only one measurement type was used. In Figure 4.27, we show $\sigma_{\ln V}$ for the clusters of profiles at these sites against the median V_{s30}. Different colors are used for sites from single and multiple measurement types. Note that we have not included data from Remi-based profiles for this compilation. We also show in the figure values of $\sigma_{\ln V}$ from the proprietary PEA profile data base for eight sites in California and South Carolina; in those cases, the cluster statics were provided by PEA (R. Darragh personal communication, 2012) and were in some cases obtained from several different measurement methods at each site (e.g., Treasure Island Geotechnical Array and Gilroy #2).
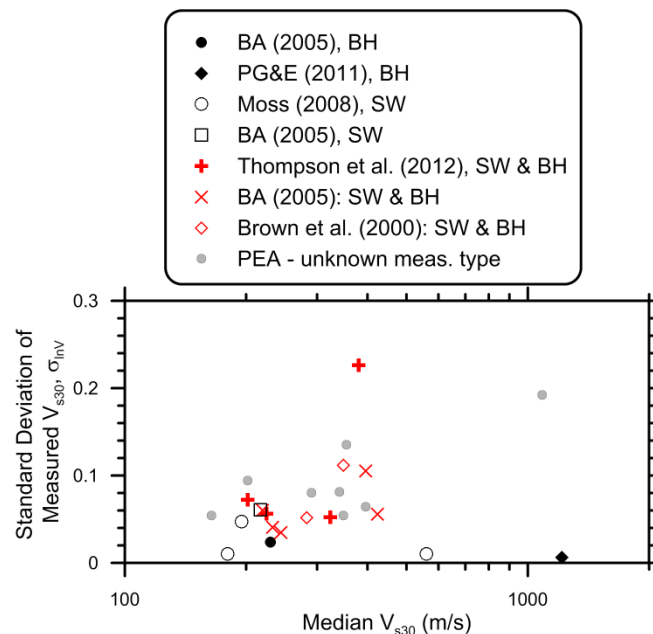
Figure 4.27. **Dispersion of V_{s30} from sites with multiple profiles obtained with surface wave (SW) and/or borehole (BH) methods.**

The velocity dispersions ($\sigma_{\ln V}$) in Figure 4.27 reflect spatial variations in seismic velocities at modest separation distances between profiles (ranging from 10 sec to 100 sec of meters; above references and R. Moss and R. Kayen, *personal communication*, 2012). For example, V_{s30} uncertainties at the Coyote Creek and William Street Park sites described by Boore and Asten (2005) are derived from profiles at various locations separated by as much as approximately 200 m (see Figure 4 of Boore and Asten, 2005). In the case of the Thompson et al. (2012), the maximum lateral separation distances of profiles are approximately 450−1400 m. As shown in Figure 4.27, the results have no clear sensitivity to test type (i.e., SW versus BH) nor to whether SW and BH methods were combined at a given site. This suggests that method-to-method variability is modest when the V_s profiles are from sources known to produce reliable results, which is the case for the data utilized here. [We note parenthetically that more method-to-method variability was observed by Moss (2008), which included Remi data from several sites.] Such inter-method variability can arise due to varying levels of quality in the underlying measurements, which can be minimized by only using data from sources known to produce reliable results (which is generally the case for the profiles used in the NGA-West 2 project). Inter-method variability can also arise from the different volumes of soils tested in surface wave techniques versus borehole techniques, in which case it largely reflects spatial variability in the velocity structure.

An outlier in Figure 4.27 is KiK-net site TKCH08 ($\sigma_{\ln V}$ = 0.23, median V_{s30} = 380 m/sec) from Thompson et al. (2012), which is one of four sites investigated with multiple V_s profiles in that study. Values of $\sigma_{\ln V}$ for the other sites range from 0.05−0.07. Google Earth imagery shows the terrain for the sites with modest values of $\sigma_{\ln V}$ to be fairly consistent; whereas site TKCH05

is located in a narrow valley in which some of the profiles are within the valley, and others are near the edge where rock is likely to occur at relatively shallow depths. This example shows that separation distance between profiles is less important than consistency in the terrain, which presumably correlates in most cases to consistent geology. The high value of $\sigma_{\ln V}$ for TKCH08 appears to result from inconsistencies in the underlying geology.

Examining all the available COV and $\sigma_{\ln V}$ values in Figure 4.27, we see the dispersion is not particularly sensitive to site stiffness, as reflected by mean V_{s30}. However, the figure shows a slight trend for increasing dispersion with increasing velocity, clearly additional measurements are required. Based on the available data, our judgment is that when the geology of the profile and strong-motion sites match, and they are separated by distances of several 100 m or less, a reasonable value of the dispersion regardless of mean V_{s30} is approximately $\sigma_{\ln V} = 0.06$. As shown by the TKCH05 site, this dispersion is much higher when the site geology is heterogeneous relative to the separation distance between the profile and strong-motion site. Considering all of the above, we consider a value of $\sigma_{\ln V} = 0.1$ to be reasonable for use with code 0, which is similar to the single data point reported for the assignment of $\sigma_{\ln V}$ in the Version 23 site database. This constant value replaces the strong increase of $\sigma_{\ln V}$ with site stiffness in the Version 23 site database (shown in Figure 4.27). Note that rock dispersion in an absolute sense is still higher than that for soil, since $\sigma_{\ln V}$ is a normalized quantity. We recognize that this value is likely on the high side for a large number of the code 0 sites where the profile and strong-motion station are located at relatively close distances ($<\sim 100$ m) on similar geology. Conversely, this value is on the low side for sites where

the profile and strong-motion stations are on different geologic conditions, although this is

expected to be relatively rare.

As shown in Figure 4.27, the database from which σ_{nV} can be evaluated is limited,

especially for firm sites with $V_{s30} > \sim 400$ m/sec and soft sites with $V_{s30} <\sim 200$ m/sec. As

additional data are added, the recommendations provided here may change.

(b) V_{s30} uncertainty for Code > 0 sites

For Code 1 sites, uncertainty arises from intra-site variability (as in Code 0) and

uncertainty associated with the V_{sz} to V_{s30} extrapolation described in Section 4.3.2. These two

sources of uncertainty are assumed to be statistically independent, and thus are combined by

summing the associated variances. The V_{sz} to V_{s30} extrapolation uncertainties are dominant, and

are based on the standard deviation of residuals as provided in Boore (2004) and Boore et al.

(2011). The resulting σ_{lnV} values are shown in Figure 4.28 and decrease with increasing total

depth of the profile.
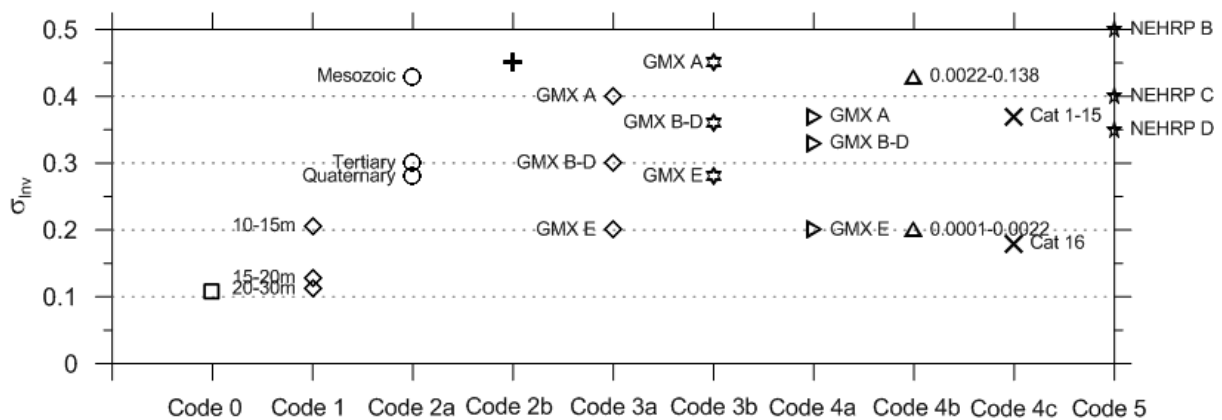
Figure 4.28.   **Recommend dispersion of V$_{s30}$ in natural log units when derived from various
information sources.**

For the proxy methods (Code > 1), we assign uncertainties on the basis of the proxy data analysis from Section 4.4.2. We assign weighted standard deviations ($\sigma_{\ln V}$) for various combinations of proxies using weights computed as described in Section 4.5.1 (Table 4.8). Values of $\sigma_{\ln V}$ for specific codes are discussed in the following and shown in Figure 4.28:

(2) (a) Values of $\sigma_{\ln V}$ are provided for three broad geologic categories, based on averaging applicable sub-category $\sigma_{\ln V}$ values provided in Wills and Clahan (2006). The values apply to California and Italian sites.

(b) We recommend $\sigma_{\ln V} = 0.45$ based on judgment.

(3) (a) Geometric means of $\sigma_{\ln V}$ values from proxy analysis are assigned for each GMX 3rd letter category. The assigned values are: $\sigma_{\ln V} = 0.4$ for Class A, 0.3 for Classes B-D and 0.20 for Class E.

(b) We sum the variances Code 3a and 0.2 (from cluster measurements reported in Section 4.4.2), giving $\sigma_{\ln V}$ values of 0.45 (A), 0.36 (B-D) and 0.28 (E).

(4) (a) Based on the Taiwan proxy analysis, we assign $\sigma_{\ln V} = 0.37$ (A), 0.33 (B-D), and 0.20 (E).

(b) Geometric means of $\sigma_{\ln V}$ values from proxy analysis are assigned for various bins of slopes; we use $\sigma_{\ln V} = 0.2$ for slopes flatter than 0.0022 and $\sigma_{\ln V} = 0.43$ otherwise.

(c) Geometric means of $\sigma_{\ln V}$ values from proxy analysis are assigned for terrain categories. We assign 0.37 for all categories except category 16, for which we assign 0.18.

(5) Values unchanged from 2006 database (Figure 5 of Chiou et al., 2008).

5 SEMI-EMPIRICAL NONLINEAR SITE AMPLIFICATION AND ITS APPLICATION IN NEHRP SITE FACTORS

5.1 INTRODUCTION

As mentioned in Chapter 1 and described in detail in Chapter 3, there are different approaches to develop site amplification factors such as theoretical and empirical methods. Whereas theoretical methods can be performed through an analytical and numerical modeling of soil layers and wave propagation associated with simulations, empirical methods utilize the recorded ground motions to evaluate the parameters of site amplification. Semi-empirical methods can be conducted by evaluating the site factors empirically for relatively low input ground motions (peak accelerations or S_l near 0.1g) and utilizing simulations to represent the levels of nonlinearity at high input ground motions. The existing site factors in NEHRP Provisions are evaluated empirically at relatively small ground motion levels in the San

Francisco Bay Area from the 1989 Loma Prieta earthquake and feature simulation-based nonlinearity. New site factors are evaluated based on the enhanced NGA-West 2 database.

The work presented in this chapter represents the results of collaborative work involving myself and Prof Stewart along with a technical committee of Task 8 group. Our role was principally to develop a nonlinear site amplification model and propose new NEHRP site factors for the next updating cycle. The results given here have been previously presented in Chapters 4 and 5 of PEER report by Stewart and Seyhan (2013) (Available in Summer).

In Section 5.2, I first present the development process of the nonlinear site amplification model with two terms representing nonlinear effects and V_{s30}-scaling and illustrate supporting work guided model development relative to regional variations in levels of nonlinearity implied by simulations and linear site amplification. The objective of this analysis is to improve the discrepancies and support the development of a proposal for revising the NEHRP site factors and to support the development of a site amplification model that is used in an NGA-West 2 GMPE (Boore et al., 2013; BEA13). Section 5.3 is concerned with the development of a proposal for revision of the NEHRP site factors and the manner by which proposed revisions to the NEHRP site factors were developed. Finally, I conclude by comparing the site amplification model developed in this research with those of other current NGA-West 2 GMPEs.

5.2   NONLINEAR SITE AMPLIFICATION FROM DATA AND SIMULATIONS

5.2.1 Equations for Nonlinear Site Amplification Model

The nonlinear site amplification model in the base-case GMPE of BEA13 is comprised of two additive terms representing V_{s30}-scaling and nonlinearity as follows:

$$F_{S,B} = \ln\left(F_{lin}\right) + \ln\left(F_{nl}\right) \tag{5.1}$$

where $F_{S,B}$ represents site amplification in natural logarithmic units; F_{lin} represents the linear component of site amplification, which is dependent on V_{s30}; and F_{nl} represents the nonlinear component of site amplification, which depends on V_{s30} and the amplitude of shaking on reference rock (taken as V_{s30} = 760 m/sec).

The linear component of the model (F_{lin}) describes the scaling of ground motion with V_{s30} for linear soil response conditions (i.e., small strains) as follows:

$$\ln\left(F_{lin}\right) = \begin{cases} c\ln\left(\dfrac{V_{s30}}{V_{ref}}\right) & V_{s30} \leq V_c \\[2ex] c\ln\left(\dfrac{V_c}{V_{ref}}\right) & V_{s30} > V_c \end{cases} \tag{5.2}$$

where c describes the V_{s30}-scaling in the model, V_c is the limiting velocity beyond which ground motions no longer scale with V_{s30}, and V_{ref} is the site condition for which the amplification is unity (taken as 760 m/sec).

The nonlinear term in the site amplification model F_{nl} modifies the linear site amplification so as to decrease amplification for strong shaking levels. The F_{nl} term is constructed so as to produce no change relative to the linear term for low PGA_r levels. The functional form for the F_{nl} term is as follows:

$$\ln\left(F_{nl}\right) = f_1 + f_2\ln\left(\frac{PGA_r + f_3}{f_3}\right) \tag{5.3}$$

where f_1 f_2 ,and f_3 are coefficients in the model and *PGA$_r$* is the median peak horizontal acceleration for reference rock (taken as V_{s30} =760 m/sec). We take $f_1 = 0.0$ to force $\ln(F_{nl})$ to zero for *PGA$_r$* << f_3. Parameter f_3 is set as 0.1g based on analyses presented in Section 5.3 of this thesis, whereas f_2 is a function of period and V_{s30} as follows:

$$f_2 = f_4 \left[\exp\left\{ f_5 \left(\min\left(V_{s30}, 760 \right) - 360 \right) \right\} - \exp\left\{ f_5 \left(760 - 360 \right) \right\} \right] \tag{5.4}$$

where f_4 and f_5 are period-dependent coefficients. This functional form for f_2 is the same as that used by Chiou and Youngs (2008).

5.2.2 Model Development

As described in BEA13, Stage 1 of the model development established the nonlinear component (terms f_2, f_3, f_4, and f_5). The evaluation of these terms considered both simulation results and empirical data analysis. The extraction of f_2 and f_3 terms from the KEA13 simulation-based nonlinear site amplification model is described in Section 5.2. The empirical data analysis began with the computation of rock residuals for each recording in the selected data set:

$$R_{ij} = \ln Y_{ij} - \left[\left(\mu_r \right)_{ij} + \eta_i \right] \tag{5.5}$$

where R_{ij} is the rock residual, Y_{ij} is the jth observed (recorded) value of the ground-motion *IM*, μ_r is the mean (in natural log units) of the BEA13 GMPE for rock conditions (including regional corrections for apparent anelastic attenuation, as applicable), and η_i is the event term for earthquake *i*. The rock site condition used in the computations was V_{s30} =760 m/sec. Nonlinearity was evaluated by regressing R_{ij} against PGA_r (median peak acceleration on rock)

within bins of V_{s30} (< 200, 200–310, 310–520, 520–760, > 760 m/sec) using Eqn. (5.3). This analysis is expanded in Section 5.3.1 to examine regional variations of nonlinearity.

Stage 2 of model building was to evaluate the linear term, F_{lin}. This analysis operates on residuals R_{ij} [Equation (5.5)] that are adjusted by removing nonlinear effects as predicted by the F_{nl} model [Eqn. (5.1)]:

$$R_k^{lin} = R_{i,j} - \ln(F_{nl})$$ (5.6)

The modified residual, R_k^{lin}, applies for linear (small strain) conditions. Subscript k in R_k^{lin} is an index spanning across all available data points; we drop the event and within-event subscripts (i and j, respectively) because of the removal of event terms in the computation of R_{ij}, which allows all data points to be weighted equally. The c coefficient in Eqn. (5.2) is evaluated as the slope in a linear regression between the natural log of R_k^{lin} against the natural log of V_{s30} for $V_{s30} < V_c$. In Section 5.3.2 we investigate regional variations of the c parameter and its dependence on data selection criteria.

5.2.3 Constraint of Parameters Using Simulation-Based Model

As described in Section 5.2, nonlinear site amplification models can be derived on the basis of equivalent-linear ground response simulations, which were undertaken by WEA08 for the original NGA project. The nonlinearity in these relations is driven by the shear modulus reduction and damping versus shear strain relations. The WEA08 study used judgment-driven

modulus reduction and damping curves known as the peninsular range curves (PEN) and curves presented by EPRI (1993).

As part of the NGA-West 2 project, KEA13 re-analyzed a larger set of ground motion simulations that includes additional site profiles and input motions relative to those utilized by WEA08, but the same PEN and EPRI nonlinear curves. Similar to WEA08, the results are presented as period-dependent nonlinear amplification models for a discrete number of mean V_{s30} values (five for WEA08; six for KEA13). The resulting KEA13 model uses the functional form for site amplification from WEA08, which has a similar structure to Eqn. (5.3) but which is considerably more complex such that the coefficients' physical meaning is not the same as the f_1, f_2, and f_3 parameters in Eqn. (5.3). Accordingly, as shown in Figure 5.1, we digitize the nonlinear functions and then fit the digitized points using Eqn. (5.3). Because the KEA13 function has a closed form expression for the equivalent of the f_3 parameter that is V_{s30}-dependent, we apply that function in advance so that the fitting process matches f_1 and f_2 only for a constrained value of f_3. Table 5.1 shows the resulting f_1, f_2, and f_3 values for the discrete V_{s30} values and various periods.
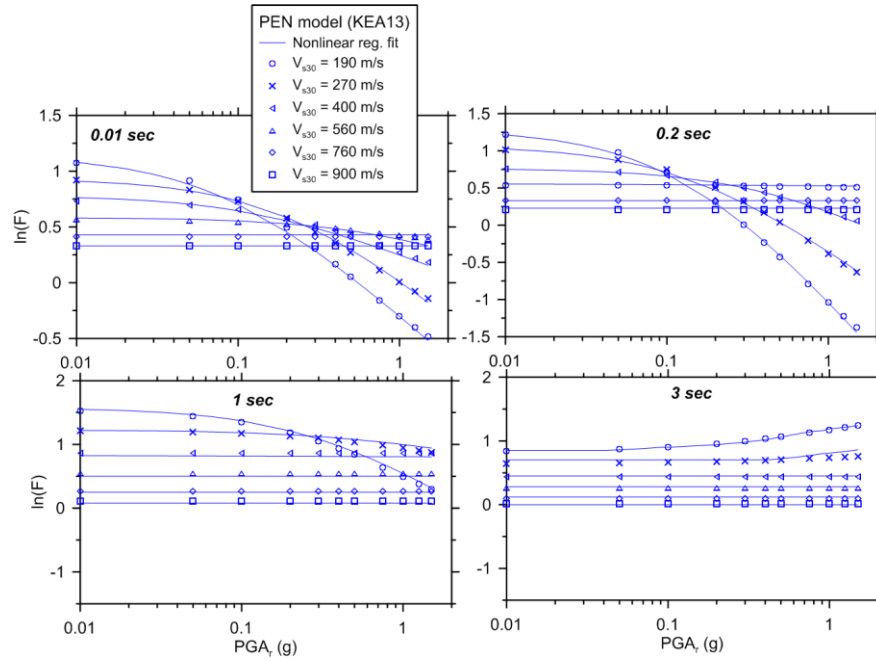
Figure 5.1(a). Site amplification as function of V_{s30}, period, and PGA_r from simulation-based model of KEA13; PEN modulus reduction and damping curves.
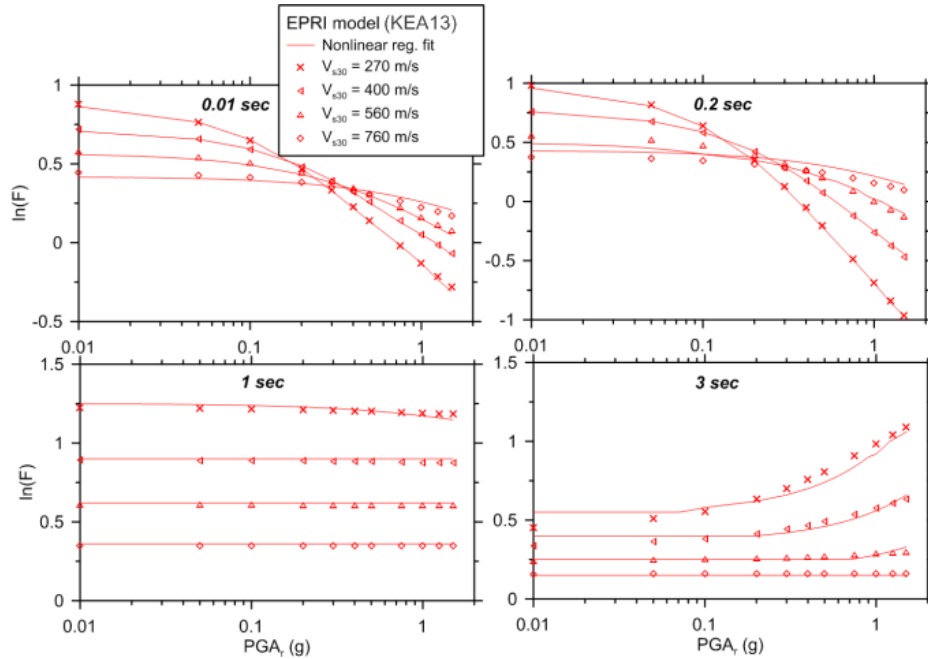
Figure 5.1(b). Site amplification as function of V_{s30}, period, and PGA_r from simulation-based model of KEA13; EPRI modulus reduction and damping curves.

130

Table 5.1.   Values of f_2 for KEA13 model based on fit using Eqn. (5.3).

Period (sec)	PEN as PGA input (V_{s30} in m/s)					
	190	*270*	*400*	*560*	*760*	*900*
0.01	-0.47±0.013	-0.33±0.018	-0.18±0.014	-0.06±0.050	0.00±0.000	0.00±0.000
0.2	-0.75±0.020	-0.53±0.030	-0.24±0.020	-0.01±0.002	0.00±0.000	0.00±0.000
1	-0.41±0.028	-0.11±0.024	0.00±0.002	0.00±0.000	0.00±0.000	0.00±0.000
3	0.13±0.000	0.04±0.09	0.00±0.000	0.00±0.000	0.00±0.000	0.00±0.000
	EPRI as PGA input (V_{s30} in m/s)					
		270	*400*	*560*	*760*	
0.01		-0.35±0.027	-0.25±0.027	-0.17±0.007	-0.09±0.068	
0.2		-0.60±0.030	-0.40±0.035	-0.23±0.022	-0.094±0.075	
1		-0.56±0.065	0.00±0.000	0.00±0.000	0.00±0.000	
3		0.20±0.081	0.09±0.110	0.015±0.090	0.00±0.003	

Values of nonlinear parameter f_2 from simulations are shown in Figure 5.2 (on next page) along with the non-regional empirical results of BEA13 and the proposed model. The simulation-based slopes are comparable to the data-based slopes, except for PSA at $T = 0.5$–3.0 sec where the data exhibits more nonlinearity than is evident from the simulations.
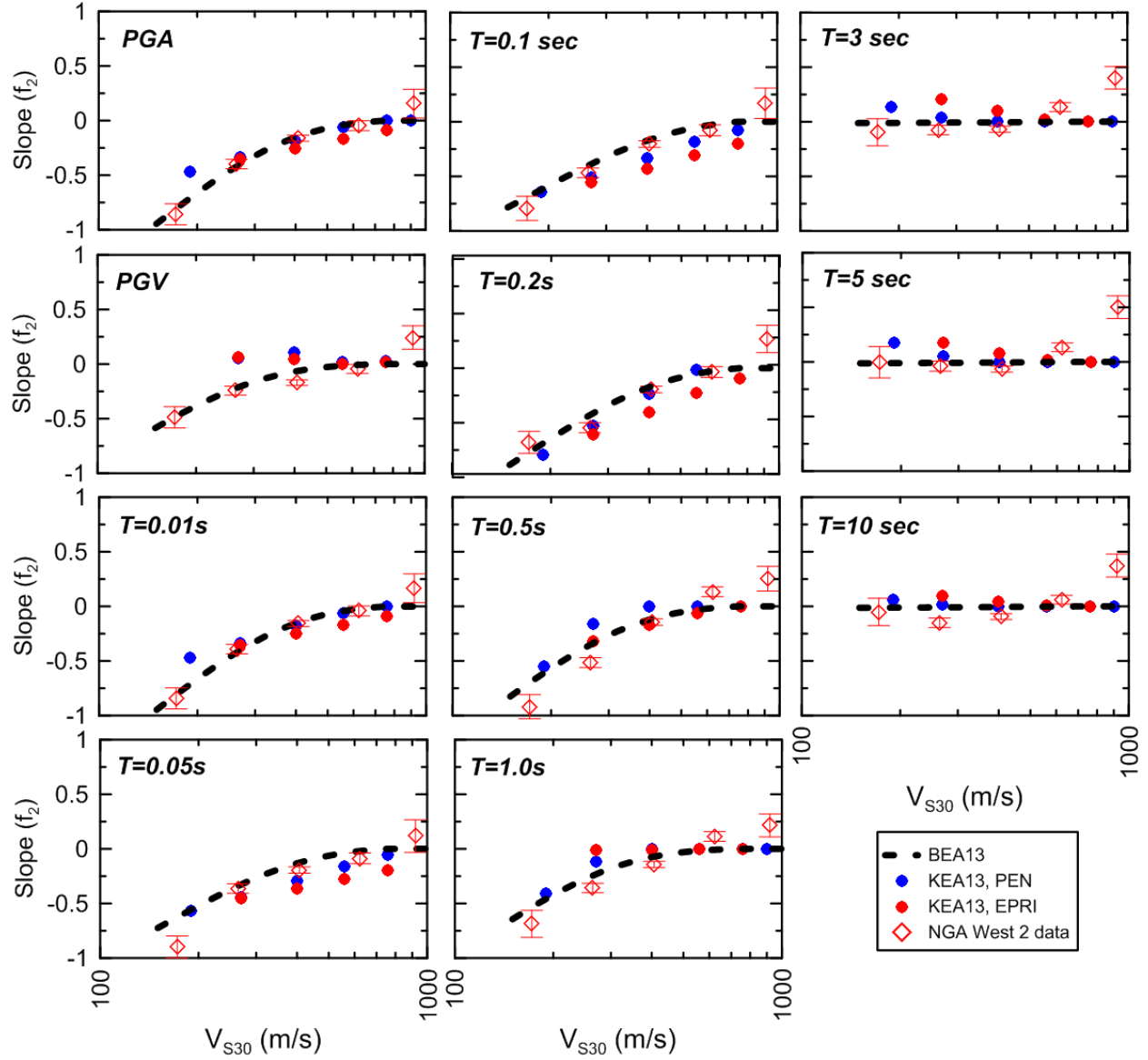
Figure 5.2. Variation of slope f_2 with V_{s30} from NGA West 2 data (from BEA13), KEA13 simulation results (using modulus reduction curves labeled PEN for Peninsular range and EPRI), and BEA13 model.

132

5.2.4 Nonlinear Component of the Model

BEA13 examined trends of R_{ij} against PGA_r within V_{s30} bins using a large portion of the NGA-West 2 data set drawn from many regions, which forms the basis for the empirical f_2 values shown in Figure 5.2 (data selection criteria are described in Section 2.1 of BEA13). A least-squares regression using Eqn. (5.3) was performed using data in each period and V_{s30} bin to estimate f_1 and f_2. Additive parameter f_3, which produces saturation of site amplification for input motion amplitudes with $PGA_r \ll f_3$, was fixed at 0.1g in these regressions because the three coefficients cannot be reliably computed simultaneously.

The fixed value of $f_3 = 0.1g$ was selected by repeating regressions using Eqn. (5.3) with variable fixed values of f_3 and finding the value that minimizes dispersion for data in the V_{s30} bins of < 200 and 200–310 m/sec. Figure 5.3 shows the resulting values of f_3, which do not exhibit trends with period. Note that values of f_3 implied from the simulation-based model of KEA13 are also shown in Figure 5.3.
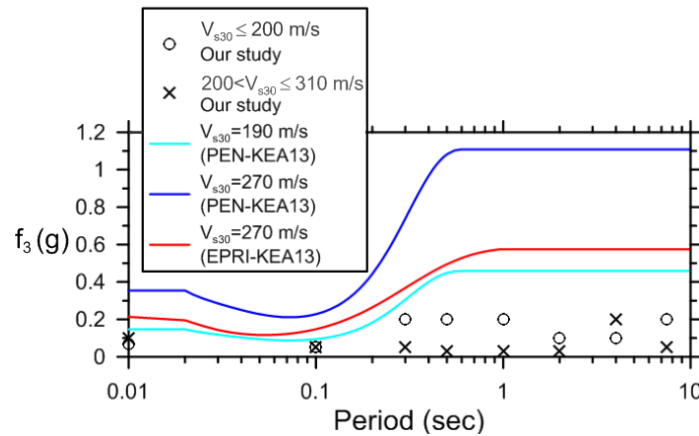
Figure 5.3.   **Variation of additive term f₃ in site amplification function with period from empirical data analysis (to minimize residuals) and from model of KEA13.**

133

Because the empirical data analysis performed to support the development of the nonlinear component of the site amplification model utilized a combined global data set, it is of interest to evaluate possible regional dependencies in the f_2 parameter. This was not formally investigated by BEA13 and is presented here.

In Figures 5.4 to 5.7, we plot R_{ij} against PGA_r by region. The data used for these plots are subsets of the dataset considered by BEA13 within California, Japan, and Taiwan. The plots show fits to the data in the respective V_{s30} bins using Eqn. (5.3) (with f_3 set to 0.1g) along with the fit for the overall (global) data from BEA13. Nonlinearity is manifest in the plots by non-zero values of slope parameter f_2 that are statistically significant, which is judged to be the case when the value of f_2 is larger than its standard error (values of f_2 by region and their standard errors are shown in Table 5.2). There are two major trends in the plots, both of which have been observed previously (e.g., Choi and Stewart, 2005): (1) nonlinearity decreases with increasing V_{s30}, generally becoming statistically insignificant for relatively stiff site categories (V_{s30} > 310 m/sec); and (2) nonlinearity decreases as period increases, being statistically significant only for T ≤ ~1 sec except for the softest soil sites (V_{s30} < 200 m/sec).

In Figure 5.8, we plot f_2 values against V_{s30} from the regional regressions, with the BEA13 model also shown for comparison. The aforementioned trends of decreasing nonlinearity with increasing V_{s30} and increasing period are evident in Figure 5.8. While there are substantial between-region variations in f_2, we do not observe specific regional trends in nonlinearity that are considered sufficiently important to carry forward into an amplification model. Therefore, regionalization of f_2 was not incorporated into the site amplification model of BEA13.
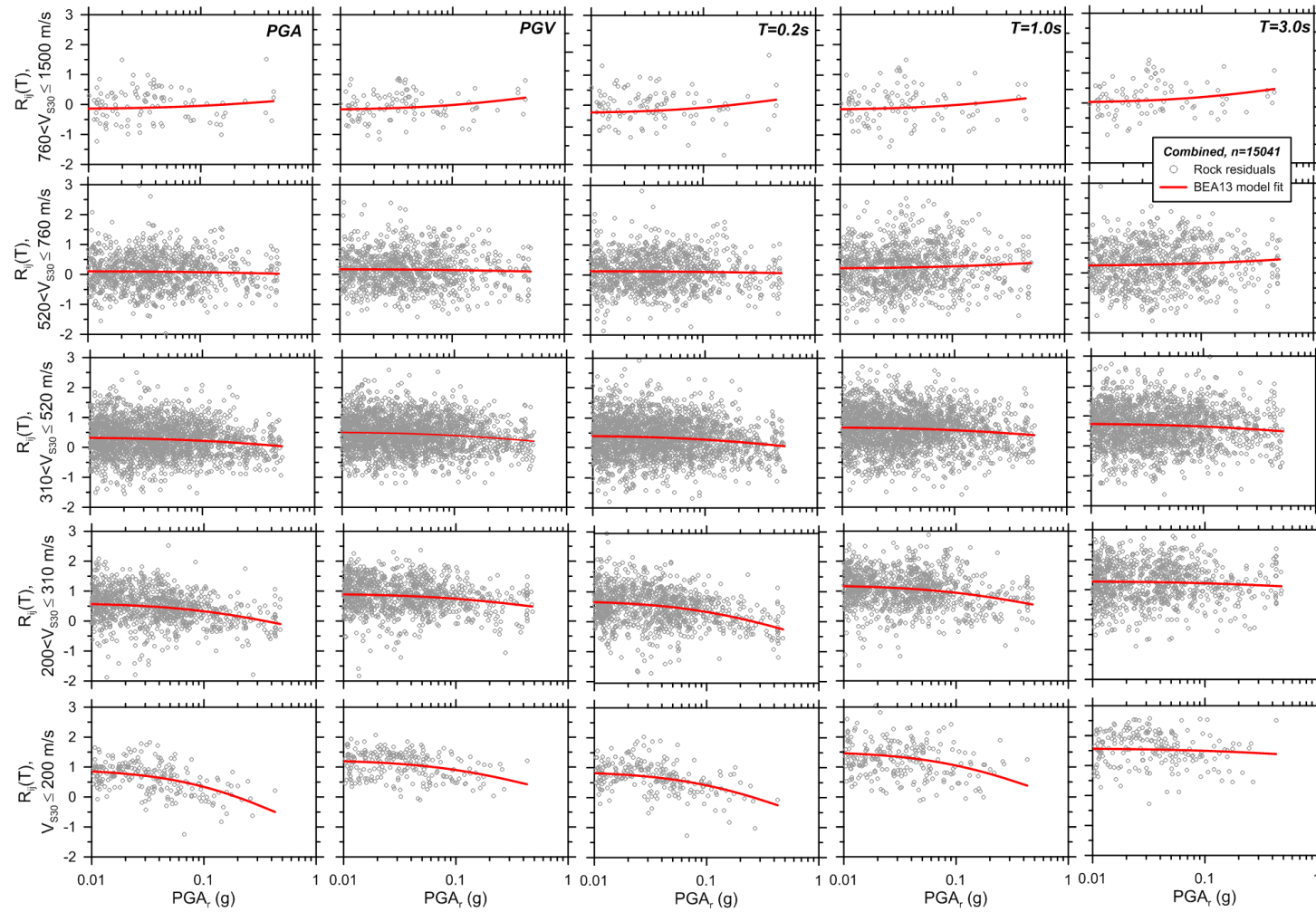
Figure 5.4. Variation of site amplification factors with PGA_r within site categories for California portion of data set. Discrete symbols are intra-event residuals [R_{ij}, Eqn. (5.5)], solid lines are nonlinear regional fit from Eqn. (5.3), dotted lines are global fit from BEA13 .

135
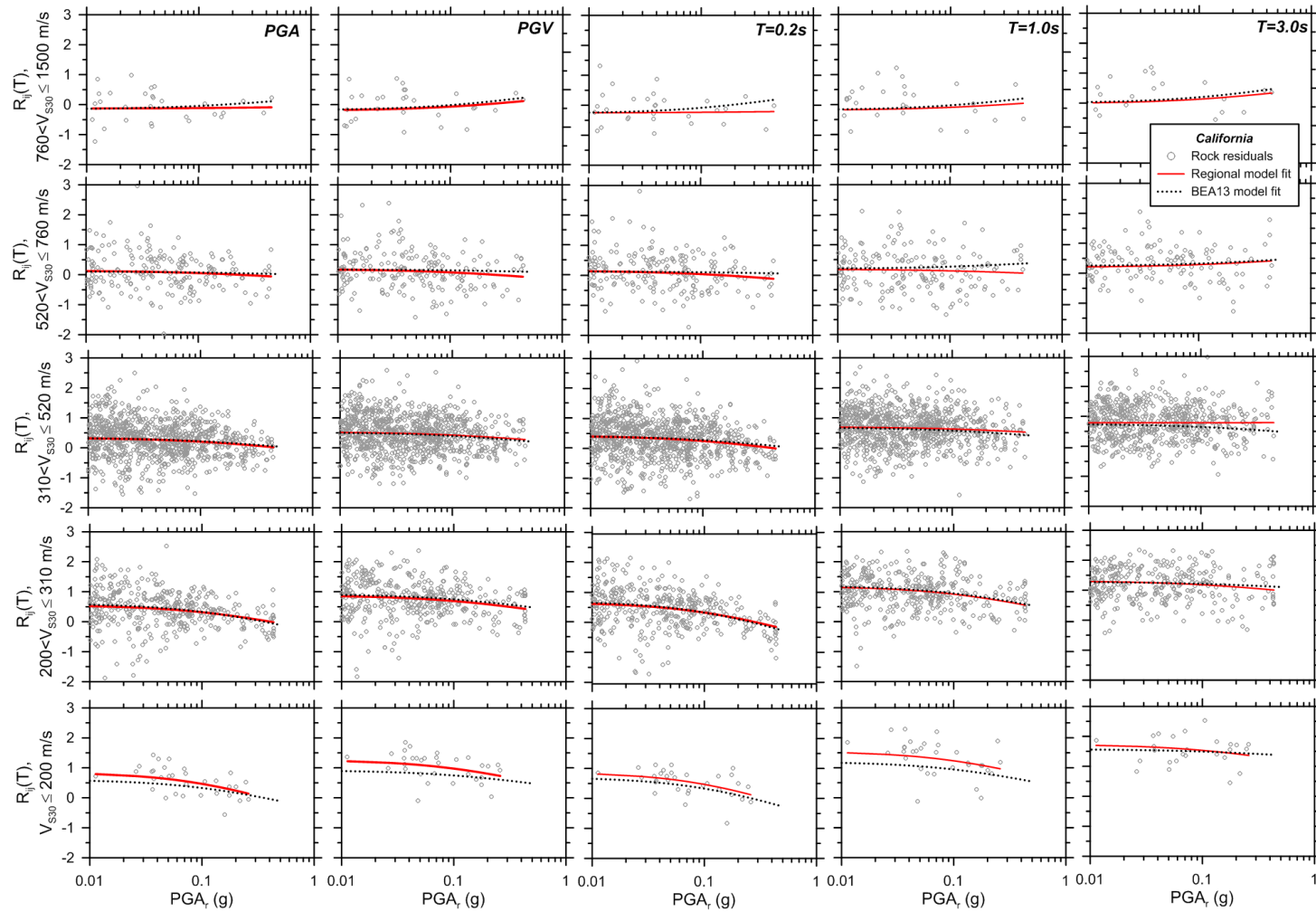
Figure 5.5. Variation of site amplification factors with PGA_r within site categories for California portion of data set. Discrete symbols are intra-event residuals [R_{ij}, Eqn. (5.5)], solid lines are nonlinear regional fit from Eqn. (5.3), dotted lines are global fit from BEA13 .
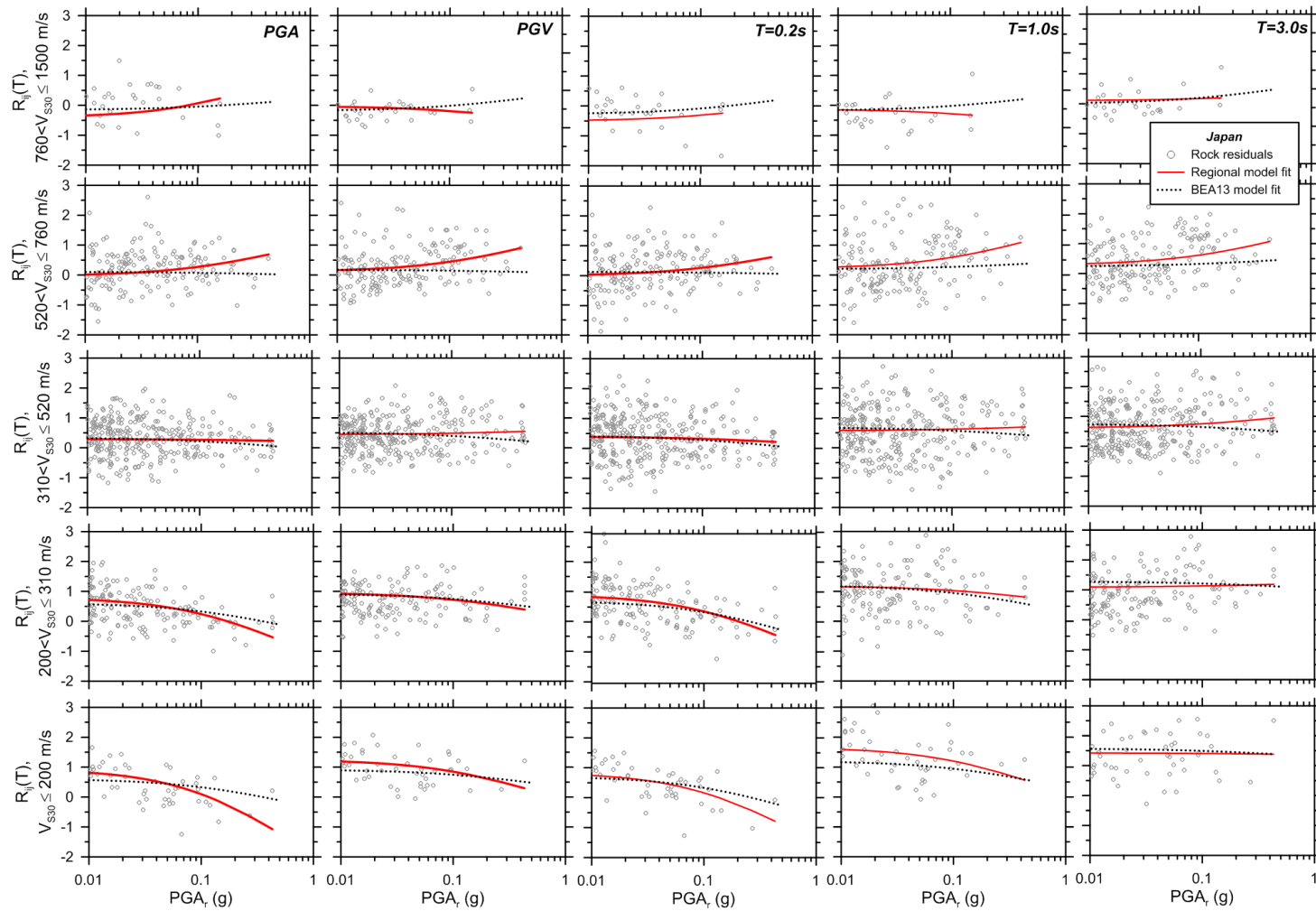
Figure 5.6. Variation of site amplification factors with PGA$_r$ within site categories for Japan. See Figure 5.4 caption for further explanation of symbols.
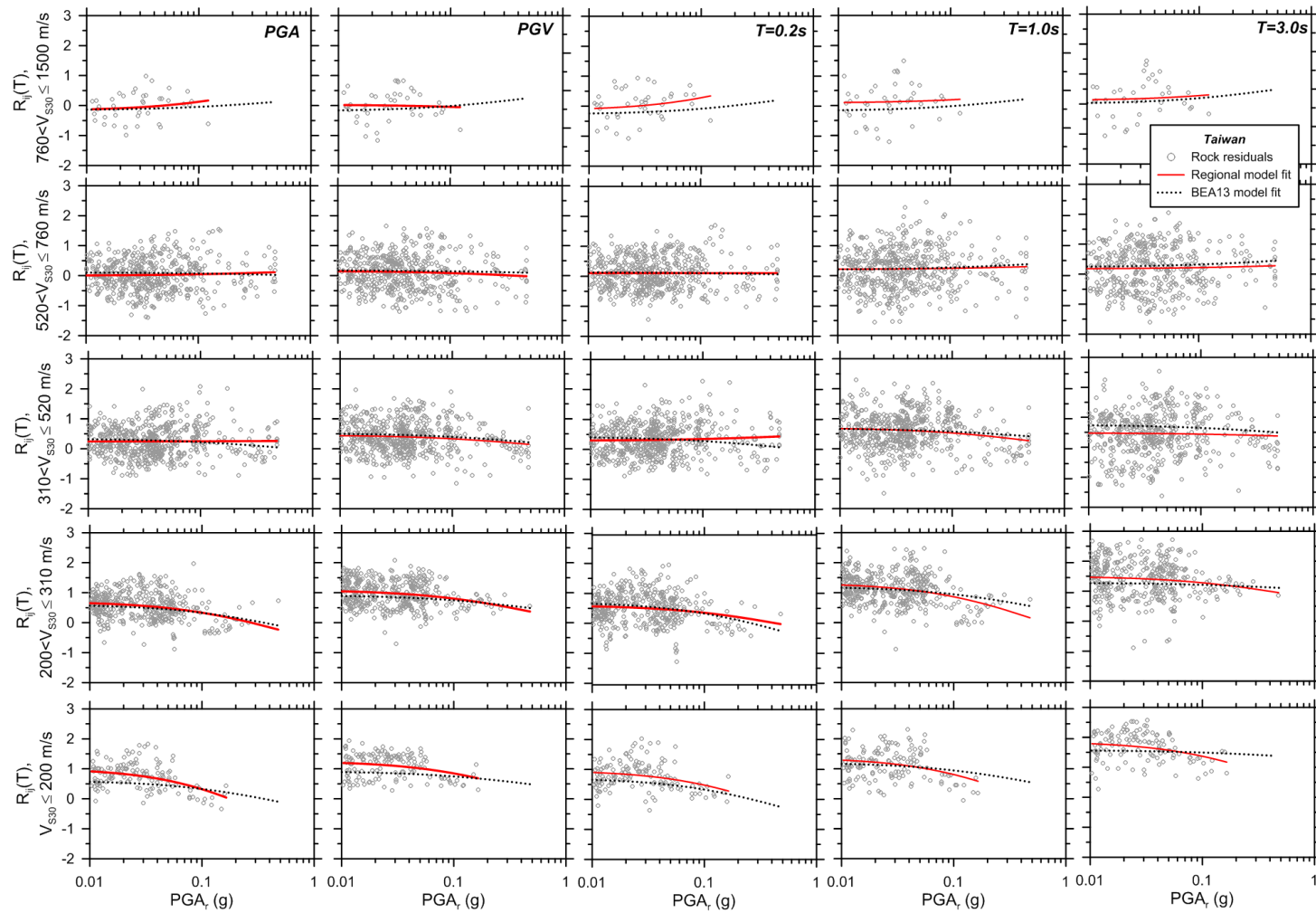
Figure 5.7. Variation of site amplification factors with PGA_r within site categories for Taiwan. See Figure 4.4 caption for further explanation of symbols.

Table 5.2.   Nonlinear parameter f_2 as established from regressions of regional data using Eqn. (5.3).

Site Class	IM/Period (sec)	California		Japan		Taiwan	
		f_2	Std. Dev.	f_2	Std. Dev.	f_2	Std. Dev.
$V_{s30} \leq 200$ m/s	PGA	-0.56+/- 0.174	0.54	-1.20 +/- 0.176	0.61	-0.99 +/- 0.176	0.43
	PGV	-0.42 +/- 0.157	0.48	-0.57 +/- 0.188	0.59	-0.58 +/- 0.175	0.41
	0.2	-0.59 +/- 0.164	0.52	-0.97 +/- 0.181	0.60	-0.71 +/- 0.200	0.46
	1	-0.46 +/- 0.185	0.56	-0.65 +/- 0.230	0.71	-0.80 +/- 0.216	0.50
	3	-0.24 +/- 0.174	0.49	-0.03 +/- 0.240	0.72	-0.46 +/- 0.231	0.50
$200 < V_{s30} \leq 310$ m/s	PGA	-0.34 +/- 0.058	0.64	-0.47 +/- 0.089	0.59	-0.79 +/- 0.104	0.44
	PGV	-0.26 +/- 0.055	0.61	-0.39 +/- 0.090	0.58	-0.33 +/- 0.109	0.44
	0.2	-0.50 +/- 0.061	0.68	-0.33 +/- 0.106	0.69	-0.81 +/- 0.124	0.51
	1	-0.35 +/- 0.051	0.56	-0.62 +/- 0.101	0.75	-0.22 +/- 0.142	0.50
	3	-0.14 +/- 0.050	0.52	-0.26 +/- 0.131	0.78	0.06 +/- 0.147	0.64
$310 < V_{s30} \leq 520$ m/s	PGA	-0.18 +/- 0.042	0.64	-0.03 +/- 0.073	0.61	0.01 +/- 0.061	0.50
	PGV	-0.15 +/- 0.038	0.59	0.06 +/- 0.068	0.57	-0.18 +/- 0.062	0.51
	0.2	-0.25 +/- 0.044	0.68	-0.10 +/- 0.087	0.73	0.09 +/- 0.064	0.53
	1	-0.11 +/- 0.041	0.62	0.07 +/- 0.093	0.78	-0.24 +/- 0.072	0.60
	3	0.05 +/- 0.040	0.60	0.19 +/- 0.086	0.73	-0.16 +/- 0.088	0.72
$520 < V_{s30} \leq 760$ m/s	PGA	-0.11 +/- 0.091	0.74	0.43 +/- 0.114	0.64	0.06 +/- 0.074	0.54
	PGV	-0.15 +/- 0.080	0.65	0.47 +/- 0.104	0.58	-0.12 +/- 0.077	0.57
	0.2	-0.16 +/- 0.096	0.78	0.37 +/- 0.131	0.72	0.00 +/- 0.074	0.54
	1	-0.09 +/- 0.077	0.62	0.52 +/- 0.143	0.80	0.03 +/- 0.094	0.69
	3	0.05 +/- 0.070	0.56	0.47 +/- 0.112	0.63	-0.01 +/- 0.100	0.73
$760 \leq V_{s30} < 1500$ m/s	PGA	0.02 +/- 0.204	0.70	0.67 +/- 0.393	0.71	0.42 +/- 0.411	0.45
	PGV	0.19 +/- 0.172	0.59	-0.23 +/- 0.250	0.45	-0.10 +/- 0.448	0.48
	0.2	0.03 +/- 0.196	0.67	0.28 +/- 0.385	0.69	0.61 +/- 0.456	0.50
	1	0.08 +/- 0.160	0.54	-0.21 +/- 0.348	0.62	0.15 +/- 0.562	0.61
	3	0.24 +/- 0.159	0.52	0.10 +/- 0.297	0.53	0.28 +/- 0.541	0.59
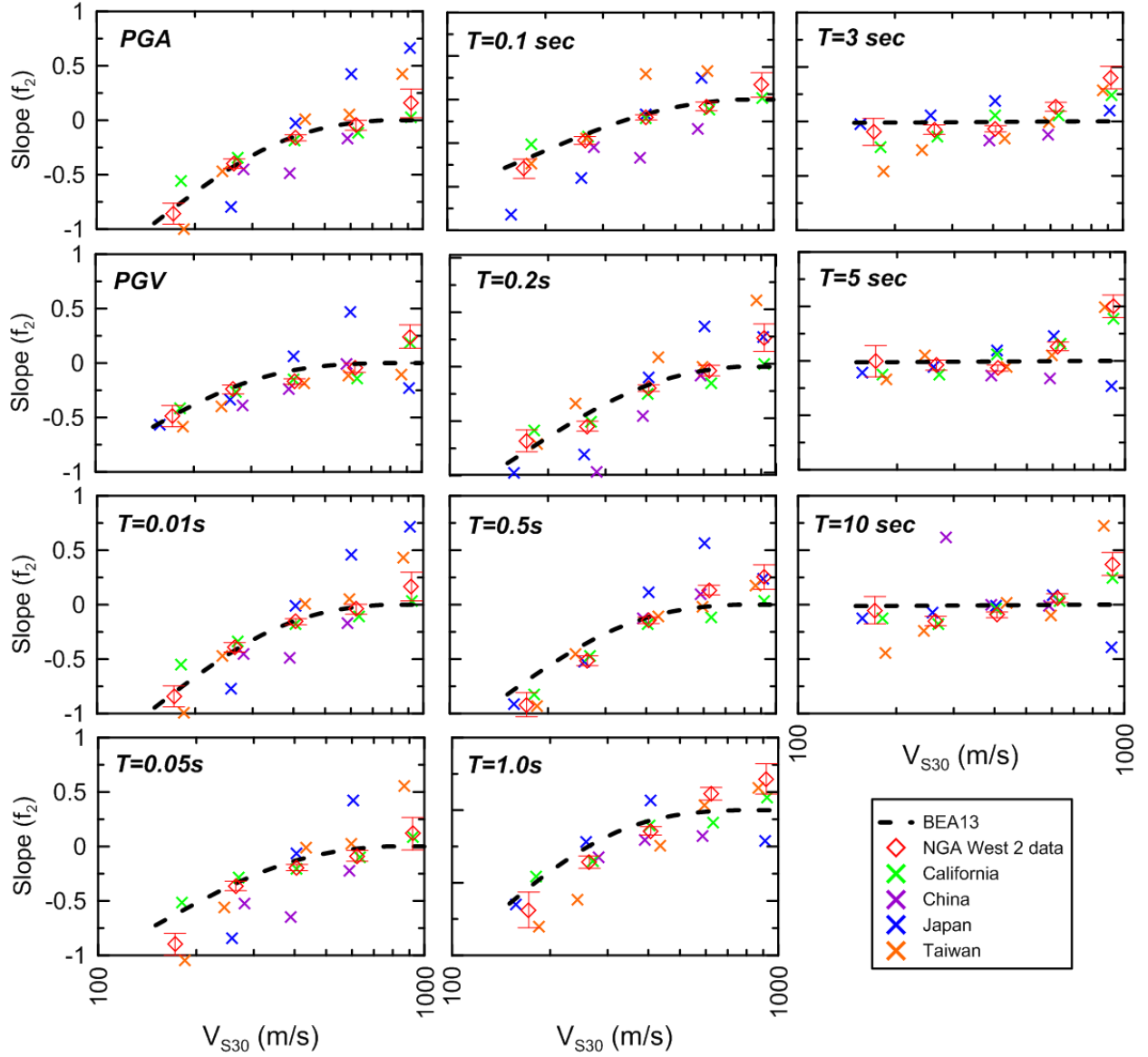
Figure 5.8. Dependence of slope (f_2) with V_{s30} for various regions along with BEA08 model.

5.2.5 Linear Component of the Model

Linear site amplification is evaluated by subtracting the nonlinear term from the total residual to obtain R_k^{lin}, as shown in Equation (5.6). Whereas the analysis of nonlinearity places a premium on close-distance sites likely to be been subject to nonlinear soil behavior, the

analysis of linear site amplification tends to be weighted towards the large number of sites at greater distance where amplitudes of shaking are low and site response is more likely linear. This places the empirical analysis of linear site response somewhat in tension with regional variations of anelastic attenuation, which can introduce systematic bias in GMPEs at large distance for specific events. If not accounted for, this bias could be mistakenly mapped into site amplification using the data analysis procedures described in Section 5.1.

This problem has previously been addressed by truncating the data set used for analysis of site response at site-source distances sufficiently small (approximately 80 km) that anelastic attenuation effects are unlikely to be significant [e.g., Campbell and Bozorgnia (2013); Stewart et al. (2013). As mentioned in Section 5.1, the approach adopted by BEA13 is different, opting instead to correct for regional anelastic attenuation effects, verify the efficacy of such corrections, and then extend the distance range much further (up to approximately 400 km).

Figure 5.9 (a-b) show the dependence of site amplification (represented by R_k^{lin}) with V_{s30} for various periods for the five regions contributing most of the NGA-West 2 data: California, Japan, Taiwan, Mediterranean (Greece, Italy, Turkey), and China. Two data selection criteria were applied: (1) the criteria used in BEA13 (see Section 2.1 of that report), which include data up to $R_{jb} \approx 400$ km; and (2) data truncation at $R_{jb} \leq 80$ km (these residuals were computed without regional anelastic attenuation corrections). Residuals R_k^{lin} were sorted by region and regressed using Eqn. (5.2) to obtain slope parameter c. These regressions are performed with V_{ref} left as a free parameter so as to obtain the most accurate slope. This causes the regression to be non-zero at 760 m/sec, which is the desired reference velocity. That offset

from zero at 760 m/sec is subtracted on a regional basis for the plots shown in Figure 5.8 (and similar diagrams in BEA13). Note that parameter c represents the V_{s30}-scaling in that it quantifies the slope of the relationship between site amplification and V_{s30} in log-log space.

The slopes in Figure 5.9 (a-b) are negative, which is expected, as this indicates stronger ground motion for softer sites. Slopes also tend to increase with period over the range considered, which is also consistent with past experience [e.g., Boore et al. (1997) and the 2008 NGA models]. Note that the results from California in Figure 5.9 indicate a break in the V_{S30} scaling for fast velocities and longer periods (as seen in the results for T = 1.0 sec). It is this break in slope that motivated the use of the corner velocity V_c in the linear portion of the site amplification function (Eqn. 5.2).
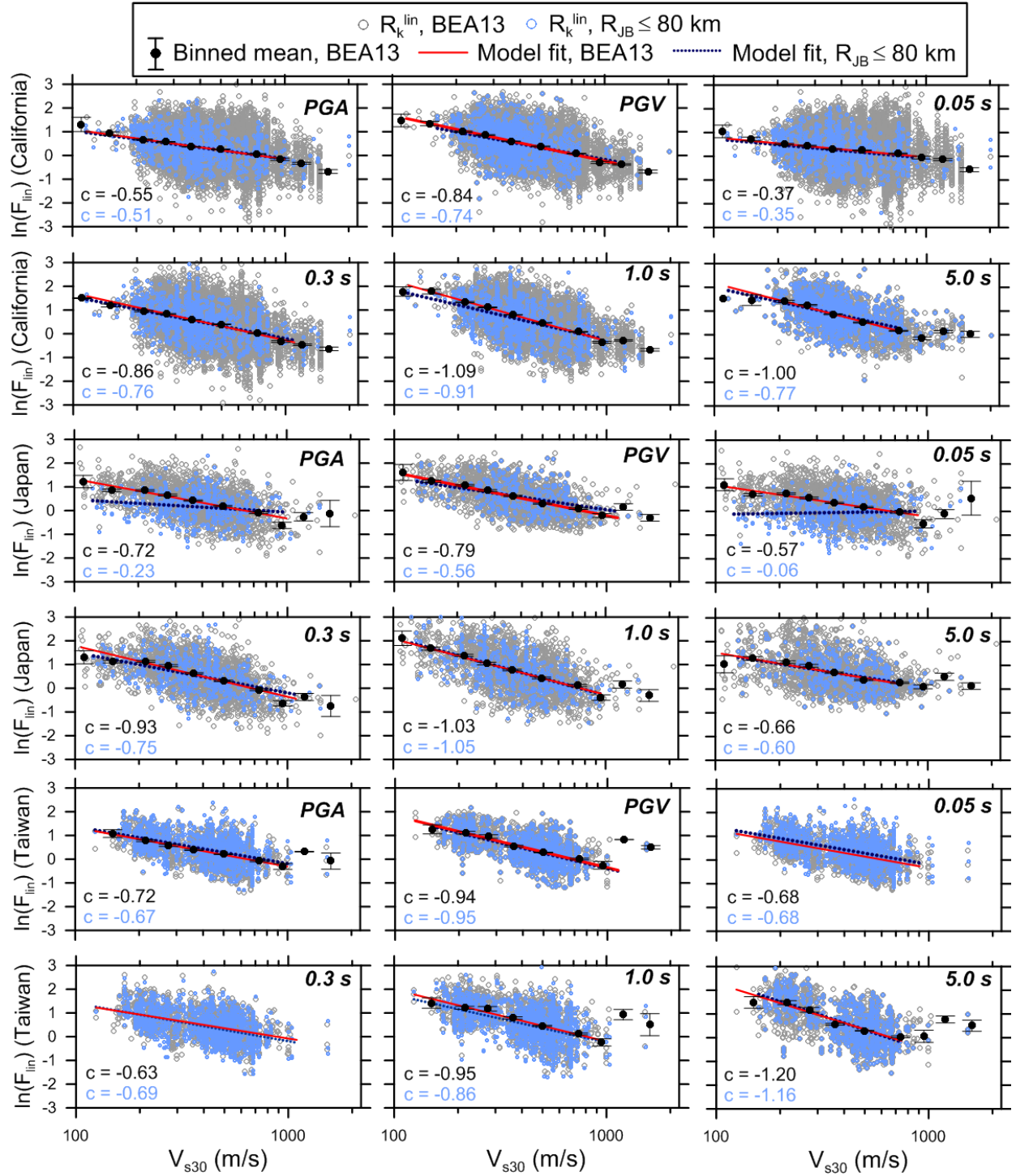
Figure 5.9(a). Variation of linearized site amplification [Eqn. (5.6)] with V_{S30} for subsets of data from California, Japan, and Taiwan. Trend lines shown for $V_{S30} < V_c$ for data sets selected using BEA13 (relatively complete) and $R_{JB} < 80$ km (more restrictive) criteria.

143
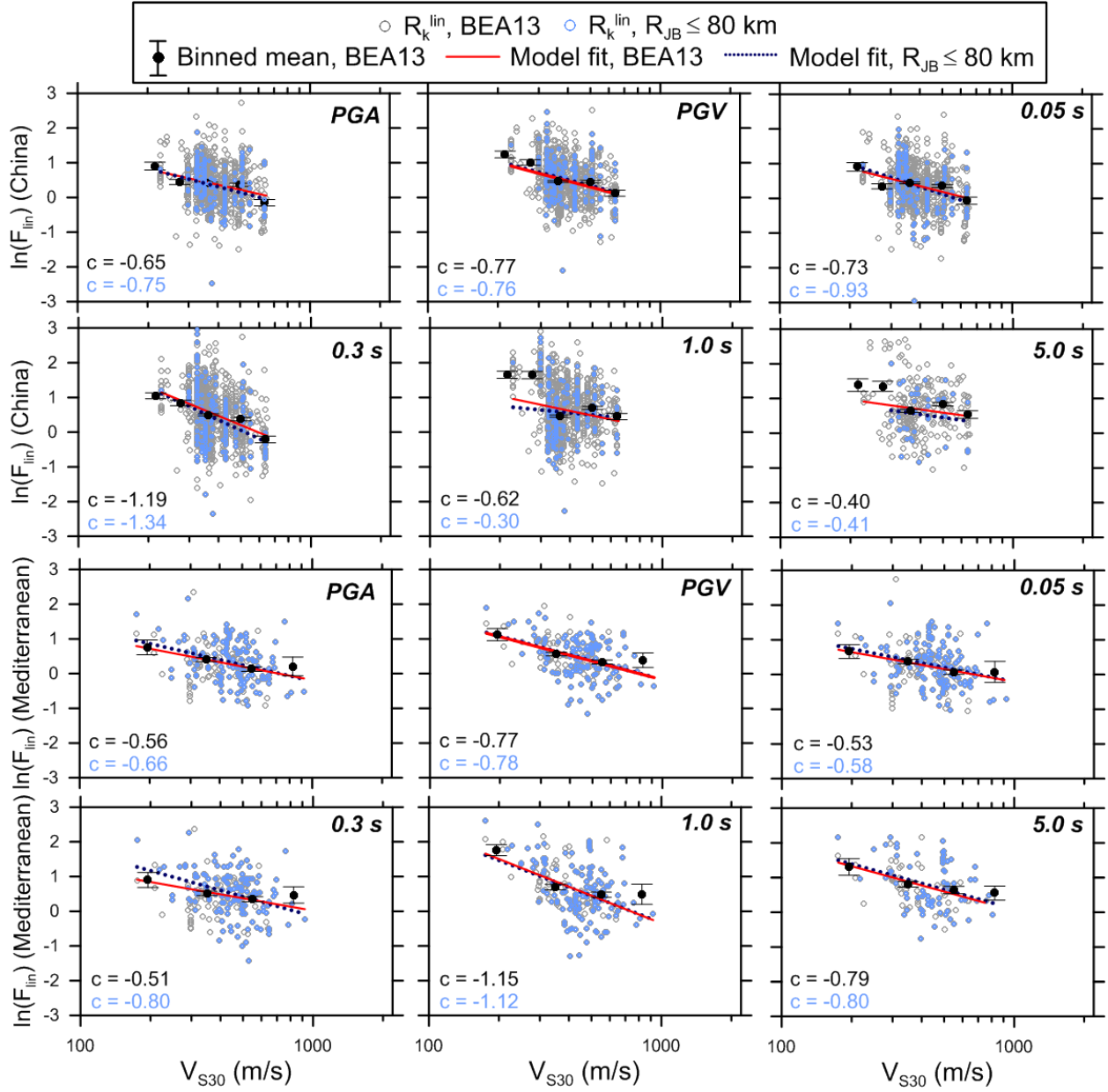
Figure 5.9(b). Variation of linearized site amplification [Eqn. (4.6)] with V_{S30} for subsets of data from Medeteranean regions and China.

Figure 5.10 shows the resulting *c* values plotted against period for the two data selection criteria. Figure 5.10(a) shows the values obtained using the BEA13 criteria in which the data extend to large distance, whereas Figure 5.10b shows the values obtained with the 80-

km cutoff distance. Using the BEA13 data selection criteria (inclusive of large distances), we find modest variations of *c* between regions. As shown in Figures 5.9 and 5.10, the two data selection criteria produce similar slopes in most regions and periods. A notable exception is Japan, where the 80-km truncated data set slopes are significantly different, being much flatter at short periods. Similar sensitivites of the V_{S30} slope parameter to data selection criteria have been observed previously by Chiou and Youngs (2012) for the Japanese data. There are slope differences at some periods for the Mediterranean and China regions as well, although these are relatively poorly constrained due to relatively sparse data (and limited V_{s30} range). Until the causes of these differences in slopes are better understood, we consider it prudent to use slopes derived from the larger (BEA13) data set. BEA13 used that relatively complete data set and elected to not regionalize the *c* parameter due to the relatively modest between-region variations evident in Figure 5.10(a).
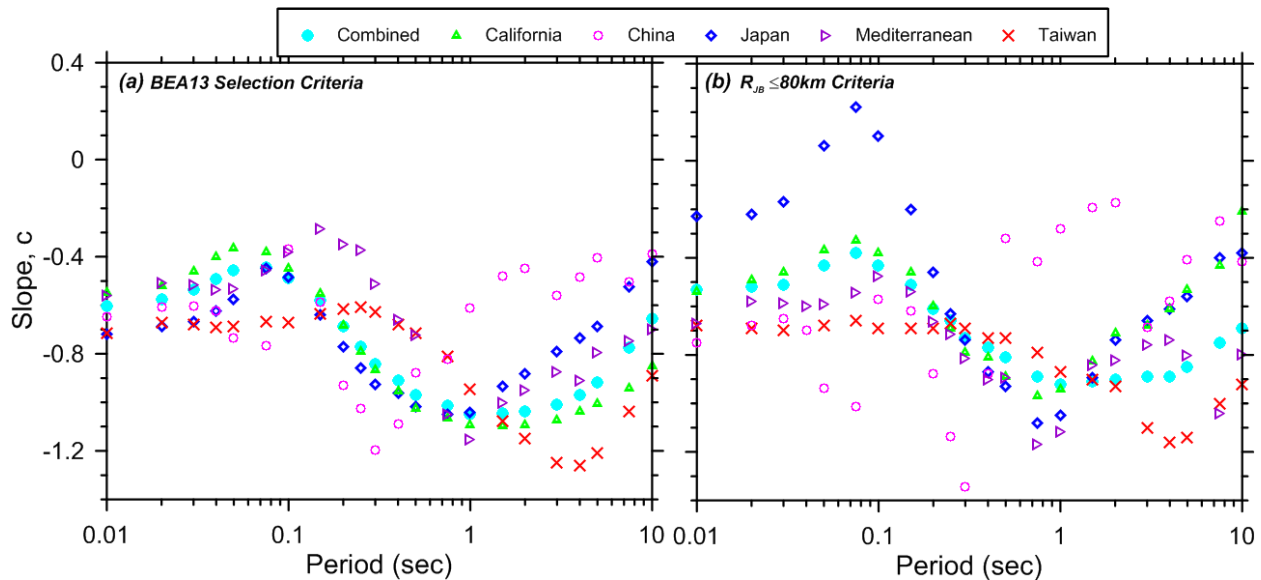
Figure 5.10. Variation of slope (c) with spectral periods for combined data set and various regions using (a) BEA13 data selection criteria and (b) restricting data sites with R_{jb} < 80 km.

145

The data shown in Figure 5.9(a-b) include sites with V_{s30} values both from measurements and inferred from proxy relationships. We also investigated whether the trends shown in Figure 5.9 are preserved when data are considered only from sites with measurement-based V_{s30} values. Figure 5.11 shows the V_{s30}-scaling using only measured V_{s30} for the combined data sets and those from three regions. There are some changes in the slope coefficients, particularly at shorter periods. The largest changes occur in the California and Japan results. The use of proxies aggregate at a series of individual V_{s30} values that would otherwise be a continuous spread of data points. Particularly for slow V_{s30}-values, this aggregation has the effect of underestimating the level of the nonlinear correction because that correction increases substantially in magnitude as V_{s30} decreases. Indeed, regressions of the type shown in Figures 5.9 and 5.11 without removal of nonlinear effects (not shown here) indicate almost no change as a result of screening the data to consider only measured sites. Despite this potential pitfall of using proxies, particularly for soft sites, in subsequent analyses we utilize data from sites with V_{s30} from measurements and proxy estimates so as to not overly restrict the size of the data set.
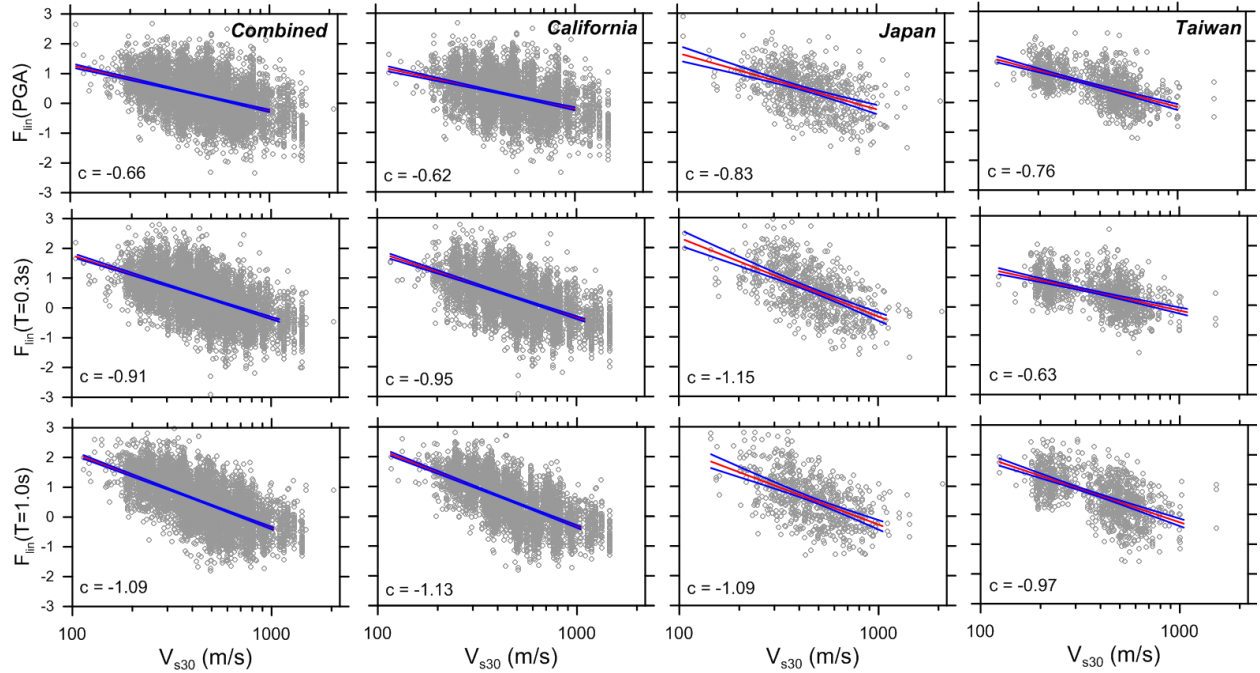
Figure 5.11. Variation of site amplification factors with V_{s30} (measured only) for combined data set and subsets from California, Japan, and Taiwan. Blue solid line: $\pm$ 95% CI, red solid line: Median fit for $V_{s30} < V_c$.

The Taiwan data set is somewhat unique in that it has a substantial volume of data from aftershocks, along with a smaller amount of mainshock data. This is of some concern because aftershocks are treated differently than mainshocks in the development of some (but not all) GMPEs. We segregate events into two types: (1) 1999 Chi Chi mainshock and (2) subsequent Chi Chi Class 2 (CL2) events (considered as aftershocks). The aftershocks are the largest in number (970 recordings) for this region. The results are shown in Figure 5.12. The Chi-Chi CL2 data (orange dots) dominate the data set and hence the trends shown previously for Taiwan in Figure 5.9(a). The aftershocks produce stronger V_{s30}-scaling than the mainshocks. It is possible that these differences result in part from nonlinearity. Recall that the nonlinear correction applied to the data represents an apparoximate global average as inferred from data analysis

147

and simulations. Individual regions can exhibit different trends, which is indeed the case for Taiwan. As shown in Figure 5.12, the Taiwan data exhibit higher than average nonlinearity for soft sites and less than average nonlinearity for stiff sites. If the nonlinear correction were modified to consider those apparent regional effects, the mainshock slopes would steepen, making them closer to aftershock slopes. Despite these differences in behavior, we retain the use of data from aftershocks in our work because we see no reason for the physical processes causing site response to be biased for one event type versus another, provided the effects of nonlinearity are taken into account.
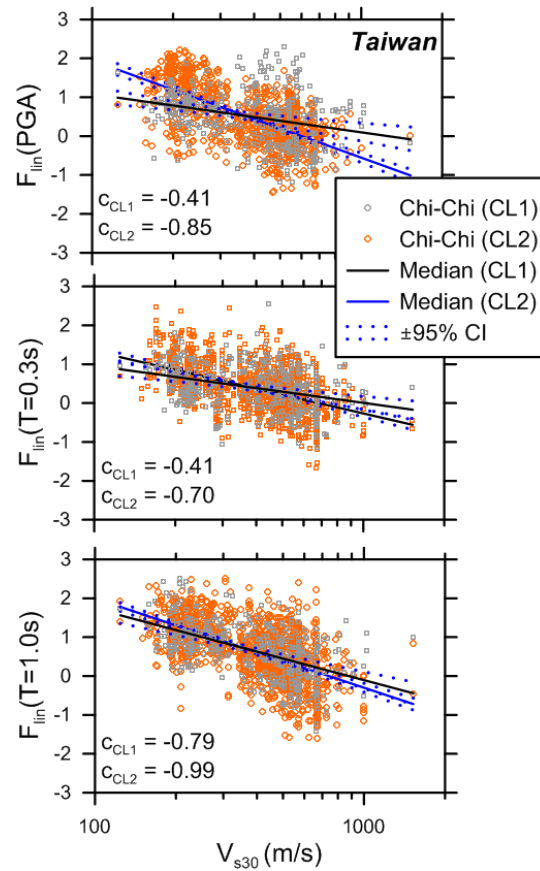
Figure 5.12. Variation of site amplification with V_{s30} for Chi Chi Taiwan Class 1 (CL1) events (mainshocks) and Class 2 (CL2) events (aftershocks).

5.2.6 Comparison to Site Terms in Other NGA West 2 GMPEs

In Section 3.2, I described the site terms in the NGA-West 1 GMPEs and showed how they compared to the NEHRP site factors. Each set of site factors has been updated for NGA-West 2 in reports by Abrahamson et al. (2013: ASK13), BEA13, Campbell and Bozorgnia (2013: CB13), and Chiou and Youngs (2013: CY13). A fifth NGA-West 2 GMPE by Idriss (2013) now includes a site term (which was not included in the 2008 version of this GMPE), but the data used in the analysis does not include most soil sites, so that study is not considered further here.

Other than BEA13, the general form of the site term equations has remained the same from NGA-West 1 to NGA-West 2. All site terms are based on empirical data analysis for V_{s30}-scaling terms, whereas nonlinear terms are evaluated from a hybrid of data analysis and simulation results from WEA08 and KEA13 in a manner very similar to that described in Section 5.2. Other than BEA13, the main change was that ASK13 now use PSA at the period of interest as the parameter driving nonlinearity (similar to CY08) in lieu of PGA_r.

Figure 5.13 shows the site terms for the four aforementioned NGA-West 2 GMPEs: ASK13, BEA13, CB13, and CY13. The site terms were all normalized to a reference condition of V_{ref} = 760 m/sec using procedures described in Section 3.1. For soil site categories C, D, and E, the ASK13 factors are typically lowest and CY13 highest, with BEA13 and CB13 values generally being intermediate. Overall, the differences between the site factors in these models are relatively modest. The current NEHRP factors are also shown on the plot for reference purposes. The misfits between the NGA-West 2 factors and NEHRP factors follow similar trends to those identified earlier for NGA-West 1 factors in Section 3.1.
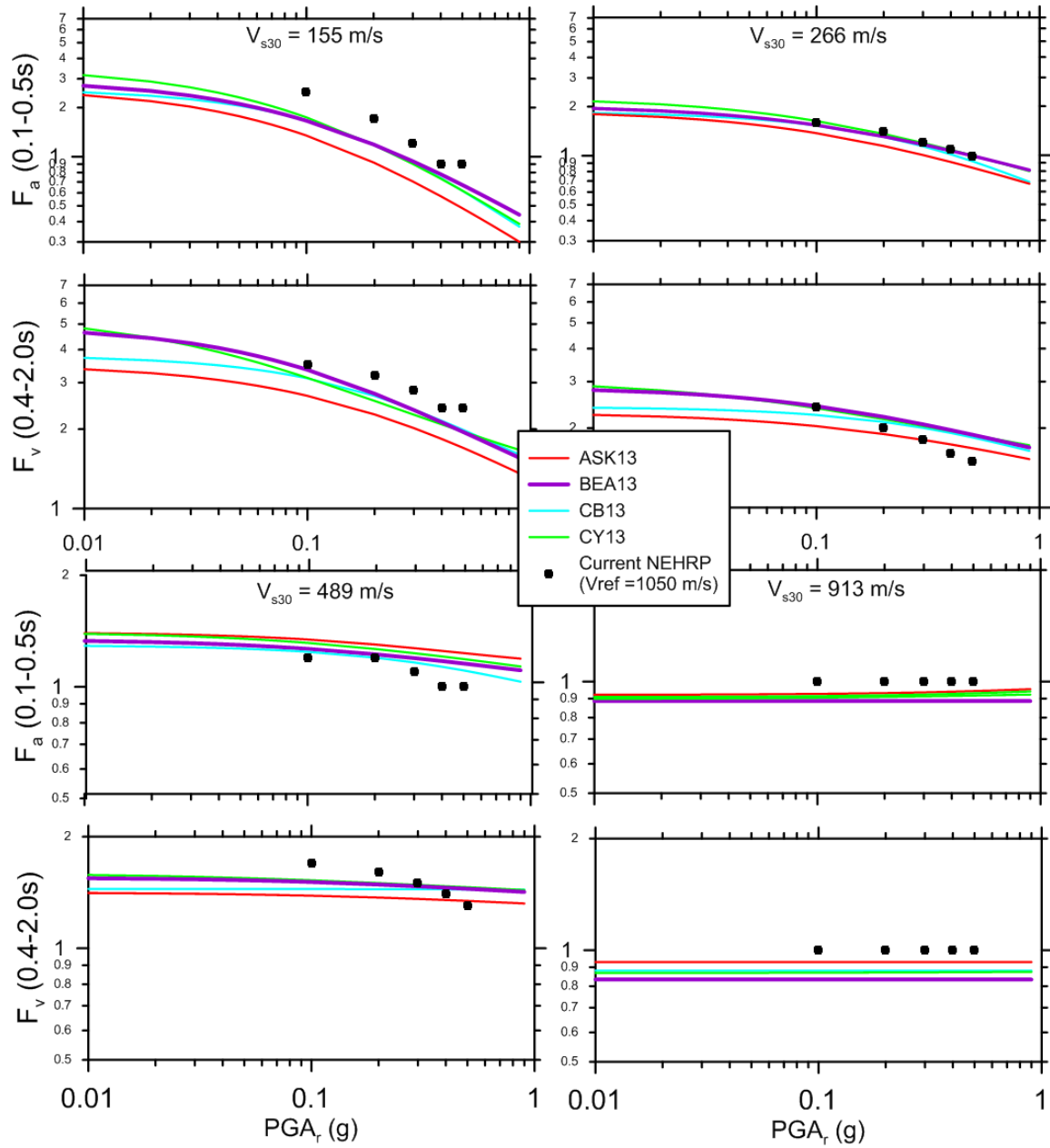
Figure 5.13. Comparison of site terms in NGA West 2 GMPEs normalized to a common reference site condition of V_{ref} = 760 m/sec along with current NEHRP site factors, which have a reference condition of 1050 m/sec. Site factors from NGA relationships are averaged across corresponding period ranges (0.1–0.5 sec for F_a; 0.4–2.0 sec for F_v).

5.3 DEVELOPMENT OF REVISED NEHRP SITE FACTORS

5.3.1 The Process

The Task 8 Working Group - under which I was the only graduate student responsible from this study - was assembled principally to support the development of a proposal to modify the NEHRP site factors. Many working group members have experience as past members of the Building Seismic Safety Council (BSSC) Provisions Update Committee (PUC), which meets on approximately four-year intervals to hear and vote on proposals to revise the *NEHRP Recommended Provisions for New Buildings and Other Structures* (BSSC 2003).

One member of the Task 8 Working Group, C.B. Crouse, is a current member of the PUC. Early in this project, we sought and received PUC approval to prepare a proposal to revise the NEHRP site factors. The PUC requested that the Task 8 working group prepare a proposal and that the group members vote on it. A unanimous or nearly unanimous Task 8 vote was considered essential for a proposal to be favorably evaluated at the PUC level.

The Task 8 working group met in person and via phone meetings on five occasions between March 2010 and June 2012. The purpose of the initial meetings was to define specific scope items that would enable the issues with the current NEHRP site factors to be clearly defined. The outcomes of this work are described principally in Chapters 3 and 5, and were publically presented in a keynote presentation at the 2012 GeoCongress in Oakland California (Seyhan and Stewart 2012). Subsequent meetings involved the review of data and analysis results developed by the authors and other committee members.

In the course of these meetings, different views of some key issues were identified and discussed in some detail, as described further in the next section. Aside from those specific

issues, the Task 8 group was able to reach consensus relatively easily on other matters. The status of the Task 8 work as of this writing is that a proposal was submitted to PUC in October 2012 and tentatively approved (with comments) by the PUC in January 2013. A response to the comments has been prepared and the proposal has been modified for further consideration by the PUC in July 2013. The resolution within Task 8 of some key technical issues, which remain sources of some contention for some PUC members, is described in the following section.

5.3.2 Recommended NEHRP Site Factors

The site amplification model described by Chapter 3 and 5 is utilized to generate site amplification factors within the V_{s30} bins, and at the PGA_r values, currently used in the NEHRP *Provisions*. Recall that the NEHRP site factors are specified for Categories A-E with the V_{s30} limits given in Table 5.3. We select representative V_{s30} values for each category from the distribution of measured data in the NGA-West2 site database, which was shown previously in Figure 3.6.

Table 5.3 presents these intra-category median V_{s30} values along with the recommended V_{s30} values from Borcherdt (1994b, Table 2, marked as 'B94'). Site amplification within each category is computed using the NGA-West 2 median V_{s30} values in Table 5.3. The rationale behind this selection is that the NEHRP factors are evaluated for the most probable V_{s30} value within the category. The resulting factors are not substantially different if they are evaluated at alternate velocities selected by Borcherdt (1994b) or at the geometric mean of the category limits (see Section 3.1 for this discussion).

Table 5.3.   Representative median V_{s30} values in NEHRP categories.

NEHRP Site Class	Mid-Range V_{s30} (m/s) from B94	NGA-West 2 Median V_{s30} (m/s)	Geometric Mean of Class limits (m/s)
E ($V_{s30} < 180$ m/s)	150	155	180
D ($180 < V_{s30} < 360$ m/s)	290	266	255
C ($360 < V_{s30} < 760$ m/s)	540	489	523
B ($760 < V_{s30} < 1500$ m/s)	1050	913	1068
A ($V_{s30} > 1500$ m/s)	1620	1620[a]	1500

[a] Adopted from B94

The NEHRP site factors are developed using the model represented by Eqn. (5.7). The $\ln(F_{lin})$ term is computed using Eqn. (5.2) by averaging slope (c) values across period ranges of 0.1–0.5 sec (for F_a) and 0.4-2.0 sec (for F_v). The averaging is not done across all NGA periods within those ranges, because they are not evenly sampled in log space. Rather, we selected 20 periods per log cycle that were (roughly) evenly sampled. The corresponding c values are -0.67 for F_a and -1.00 for F_v. As described in Section 5.2, V_{ref} is taken as 760 m/sec.

The $\ln(F_{nl})$ term is computed using Eqn. (5.3), in which slope f_2 is computed using Eqn. (5.4) from averaged f_4 and f_5 values for the respective period ranges computed as described above and for the V_{s30} values shown in Table 5.1, f_1 is zero, and f_3 is taken as $0.1\underline{g}$ independent of period.

Coefficients for c, f_4 and f_5 that were used in the above calculations are given in the appendix of BEA13.

Since reference site ground motion amplitudes are specified in the NEHRP *Provisions* in terms of spectral ordinates instead of PGA_r, we apply the following conversions:

$$S_s \approx 2.3 \times PGA_r$$
$$S_1 \approx 0.7 \times PGA_r$$

(5.7)

Site factors are computed at PGA_r = 0.11, 0.22, 0.33, 0.43, and 0.54g (for F_a) and PGA_r = 0.14, 0.29, 0.43, 0.57, and 0.71g (for F_v), which is consistent with the tabulated S_s and S_1 values in the current NEHRP *Provisions*.

We compute period-averaged (equally spaced in log scale) site amplification for the specified ranges of V_{s30} and PGA_r. The results are given in Figure 5.1 and Table 5.2. For the case of Site Class A, we maintain the current values of 0.8, which are generally consistent with amplification for $V_{s30} > V_c$ in Chapter 5. For Site Class E, median estimates of site amplification were computed using the complete model as with the other classes. However, the recommended factors for Site Class E are increased above the median by one-half of the within-event standard deviation derived from the data, which increases site factors by approximately a factor of 1.3 - 1.4. This introduces a conservative bias to the Class E factors that is considered desirable due to the relatively modest amount of data for this site condition. A conservative bias was applied in the original site factors for Class E as well (Dobry et al. 2000). As shown in Figure 5.14, other than Class E, the recommended site factors are matching the BEA13 model and are consistent with those in the NGA-West 2 models. It should be noted that rounding the plotted site factors and averaging the parameters prior to calculating the factors cause a mismatch with BEA13 model.

Figure 5.14 shows the recommended site factors as a function of V_{s30} for the levels of excitation (specified as values of S_s and S_1) given in the NEHRP tables (i.e., Table 5.5). The trends in the plot show the expected patterns of relative V_{s30}-scaling (stronger for F_v than F_a) and

nonlinearity (strong for soft soil, decreasing effects for stiff soil and rock; stronger for F_a than F_v).

Table 5.5 compares the current and proposed site factors. Values for F_{PGA} are also shown in the table. The proposed site factors are generally smaller than original values due to the change in reference velocity from 1050 to 760 m/sec. For stronger shaking levels and Class C-E soils, the recommended site factors become close to, or slightly greater than, original values because of reduced levels of nonlinearity, especially at long period (i.e., in the F_v parameter). When these rounded numbers are plotted in Figure 5.14, there will be some misfits with respect to BEA13 model.

As noted previously, the nonlinear model, described in Section 5.1, has a substantial effect on the computed factors for Class E. There are large epistemic uncertainties in this model, especially at long periods where the empirical and simulation results underlying the model are divergent. Our introduction of conservatism in the Site Class E factors, as described above, is intended to approximately account for this epistemic uncertainty.
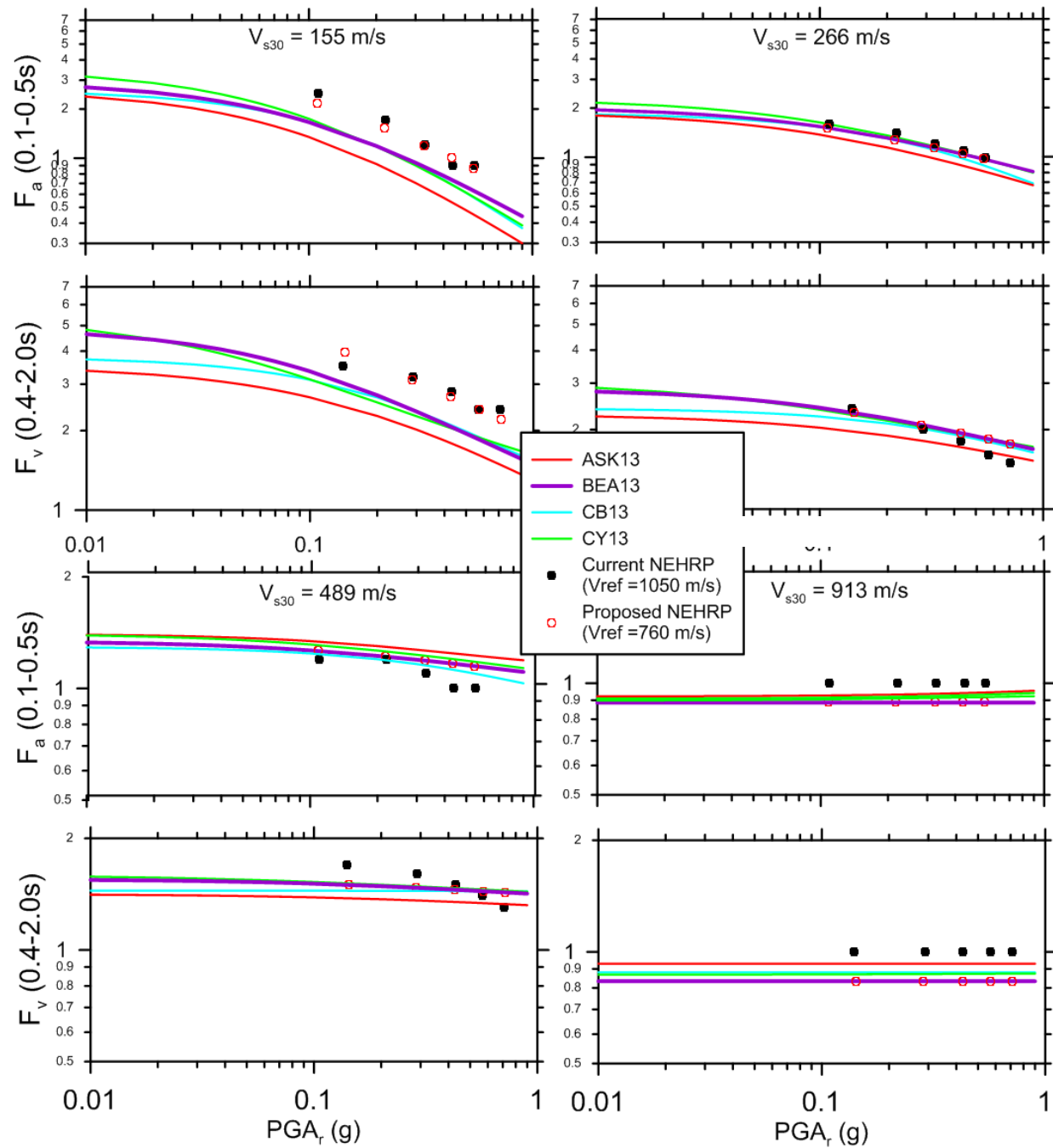
Figure 5.14. Comparison of proposed and current NEHRP site factors with site terms in NGA West 2 GMPEs normalized to a common reference site condition of V_{ref} = 760 m/sec.
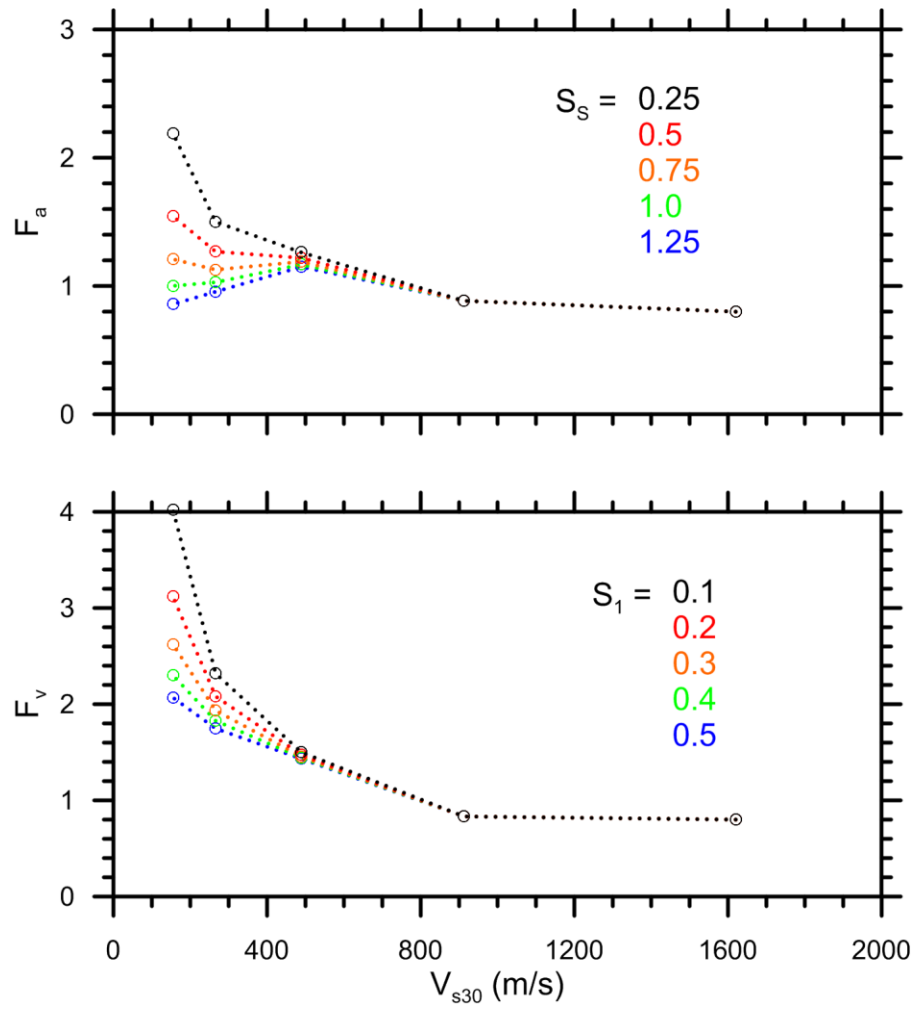
Figure 5.15. Recommended NEHRP site factors for F_a and F_v as function of V_{s30}.

Table 5.4. Original (ASCE) and recommended (PEER) site amplification factors F_a, F_v, and F_{PGA}.

$$F_a$$

Site	$S_s < 0.25$		$S_s = 0.5$		$S_s = 0.75$		$S_s = 1.0$		$S_s > 1.25$	
Class	*PEER*	*ASCE*	*PEER*	*ASCE*	*PEER*	*ASCE*	*PEER*	*ASCE*	*PEER*	*ASCE*
A	0.8	**0.8**	0.8	**0.8**	0.8	**0.8**	0.8	**0.8**	0.8	**0.8**
B	0.9	**1.0**	0.9	**1.0**	0.9	**1.0**	0.9	**1.0**	0.9	**1.0**
C	1.3	**1.2**	1.2	**1.2**	1.2	**1.1**	1.2	**1.0**	1.1	**1.0**
D	1.5	**1.6**	1.3	**1.4**	1.1	**1.2**	1.0	**1.1**	1.0	**1.0**
E	2.2	**2.5**	1.5	**1.7**	1.2	**1.2**	1.0	**0.9**	0.9	**0.9**

$$F_v$$

Site	$S_1 < 0.1$		$S_1 = 0.2$		$S_1 = 0.3$		$S_1 = 0.4$		$S_1 > 0.5$	
Class	*PEER*	*ASCE*	*PEER*	*ASCE*	*PEER*	*ASCE*	*PEER*	*ASCE*	*PEER*	*ASCE*
A	0.8	**0.8**	0.8	**0.8**	0.8	**0.8**	0.8	**0.8**	0.8	**0.8**
B	0.8	**1.0**	0.8	**1.0**	0.8	**1.0**	0.8	**1.0**	0.8	**1.0**
C	1.5	**1.7**	1.5	**1.6**	1.5	**1.5**	1.4	**1.4**	1.4	**1.3**
D	2.3	**2.4**	2.1	**2.0**	1.9	**1.8**	1.8	**1.6**	1.7	**1.5**
E	4.0	**3.5**	3.1	**3.2**	2.6	**2.8**	2.3	**2.4**	2.1	**2.4**

$$F_{PGA}$$

Site	PGA < 0.1		PGA = 0.2		PGA = 0.3		PGA = 0.4		PGA > 0.5	
Class	*PEER*	*ASCE*	*PEER*	*ASCE*	*PEER*	*ASCE*	*PEER*	*ASCE*	*PEER*	*ASCE*
A	0.8	**0.8**	0.8	**0.8**	0.8	**0.8**	0.8	**0.8**	0.8	**0.8**
B	0.9	**1.0**	0.9	**1.0**	0.9	**1.0**	0.9	**1.0**	0.9	**1.0**
C	1.2	**1.2**	1.2	**1.2**	1.2	**1.1**	1.2	**1.0**	1.1	**1.0**
D	1.4	**1.6**	1.3	**1.4**	1.2	**1.2**	1.1	**1.1**	1.0	**1.0**
E	2.1	**2.5**	1.6	**1.7**	1.4	**1.2**	1.2	**0.9**	1.1	**0.9**

5.4 CONCLUSIONS

The research study described here achieved the development of a proposal for revising the NEHRP site amplification factors and supporting work for NGA-West2 GMPE developers related to site terms and site amplification modeling. As described in Chapter 5, the scope of work undertaken to realize those objectives included:

- Review of the technical basis of the NEHRP factors and NGA site factors

- Comparisons of site amplification factors from NEHRP provisions and the 2008 NGA models, including interpretation of the principal causes of differences

- Enhancement and development of the site database used to support the NGA-West 2 flatfile [details in Ancheta et al., (2013)]

- Development of a site amplification model using NGA-West 2 data and simulation results

- Developing consensus within the Task 8 working group on the manner by which revised site factors can be developed, followed by the development of the factors

- The NGA and NEHRP site factors are consistent in certain respects (e.g., the scaling of linear site amplification with V_{s30}), but have discrepancies in linear site amplification (applicable for $PGA_r \leq 0.1g$) for site Classes B to E and in the levels of nonlinearity for Classes C and D. The amount of these discrepancies ranges from up to 50% for Class E to amounts ranging from about 0 to 20% for Classes B-D. Previous work has identified similar discrepancies in NEHRP and NGA site factors (Huang et al. 2010), but the discrepancies were not clearly associated

with differences in linear site amplification levels and nonlinearities. Such associations are useful to understand causes of misfits and to formulate revisions to NEHRP factors.

A major cause of the weak motion amplification misfit is that the NEHRP factors are normalized relative to a reference site condition of V_{ref} =1050 m/sec, whereas their current application is relative to V_{s30} = 760 m/sec. When re-normalized to V_{s30} = 760 m/sec, the NEHRP factors are much closer to NGA factors (especially for Class D), although misfits remain for Classes B, C, and E.

We find that the nonlinearity in F_a and F_v from simulation-based work in the 2008 NGA project (WEA08) is smaller than the nonlinearity in the NEHRP factors (Dobry et al. 2000). Those reduced levels of nonlinearity are consistent with trends from empirical ground motion data from the 2008 NGA project.

Examining the NGA-West 2 data, we find the V_{s30}-scaling to follow regional trends, but the significance of the regional differences is strongly sensitive to the method of data selection. When regional anelastic attenuation effects are considered in the data analysis and the data is extended to large distances, regional site response effects are relatively modest. On the other hand, when a relatively short cut-off distance is used to minimize anelastic attenuation effects (less than approximately 80 km), regional effects are much stronger, especially for Japanese data at short periods. The nonlinearity in site amplification does not show strong evidence of regional variability.

We developed a semi-empirical site amplification model for shallow crustal regions in which V_{s30}-scaling is parameterized using the NGA-West 2 data. The development of that site

amplification model is described by BEA13; this work presents supporting work that guided model development relative to regional variations in site amplification and levels of nonlinearity implied by simulations. The nonlinear component of the model is constrained jointly by NGA-West 2 data and simulation results.

The complete model (for V_{s30}-scaling and nonlinearity) is used to derive recommended new NEHRP site factors using a reference velocity of 760 m/sec. For relatively weak levels of shaking, the recommended NEHRP site factors are generally smaller than current values due to the change in reference velocity from 1050 to 760 m/sec. For stronger shaking levels and Class C, D, and E soils, the recommended site factors become close to, or slightly greater than, those used currently because of reduced levels of nonlinearity, especially at long period (i.e., in the F_v parameter). Factors for soft soil (Class E) were set conservatively, as were the original NEHRP site factors, to account for larger epistemic uncertainty in the nonlinearity for this site class as compared to others.

6　EQUATIONS FOR THE MODEL OF PREDICTING RESPONSE SPECTRAL ACCELERATIONS FOR SHALLOW CRUSTAL EARTHQUAKES

6.1　INTRODUCTION

Ground motion prediction equations (GMPEs) are used in seismic hazard applications to specify the expected levels of ground shaking as a function of various predictor variables such as earthquake magnitude, site-to-source distance and site conditions. GMPEs are typically developed from an empirical regression of observed motions against an available set of predictor variables. It is inevitable that GMPEs become more complex and sophisticated over time as a result of the enhanced ground motion databases and associated metadata. Early GMPEs were very simple equations giving peak ground acceleration as a function of magnitude and epicentral distance (e.g., Douglas, 2003). Modern GMPEs express peak motions and response spectra as functions of moment magnitude, distance to the rupture surface, and site condition variables such as the time-weighted average shear-wave velocity over the upper 30 m

of the profile (V_{s30}); other predictor variables such as focal mechanism, depth to the top of the rupture, and depth to basement rock, may also be used (e.g. see NGA-West 1 equations, as described by Power et al., 2008 and references therein, as well as the compilation by Douglas, 2011). The resolving power of empirical regression techniques to sort out the many effects that control ground motions is advanced with larger and more comprehensive databases.

The work presented in this chapter represents the results of collaborative work involving myself and Prof Stewart along with David M. Boore and Gail M. Atkinson. Our role was principally to perform Phase I and Phase III analysis. The results given here have been previously presented in Boore et al. (2013) (BEA13).

In this study, we use a three-phase model building approach to the GMPE development; our aim is to take advantage of the rich NGA-West 2 database to develop a GMPE model for shallow crustal earthquakes in active tectonic regions that strikes a balance between accuracy of the prediction and simplicity of form and application. Our philosophy is as follows. The primary variables that control ground motion at a site are the earthquake magnitude (the primary source variable), distance to the fault (the primary path variable) and V_{S30} (the primary site variable). After constraining some variables based on an initial analysis of the data, in what we call Phase I of the study, we perform regressions to develop a base-case GMPE (for peak ground motions and response spectra) based on a simple functional form using just these variables, as well as fault type (Phase II). I then refine the model as required, based on examination of the residuals (defined by the difference, in natural log units, between the observed and predicted amplitude of motion) of the regression against secondary predictor

variables that are available as part of the NGA-West 2 metadata (Phase III). These secondary parameters include the region in which the event occurs, whether the source is a mainshock or aftershock, the depth to the top of fault rupture, the depth to basement rock, etc. We assess the extent to which these additional variables improve the accuracy of the GMPE in a way that is both statistically significant and practically meaningful. We implement the inclusion of secondary variables, where warranted, as optional correction factors that may be applied to the base-case GMPEs. In this way, we aim to ensure that our GMPE is centered for the general case of future events in regions for which site-specific fault rupture, path and site parameters may be unknown. As mentioned in Chapter 1, it should again be noted that the details on Phase II analyses are intentionally left out of this dissertation since the effort was made by David M. Boore.

The scope of our GMPEs includes the prediction of horizontal-component peak ground acceleration (PGA), peak ground velocity (PGV) and response spectra (PSA, the 5% damped pseudo response spectral acceleration), for earthquakes of moment magnitude (M) 3.0 to 8.5, at distances from 0 to 400 km, at sites having V_{s30} in the range from 150m/s to 1500 m/s, for periods between 0.01 s and 10 s. We consider regional variability in source, path and site, and selected secondary source and site effects, but do not address directivity effects.

This study builds on the GMPEs of Boore and Atkinson (2008), which were part of the NGA-West 1 project (Power et al., 2008 and references therein). NGA-West 1 was founded on the development of a comprehensive and consistent database of ground-motion variables for shallow crustal earthquakes in active regions, including assembling associated metadata parameters, as described by Chiou et al. (2008). The NGA-West 1 project involved a novel

collaborative process in which several developer groups interacted in using various subsets of the same master database to derive alternative GMPEs. The process was highly successful in initiating significant improvements to the GMPEs available for seismic hazard applications. Based on the success of NGA-West 1, the NGA-West 2 project was formed to take advantage of new data available since NGA-West 1, address some weaknesses in the NGA-West 1 database, and allow the developers to reconsider their functional forms.

One improvement needed to the NGA-West 1 equations involved adding data at small-to-moderate magnitudes. The need to enrich the database at the low-magnitude end to ensure robust magnitude scaling was highlighted by several studies (Atkinson and Morrison, 2009; Chiou et al., 2010; Atkinson and Boore, 2011), and two of the NGA-West 1 developers provided amendments to improve their equation performance at low magnitudes (Chiou et al., 2010; Atkinson and Boore, 2011); the revised Boore and Atkinson GMPEs that account for this adjustment are referred to as BA08'. Studies by Atkinson and Morrison (2009) and Chiou et al. (2010) also pointed to the need to consider regional variability of path effects, as the attenuation of motions with distance is faster in some active regions than in others.

An important issue not addressed in NGA-West 1 was the regional variability of site effects; this issue stems from the inherent limitations of using V_{s30} as the primary site condition variable. In reality, site amplification depends not only on soil stiffness (V_{s30}), but also on soil depth and other factors. There are regional variations in the period at which site amplification peaks, due to regional differences in the depths of typical soil profiles; the site amplification function versus period for a given value of V_{s30} should thus be regionally dependent. In

particular, peak site response occurs at shorter periods in Japan than in western North America, even for the same value of V_{s30} (Atkinson and Casey, 2003; Ghofrani et al., 2013; Stewart et al., 2013; Anderson et al., 2013). Thus we can potentially improve on the NGA-West 1 equations by allowing the site response function to vary with region, in addition to V_{s30}. We wish to note here that we recognize different variables could be used to characterize site effects, such as the quarter-wavelength shear wave velocity (Joyner and Fumal, 1984, 1985; Douglas et al., 2009) or V_{s30} in combination with peak response period. This option was not pursued in the present work because this level of site description is not yet part of the NGA-West database or used in common practice.

Other improvements to the treatment of site effects are also made possible by better data. Boore and Atkinson (2008) used empirical site amplification factors based on the work of Choi and Stewart (2005). Stewart and Seyhan (2013) have updated this work based on additional data, which now allows a more robust description of linear and nonlinear site amplification effects over a wider range of V_{S30}.

Finally, the richer database available for NGA-West 2 allows us to improve on prior work by considering additional variables that could not previously be adequately resolved. However, as described in the next sections, we maintain the same basic functional form for the equations as used in Boore and Atkinson (2008).

6.2 DATA SELECTION

6.2.1 Data Sources and Data Exclusion Criteria

We use the strong-ground motion database developed in the NGA-West 2 project (http://peer.berkeley.edu/ngawest2/). As described in Ancheta et al. (2013), the NGA-West 2 database consists of a site database containing metadata for all stations producing usable recordings; a source database containing magnitudes, locations, and geometries of earthquake sources producing recordings; and a flatfile that merges critical site and source information with distance parameters and computed ground-motion intensity measures. The flatfile was a continuously evolving file over the project duration, hence in referring to the flatfile, it becomes necessary to specify a date or version number. Since the development of GMPEs is a gradual process, many versions of the flatfile were used in this project, starting with one dated July 12 2012 and concluding with one dated March 14 2013. The changes in the flatfile over this time period were substantial, with the number of recordings increasing by almost a factor of three due to the inclusion of a large volume of small magnitude recordings from California (details in Ancheta et al., 2013).

All of the GMPEs developed in the NGA-West 2 project (including the model presented) used some version of the flatfile, but each developer team made different decisions regarding what portion of the database to use. As will be described further in this Chapter, we use variable subsets of the data for different phases of the analysis. Consistent criteria (i.e., applied in all analysis phases) were applied with respect to the following considerations:

- Availability of critical metadata: We required the presence of magnitude, distance, and site metadata in order to include the record in analysis.

- Co-located stations: We do not use more than one record when multiple records are recorded at the same site (e.g. in a differential array or different sensors at the same site).

- Single-component motions: We only use records having two horizontal-component recordings.

- Inappropriate crustal conditions: We exclude recordings from earthquakes originating in oceanic crust or in stable continental regions.

- Soil-structure interaction (SSI): We exclude records thought to not reasonably reflect free-field conditions as a result of SSI that potentially significantly affects the ground motions at the instrument. The flatfile contains site parameters referred to as the Geomatrix 1st letter, which indicate housing information for the recording stations as shown in Table 4.1. We recognize that the Geomatrix 1st letter criteria are not optimized with respect to the identification of possible SSI effects on the recorded ground motions (Stewart, 2000), but they are the only available information at present. The selected stations are marked in bold (with highlighting) in Table 4.1.

- Proprietary data: Data not publicly available are not used.

- Problems with record: Based on visual inspection by an NGA Database Working Group, we exclude records with S-triggers, second trigger (i.e., two time series from the same event due to consecutive triggers), noisy records, or records with time step problems.

- Usable frequency range: We only use a given record within its usable frequency range (described further in Section 6.2).

- An earthquake is only considered if it has at least four recordings.

- Magnitude and distance-dependent screening criteria (details below and in Figure 6.1).

The phase of model development in which the base-case model is regressed (referred to as Phase II in BEA13), applies the following additional criteria:

- Class 2 events (commonly known as aftershocks; Wooddell and Abrahamson, 2012) were excluded. We did not use Class 2 events because there is some concern that the magnitude scaling of these events differs from that of mainshocks (Class 1 events) (see Boore and Atkinson, 1989, and Atkinson, 1993), although others have found aftershock and mainshock motions for similar magnitudes to not be significantly different (Douglas and Halldórsson, 2010). After some experimentation, we used a Centroid R_{jb} distance of 10 km to differentiate between Class 1 and 2 events. Excluding Class 2 events per this criterion cut the dataset for the regression substantially.

Only recordings at a closest distance to the surface projection of the fault (R_{jb}) of 80 km and under were considered in the actual regression. This limit was found to be necessary to achieve reasonable magnitude-scaling results from the regression when a magnitude-dependent geometric spreading term is used. However, fixed apparent anelastic attenuation coefficients were used in the Phase II regressions in the hope that the resulting GMPEs would

be applicable at greater distances. The accuracy of the GMPEs at greater distances is

subsequently assessed through residual analysis.

Table 6.1. **Geomatrix 1st letter descriptions of station housing. Station types marked in bold were considered for use (some H recordings were used if they were from toe locations of small dams). Not all records having the indicated Geomatrix letters were used, as they could be excluded on the basis of lacking metadata, lacking ground-motion values, event class, etc.**

GMX 1st Letter	Description
I	Free-field instrument or instrument shelter. Instrument is located at or within several feet of the ground surface, and not adjacent to any structure.
A	One-story structure of lightweight construction. Instrument is located at the lowest level and within several feet of the ground surface.
B	Two- to four-story structure of lightweight construction, or tall one-story warehouse-type building. Instrument is located at the lowest level and within several feet of the ground surface.
A,B	Used for small generally lightweight structures for which we can not determine the number of stories from the available information. These sites generally have COSMOS site code 4 which defines a reference station described as either a 1- or 2-story, small, light building. This classification is mainly used in the small-moderate magnitude data set.
C	One- to four-story structure of lightweight construction. Instrument is located at the lowest level in a basement and below the ground surface.
D	Five or more story structure or heavy construction. Instrument is located at the lowest level and within several feet of the ground surface.
E	Five or more story structure or heavy construction. Instrument is located at the lowest level in a basement and below the ground surface.
F	Structure housing instrument is buried below the ground surface about 1-2 m, at a shallow depth. e.g. tunnel or seismic vault (e.g. U. S. Array design) but shallow embedment (use 'T' for deeper embedments or 'V' for deeply embedded vaults, both not considered "free-field")
I,F	These sites generally have COSMOS site code 3 for which the sensors have been buried/set in ground at shallow or near surface depths (e.g. the U. S. Array station design). This classification is mainly used in the small-moderate magnitude western and EUS data sets.
G	Structure of light or heavyweight construction, instrument not at lowest level.
H	Earth dam (station at toe of embankment or on abutment).
J	Concrete Dam (none in database).
K	Near a one-story structure of lightweight construction. Instrument is located outside on the ground surface, within approximately 3 m of the structure.
L	Near a two- to four-story structure of lightweight construction. Instrument is located outside on the ground surface, within approximately 6 m of the structure.
M	Near a two- to four-story structure of lightweight construction with basement. Instrument is located outside on the ground surface, within approximately 6 m of the structure.
N	Near a five- to eight-story structure. Instrument is located outside on the ground surface, within approximately 10 m of the structure.
O	Near a five- to eight-story structure with basement. Instrument is located outside on the ground surface, within approximately 10 m of the structure.
T	Associated with a deep tunnel, e.g. a) L'Aquila - Parking: Pleistocene terrace above a pedestrian tunnel on the edge'slope of the terrace, nearby structure to the station is a car park. b) Various BDSN stations (e.g. WDC, WENL, YBH).
V	Deeply embedded seismic vault
W	Structural response e.g roof, penstock, etc. (e.g. CSMIP 23732, San Bernardino - Devil's Canyon Penstock)
Z	Embedded in a borehole or missile silo
P	Castle of masonry construction, massive 1-3 stories (used for the L'Aquila earthquake sequence).
Q	Associated with a structure, size of structure is not known (used for the L'Aquila earthquake sequence).
S	Associated with a structure and in the basement, size of structure is not known (used for the L'Aquila earthquake sequence).
U	Il Moro is on an embankment between two roads and retaining walls (used for the L'Aquila earthquake sequence).

All phases of model development applied the magnitude and distance-dependent screening criteria shown in Figure 6.1. These criteria are intended to minimize potential sampling bias, which can occur at large fault distances where ground motions are generally weak; at large distances, instruments may only be triggered by stronger-than-average motions. The inclusion of such records would lead to a bias in the predicted distance decay of the ground motion − there would be a tendency for the predicted ground-motions to decay less rapidly with distance than the real data. Boore et al. (1997) (BJF) avoided this bias by excluding data for each earthquake beyond the closest distance to an operational, non-triggered station (most of the data used by BJF were obtained on triggered analog stations). Unfortunately, information is not available in the NGA-West 2 flatfile that would allow us to apply a similar distance cutoff, at least for the case of triggered analog recordings. Furthermore, a similar bias can also exist in non-triggered digital recordings because of the presence of long-period noise. The criteria in Figure 6.1, adapted from correspondence with Norm Abrahamson (2012, personal communication), provides exclusion criteria that we used to avoid this potential bias.
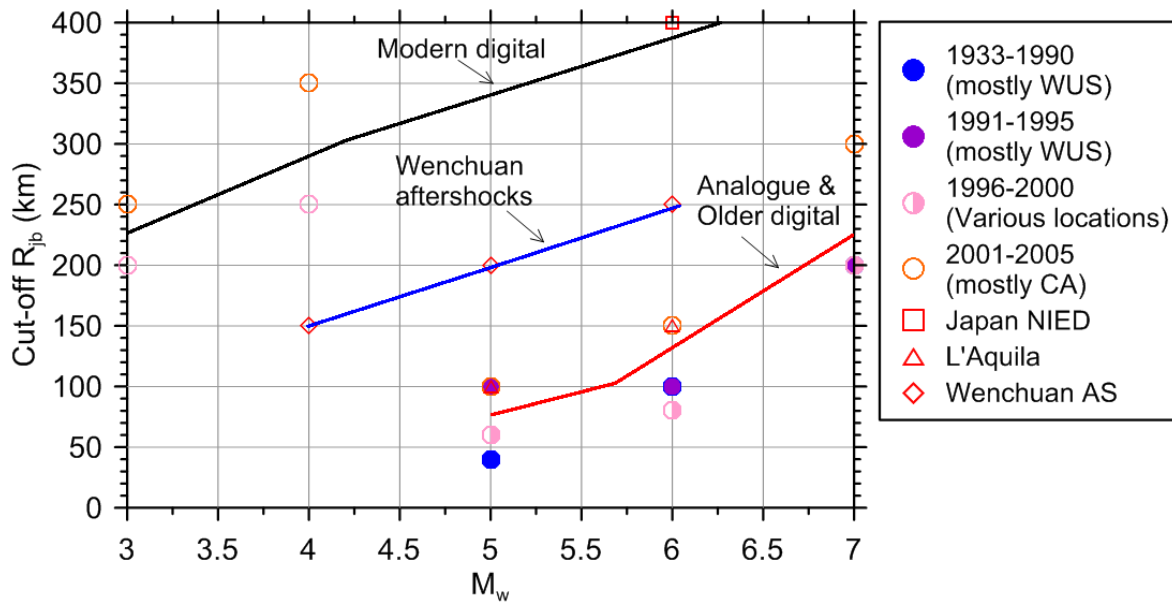
Figure 6.1. **Magnitude- and distance-dependent cutoff criteria for using records. The symbols in the figure represent judgment-based cutoffs of data reliability derived from discussions with Norm Abrahamson (2012, pers. communication).**

6.2.2 Intensity Measures Considered

The ground-motion parameters comprising the dependent variables of the GMPEs (also called ground-motion intensity measures, IMs) include peak ground acceleration (PGA), peak ground velocity (PGV) and response spectra (PSA, the 5% damped pseudo-acceleration), all for the horizontal component. Unlike BA08', we do not use response variables defined as the GMRotI50 parameter (effectively the median of all possible geometric means for various non-redundant horizontal rotation angles; Boore et al., 2006) due to confusion among some engineers regarding its definition. Rather, we use the RotD50 parameter (Boore, 2010), which is the median single-component horizontal ground motion across all non-redundant azimuths— no geometric means are used in calculating RotD50. As shown in Figure 3 of Boore (2010), RotD50 is about a factor of 1.06 larger than GMRotI50 at a period of 10 sec, with the factor

decreasing as period decreases; the standard deviation of RotD50 is about a factor of 1.05 larger than for GMRotI50 at short periods, and increasing to a factor of 1.08 at a period of 10 sec.

The GMPEs described here predict PGA, PGV, and 5%-damped PSA for periods between 0.01 s and 10 s. We do not include equations for peak ground displacement (PGD), which we believe to be too sensitive to the low-cut filters used in the data processing to be a stable measure of ground shaking. In addition there is some bias in the PGD values obtained in the NGA dataset from records for which the low-cut filtering was not performed as part of the NGA project. Appendix C of Boore and Atkinson (2007) contains a short discussion of these points. We recommend using response spectra at long periods instead of PGD.

The record processing procedures applied to all records in the flatfile include selection of record-specific corner frequencies to optimize the usable frequency range. The most important filter applied to the data is the low-cut filter, which removes low frequency noise. For each record the maximum usable period used in our analysis was taken as the inverse of the lowest usable frequency given by column EA in the NGA-West 2 flatfile. The lowest usable frequency is given by $\max(factor * f_{HP1}, factor * f_{HP2})$, where $factor$ usually equals 1.25, and f_{HP1} and f_{HP2} are the high-pass (equivalent to low-cut) corner frequencies used in the processing the two horizontal components.

6.2.3 Predictor Variables

The predictor variables (independent variables in the regression analysis) in the base model are moment magnitude M, R_{jb} distance (closest distance to the surface projection of the

fault plane), and V_{S30} (time-weighted average shear-wave velocity over the top 30 m) for site characterization. Secondary parameters for which correction factors are developed through residuals analysis include depth to top of rupture Z_{tor} and basin depth $Z_{1.0}$ (depth from the ground surface to the 1.0 km/sec shear-wave horizon).

We also considered the effect of fault type (i.e., normal, strike-slip, and reverse) and event type classified as Class 1 and 2 (CL1 and CL2). Each of these predictor variables was taken from the NGA-West 2 database. The fault type was specified by the plunge of the *P*- and *T*-axes, as shown in Table 6.2. This classification method provides the expected mechanism for the stress regime, as based on the orientation of the principal stress axes; it produces results that are similar to those based on the rake angle of the fault, but is more diagnostic for cases in which one of the two possible fault planes is shallowly dipping (Bommer et al., 2003).

Table 6.2. **Fault-type definitions (*pl* is plunge angle, from horizontal).**

P-axis	T-axis	Fault Type
$pl > 40°$	$pl \leq 40°$	Normal
$pl \leq 40°$	$pl > 40°$	Reverse
$pl \leq 40°$	$pl \leq 40°$	Strike-slip

6.2.4 Data Distribution

The distribution of data we used to develop our GMPEs is shown in Figure 6.2 by *M* and R_{jb}. For comparison, the distribution of data used in BA08 is also shown. Many more small magnitude data are used in the new GMPEs, as well as a few new large events such as the 2008

M7.9 Wenchuan, China earthquake. Note that the data used to develop the base-case GMPE is a subset of the data shown in Figure 6.2 for mainshock events and distances under 80 km. The full data set shown in the figure was used in the Phase 3 analyses described subsequently.
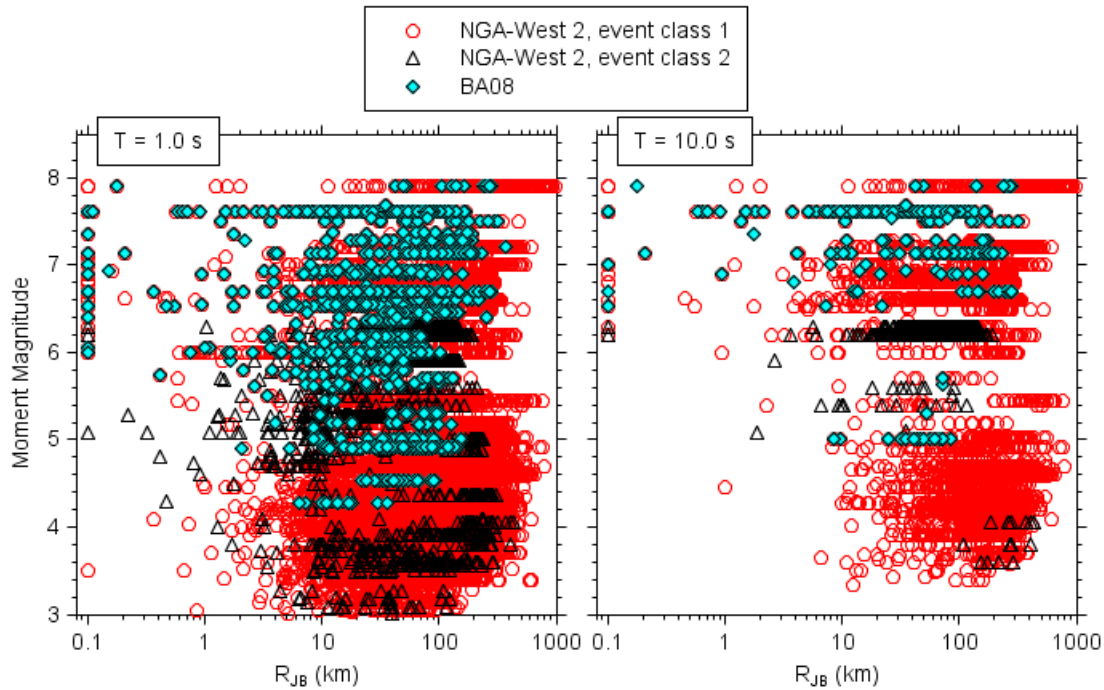
Figure 6.2.   **Distribution of data used to develop present GMPEs (BEA13) compared to that used for BA08. The distributions for PGA and periods less than T = 1.0 sec are virtually ideintical to the distribution for T = 1 sec (Adapted from BEA13).**

The data distribution separated by fault type is shown in Figure 6.3. The distribution of the data by fault type, rake angle, and dip angle is shown in Figure 6.4. The widest range of available magnitudes is for strike-slip earthquakes, while the narrowest range is for normal-slip earthquakes (see Figure 6.3). This suggests that the magnitude scaling will be better determined for strike-slip than for normal-slip earthquakes – a problem that we circumvented by using a common magnitude scaling for all types of events, as discussed later.
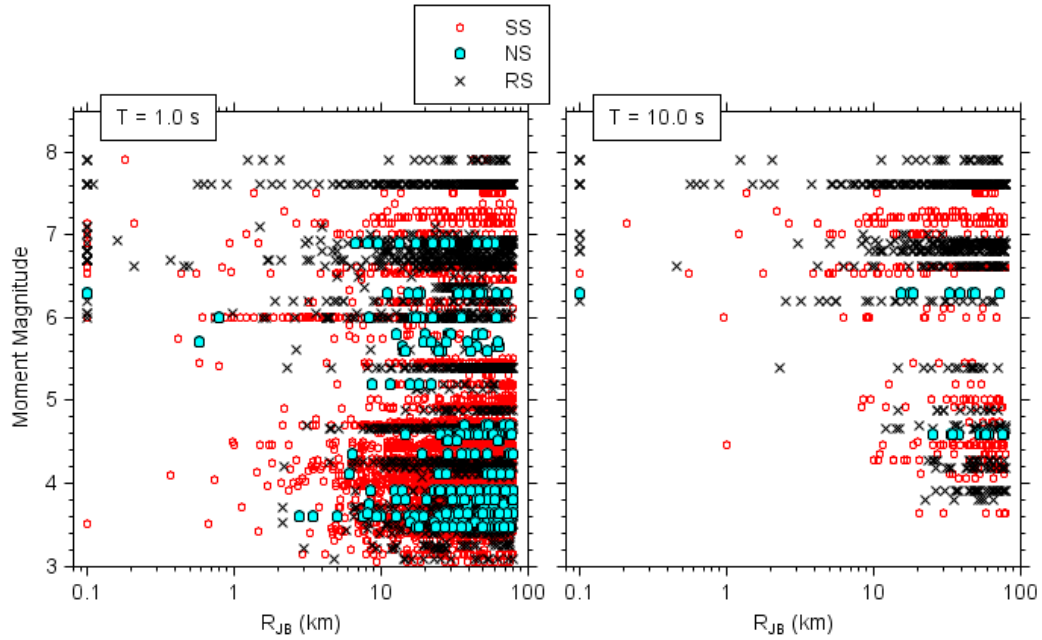
Figure 6.3 (a). Distribution of data, according to fault type, used to develop present base-case GMPEs. The data distribution shown here is that applied during the Phase II analysis. SS=strike-slip; NS=normal-slip; RS=reverse-slip (Adapted from BEA13).
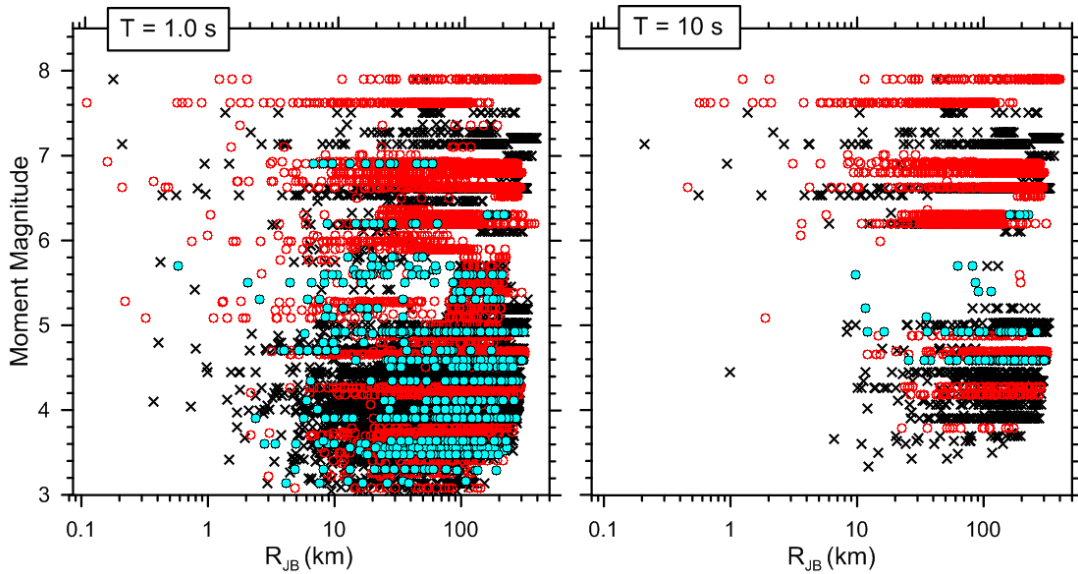
Figure 6.3 (b). Distribution of data used in residuals analysis of GMPE (Phase II). Same legend as Figure 6.3(a).

177
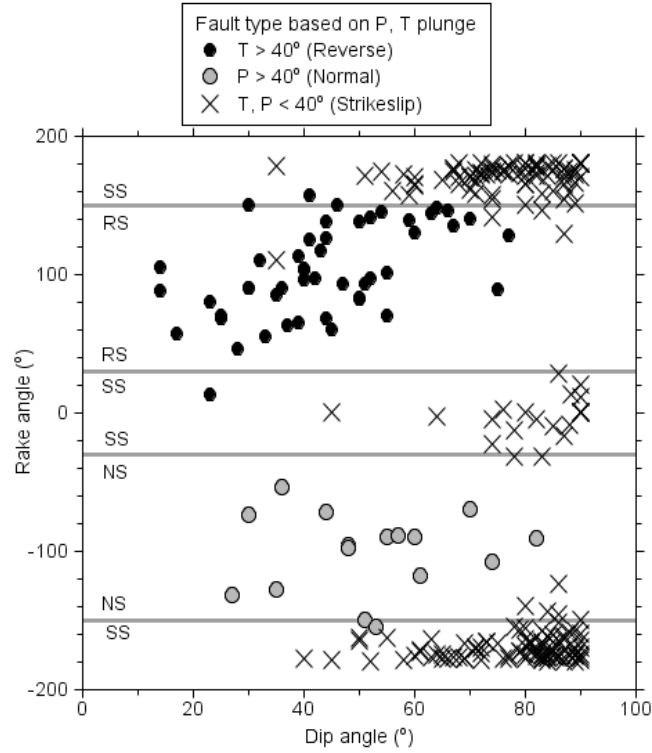
Figure 6.4. Distribution of the data we used in rake-angle and dip-angle space. The horizontal gray lines indicate boundaries between fault types used by Boore et al. (1997), and the symbols and colors indicate our classification based on the plunges of the P- and T-axes (our classification scheme is indicated in the legend; see Appendix D in BA07) (Adapted from BEA13).

The number of recordings and earthquakes used in the base-case (Phase II) regression analysis are shown in Figure 6.5. The numbers are differentiated by fault type. As in BA08, there is a rapid decrease in available data for periods longer than several seconds, but there are many more data available at the longest periods than were available in BA08. For example, there were no normal-slip (NS) records available in BA08 for T = 10 s, whereas 23 recordings were used in the analysis described here.
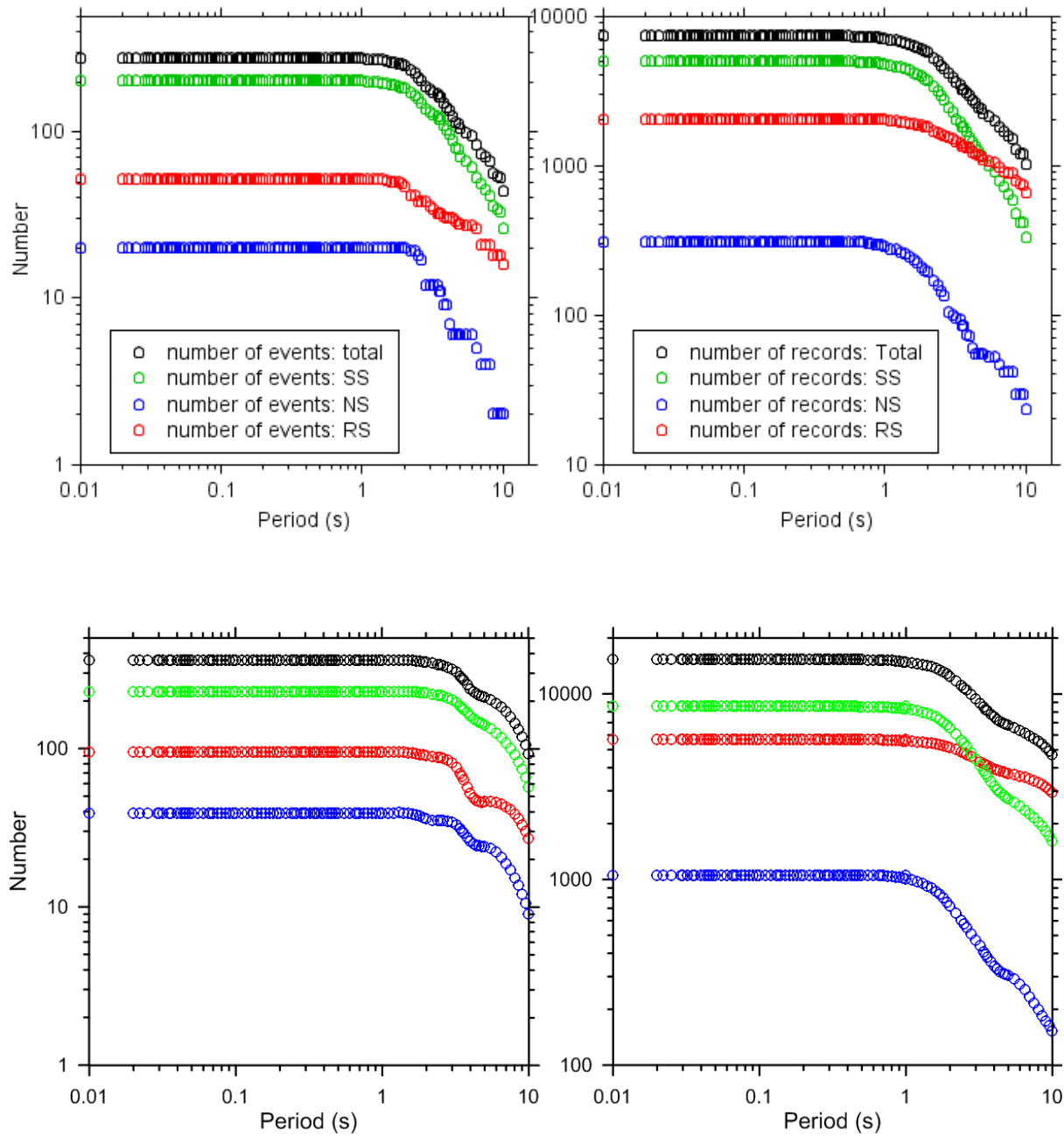
Figure 6.5. Number of events (left) and recordings (right) used to develop Phase II model (top) and Phase III residuals analysis (bottom). The numbers are differentiated by fault type. SS=strike-slip; NS=normal-slip; RS=reverse-slip (Adapted from BEA13).

The distribution by V_{s30} is given in Figure 6.6. Also shown for convenience are the NEHRP site classes, although these were not used in the analyses. There are more rock sites

179

(Class B) used for the residuals analysis (120 sites and 1022 recordings) than for the base-case

model development (58 sites and 230 recordings).
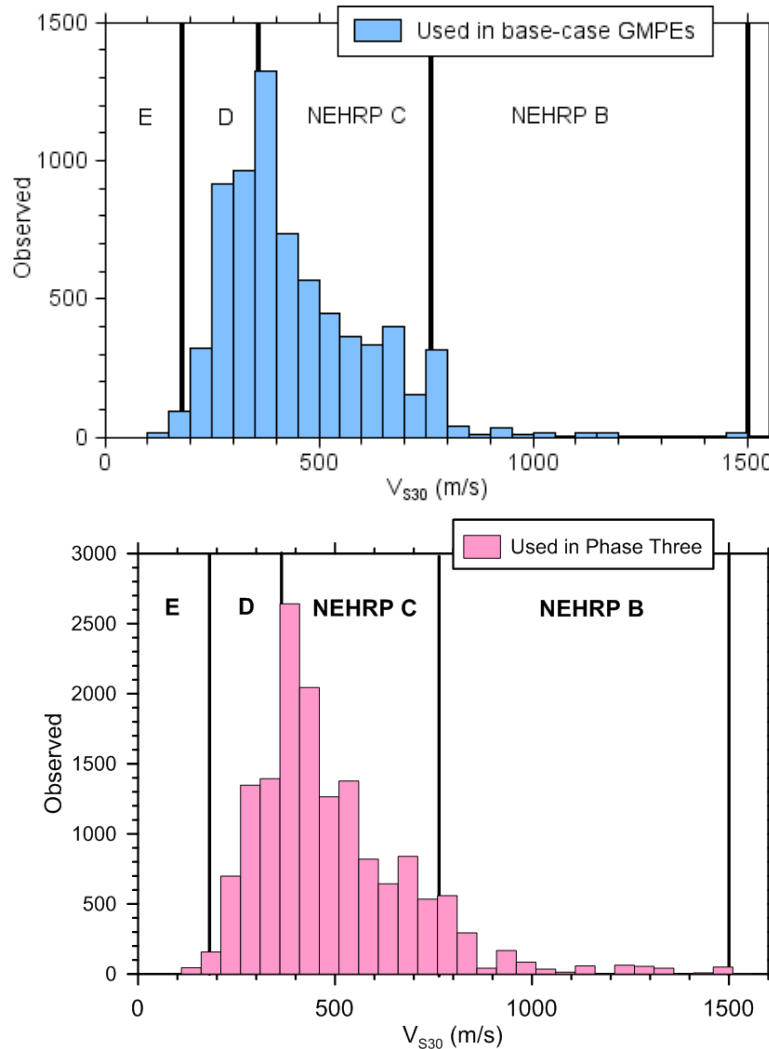
Figure 6.6. **Histogram of V_{s30} for records used in Phase II analysis (top) and Phase III residuals analysis (bottom), with NEHRP site classes indicated by the vertical lines. Only two records had a V_{s30} value (1526 m/s and 2016 m/s) corresponding to NEHRP class A, and thus the abscissa only extended slightly beyond 1500 m/s**

The distributions of the data over the predictor variable space, as shown in Figures 6.2

to 6.6, necessarily influence the GMPEs. Note in particular the lack of data at close distances for

small earthquakes. This means that the near-source ground motions for small events will not

be constrained by observations. In addition, there are many fewer small magnitude data for long periods than for short periods, which means that the small-earthquake magnitude scaling will be less well determined for long oscillator periods than for short oscillator periods.

The distribution by site class (Figure 6.6) shows that very few data were from Class A sites (hard rock). The bulk of the data are from Class B to D sites, which range from firm rock to medium stiff soil. More detail can be found in Chapter 6, which provides recommendations to use in applying our equations at the limits of the V_{s30} range.

6.3   FORMS OF THE EQUATIONS

6.3.1 Source and Path Terms

We followed the philosophy of BJF97 and BA08 in seeking simple functional forms for our GMPEs, with the minimum required number of predictor variables. We call these the "base-case GMPEs". The selection of functional form was heavily guided by subjective inspection of nonparametric plots of data; many such plots were produced and studied before commencing the regression analysis. Figure 6.7 provides an example, in which the data (for strike-slip, CL1 events) are overlain to gain a sense of the general behavior. Close inspection of data-amplitude plots (such as Figure 6.7, and others not shown here) revealed several key features that the functional form must accommodate: magnitude-dependent geometric spreading; an apparent anelastic attenuation term to account for curvature in the decay of log ground motions versus log distance for distances beyond about 80 km; and strongly nonlinear (and period dependent) magnitude dependence of amplitude scaling at a fixed distance, with a tendency toward saturation (no magnitude dependence) with increasing magnitude for short periods and close

distances. (Note: We add the modifier "apparent" to "anelastic attenuation" because the

decay captured by this term represents an average over the propagation path of a number of

processes; it includes scattering and other effects in addition to anelasticity.)
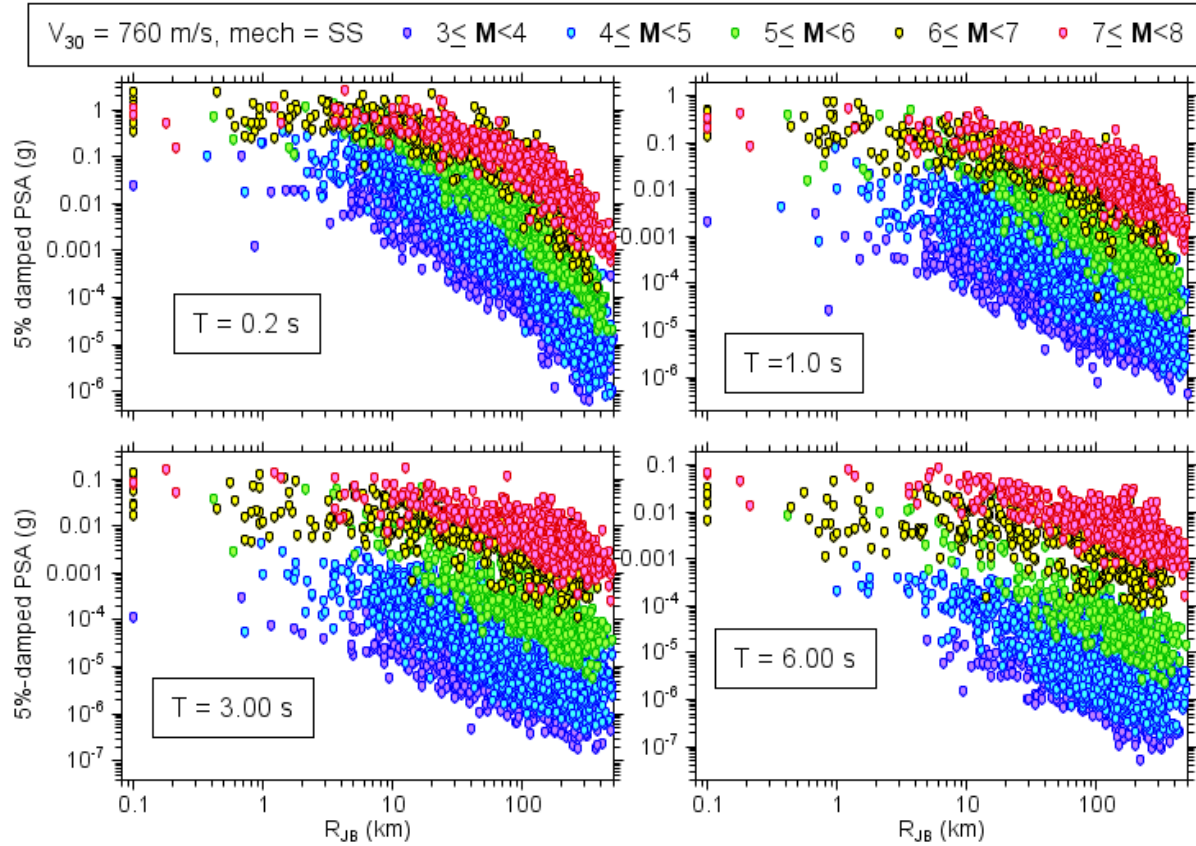
Figure 6.7.   **PSA at four periods for strike-slip earthquakes. All amplitudes corrected to V_{s30} = 760 m/s using the soil correction factors of this study (Adapted from BEA13).**

The functional forms of the equations used for the base-case GMPEs are the same as

those used by BA08, except for the site response equations, which are discussed in Section 6.2.

We investigate the statistical and practical utility of including adjustment factors involving

additional predictor variables in an analysis of residuals from the base-case GMPEs in Section

6.4.

Our base-case equation for predicting ground motions is:

$$\ln Y = F_E\left(\mathbf{M}, mech\right) + F_{P,B}\left(R_{jb}, \mathbf{M}\right) + F_{S,B}\left(V_{s30}, R_{jb}, \mathbf{M}\right) + \varepsilon_n \sigma\left(\mathbf{M}, R_{jb}, V_{s30}\right) \tag{6.1}$$

where ln$Y$ represents the natural logarithm of a ground-motion intensity measure (PGA, PGV, or PSA); F_E, $F_{P,B}$, and $F_{S,B}$ represent the source-dependent function ("E" for "event"), path function ("P"), and site amplification function ("S"), respectively (subscript 'B' indicates base-case model; not used for event function since the same equations are used for the base-case and adjusted models). The predictor variables are M, $mech$, R_{JB}, and V_{s30}, which represent moment magnitude, fault type, Joyner-Boore distance (defined as the closest distance to the surface projection of the fault), and time-weighted average shear-wave velocity over the top 30 m of the site, respectively; ε_n is the fractional number of standard deviations of a single predicted value of ln$Y$ away from the mean value of ln$Y$ (e.g., $\varepsilon_n = -1.5$ would be 1.5 standard deviations smaller than the mean value); and σ is the total standard deviation of the model. The F_E, $F_{P,B}$, $F_{S,B}$, and σ functions are period dependent.

The total standard deviation σ is partitioned into components that represent between-event variability (τ) and within-event variability (ϕ) as follows:

$$\sigma\left(\mathbf{M}, R_{jb}, V_{s30}\right) = \sqrt{\phi^2\left(\mathbf{M}, R_{jb}, V_{s30}\right) + \tau^2\left(\mathbf{M}\right)} \tag{6.2}$$

The dependence of τ and ϕ terms on the predictor variables of M, R_{jb}, and V_{s30} is presented in Section 6.4.4.

The base-case model in Eqn. (6.1) can be supplemented with the optional predictor variables accounting for regional apparent anelastic attenuation and basin depth z_1. The regional attenuation terms appear in the path function (Section 6.1.2). Parameter z_1 enters into the site amplification terms as described in Section 6.2.

6.3.1.1 Path and Source Functions

The base-case path-dependent function is given by:

$$F_{P,B}\left(R_{jb}, \mathbf{M}\right) = \left[c_1 + c_2\left(\mathbf{M} - \mathbf{M}_{ref}\right)\right]\ln\left(R / R_{ref}\right) + c_3\left(R - R_{ref}\right) \tag{6.3}$$

where

$$R = \sqrt{R_{jb}^2 + h^2} \tag{6.4}$$

and c_1, c_2, c_3, M_{ref}, R_{ref}, and h are the coefficients determined by regression.

The event-specific function is given by:

$$F_E\left(\mathbf{M}, mech\right) = \begin{cases} e_0 U + e_1 SS + e_2 NS + e_3 RS + e_4\left(\mathbf{M} - \mathbf{M}_h\right) + e_5\left(\mathbf{M} - \mathbf{M}_h\right)^2 & \mathbf{M} \leq \mathbf{M}_h \\ e_0 U + e_1 SS + e_2 NS + e_3 RS + e_6\left(\mathbf{M} - \mathbf{M}_h\right) & \mathbf{M} > \mathbf{M}_h \end{cases} \tag{6.5}$$

where U, SS, NS, and RS are dummy variables (taking on values of 1 or 0, as indicated in Table 6.1) used to specify unspecified, strike-slip, normal-slip, and reverse-slip fault types, respectively; and M_h, the "hinge magnitude" for the shape of the magnitude scaling, is a coefficient to be set during the analysis. Unlike in BA08, M_h is period-dependent, as discussed below. The determination of the coefficients in the distance and magnitude functions is discussed in following sections.

Table 6.1.   **Values of dummy variables for different fault types.**

Fault Type	U	SS	NS	RS
Unspecified	1	0	0	0
Strike-slip	0	1	0	0
Normal-slip	0	0	1	0
Reverse-slip	0	0	0	1

Adjustments to the base-case model for the effects of regional apparent aneleastic attenuation and basin depth are made on the basis of residuals analysis described in Section 4.4. With these adjustments, the main equation for the GMPE becomes:

$$\ln Y = F_E\left(\mathbf{M}, mech\right) + F_P\left(R_{jb}, \mathbf{M}, region\right) + F_S\left(V_{s30}, R_{jb}, \mathbf{M}, z_1\right) + \varepsilon_n\sigma\left(\mathbf{M}, R_{jb}, V_{s30}\right)$$

(6.6)

Note that the F_E term is unchanged, because residuals analysis did not support the addition of terms related to Class 2 events or source depth. We discuss the details of the path-specific adjustments in the next subsection; the site function is discussed in Section 6.2.

6.3.1.2 Adjusments to Path Functions

The adjusted path-dependent function is given in Eqn. (6.7), in which case Δc_3 can be region-dependent.

$$F_P\left(R_{jb}, \mathbf{M}, region\right) = F_{P,B}\left(R_{jb}, \mathbf{M}\right) + \Delta c_3\left(R - R_{ref}\right)$$

(6.7)

The tables of coefficients for our GMPEs include c_3 and Δc_3, with a different column of Δc_3 coefficients for each region.

6.3.2 Site Terms

The nonlinear site amplification model is as described in Section 5.2.1. The nonlinear site amplification component of the base-case GMPE (introduced in Eqn. 6.1) is comprised of two additive terms representing V_{S30}-scaling and nonlinearity as follows:

$$F_{S,B} = \ln\left(F_{lin}\right) + \ln\left(F_{nl}\right) \tag{6.8}$$

where $F_{S,B}$ represents site amplification in natural logarithmic units; F_{lin} represents the linear component of site amplification, which is dependent on V_{S30}; and F_{nl} represents the nonlinear component of site amplification, which depends on V_{s30} and the amplitude of shaking on reference rock (taken as V_{s30} = 760 m/s).

The linear component of the model (F_{lin}) which describes the scaling of ground motion with V_{s30} for linear soil response conditions (i.e., small strains) was presented in Section 5.2.1 in Eqn. 5.2. Parameters c and V_c in $ln(F_{lin})$ are period-dependent and are determined by regression as described in Section 6.2. Parameter c may be region-dependent, especially at long periods, but as discussed later, we do not allow c to be regionally dependent.

The nonlinear term in the site amplification model (F_{nl}) is desribed in Section 5.2.1 in Eqn. 5.3. It modifies the linear site amplification so as to decrease amplification for strong shaking levels. The F_{nl} term is constructed so as to produce no change relative to the linear term for low PGA_r levels.

In order to apply the site amplification function, we must first evaluate PGA_r for applicable magnitude and distance using Eqn. (6.1) for rock site conditions. Peak acceleration is

186

used to represent the intensity of rock shaking in lieu of PSA at the period of interest. We are aware of the convenience of using PSA, but we retain the use of PGA for physical reasons. In particular, PGA is directly related to soil shear stress, which in turn is related to shear strain in an equivalent-linear sense.

The adjusted site amplification model used with Eqn (6.6) is formulated as:

$$F_S\left(V_{s30}, \mathbf{M}, R_{jb}, z_1\right) = F_{S,B}\left(V_{s30}, \mathbf{M}, R_{jb}\right) + F_{\delta Z_1}\left(\delta z_1\right)$$

(6.9)

where $F_{\delta Z_1}$ is an adjustment to the base model to consider the effects of basin depth on ground-motion amplitude. This adjustment is based on residuals analysis described in Section 6.4. It is cast as follows:

$$F_{\delta Z1}\left(\delta z_1\right) = \begin{cases} 0 & T < 0.65 \\ f_6 \delta z_1 & T \geq 0.65 \,\&\, \delta z_1 \leq f_7/f_6 \\ f_7 & T \geq 0.65 \,\&\, \delta z_1 > f_7/f_6 \end{cases}$$

(6.10)

where f_6 and f_7 are estimated as described in Section 6.4, and the ratio f_7/f_6 is in units of km. The parameter δz_1 is the difference between basin depth z_1 and the prediction of an empirical model relating z_1 to V_{S30} (given in Eqn. 6.17; Eqn. 6.17a for California, 6.17b for Japan). The adjustment factor $F_{\delta Z_1}$ is an optional feature of the model. For many applications z_1 may be unknown; in such cases we recommend using the default value of $\delta z_1 = 0.0$, which turns off this adjustment factor (i.e., $F_{\delta Z_1} = 0$). We believe this to be a reasonable default condition, because the remaining elements of the model are 'centered' on a condition of no $F_{\delta Z_1}$ correction, as shown in Section 6.4.

6.4   THREE-PHASE MODEL BUILDING PROCESS

In this Chapter, we describe the procedures used to build the GMPE. Model building occurred in three phases, which are described in detail in the following sections.

In Phase I, we analyze subsets of data and simulation results to evaluate elements of the base-case model that would not be well-constrained if left as free parameters in the regression. Model elements evaluated in this way are c_3 (for apparent anelastic attenation) and F_S (for site response). Phase II comprises the main regression for the base-case model shown in Eqn. (6.1). Phase III consists of mixed-effects regression analysis to check model performance and to develop develop adjustment factors for various secondary factors beyond M, *mech*, R_{jb}, and V_{s30}. The standard deviation model is also developed from Phase III analysis.

6.5   PHASE I: SETTING OF FIXED PARAMETERS

There are several parameters that we "pre-set" before beginning the regression in order to ensure its stability and force behavior that we wish to constrain. In this section, we describe the parameters that are pre-set within the Phase I regression.

6.5.1 Apparent Anelastic Attenuation

Due to trade-offs between apparent geometric and apparent anelastic attenuation, regression cannot simultaneously determine both robustly; this arises because we cannot distinguish between the slope and the curvature of the distance decay from data with significant scatter. In this section, we describe regressions undertaken to constrain the apparent anelastic attenuation term, c_3, as part of Phase I model building.

In BA08, c_3 was constrained using four well-recorded small events (**M**4.3–6.0) in California. Much of the data used in that analysis was not contained in the NGA-West 1 flatfile. For the present analysis, we used the large inventory of data from small events (M ≤ 5.0) in California that are now available as part of the NGA-West 2 flatfile (this was a larger subset of data than used to derive the Phase II base-case GMPEs). Low magnitude earthquakes were chosen to minimize possible complexities in the data associated with possible finite fault effects and nonlinear site effects. Using the model described in Section 6.2.2, we apply a site adjustment to correct each observation to a reference V_{S30} of 760 m/s. The data were then grouped into magnitude bins 0.5 in width (magnitude units), as shown in Figure 6.8, and regressed using an equation similar to Eqn. (6.3) but without the *M*-dependent geometric spreading term:

$$\ln Y_{ij} = \eta_i' + c_1' \ln \left(R/R_{ref} \right) + c_3 \left(R - R_{ref} \right) \tag{6.11}$$

where η_i' is the event term for event *i*, *j* indicates a particular observation (and is implicitly contained in the distance *R*), $R_{ref} = 1.0 \text{ km}$ and c_1' and c_3 are parameters fixed by the regression. The c_1' term represents the apparent geometric spreading for the magnitude bin; it would be expected to change with magnitude. The prime (') is used on the event term and apparent geometric spreading term to indicate these are associated with the present analyses of binned data and are distinct from the Phase II regressions.
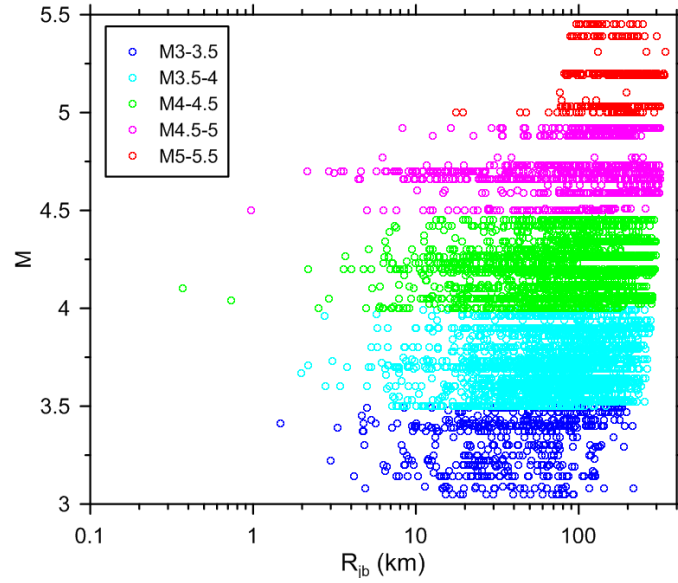
Figure 6.8. **Binned groups of California data in NGA West 2 flatfile used for constraint of apparent anelastic attenuation term. The data for the M5-5.5 bin was not used due to poor sampling for R_{jb} < 80 km.**

Examples of the distance dependence for several ground-motion intensity measures for the **M**4–4.5 bin are given in Figure 6.9. Note that the data at high frequencies (e.g., PGA) exhibit substantial curvature (indicating negative c_3) whereas the data for medium to long periods (e.g., PSA at 1.0 sec) exhibit negligible curvature. The resulting values of c_1' and c_3 are plotted for the various M bins in Figure 6.10. As expected, the c_1' terms are all negative, indicating attenuation with distance, with the absolute value decreasing (less decay) as magnitude increases. Conversely, the c_3 terms are relatively independent of M, which is expected if they represent processes other than geometric spreading, such as apparent anelastic attenuation. The selected coefficients for c_3 are also shown in Figure 6.10. The applicability of these coefficients, which are based on California data, for other regions is examined in Section 6.4.

Figure 6.11 compares the selected coefficients with those used in BA08. The c_3 terms are roughly similar between the two models, but the BSSA c_3 values are based on many more data.
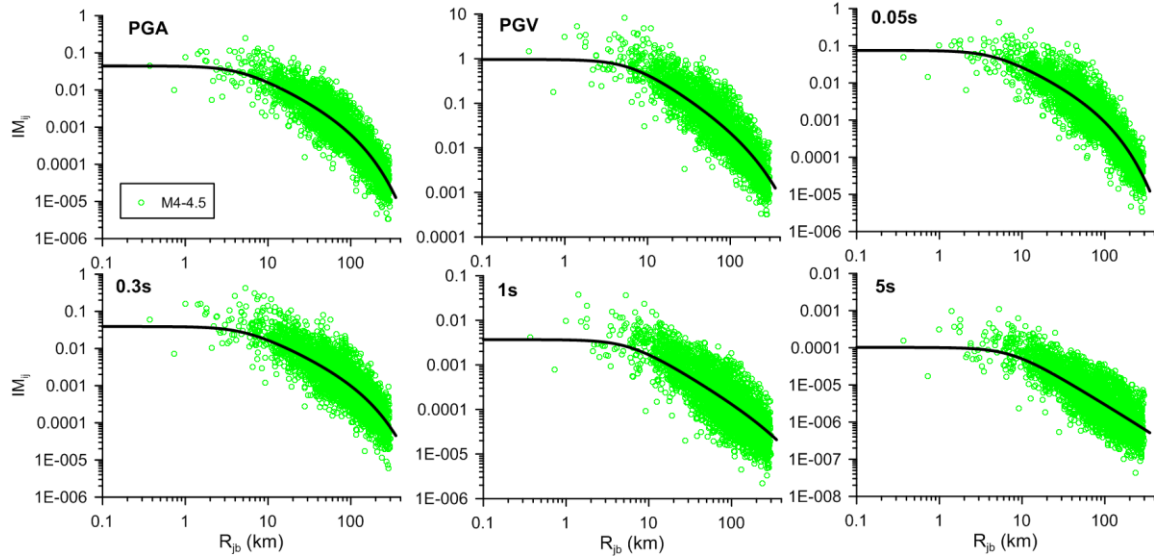
Figure 6.9. California data and fit curve (Eqn. 6.1) for M4-4.5 events. Data corrected to V_{s30}=760 m/s. Results show strong effects of apparent anelastic attenuation at high frequencies and negligible effects for T ≥ 1 sec.
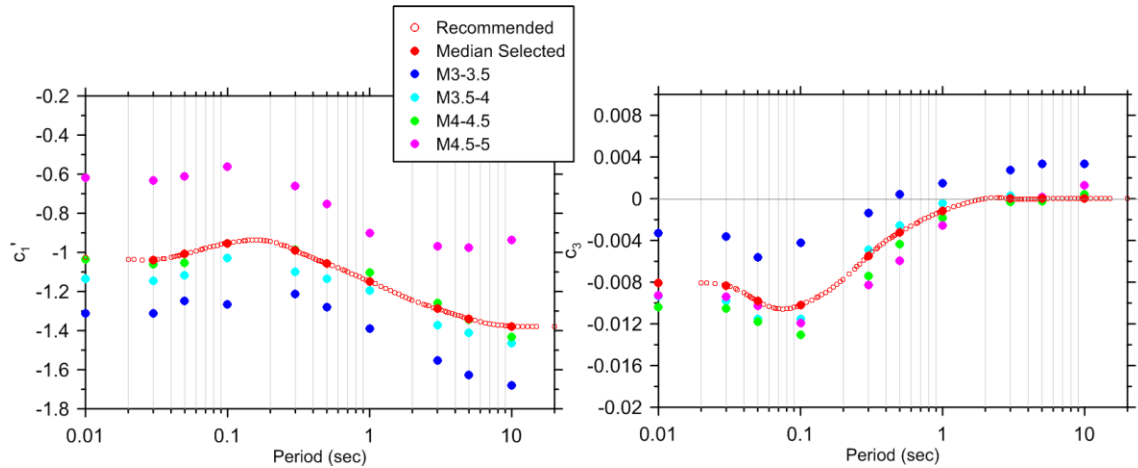
Figure 6.10. Trends of apparent geometric spreading (c_1') and apparent anelastic attenuation (c_3) terms with period and magnitude. Results show significant M-dependence for c_1' but not for c_3.

191
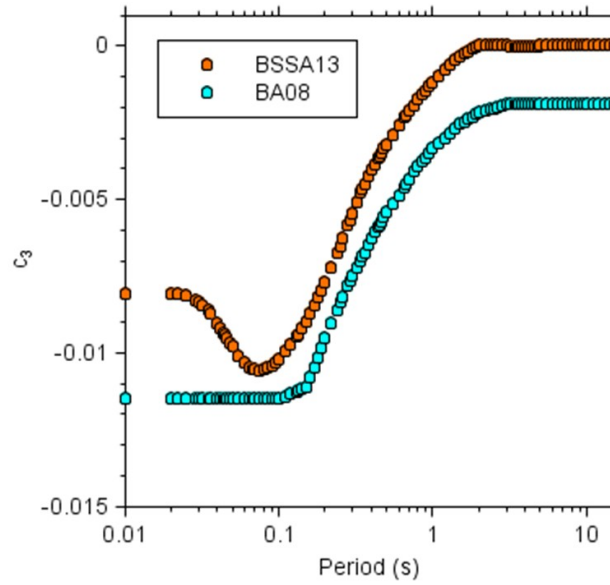
Figure 6.11. Apparent anelastic attenuation terms (c_3) used in present model (BEA13) and in BA08 (Adapted from BEA13).

6.5.2 Site Response

The model equations are as given in Section 6.2 with the $\ln(F_{lin})$ term representing V_{S30}-scaling and the $\ln(F_{nl})$ term representing nonlinear site response. We first constrain the nonlinear portion of the site response, to enable robust determination of the linear part of the model. The nonlinear site response model is described in greater details in Chapter 5. In this section, I briefly present the process by which the site factors were developed.

Model development occurs in two stages, the first to develop the nonlinear model and the second to develop the V_{S30}-scaling model. (Note: both of these two "stages" are substeps within the Phase I GMPE model building framework).

Stage 1 Analysis of Site Response: The Stage 1 analyses develop estimates of parameter f_2 (see Eqn. 5.4) on the basis of available simulations and from the interpretation of NGA-West 2 data. The considered simulations are of one-dimensional ground response for many site profiles and input motions (Kamai et al., 2013; hereafter KEA13). Our synthesis of the results from KEA13, and the manner by which f_2 values were extracted, is described in Section 5.2.4 and is not repeated here.

The NGA-West 2 data analysis begins with the computation of rock residuals for each recording in the selected data set:

$$R_{ij} = \ln Y_{ij} - \left[\left(\mu_r \right)_{ij} + \eta_i \right] \tag{6.12}$$

where R_{ij} is the rock residual, Y_{ij} is the jth observed (recorded) value of the ground-motion IM, μ_r is the mean (in natural log units) of a GMPE for rock conditions, and η_i is the event term for earthquake *i*. The rock site condition used in the computations is $V_{s30} = 760 \,\text{m/s}$. Regarding the GMPE used to compute μ_r, our analyses were performed iteratively with respect to the development of the Phase II GMPE. Essentially, we began with an early (Nov. 2012) version of the Phase II GMPE, from which site terms were regressed. Those site terms were then used in a subsequent Phase II GMPE derivation, and so on. The final set of site terms are consistent with the base-case GMPE and include adjustments for regional apparent anelastic attenuation in high-Q and low-Q regions described in Section 6.6. In these analyses, we consider a much broader set of distances per the data selection criteria shown in Figure 6.1.

To investigate nonlinearity, we compile values of R_{ij} within bins of V_{S30} (≤ 200, 200–310, 310–520, 520–760, > 760 m/s), which are plotted against PGA_r (median peak acceleration on rock) in Figure 6.12. We use least-squares regression to fit to the data an expression of the form given in Eqn. (5.3) with f_3 fixed at 0.1g (justification for this is given in Section 5.2.4) to provide estimates of f_1 and f_2. The results illustrate similar trends between the simulations and the data.

Figure 6.13 shows values of the nonlinear parameter f_2 from data analysis and simulations. Also shown are slopes evaluated by Afacan et al. (2013) - hereafter AEA13 - (using a fitting procedure similar to that described above), based on centrifuge modeling of soft clays. The simulation-based slopes are slightly steeper than the data-based slopes at short periods (*T* < 0.5 sec) but flatter (and even positive) for longer periods (*T* > 1.0 sec). The slopes derived from centrifuge modeling (at 100-120 m/s) are similar to those at the lower limit of V_{s30} ($V_{s30} = 150 - 200 m/s$) from simulations and data analysis for *T* ≤ 1.0 sec. This suggests that a minimum floor on nonlinearity may be present for very soft sites, although such a feature is not presently included in our model, which we consider applicable for $V_{s30} > 150 m/s$.
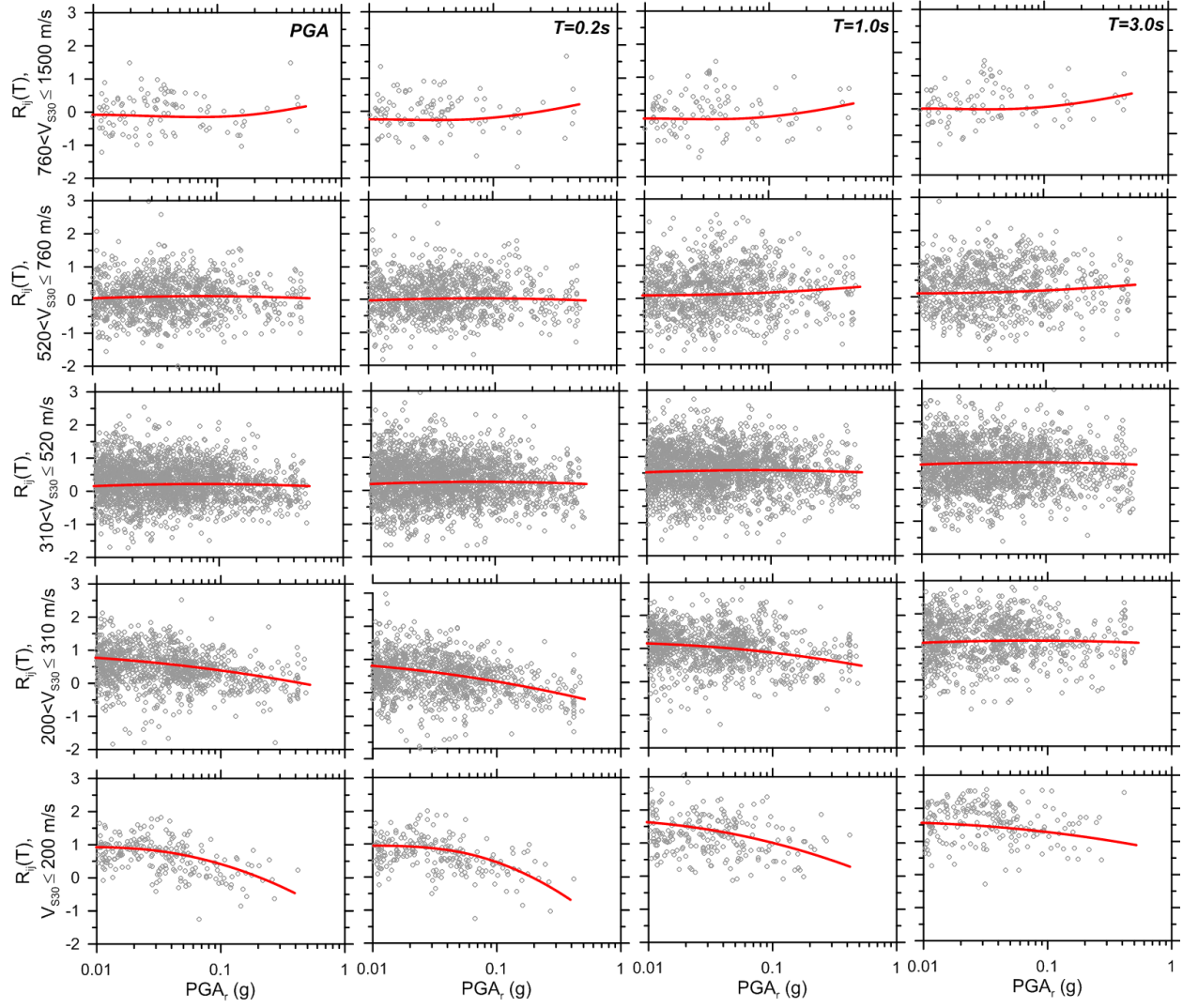
Figure 6.12. Variation of site amplification factors with PGA$_r$ within V_{S30} bins using full data set. Discrete symbols are intra-event residuals (R$_{ij}$, Eqn. 6.12), line is nonlinear fit from Eqn. 5.3.

195
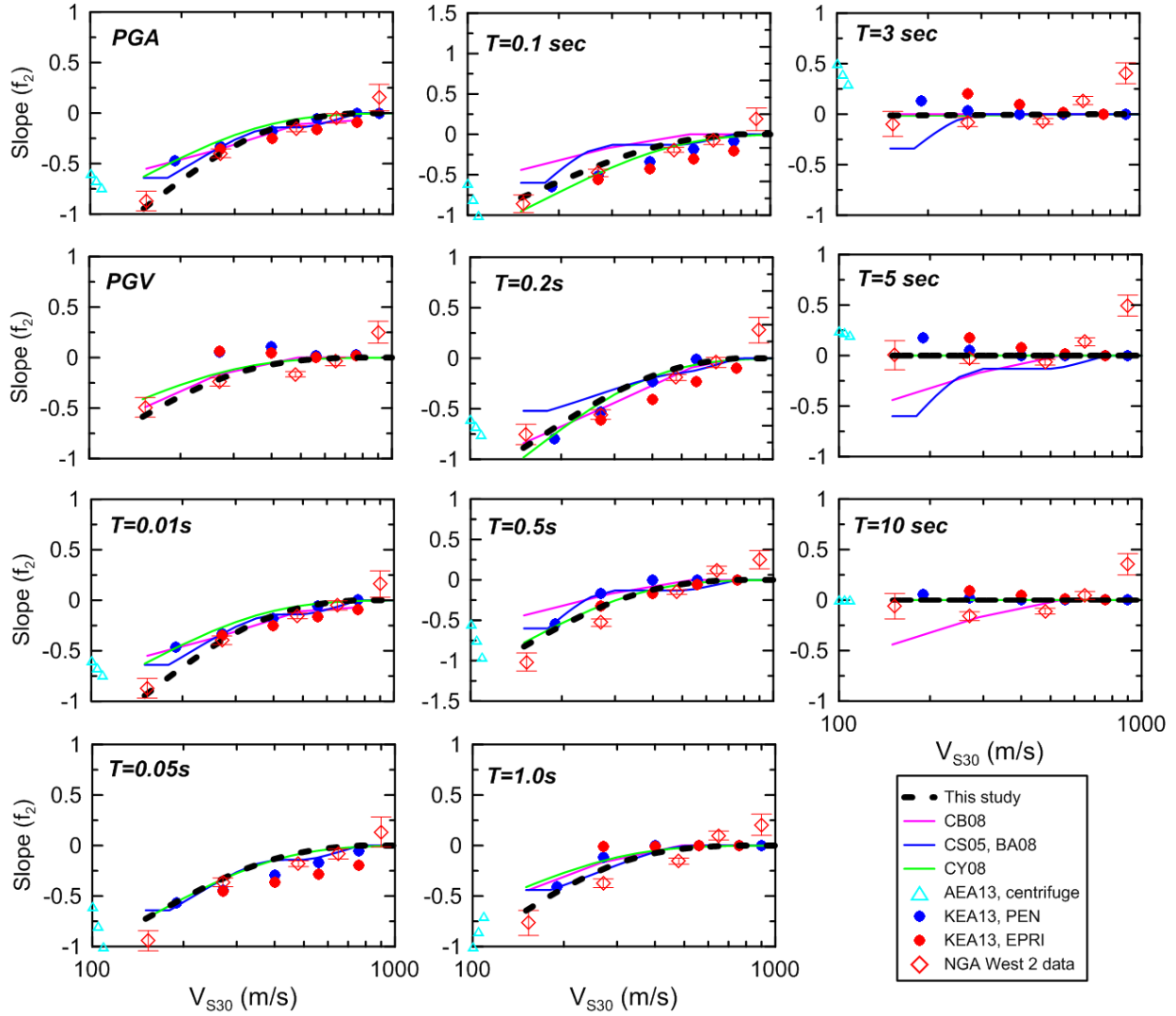
Figure 6.13. Variation of slope f₂ with V_S30 from NGA West 2 data, centrifuge test data of AEA13, KEA13 simulation results (using modulus reduction curves labeled PEN for Peninsular range and EPRI), and site models in CB08 and CY08 GMPEs. The proposed model for this study is also given.

The nonlinear term f_2 is parameterized relative to V_{S30} following the functional form of Chiou and Youngs (2008) as given in Eqn. (5.4). Parameter f_4 controls the overall level of nonlinearity for soft soils. Parameter f_5 controls the shape of the V_{s30} dependency of the slope

196

f_2. These parameters are plotted against period in Figure 6.14, along with the corresponding values used in CY08 (for comparison).
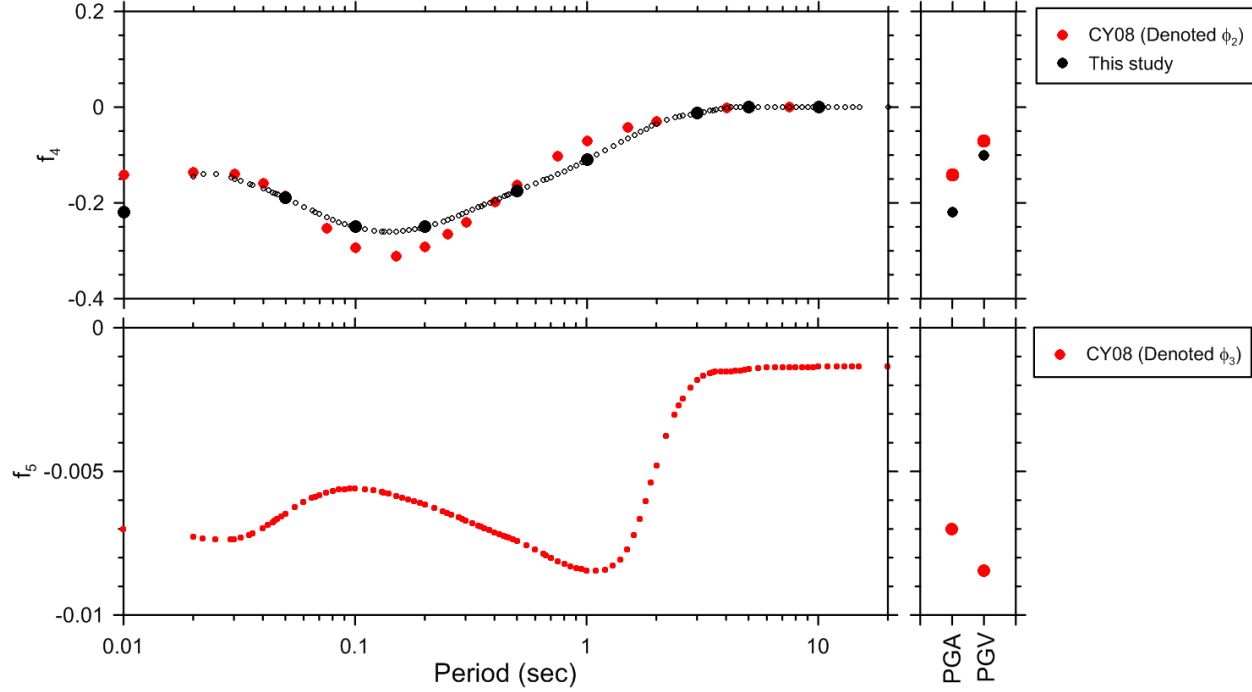
Figure 6.14. Parameters f₄ and f₅ for nonlinear site amplification model as proposed by Chiou and Youngs (2008) (CY08) and revised for present study. Parameter f₄ and f₅ as used here were denoted ϕ₂ and ϕ₃ by CY08. We adopted CY08 values of f₅.

Stage 2 Analysis of Site Response: We begin with residuals R_{ij} (Eqn 6.12), which are adjusted by removing nonlinear effects as predicted by the F_{nl} model (Eqn 5.3):

$$R_k^{lin} = R_{i,j} - \ln(F_{nl}) \qquad (6.13)$$

The modified residual, R_k^{lin}, is intended to apply for linear (small strain) conditions. Subscript k in R_k^{lin} is an index spanning across all available data points; we drop the event and within-event subscripts (*i* and *j*, respectively) because of the removal of event terms in the

197

computation of R_{ij}, which allows all data points to be weighted equally. The residuals for the full (combined) data set and individual regions are then regressed in a least-squares sense against V_{s30} (using Eqn. 5.2) to establish the c parameter for $V_{s30} < V_c$. Results for several periods and regions are plotted in Figure 6.15. Slopes are generally negative, which is expected, as this indicates stronger ground motion for softer soils. Slopes also tend to increase with period over the range considered, which is also consistent with past experience (e.g., BJF97 and the 2008 NGA models).
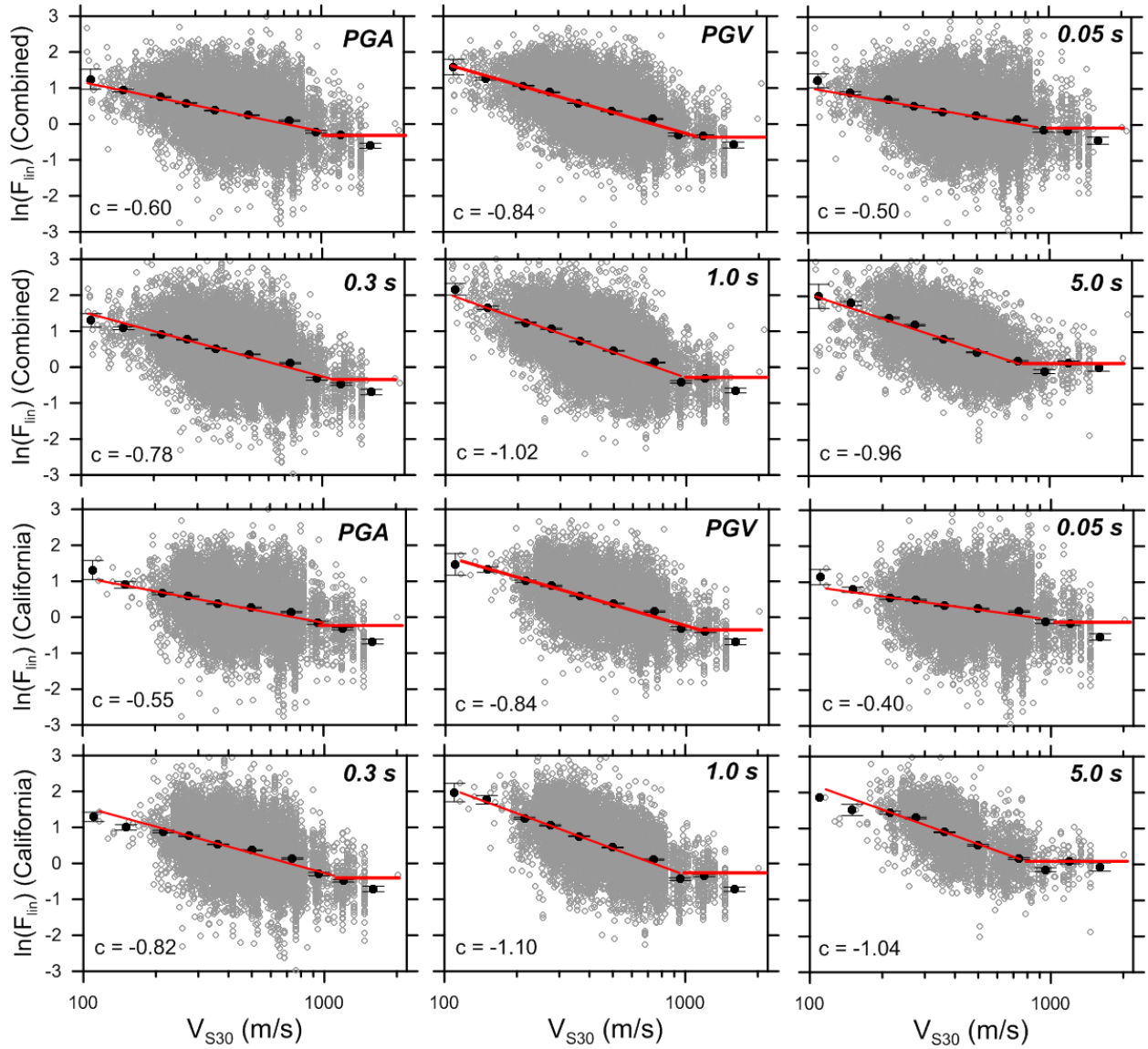
Figure 6.15(a). Variation of linearized site amplification (Eqn. 6.13) with V_{S30} for combined data set and subset from California. Red line indicates model prediction, black dots are binned means and their 95% confidence intervals.
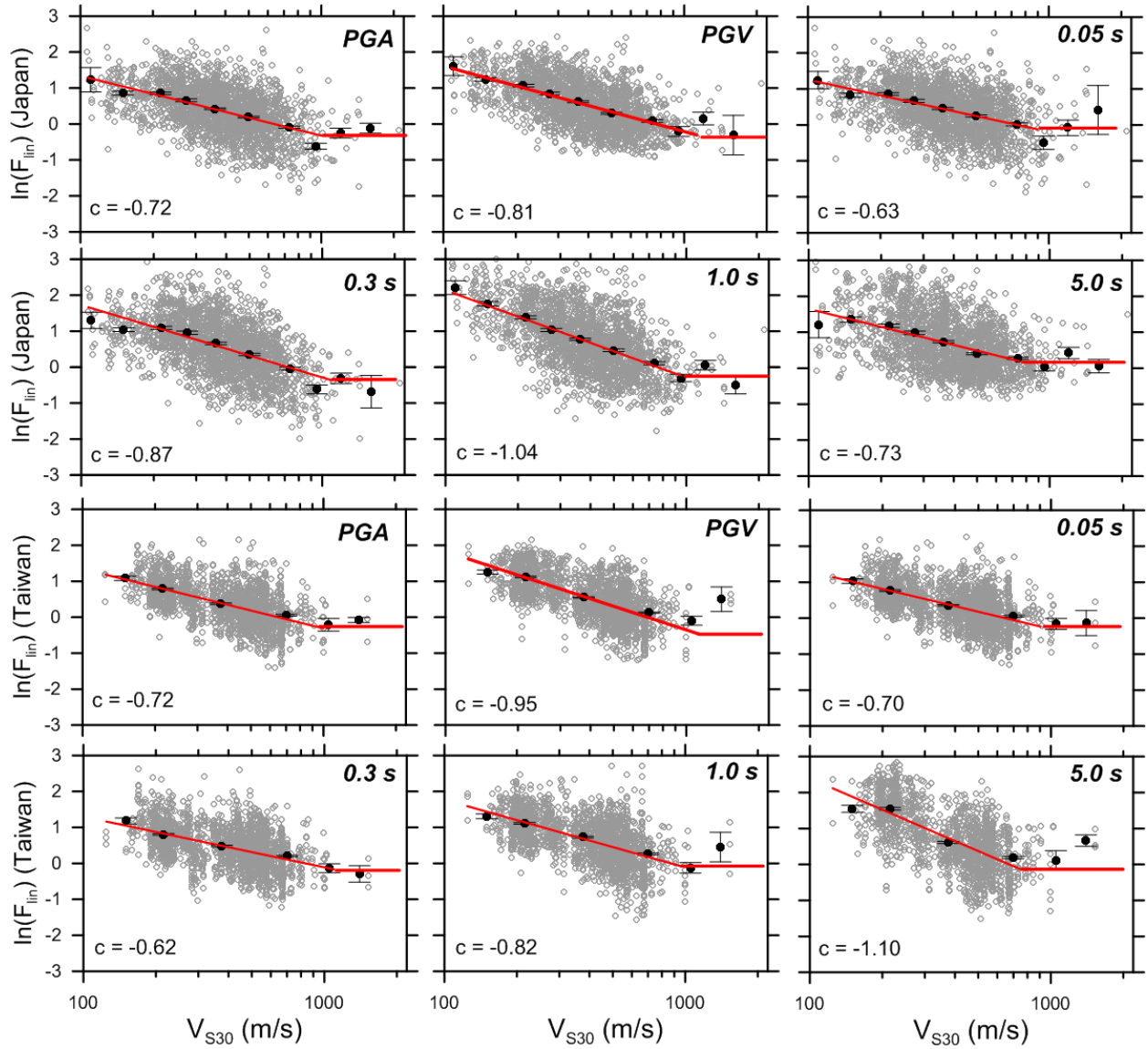
Figure 6.15(b). Variation of linearized site amplification (Eqn. 6.13) with V$_{S30}$ for subset of data from Japan and Taiwan.

Note that the results from California in Figure 6.15(a) indicate a break in the V_{s30} scaling for fast velocities and longer periods (as seen in the results for T = 1.0 sec). It is this break in slope that motivated the use of the corner velocity V_c in the linear portion of the site amplification function (Eqn. 5.2).

I plot in Figure 6.16 the slope parameter *c* for V_{s30} -scaling as a function of spectral period for the combined data set and various regions (California, Japan, Taiwan, and other). Additional regions are considered in Chapter 5. Since the regression for *c* is least squares, all data points are weighted equally. Accordingly, the 'Combined' result is influenced strongly by regions with large amounts of data relative to those with fewer data (weights are listed in Figure 6.16). We find relatively consistent values of *c* for all regions, especially at short periods. As shown in Section 5.2.5, strong regional variations in *c* could be found if the data were interpreted differently. In particular, if a data cut-off distance of 80 km is applied (i.e., to avoid the use of recordings having potentially significant effects of anelastic attenuation), *c* values vary strong between regions. Similar sensitivites of the V_{s30} slope parameter have been observed previously by Chiou and Youngs (2012).
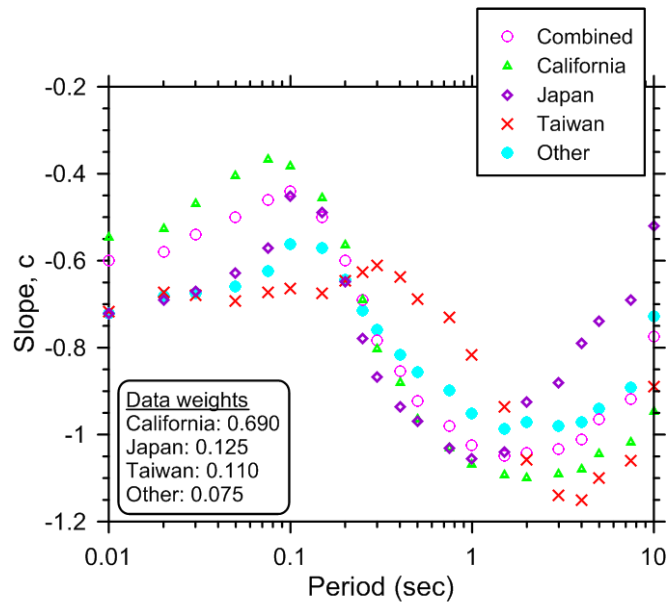
Figure 6.16. Variation of slope (c) within spectral periods for combined data set and various regions. Data weights refer to the relative contributions to the 'Combined' slope.

201

At this stage, we are not recommending a regional c term for V_{s30}-scaling. However, we recognize that: (*i*) the variability of c terms is relatively high, especially at longer periods; and (*ii*) the lack of a dependence of c on region is difficult to reconcile with the findings of previous site-response studies pointing to the strong amplification of sites in Japan at short periods (e.g. Atkinson and Casey, 2003; Ghofrani et al., 2013; Stewart et al., 2013; Anderson et al., 2013). Thus, we may return to this issue of regionalization of the site-response term at a later stage.

6.6   PHASE II: TWO-STAGE REGRESSIONS

The selected ground motion *IMs* of PGA, PGV, and PSA from the NGA-West 2 flatfile were regressed against predictor variables using Eqn. (6.1) to determine $F_{P,B}$ and F_E, after first adjusting all observations to the reference velocity of 760 m/s, using the site amplification model given in Section 5.2. The analyses were performed by David M. Boore by using the two-stage regression discussed by Joyner and Boore (1993, 1994). In Stage 1, $F_{P,B}$ component of the model is evaluated, the average motions at the reference distance R_{ref} (which are used in Stage 2), and the within-event aleatory variability, ϕ. In Stage 2, F_E component of the model and the between-event variability, τ are evaluated. The term $\overline{\ln Y}$ from Stage 1 regressions were used in weighted Stage 2 regressions to evaluate magnitude scaling of ground motion *IMs*. All regressions were done period-by-period without smoothing, although some of the constrained coefficients were smoothed. The details of Phase II are presented in BEA13.

6.7 PHASE III: MIXED EFFECTS RESIDUALS ANALYSIS AND MODEL REFINEMENT

In this section, I perform mixed effects residuals analyses having two purposes: (1) to check that the base-case GMPEs developed through the Phase I and II analyses are not biased with respect to *M*, R_{jb}, or site-scaling; and (2) to examine trends of residuals against parameters not considered in the Phase I and II analyses, including regional effects. We also consider a broader set of data. Recall that data were excluded from our Phase II analyses based on a number of criteria. For example, no aftershock recordings were used, because there is some concern that the spectral scaling of aftershocks differs from mainshocks (see Boore and Atkinson, 1989, and Atkinson, 1993). In this section, we consider the influence of additional factors/data not considered in Phase II, using residual analysis. The equations were adjusted on the basis of these residuals analyses.

6.7.1 Methodology

The methodology for the analysis of residuals employed here is similar to that described in Scasserra et al. (2009). We begin by evaluating residuals between the data and the base case GMPE described in Section 6.3 (without the adjustments described in Section 6.3.1). Residuals are calculated as:

$$R_{ij} = \ln Y_{ij} - \mu_{ij}\left(\mathbf{M}, R_{jb}, V_{S30}\right) \tag{6.14}$$

Index *i* refers to the earthquake event and index *j* refers to the recording within event *i*. Hence, R_{ij} is the residual of data from recording *j* in event *i* as calculated using the base case GMPE. Term Y_{ij} represents the RotD50 ground-motion *IM* (Boore, 2010) computed from recording *j*. Term μ_{ij} (*M*, R_{jb}, V_{s30}) represents the GMPE median in natural log units.

The analysis of residuals with respect to M, distance, and site parameters requires between-event variations to be separated from within-event variations. This is accomplished by performing a mixed effects regression (Abrahamson and Youngs, 1992) of residuals according to the following function:

$$R_{ij} = c_k + \eta_i + \varepsilon_{ij} \tag{6.15}$$

where c_k represents a mean offset (or bias) of the data relative to the GMPE (i.e., $c_k = \bar{R}$), η_i represents the event term for event i (explained below), and ε_{ij} represents the intra-event residual for recording j in event i. Event term η_i represents approximately the mean offset of the data for event i from the predictions provided by the GMPE median (after adjusting for mean offset c_k, which is based on all events). Event terms are used to evaluate GMPE performance relative to source predictor variables, such as M. Event terms have zero mean and standard deviation = τ (natural log units). Within-event error has zero mean and standard deviation = ϕ. Mixed-effects analyses per Eqn. (6.15) are performed using the NLME operator in program R (Pinheiro et al., 2013).

In particular, in Phase III we consider data to distances much larger than R_{jb} = 80 km, with cutoff distances being based on magnitude and instrument type (Figure 6.1). We also consider Class 2 (CL2) events (aftershocks); as mentioned in Section 6.2.1, CL2 events are differentiated from CL1 events (mainshocks) using a minimum centroid R_{jb} separation of 10 km per the criteria of Wooddell and Abrahamson (2012). The data set obtained with these criteria is approximately twice the size of that used for Phase II analysis.

Figure 6.17 shows the average data misfit to the base case GMPE as expressed by parameter c_k (note: this is not the $F_{P,B}$ parameter c_i, where i = 1, 2, or 3). Parameter c_k has some offset from zero and fluctuates with period, being largest at long periods ($T \geq 5$ sec). The non-zero values of c_k result from the difference between the Phase III and II data sets; c_k values from the data used in Phase II are nearly zero.
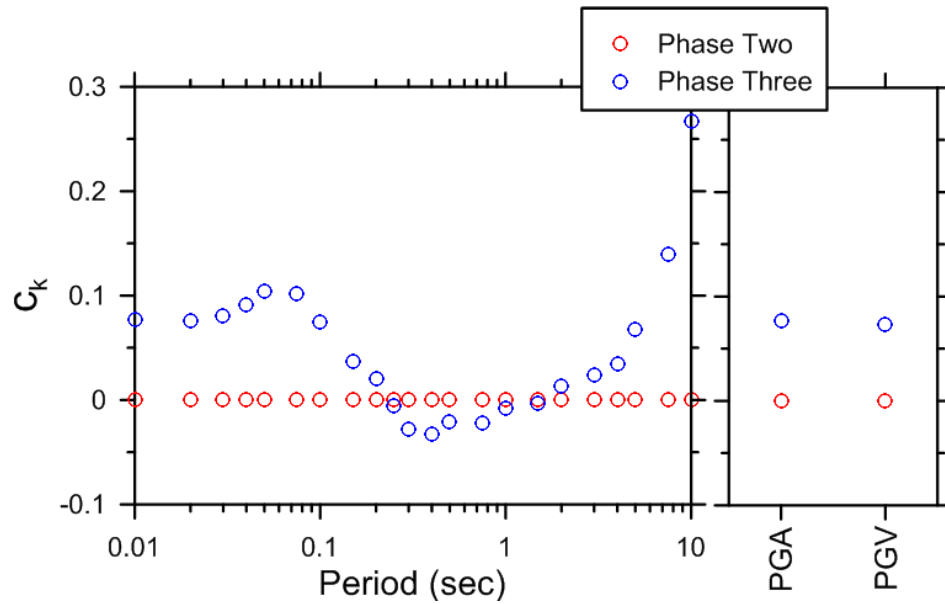
Figure 6.17. **Period-dependence of mean GMPE bias using Phase III and Phase II data sets.**

Subsequent sections examine within-event residuals, between-event residuals (event terms), and standard deviation terms evaluated from these analyses.

6.7.2 Within-Event Residuals Analysis of Path and Site Effects

We use the within-event residuals (ε_{ij}) to examine the performance of the Phase II equations relative to the broader Phase III data set with respect to path and site effects. The main issue examined through the path analysis is regional variations of apparent anelastic attenuation;

since the base-case model uses c_3 terms derived from California data, potential variations for other regions are investigated. The site analyses consider trends of residuals ε_{ij} with V_{s30} and $Z_{1.0}$ (to examine possible sediment depth effects).

Path Effects: In Figure 6.18, I plot residuals (ε_{ij}) against R_{JB} using the full data set, with means and standard errors shown within bins equally spaced with respect to $\log R_{jb}$. The results show no perceptible trend, indicating that the base-case path-scaling terms for apparent geometric spreading and apparent anelastic attenuation reasonably represent the data trends. This is an encouraging finding because the base-case regressions were performed using only data at $R_{jb} < 80$ km with constraint of c_3 from small magnitude data in California (Section 6.2.1). The flatness of the trends for $R_{jb} > 80$ km indicates that the California-derived c_3 values may be a reasonable global average for active crustal regions.
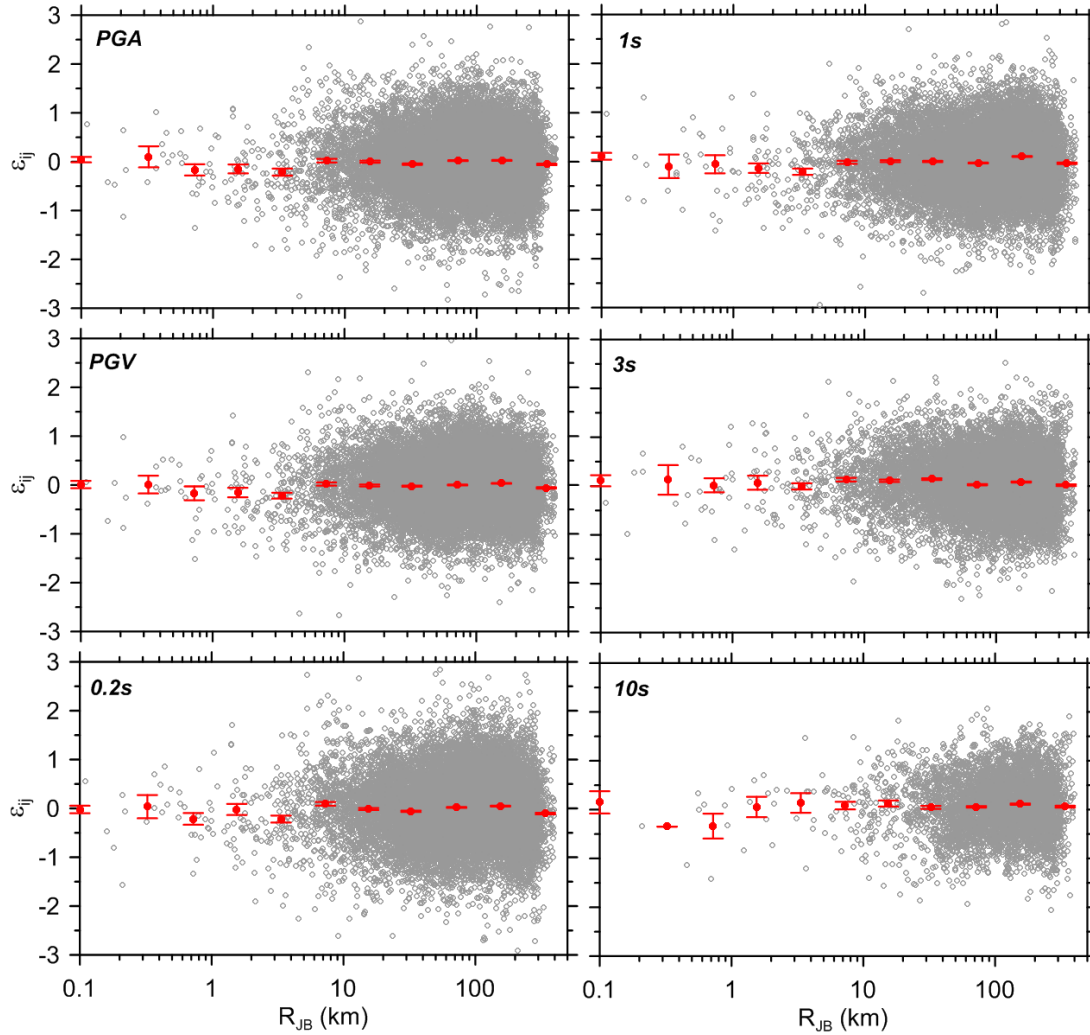
Figure 6.18. Within event residuals for full Phase III data set versus distance, with binned medians (red dots with bars indicating standard errors).

Figures 6.19 to 6.21 show within-event residuals (ε_{ij}) against R_{jb} using data from various global regions grouped according to their distance-attenuation trends for $R_{jb} > \sim 50\text{-}100$ km. Figure 6.19 shows data from California and Taiwan, for which the flat trends in the global data set are preserved (these same general features are found if the data are plotted for California-only or Taiwan-only). In the figure, this is indicated as an 'average Q' result. Figure 6.20 shows data from Japan and Italy, for which a downward trend is observed indicating faster distance

attenuation (marked as 'low Q'). Similarly fast distance attenuation trends have been observed previously in these regions (e.g., Stewart et al., 2013; Scasserra et al., 2009). Figure 6.21 shows data from China and Turkey, for which slower attenuation is observed ('high Q'). The slower attenuation for China is not surprising given the location of the Wenchuan event near the western boundary of a stable continental region as defined by Johnston et al. (1994), with the recordings having been made at sites both in stable continental and active crustal regions (Kottke, 2011). This result for Turkey was not expected, but has been observed by others using larger Turkish data sets (Z. Gulerce, *personal communication*, 2013).

For the low and high Q cases, we fit a linear expression through the data according to:

$$\varepsilon = \Delta c_3 \left(R - R_{ref} \right) \tag{6.16}$$

where Δc_3 is additive to the c_3 terms developed in Section 6.5.1 from California (Eqn. 6.11). Values of Δc_3 are plotted against period for average, low, and high Q conditions in Figure 6.22. These adjustments are considered to be statistically significant, and Δc_3 was used in the computation of residuals for the remainder of Phase III analyses presented below.
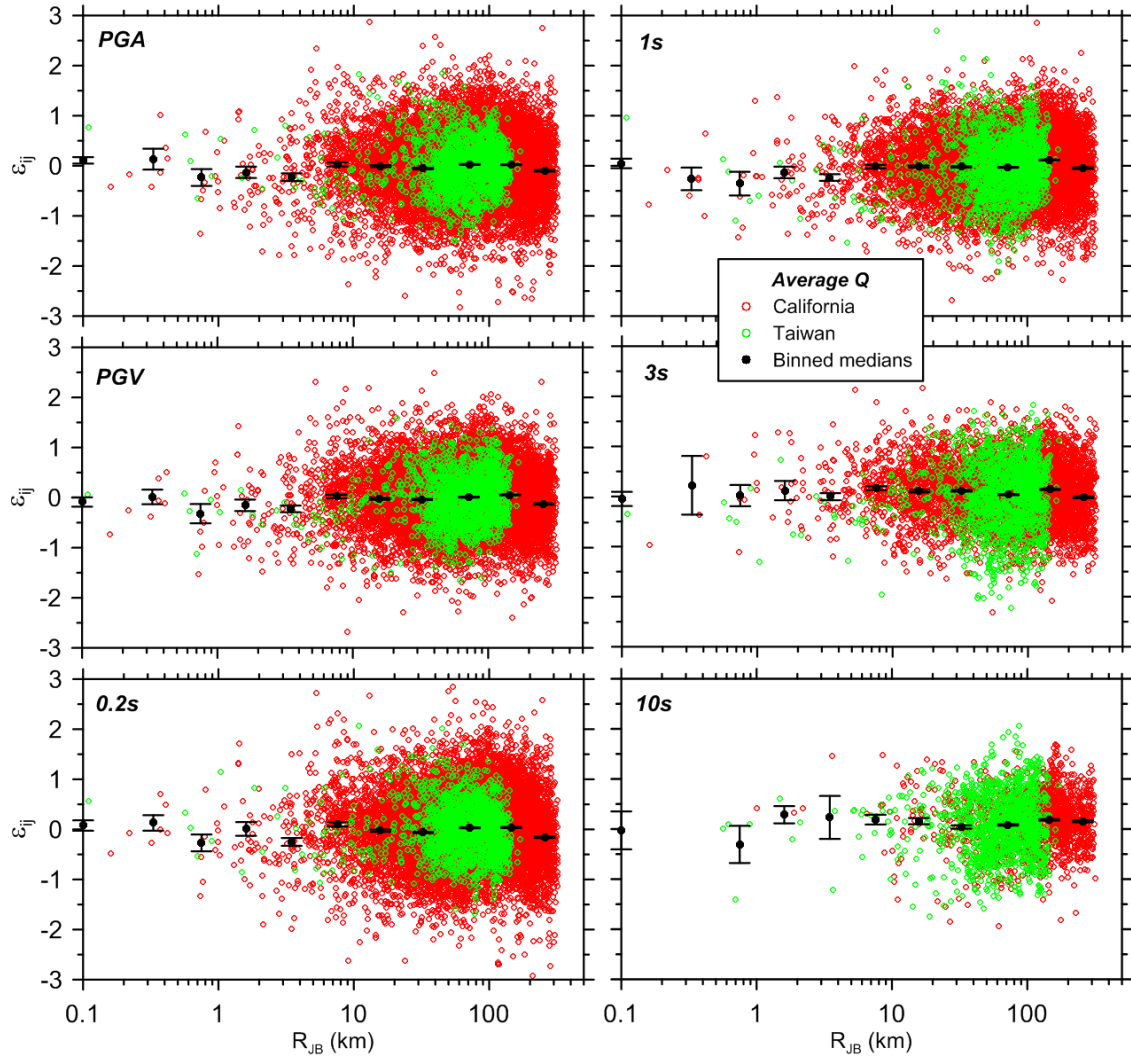
Figure 6.19. Within event residuals for regions identified as 'average Q' (California and Taiwan) within the flatfile. The residuals in this case demonstrate a flat trend with distance. The larger scatter of California data is due to more small M events.
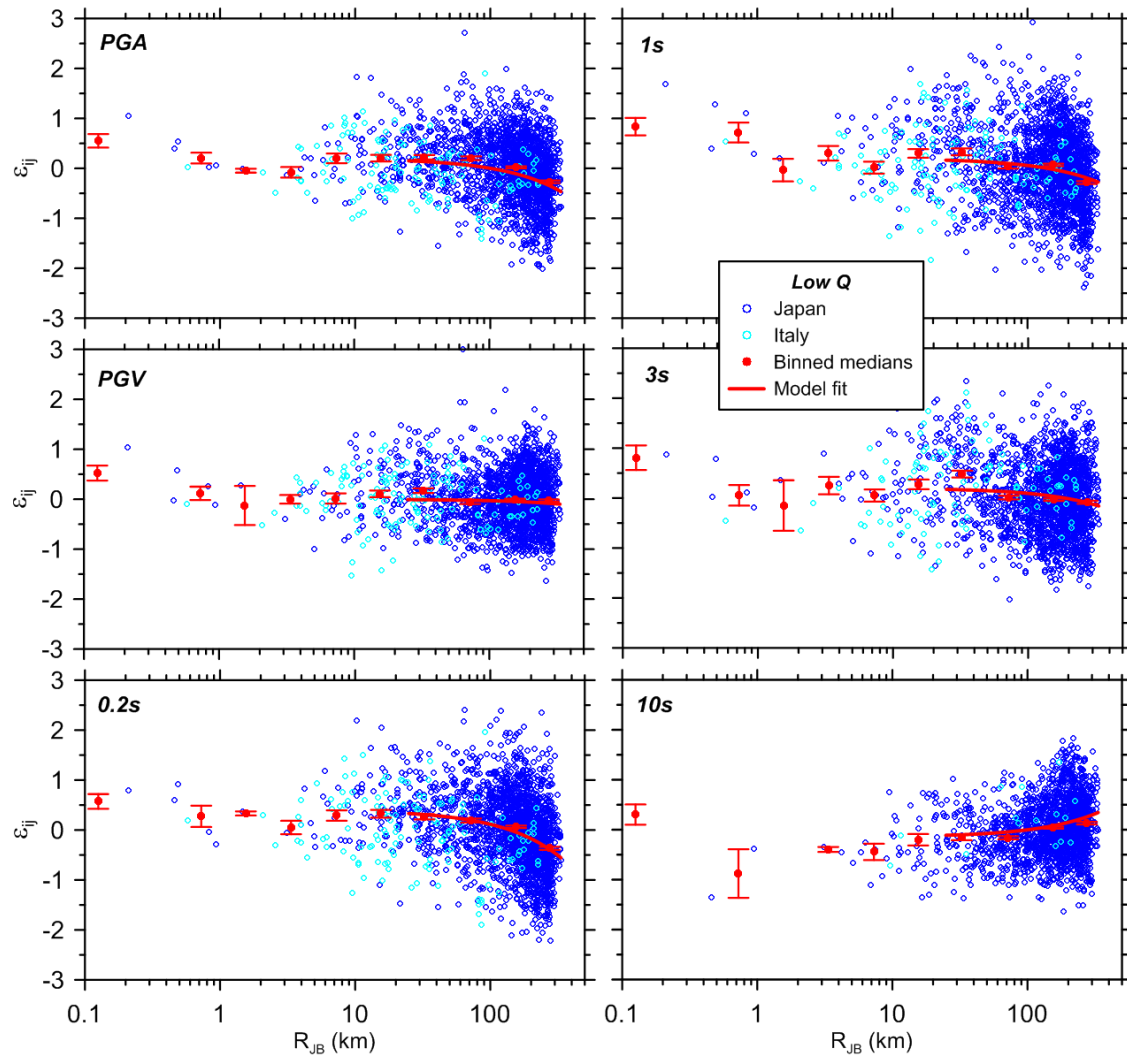
Figure 6.20. Within event residuals for regions identified as 'low Q' (Italy and Japan) within the flatfile and trend line per Eqn. (6.16). The residuals demonstrate a decreasing trend with distance.
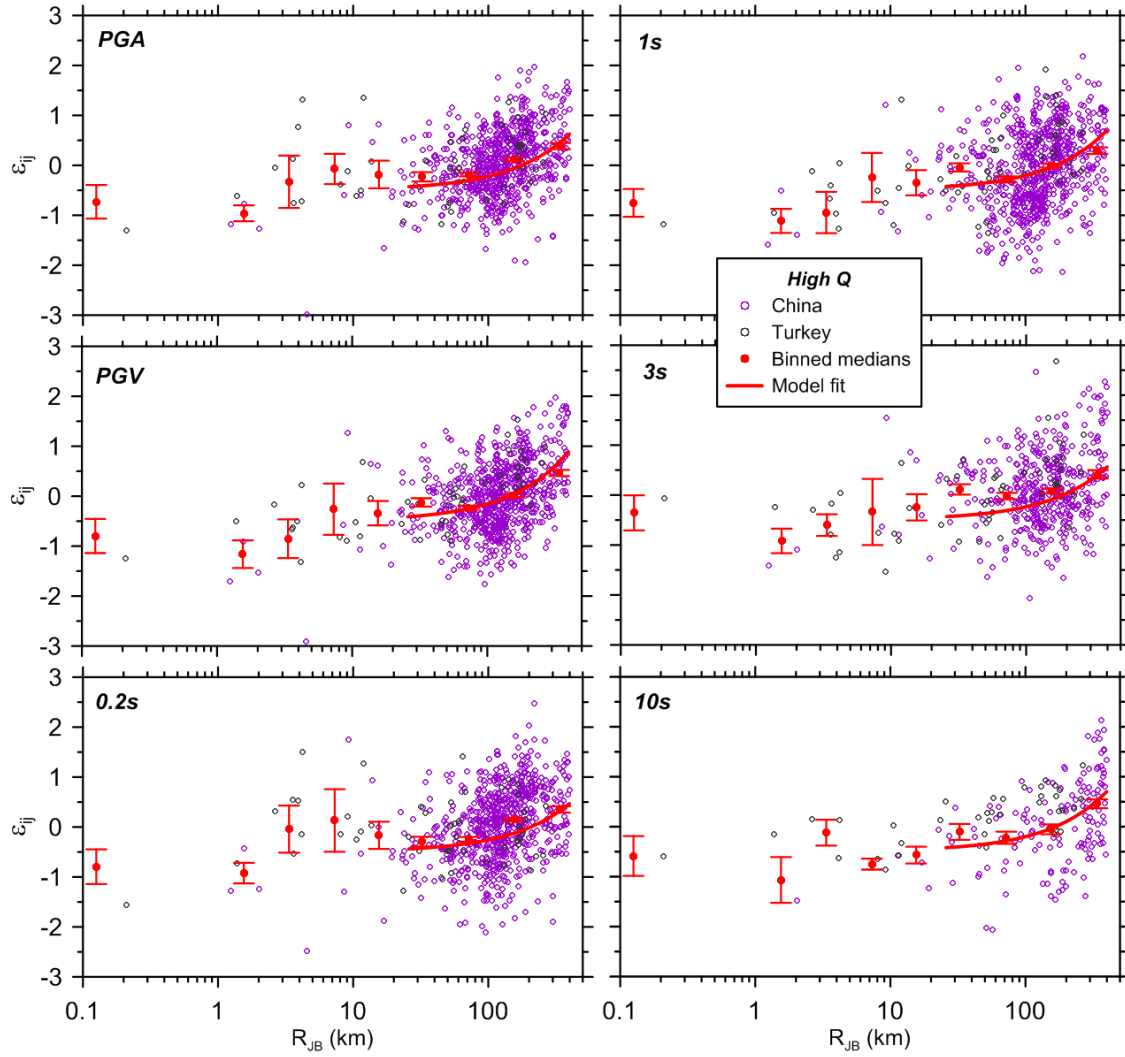
Figure 6.21. Within event residuals for regions identified as 'high Q' (China and Turkey) within the flatfile and trend line per Eqn. (6.16). The residuals demonstrate an increasing trend with distance.
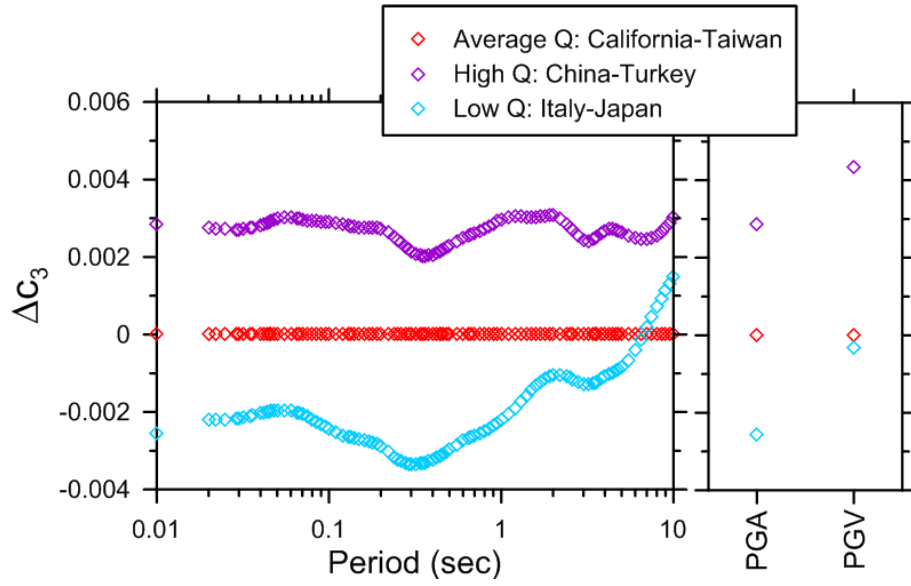
Figure 6.22. Additive adjustment factors for apparent anelastic attenuation term c_3 for regions exhibiting various distance attenuation rates.

Check of V_{s30}-scaling: In Figure 6.23, I show intra-event residuals (ε_{ij}) against V_{s30} using the full data set. We find no trends, indicating satisfactory performance of the model. When the data is plotted by region, the trends remain flat (not shown).
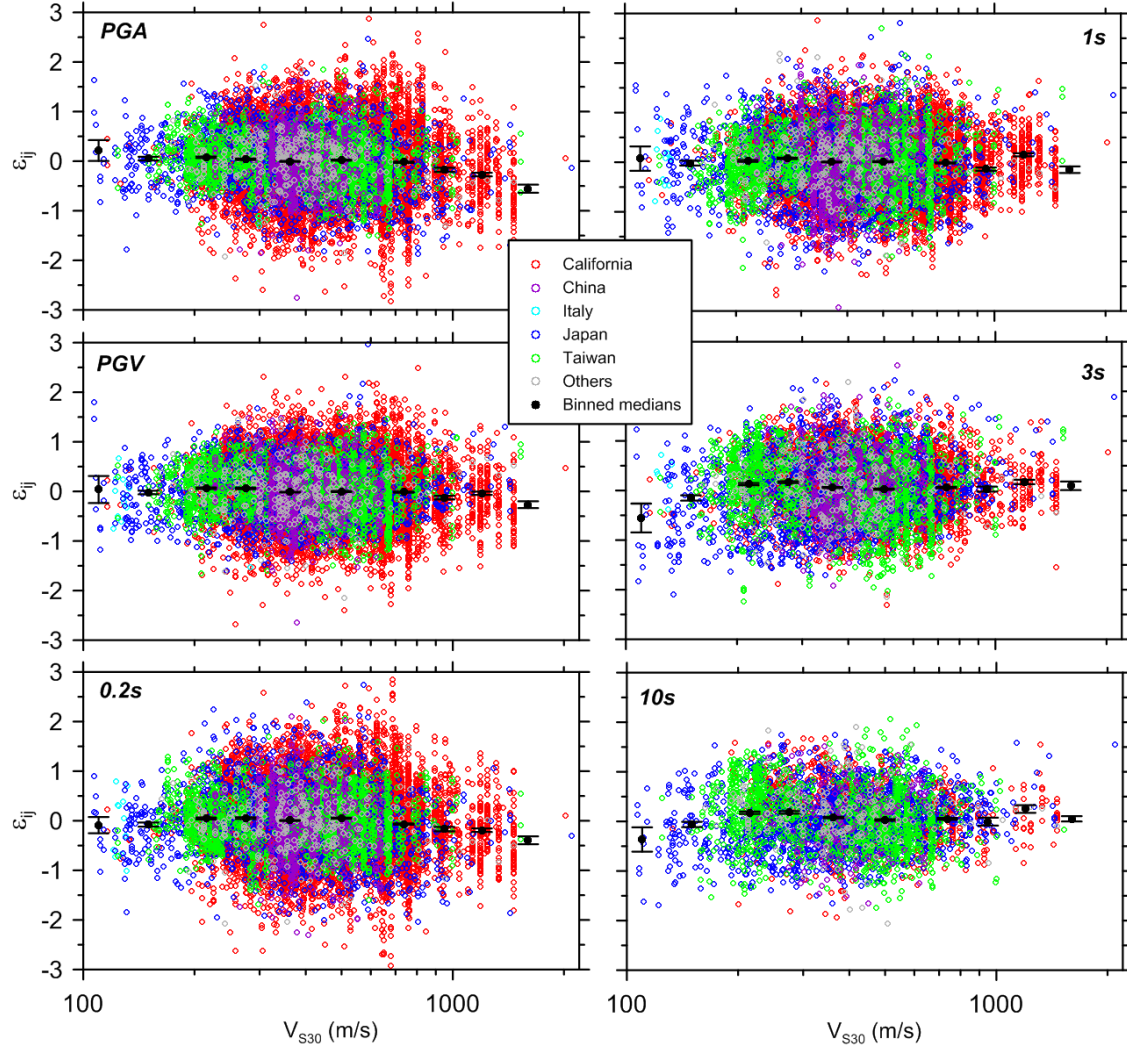
Figure 6.23. Within event residuals against V$_{S30}$.

Sediment Depth Effects: The site parameter V_{s30} strictly describes only the characteristics of sediments in the upper 30 m, even though it has been shown to be correlated to deeper structure (e.g., Boore et al., 2011). There may be additional site amplification effects that are related to the depth of the deposit and that are not captured by the use of V_{s30} alone as a site descriptor. For example, GMPE residuals for ground-motion models that include a

V_{s30}-based site term (or similar site terms related to surface geology) have been shown to correlate to basin depth parameters (e.g., Field, 2000; Lee and Anderson, 2000; Steidl, 2000; Choi et al., 2005; Abrahamson and Silva, 2008; Campbell and Bozorgnia, 2008; Chiou and Youngs, 2008). This indicates that depth is describing elements of the site characteristics relevant for ground motion prediction. Since residual trends in prior work are typically strongest at long spectral periods ($T > \sim 1.0$ sec), the depth parameter is descriptive of low-frequency components of the ground motion which may be related to resonances of sedimentary basin structures. The BA08 model did not include a basin-depth term; here we investigate whether the data support the use of such a term in the present equations.

Basin-depth parameters used to investigate site effects are generally defined as the vertical distance from the ground surface to the first occurrence of a particular shear-wave iso-surface (typically 1.0, 1.5, or 2.5 km/sec). We consider the shallowest metric of z_1 (depth to 1.0 km/sec iso-surface) due to its greater practical utility (i.e., a 1.0 km/sec velocity can be reached through geotechnical drilling in some cases; whereas 2.5 km/sec can rarely be reached) and a lack of clear evidence from prior work indicating that deeper metrics are more descriptive of long-period site effects (Day et al., 2008).

As described in Ancheta et al. (2013), a substantial effort was made in NGA-West 2 to update basin depths in the site database based on new information. Depth parameters have been updated for basin regions in southern California (SC) and the San Francisco Bay Area (SFBA). Depth parameters have also been added for stations in Japan. In total, 54% of the stations in the flatfile have an assigned basin depth. Figure 6.24 shows the distribution of z_1

values against V_{S30} for SC, SFBA, and Japan. Also shown are two correlation relationships developed by B. Chiou (personal communication, 2013):

$$\text{California: } \ln(\mu_{z1}) = \frac{-7.15}{4}\ln\left(\frac{V_{S30}^4 + 570.94^4}{1360^4 + 570.94^4}\right) \tag{6.17a}$$

$$\text{Japan: } \ln(\mu_{z1}) = \frac{-5.23}{2}\ln\left(\frac{V_{S30}^2 + 412.39^2}{1360^2 + 412.39^2}\right) \tag{6.17b}$$

These relationships can be used to estimate z_1 when only V_{s30} is available. They also provide a convenient mechanism for defining a representative depth for any given V_{s30}. The latter point is important with respect to understanding the implications for basin depth of using the base case GMPE, in which z_1 does not appear. The absence of z_1 in the model does not mean the sites have no depth; rather, when the base-case GMPE is used it is providing estimates of site response for an 'average' depth, an approximate estimate of which is given by Eqns. (6.17).
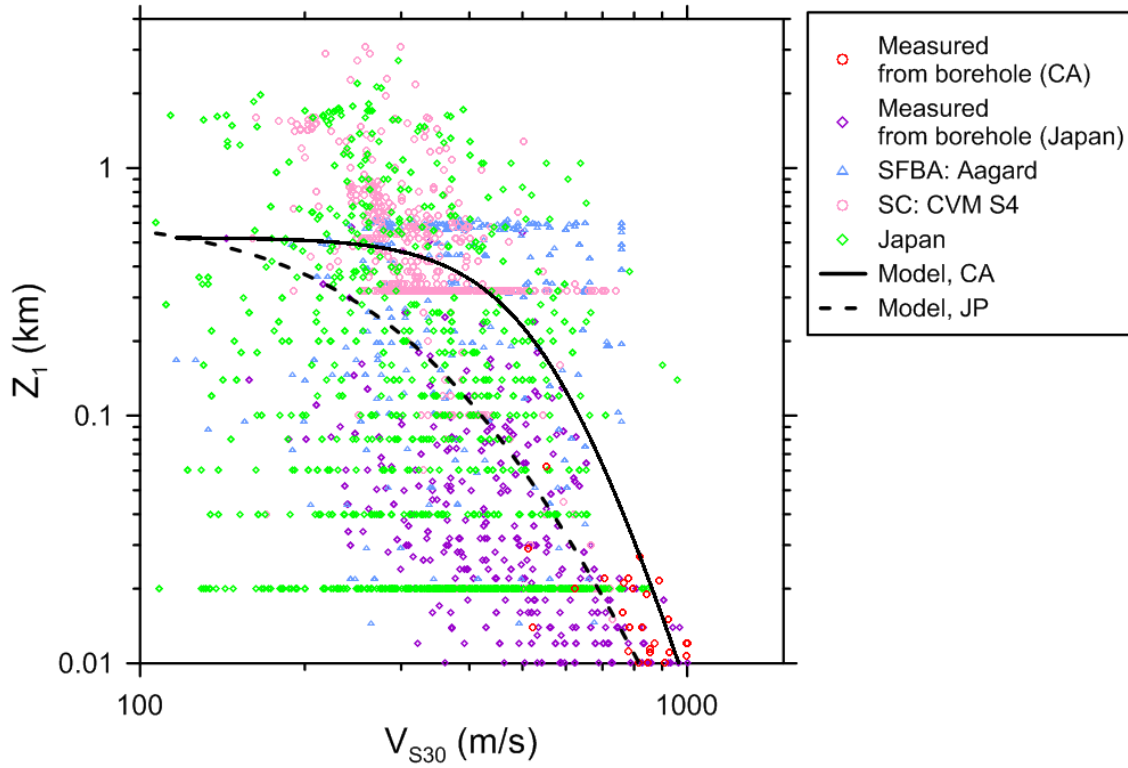
Figure 6.24. Sediment depth z_1 variation with V_{S30} for basins in southern California (SC), San Francisco Bay Area (SFBA), and Japan. Equations for CA and Japan are from B. Chiou (Eqns. 6.17).

Figure 6.25 shows intra-event residuals (ε_{ij}) against basin depth z_1. There is little trend for short periods ($T < 1.0$ sec), but at longer periods the trend is strong. Interestingly, the residuals are near zero, with little dependence on z_1, for $z_1 < 0.25$-0.5 km, and again show little change with z_1 for $z_1 > {\sim}1.5$ km (but with a nearly constant offset from 0). Since the V_{S30} component of the GMPE already implicitly includes average basin depths (approximately represented by Eqn. 6.17), we investigate the possibility of using the differential from the average basin-depth predictor variable:

$$\delta z_1 = z_1 - \mu_{z1}\left(V_{S30}\right) \tag{6.18}$$

216

where $\check{\delta z}_1(V_{s30})$ is the mean basin depth from the relations in Eqns. (6.17). In Figure 6.26(a), we plot residuals ε_{ij} against $\check{\delta z}_1$ along with the model fit from Eqn. (6.10). As before, at short periods there is no effect. For $T \geq 1$ sec, the trends are strong, indicating negative residuals for negative $\check{\delta z}_1$ and a flat trend beyond approximately $\check{\delta z}_1 = 0.5$ km. The $\check{\delta z}_1$ parameter is more descriptive of data trends and was adopted as the predictor variable (Eqn. 6.18).
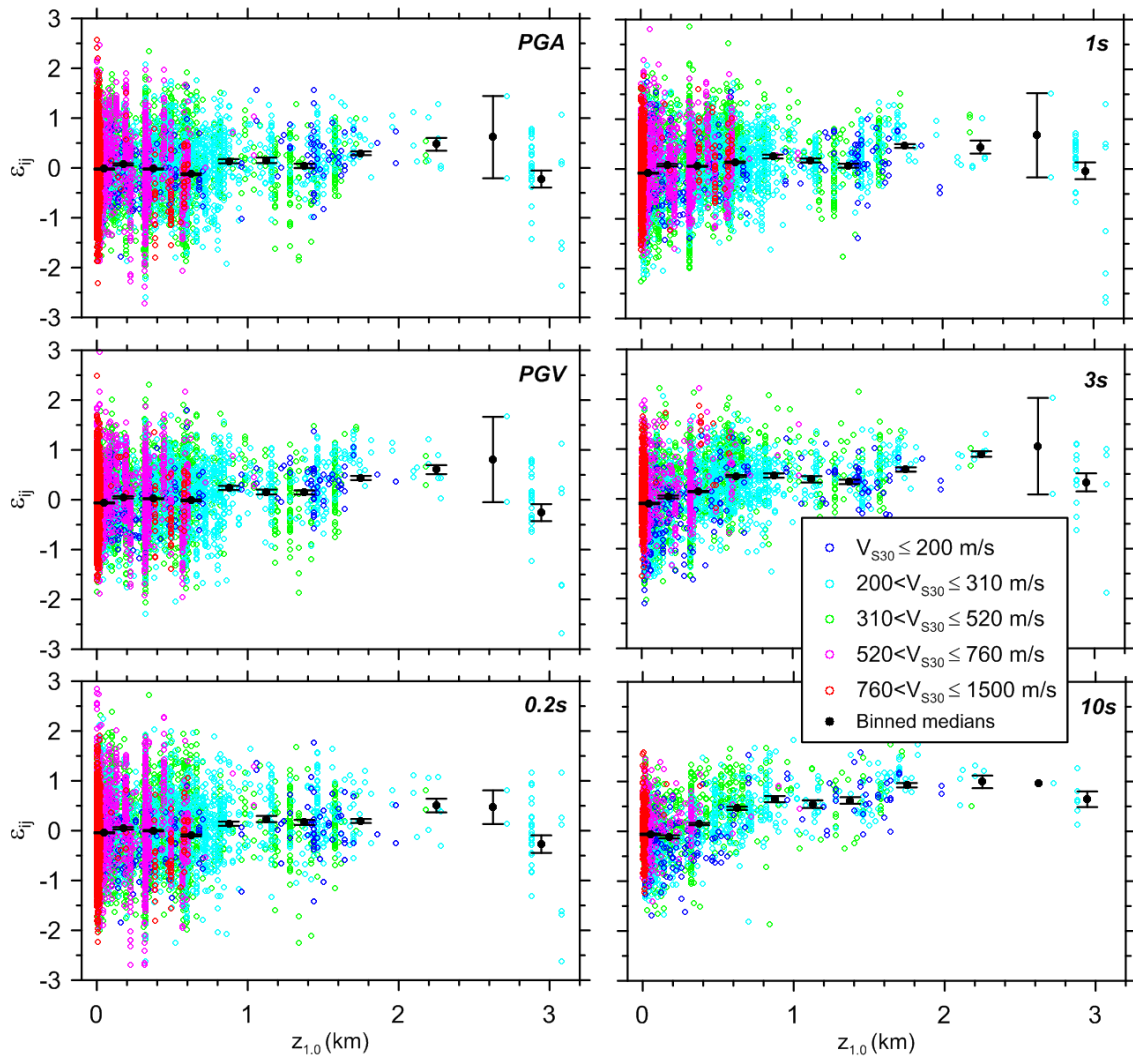
Figure 6.25. Within event residuals against sediment depth parameter z_1.
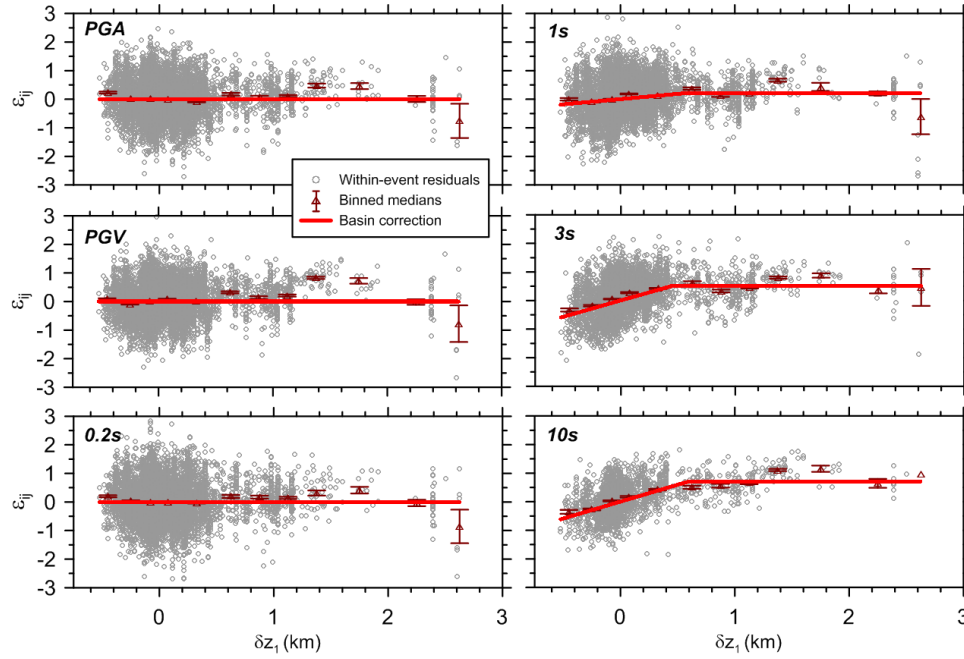
Figure 6.26(a). Within event residuals against sediment depth differential δz_1 along with proposed basin model.
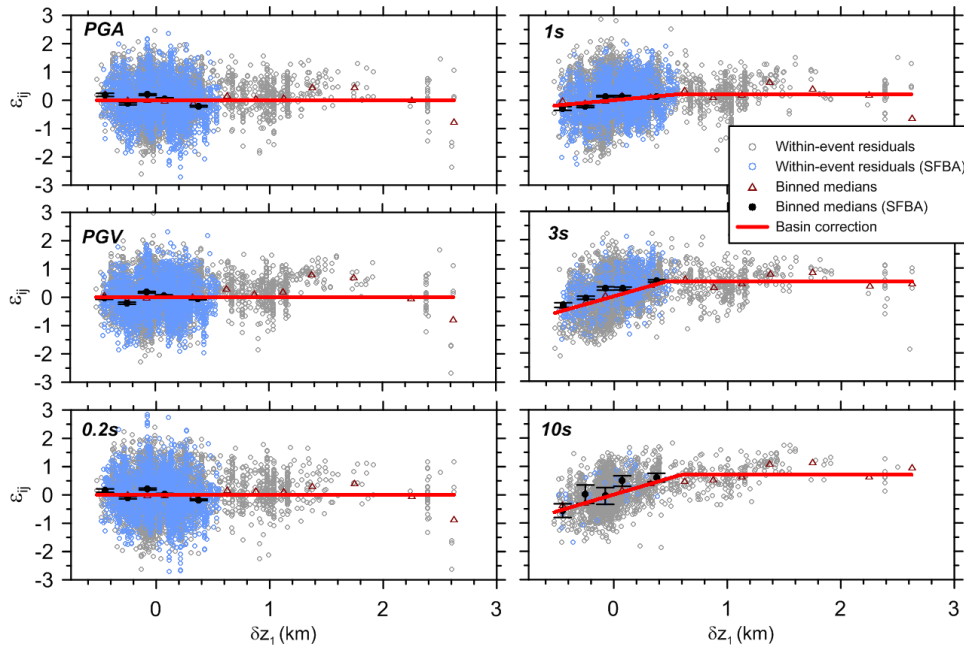
Figure 6.26(b). Within event residuals against sediment depth differential δz_1, highlighting SFBA sites. Non-SFBA sites shown with grey circles.
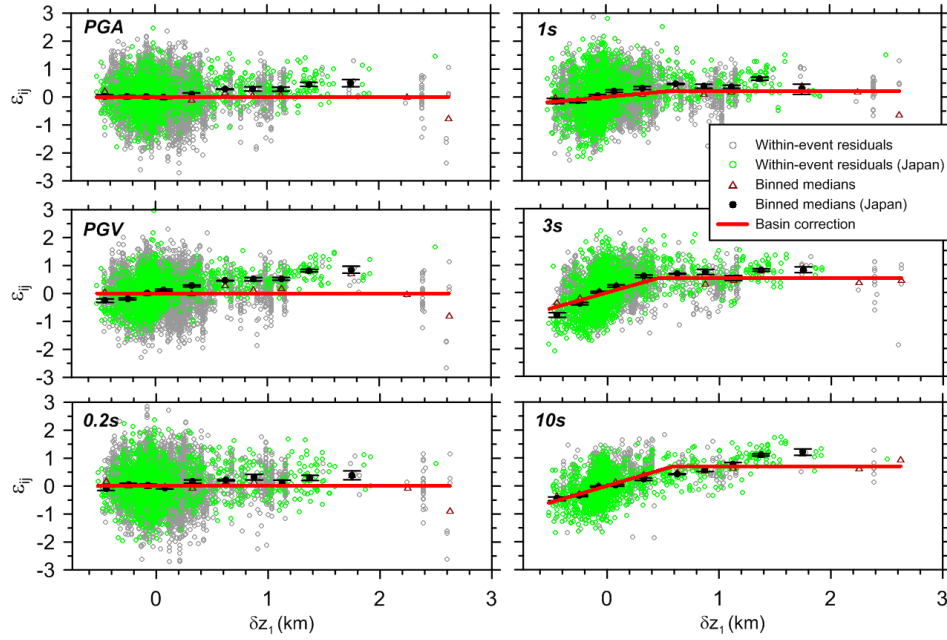
Figure 6.26(c). Within event residuals against sediment depth differential δz_1, highlighting Japan sites. Non-Japan sites shown with grey circles.
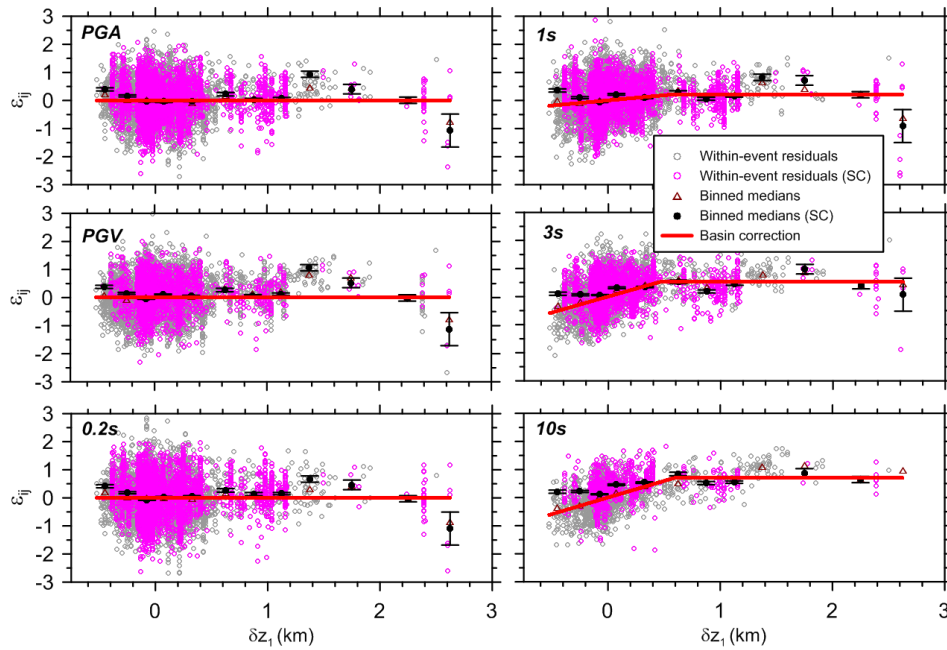
Figure 6.26(d). Within event residuals against sediment depth differential δz_1, highlighting SC sites. Non-SC sites shown with grey circles.

Figures 6.26b-d show the residuals trends with δz_1 for the three regions contributing data (SFBA, Japan, and SC). The trends are strongest for Japan, particularly for negative values of δz_1, and weakest for SC. The levels of maximum mean amplification for positive δz_1 are relatively consistent across regions, being approximately 0.5 to 0.75 (in natural log units) at long periods. Although some regional trends are evident in Figures 6.26, we have chosen to not regionalize the $F_{\delta z1}$ model, aside from the regional nature of the mean V_{s30} - z_1 model (Eqn. 6.17).

6.7.3 Analysis of Source Effects Using Between-Event Residuals

In Figure 6.27, we show event terms for both CL1 and CL2 events against magnitude for the five regions contributing most of the data for NGA-West 2. The majority of the events, especially at small M, are from California. China contributes a substantial number of events, which are CL2, for $M \sim 4.5$–6. These China CL2 events exhibit unusual trends with respect to M-scaling (indicated by the trend for PGA, PGV and 0.2 sec PSA) or significant negative bias (1.0 and 3.0 sec PSA). We do not understand these unusual features and have elected to not consider further the China CL2 events for subsequent analyses.

Figure 6.28 shows CL1 event terms against M along with medians in bins 0.5 M in width. From this figure we see that the magnitude-scaling function adequately captures the trends from CL1 events in the broader Phase III data set.
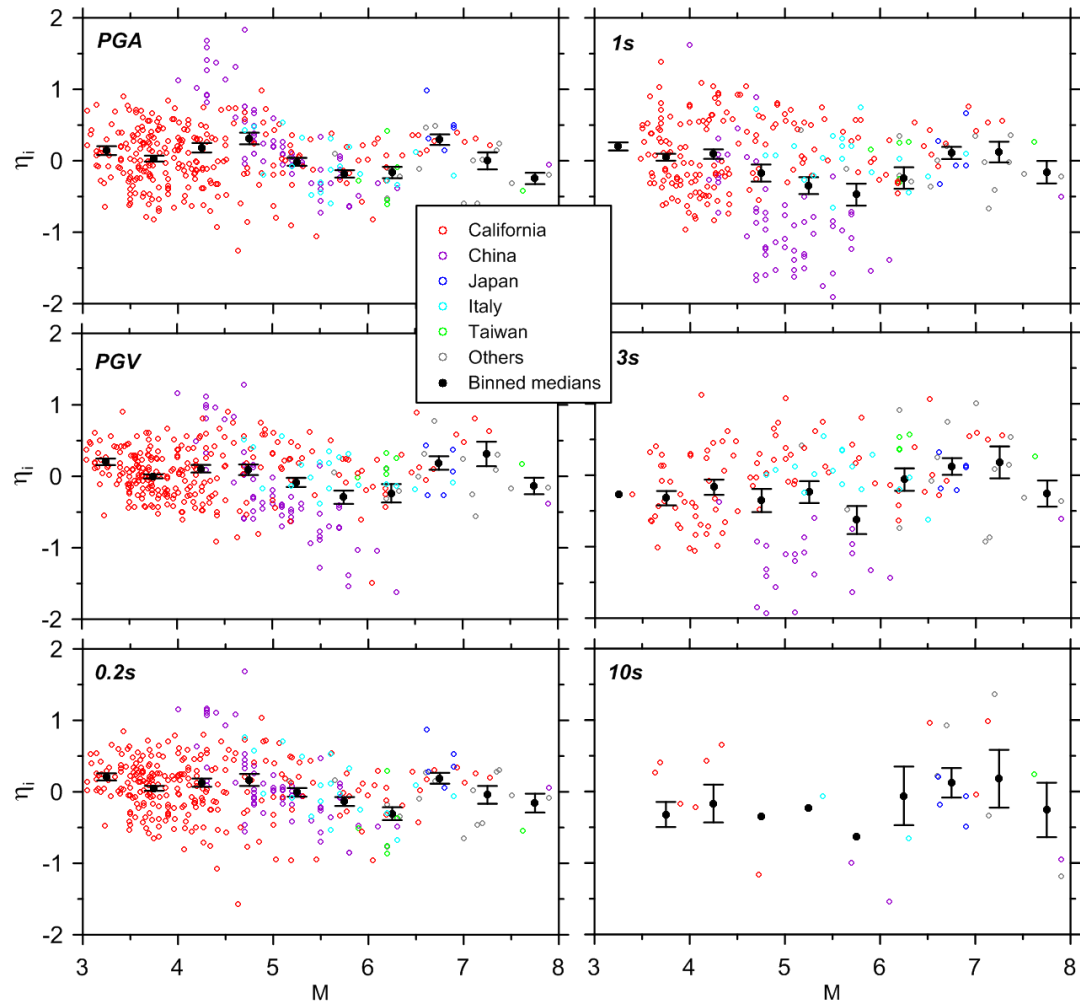
Figure 6.27. Event terms vs magnitude for CL1 and CL2 events sorted by region.
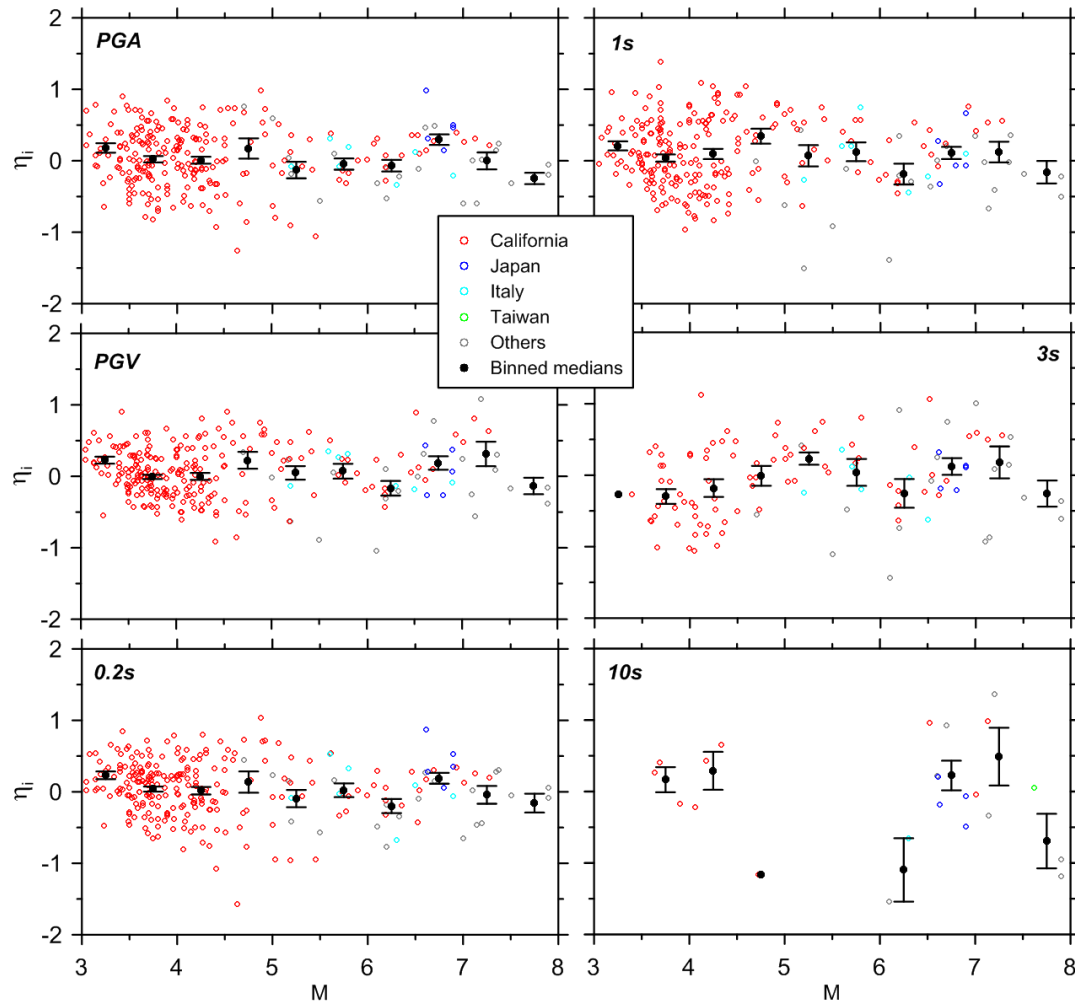
Figure 6.28.   Event terms vs magnitude for CL1 events sorted by region.

Potential Bias of CL2 events: Recall that all earthquake events in the NGA-West 2 flatfile

have been designated as CL1 (foreshocks or mainshocks) or CL2 (interpreted as aftershocks

based temporal and spatial attributes; Wooddell and Abrahamson, 2012). Our examination of

the event term results from Phase III analysis indicated that for selected regions (e.g., Taiwan),

a particular feature of CL1 event terms was often also seen in the subsequent CL2 events

associated with the 'parent' CL1 event. In Figure 6.29, we examine such correlations for all CL1

events having CL2 'children' events, sorted by region. The plots show the event term for the CL1 event (η_{C1}) on the x-axis against the mean of the 'children' event terms ($\bar{\eta}_{C2}$) on the y-axis (similar procedures were used to look at mainshock and aftershock site factors by Lee and Anderson, 2000). Although the data do not provide a large correlation coefficient (computed values are generally less than 0.3), there are a striking number of events falling on or near the 45 degree line. Given the modest relationship between CL1 and CL2 event terms, we elect to examine aftershock effects in the form of the difference $\Delta\eta = \bar{\eta}_{C2} - \eta_{C1}$.
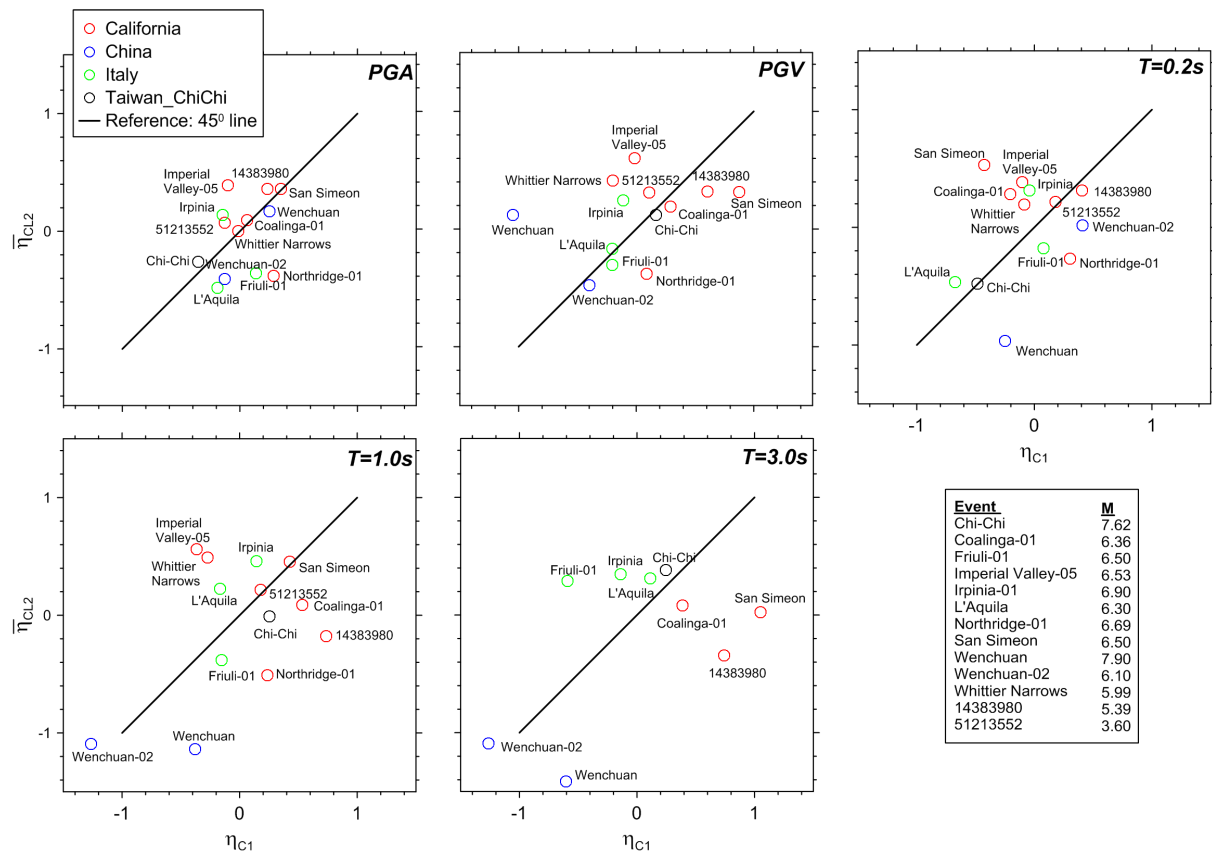
Figure 6.29.   **Event terms vs magnitude for CL1 events sorted by region. The numbered events (e.g. 14383980) are California small M events, which were not named in the NGA-West 2 database.**

In Figure 6.30, we show $\Delta\eta$ against M for various ground-motion *IMs*. We see no compelling evidence for $\Delta\eta$ being *M*-dependent nor significantly different from zero relative to the data scatter. In Figure 6.30, we show the mean value of $\Delta\eta$ (denoted $\overline{\Delta\eta}$) against period using all data except for the China CL1 event at **M**6.1, which is a clear outlier and may be unreliable for the same unknown reasons as the China CL2 events discussed above. For comparative purposes, we have also computed the weighted average of CL2 event terms (weights assigned based on the number of data points) for the regions contributing most of the aftershock data (California and Italy). This is denoted in Figure 6.31 as $\left(\overline{\eta}_{CL2}\right)_{CA,IT}$. The values are numerically similar to those for $\overline{\Delta\eta}$, and are computed for more periods. After studying these results, our conclusion is that the data do not justify the use of a CL2 adjustment to the base-case GMPEs.
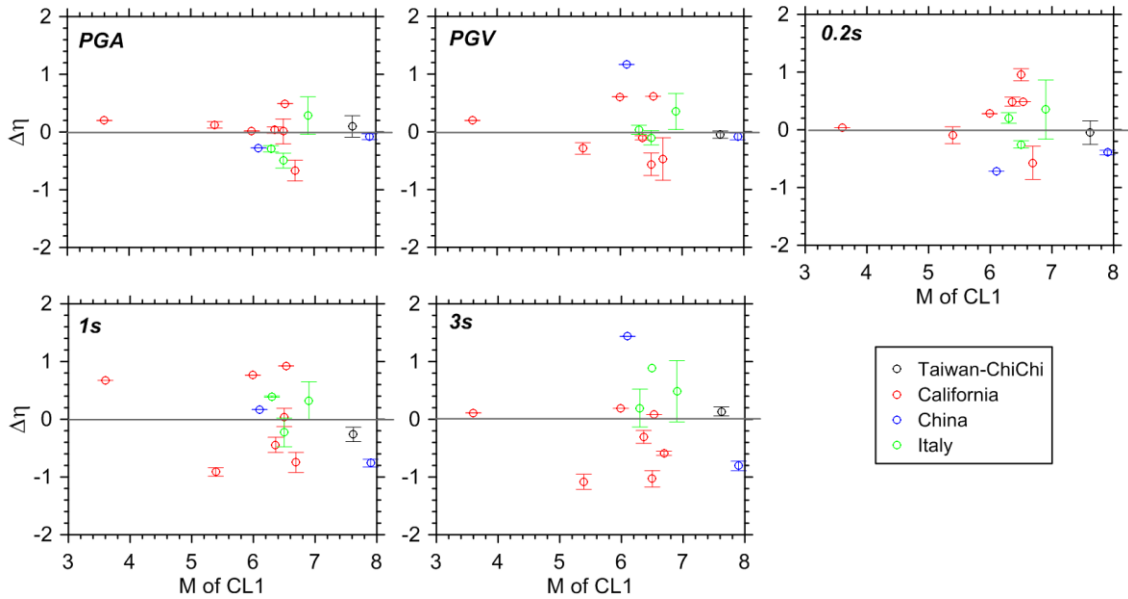
Figure 6.30. CL2 event term differential $\Delta\eta$ (with standard errors) as function of magnitude for various regions and IMs.
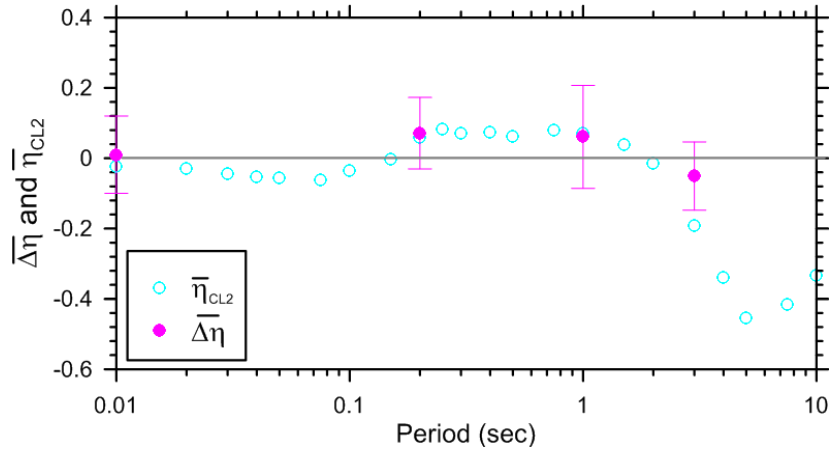
Figure 6.31. Mean CL2 event term differential (with standard errors) and mean of CL2 event terms.

Source Depth: Our path function (Eqn. 6.3) takes site-source distance as R_{jb}, which is the closest horizontal distance of the site to the surface projection of the fault plane. As such, the depth of rupture is not considered. This could conceivably lead to overprediction of deep events, because the ground motions for such events have a longer travel path to reach recording sites. On the other hand, there are some studies indicating that the stress parameter for earthquake sources tends to increase with depth (e.g., Fletcher et al., 1984), which could offset the distance effect. In this section, we examine trends of event terms with two depth parameters provided in the NGA-West 2 flatfile: depth to top of rupture (Z_{tor}) and depth to hypocenter (Z_{hypo}).

Figures 6.32 and 6.33 show trends of event terms with Z_{tor} and Z_{hypo} for CL1 and CL2 events sorted by M (M < 5 and M ≥ 5). The M < 5 data (Figure 6.32) indicate increasing event terms as depth increases for short periods (PGA and PSA for T < 0.5 sec) and a reversal towards a decreasing trend with depth for T ≥ 1.0 sec PSA. Those trends are present for both considered source depth parameters. However, those trends are not apparent for M ≥ 5 data (Figure 6.33).

Since the hazard for most engineering applications is governed by relatively large magnitude events, we opted not to include a source depth adjustment to our base-case GMPEs.
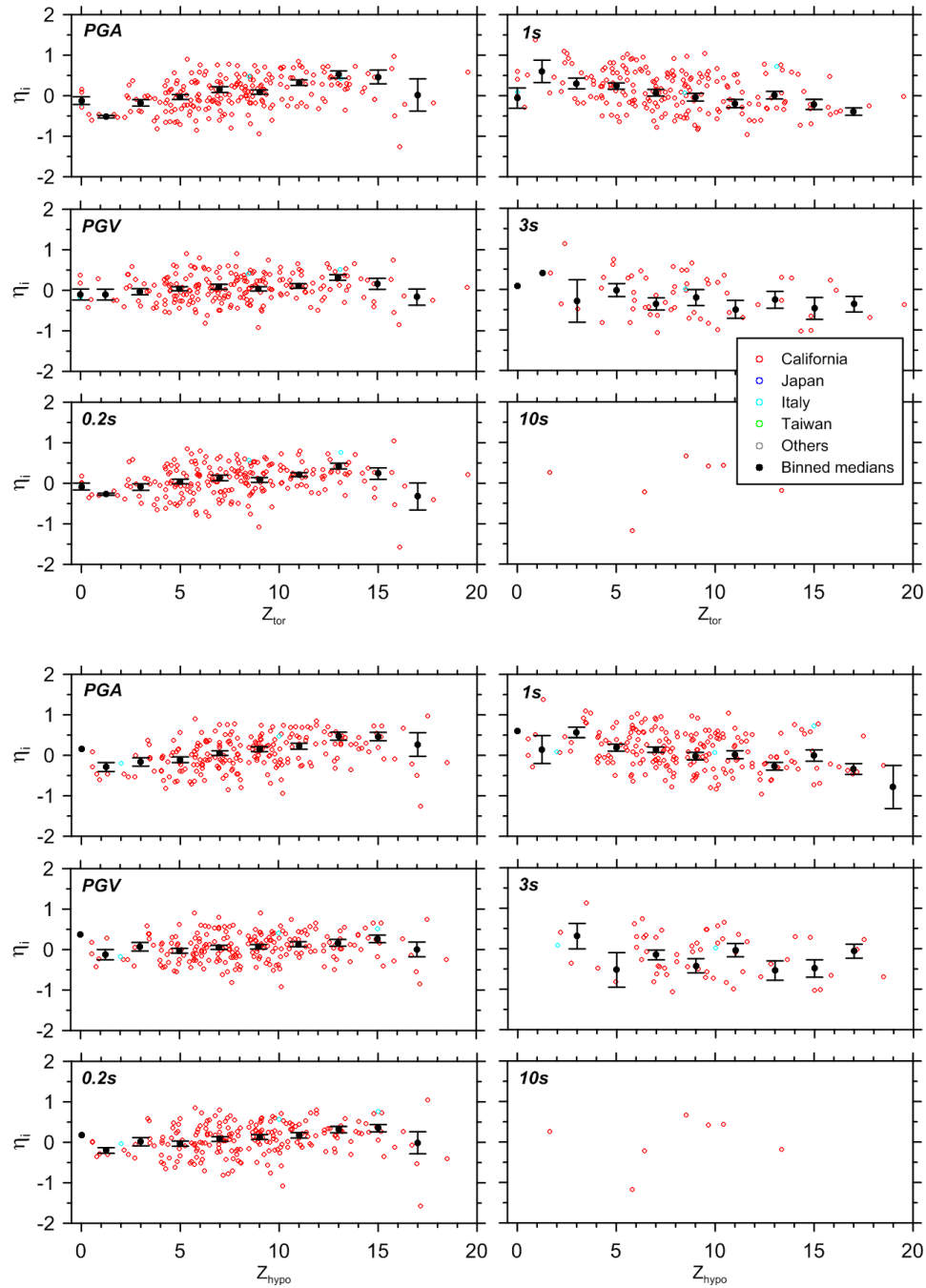
Figure 6.32. Event terms against depth to top of rupture (Z_{tor}) (top) and hypocentral depth (Z_{hypo}) (bottom) for M < 5 CL1 and CL2 events, for which most events are from CA.
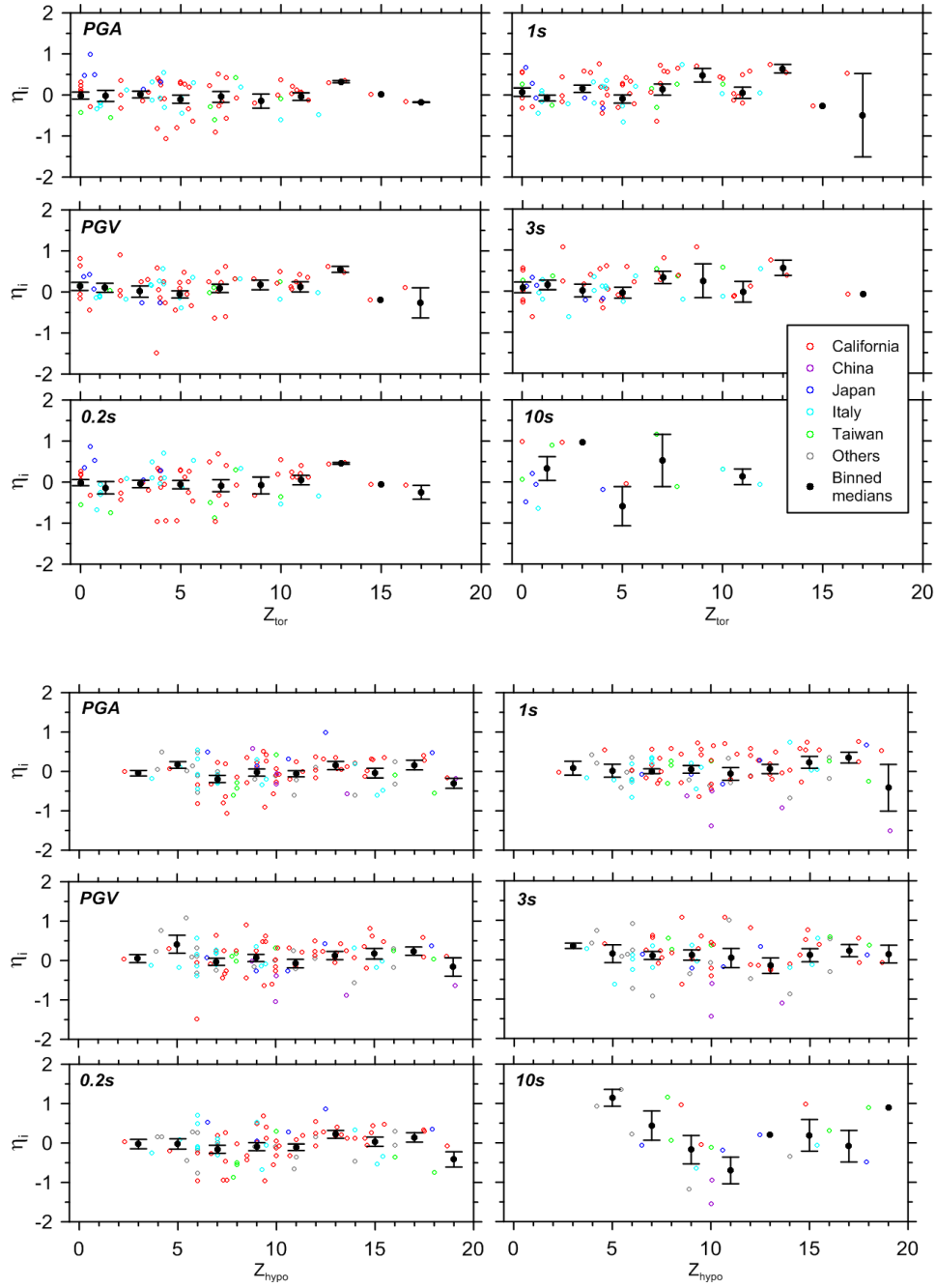
Figure 6.33. Event term variation with depth to top of rupture (Z_{tor}) (top) and hypocentral depth (Z_{hypo}) (bottom) for M ≥ 5 CL1 and CL2 events.

Focal Mechanism: Phase II regressions include the evaluation of constant terms that depend on dummy variables for four variants of focal mechanism (SS = strike-slip, RS = reverse slip, NS = normal-slip, and U = unknown). Those mechanism descriptors are based on orientations of principal stress axes and not strictly on rake angle, although they are strongly correlated, as shown in Figure 6.4.

The GMPE focal mechanism terms (Eqn. 6.5) are independent of magnitude. Figures 6.34 and 6.35 show the trends of event terms with respect to rake angle for two magnitude ranges ($M < 5$ and $M \geq 5$). The $M < 5$ results in Figure 6.34 indicate essentially zero residuals for SS and RS conditions, but positive residuals for NS. The amount of positive bias is comparable to the magnitude of the NS term, suggesting that had that term been zero, the bias would be removed. On the other hand, the $M \geq 5$ results appear unbiased for SS and NS, but positive bias occurs at long periods for RS, suggesting that the RS term could be increased for $T > 1.0$ sec PSA. This will be considered in future revisions to the GMPE.
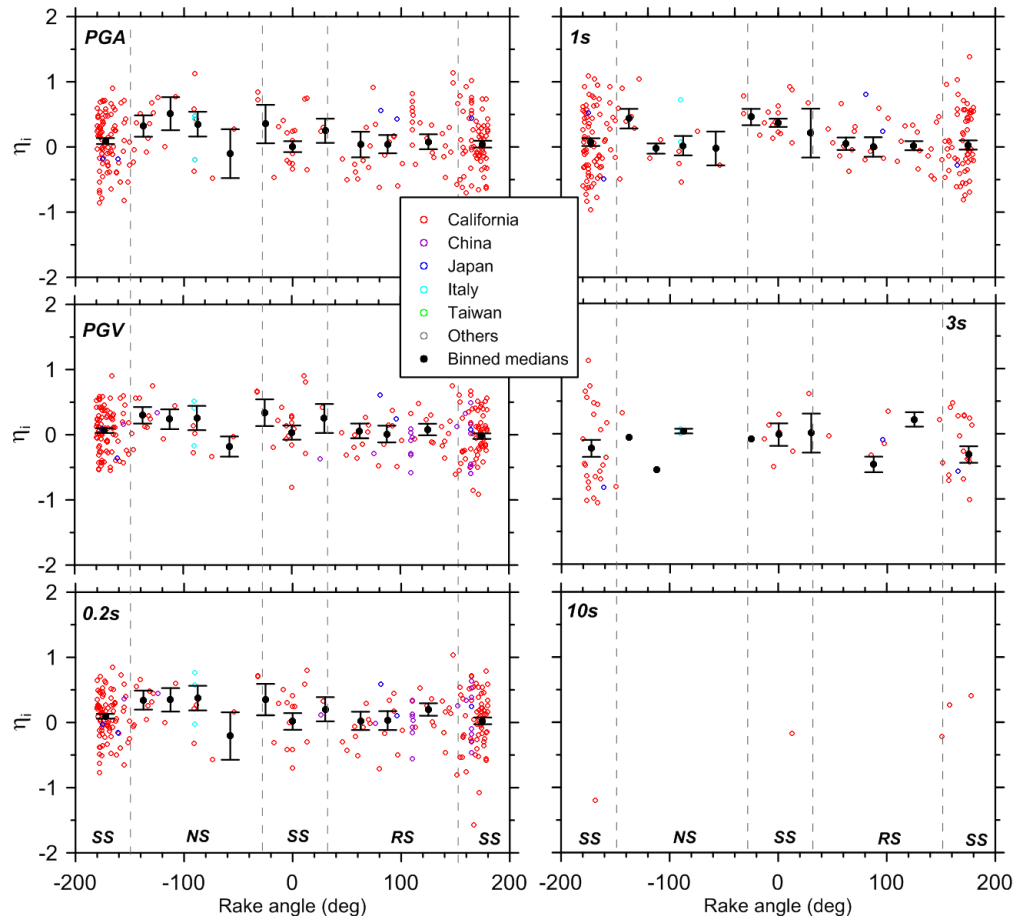
Figure 6.34. Event term variation with rake angle for M < 5 CL1 and CL2 events.

229
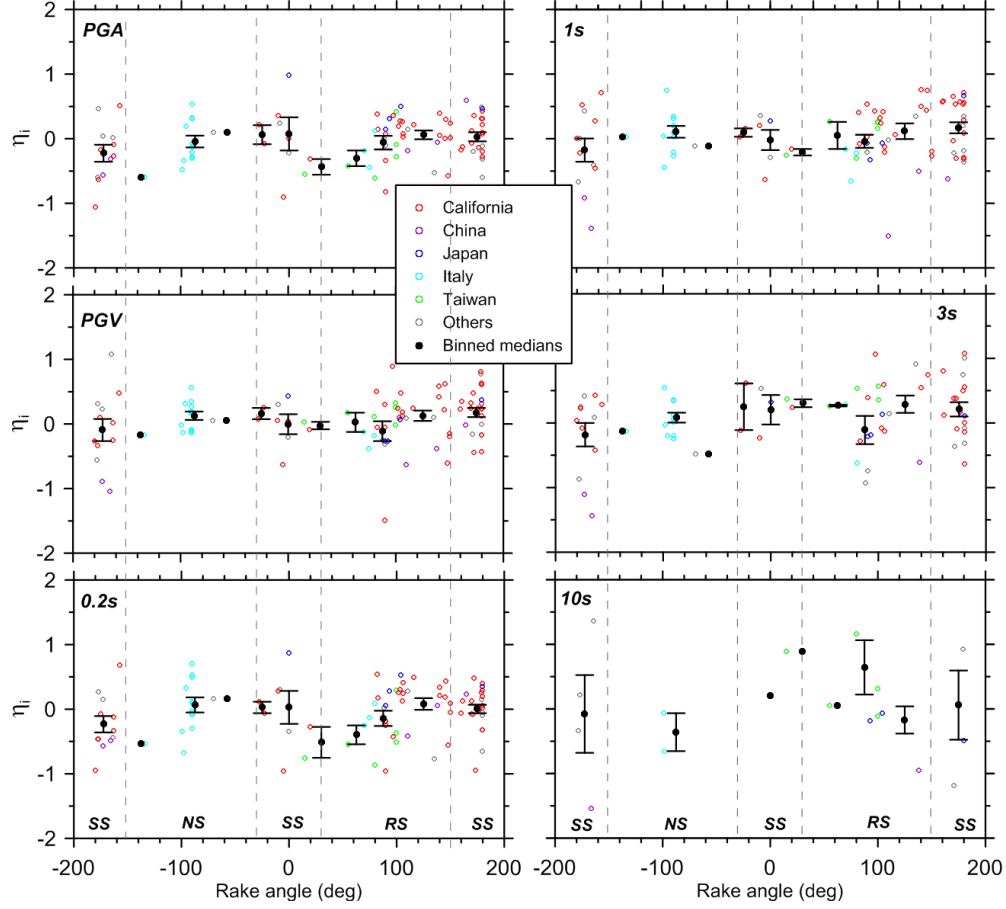
Figure 6.35. Event term variation with rake angle for M ≥ 5 CL1 and CL2 events.

6.7.4 Standard Deviation Terms

Our GMPE is formulated with separation of standard deviation terms into between-event and within-event components, τ and ϕ, respectively (Eqn. 6.2). Figure 6.36 plots τ and ϕ for the base case (Phase II) GMPE in which the data selection criteria require $R_{jb} < 80$ km and use of only CL1 events. The present standard deviation terms are significantly higher than those in BA08 and have a different period-dependence in which a short-period peak is observed. We

believe there is a physical justification for these trends — PGA and very short period PSA is controlled by longer ground motion periods (in the range of 0.2-1.0 sec), so dispersions for these periods might be expected to be similar, as observed. At intermediate periods, there is likely energy content in the ground motions affecting the oscillator response, which has high dispersion perhaps from kappa variability. In the remainder of this section, we investigate factors affecting standard deviation and propose appropriate equations for τ and ϕ.
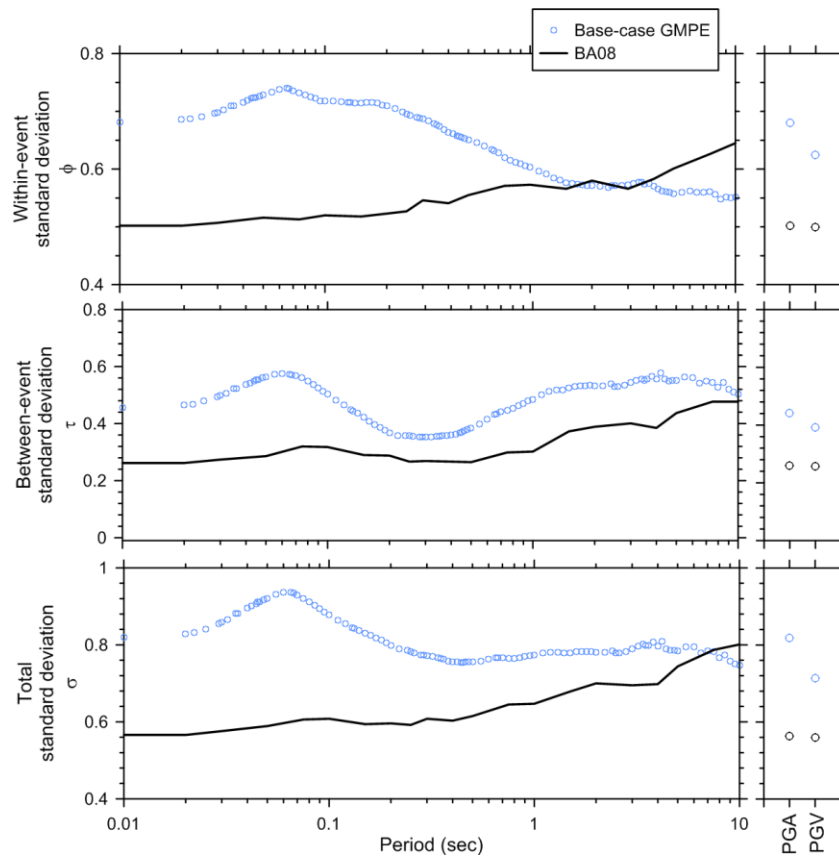
Figure 6.36. Standard deviation terms against period from base-case model from this study and BA08'. Base-case model applies for $R_{jb} \leq 80$ km and CL1 events.

Using event terms from the Phase II data set, I plot in Figure 6.37 values of τ within 0.5M bins for several *IMs.* We observe that τ decreases with increasing *M*, with most of the

change occurring between magnitudes of approximately 4.5 to 5.5. Accordingly, we propose an

M-dependent between-event standard deviation term as follows:

$$\tau(M) = \begin{cases} \tau_1 & \mathbf{M} \leq 4.5 \\ \tau_1 + (\tau_2 - \tau_1)(\mathbf{M} - 4.5) & 4.5 < \mathbf{M} < 5.5 \\ \tau_2 & \mathbf{M} \geq 5.5 \end{cases}$$

(6.18)

Values of τ_1 and τ_2 were computed as weighted standard deviations of event terms within the respective magnitude ranges using the Phase II data set and GMPE without regionalization (Δc_3 = 0). In those calculations, weights are proportional to the number of recordings from which the event terms were established (N_i). Results are shown with the binned values of τ in Figure 6.37 and as a function of period in Figure 6.38(a). Next, we investigated several factors not considered in the Phase II analyses that might influence τ. In Figure 6.38(b), we show τ_1 and τ_2 computed using the same Phase II data set, but incorporating regional anelastic attenuation (non-zero Δc_3) and the basin model into the GMPE (labeled as 'Complete GMPE'). The effect of using the modified GMPE is to reduce τ_1, although τ_2 is not much affected. In Figure 6.38(c), we add CL2 events to the data set (both CL1 and CL2 are now included), which significantly increases τ_2 but does not affect τ_1. There are a substantial number of CL2 events with M > 5.5, which contribute to the τ_2 increase. These are principally from five California mainshocks (including 1994 Northridge and 1983 Coalinga), Chi-Chi Taiwan, Wenchuan China, and six earthquakes in Italy (including 2009 L'Aquila). For application, we propose the use of the τ_1 and τ_2 values in Figure 6.38(b), which apply for CL1 events only; if an analysis requires consideration of aftershocks, we recommend increasing τ_2 by 0.06 at all periods.
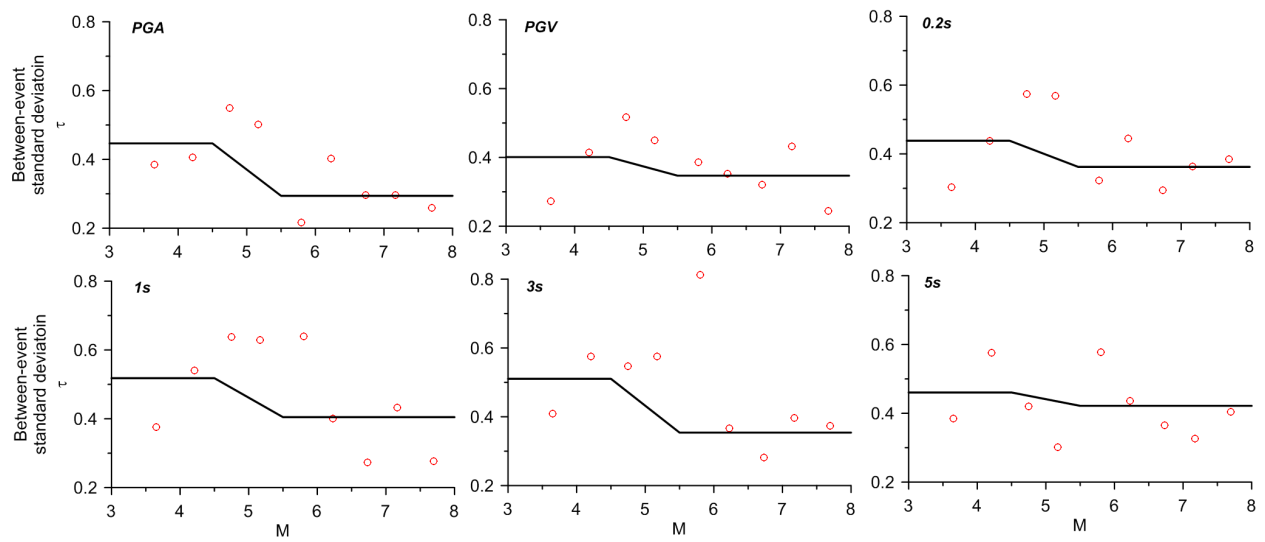
Figure 6.37. Between-event standard deviation terms against magnitude using Phase II data set and base-case GMPE. Horizontal black lines indicate τ values for M < 4.5 and M > 5.5.
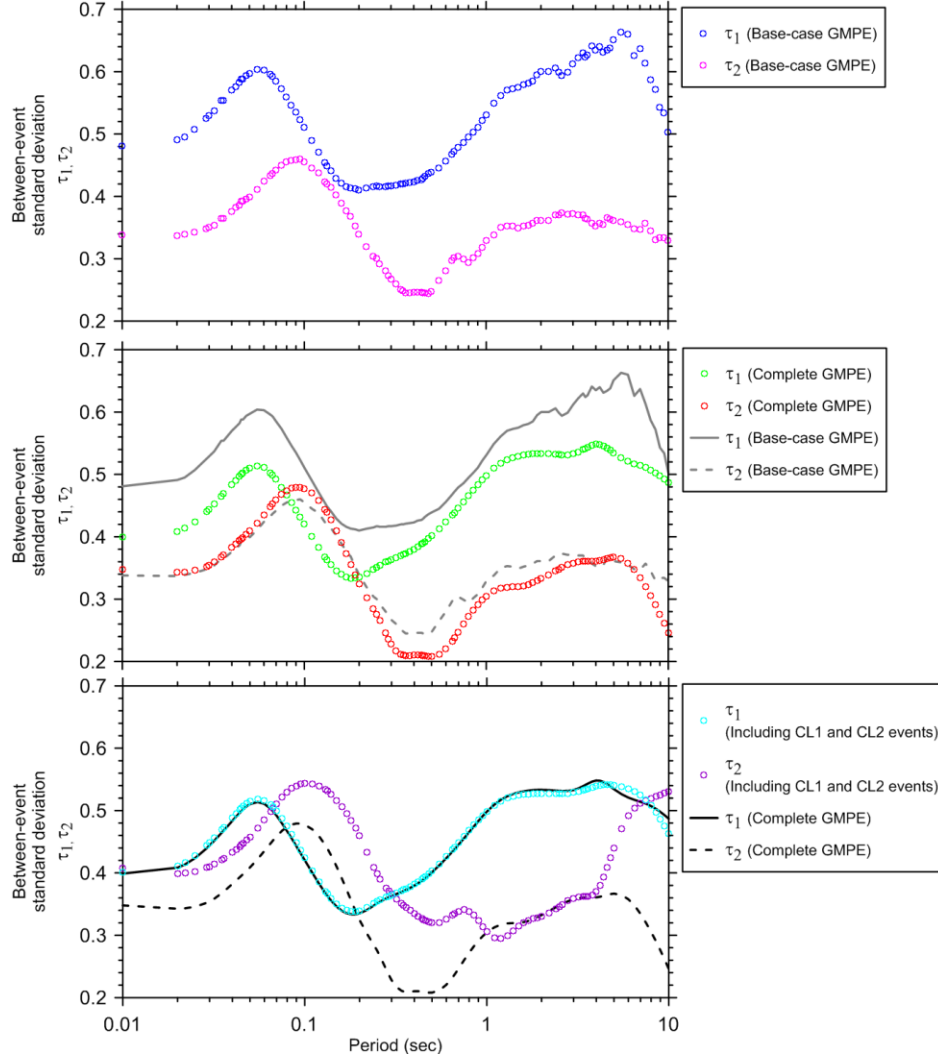
Figure 6.38. Between-event standard deviation terms against period for (a) base-case GMPE; (b) complete GMPE, which includes regional anelastic attenuation and basin depth terms but not CL2 events; and (c) including both CL1 and CL2 events with the complete GMPE.

In Figure 6.39, we plot values of within-event standard deviation ϕ within M bins using the base-case GMPE and Phase II data set. Parameter ϕ has a relatively complex relationship with M, decreasing with M at short periods and increasing with M at long periods. The decreasing trends with M for short periods could result from variability in site-related κ (e.g.,

Douglas and Jousset, 2011). For distances under 80 km, we propose an *M*-dependent within-event standard deviation term as follows:

$$\phi(\mathbf{M}) = \begin{cases} \phi_1 & \mathbf{M} \le 4.5 \\ \phi_1 + (\phi_2 - \phi_1)(\mathbf{M} - 4.5) & 4.5 < \mathbf{M} < 5.5 \\ \phi_2 & \mathbf{M} \ge 5.5 \end{cases} \quad (6.19)$$

Values of ϕ_1 and ϕ_2 were computed within the respective magnitude ranges using the Phase II data set and GMPE without regionalization ($\Delta c_3 = 0$), with the results shown in Figure 6.39 and 6.40(a). As with the analysis of σ terms describe above, we considered the effects of including regional anelastic attenuation and the basin depth terms [Figure 6.40(b)] and including CL2 events [Figure 6.40(c)]. These additional factors have a relatively minor effect on ϕ terms; the small effect of the regionalized anelastic attenuation resulted from restricting the data set to $R_{jb} \le 80$ km.
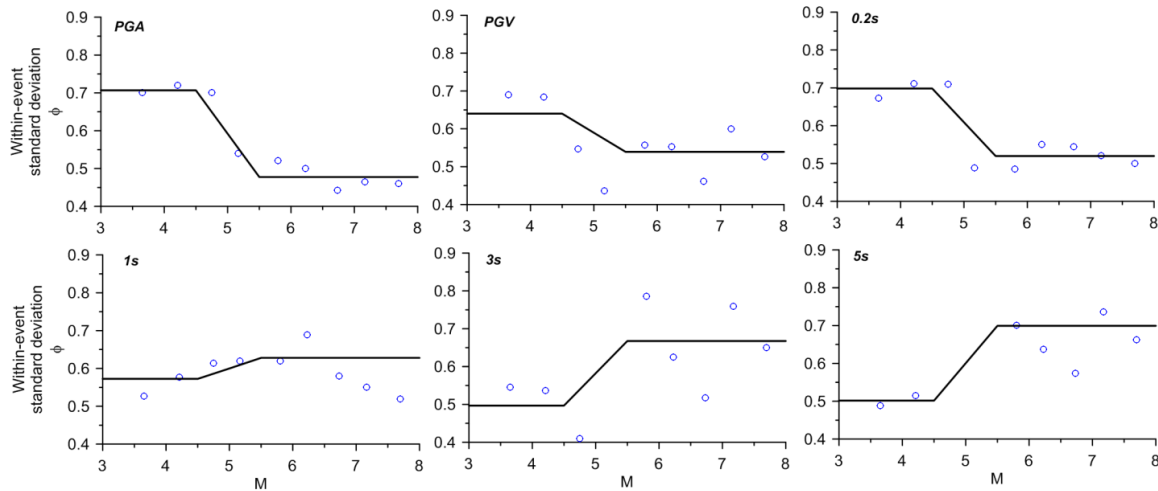
Figure 6.39. Within-event standard deviation terms against magnitude using Phase II data set and base-case GMPE. Horizontal black lines indicate σ values for M < 4.5 and M > 5.5.
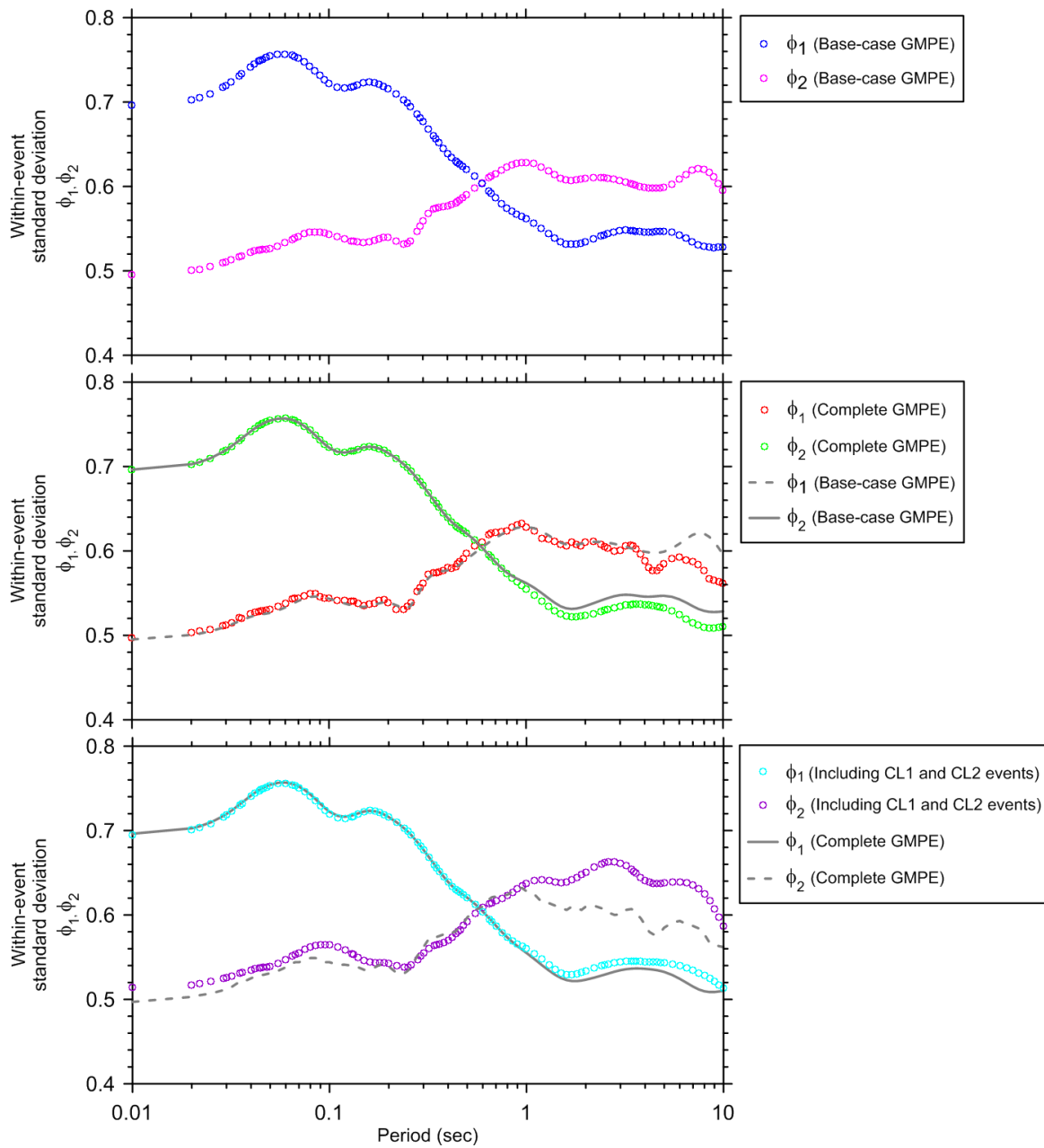
Figure 6.40. Within-event standard deviation terms against period for (a) base-case GMPE; (b) complete GMPE, which includes regional anelastic attenuation and basin depth terms; and (c) including both CL1 and CL2 events.

Because many applications of our GMPE will involve source-site distances beyond 80 km, we next consider standard deviations for data beyond 80 km (these analyses use CL1 events only). Because data beyond 80 km is poorly suited to the analysis of event terms, we maintain the event terms and ϕ evaluated using the Phase II data set and 'Complete GMPE', as described above. We compute within-event standard deviations for various distance ranges beyond 80 km, with the results shown in Figure 6.41. We see that ϕ rises as the distance range increases. We attribute this increased standard deviation to variability in regional anelastic attenuation effects that are not fully captured by our model (e.g., there are regions in the data set for which we do not have a regional Δc_3 term). To capture this effect, we adjust the ϕ model from Eqn (6.19) to include an additive term that is applicable for $R_{JB} > 80$ km as follows:

$$\phi\left(\mathbf{M}, R_{JB}\right) = \begin{cases} \phi\left(\mathbf{M}\right) & R_{JB} \leq R_1 \\ \phi\left(\mathbf{M}\right) + \Delta\phi_R\left(\dfrac{\ln\left(R_{JB}/R_1\right)}{\ln\left(R_2/R_1\right)}\right) & R_1 < R_{JB} \leq R_2 \\ \phi\left(\mathbf{M}\right) + \Delta\phi_R & R_{JB} > R_2 \end{cases} \qquad (6.20)$$

The term $\Delta\phi_R$ in Eqn. (6.20) is computed using data for M ≥ 5.5 only, because we consider the small-magnitude and large-distance results to have little practical significance for hazard assessment. Terms R_1 and R_2 are selected by visual inspection of many plots similar to those in Figure 6.41; they represent the maximum distance to which the complete GMPE ϕ terms are considered applicable (R_1, generally 80 to 130 km) and the distance beyond which we capped ϕ increases with distance (R_2, generally 200 to 270 km). Parameter $\Delta\phi_R$ ranges from about 0.15 at short periods to about 0.05 at long periods, with PGA at 0.1.
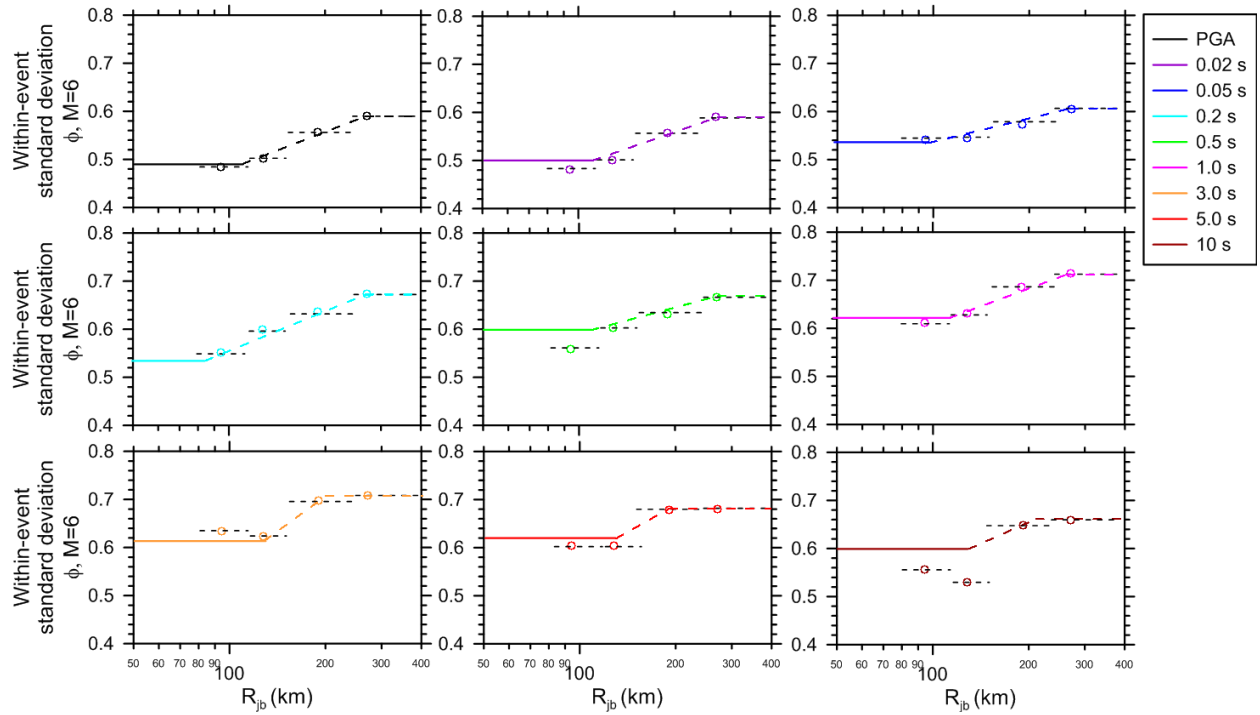
Figure 6.41. **Effects of distance on within-event standard deviation terms for M ≥ 5.5 earthquakes. The discrete symbols indicated computed values of ϕ in non-overlapping distance bins for R_{jb} > 80 km. The horizontal solid lines are values of ϕ_2 shown previously (e.g., from Figures 6.39-6.40). The dotted lines are the proposed distance-dependent model from Eqn. (6.20).**

It should be realized that the increased value of σ at distances beyond 80 km may be reflecting regional variability in attenuation amongst the data included in the NGA-West 2 database. Thus, we expect that this increase is being strongly influenced by epistemic uncertainty in regional attenuation rates, not random site-to-site variability. If such epistemic uncertainty is being captured in a seismic hazard analysis by the use of alternative GMPEs, it should not be double-counted by including it also within the aleatory uncertainty of each GMPE. Mean seismic hazard analysis results are insensitive to whether uncertainty is treated as being epistemic or aleatory (e.g. McGuire, 2004), but the total amount of uncertainty is

important. It is therefore important to recognize the extent to which some components of apparent aleatory variability may be epistemic, and avoid double counting of uncertainty in practical applications.

In Figure 6.42, we plot values of ϕ within V_{S30} bins (four equally-spaced bins per log cycle of V_{s30}). We observe ϕ to decrease with V_{s30} at short periods over the approximate range of 150 to 300 m/s (there are also large changes in ϕ for the fastest V_{s30} bin relative to those before, which is affected by relatively small data size and is not considered meaningful). Similar features have been observed previously (Choi and Stewart, 2005), with the lower ϕ values for soft sites being attributed to nonlinear site response, which amplifies weak motions and de-amplifies strong motions, thus reducing standard deviation relative to motions on the underlying reference site conditions.
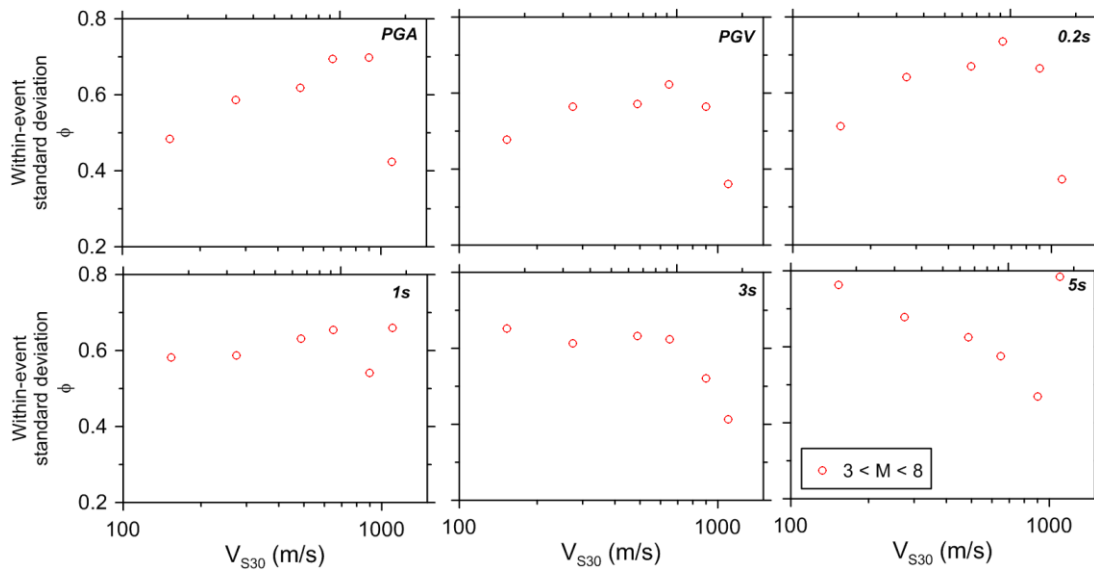
Figure 6.42. **Within-event standard deviation terms against V$_{S30}$ using complete GMPE and using CL1 data for R$_{jb}$ < 300 km and all M.**

239

In Figure 6.43, we evaluate the V_{s30}-dependent shift of ϕ within M and R_{jb} bins for subsets of data with $V_{s30} > 300$ m/s and $V_{s30} < 225$ m/s. For comparison, the ϕ values from the M- and R_{jb}-dependent model (Eqn. 6.19-6.20) are also shown. We observe that in the close-distance data sets ($R_{jb} \leq R_1$), the ϕ terms for $V_{s30} > 300$ m/s match those from the models, so no adjustment is needed for this condition (some offsets are observed for larger distances, which are not considered for our standard deviation models). On the other hand, for $V_{s30} < 225$ m/s, ϕ terms are reduced relative to the model by amounts generally ranging from 0.05 to 0.1. We capture this effect as follows:

$$\phi\left(\mathbf{M}, R_{JB}, V_{S30}\right) = \begin{cases} \phi\left(\mathbf{M}, R_{JB}\right) & V_{S30} \geq V_2 \\ \phi\left(\mathbf{M}, R_{JB}\right) - \Delta\phi_V \left(\dfrac{\ln\left(V_2/V_{S30}\right)}{\ln\left(V_2/V_1\right)} \right) & V_1 \leq V_{S30} \leq V_2 \\ \phi\left(\mathbf{M}, R_{JB}\right) - \Delta\phi_V & V_{S30} \leq V_1 \end{cases} \qquad (6.21)$$

The term $\Delta\phi_V$ in Eqn. (6.21) represents the ϕ term correction, and is shown in the lower-left panel of Figure 6.43. Limiting velocities V_1 and V_2 are taken as 225 and 300 m/s, respectively. The term ϕ (M, R_{jb}) in Eqn. (6.21) represents the model from Eqn. (6.20); as such, the relation in Eqn. (6.19), when combined with Eqn. (6.19) and (6.20), represents the recommended relationship for ϕ in our GMPEs (Eqn. 6.21).
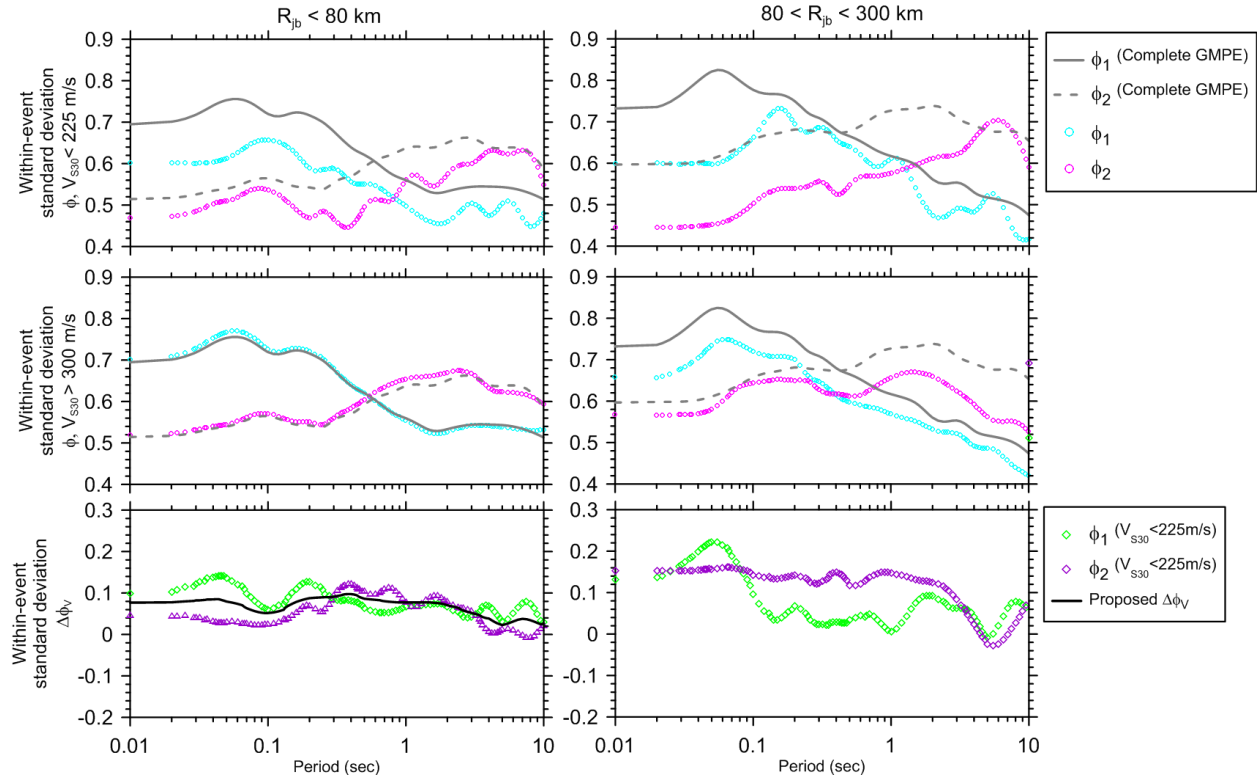
Figure 6.43.   **Effects of V_{S30} on within-event standard deviation terms. We define correction factor $\Delta\phi_V$ from data with $V_{S30} \leq 225$ m/s and $R_{jb} \leq 80$ km.**

6.8   COMPARISON TO BA08' MODEL

Figure 6.44 compares median predictions of BA08' (as modified in Atkinson and Boore, 2011) to the proposed model. The biggest differences between the predictions from the new GMPEs and those of BA08' are for small magnitudes at distances less than 10 to 20 km, where the motions predicted from the new equations are substantially smaller than those from BA08'. In addition, the predicted motions from the new equations are substantially larger than those from BA08' at the longest period (T = 10 s), for which there were few data available to BA08' (and the available data were dominated by one earthquake—the 1999 Chi-Chi earthquake, as shown in

Figure 16 of BA08). The two situations noted (small magnitudes and long periods) correspond to the magnitudes and distances for which there is the most increase of data used in our new work, compared to that available to BA08'.
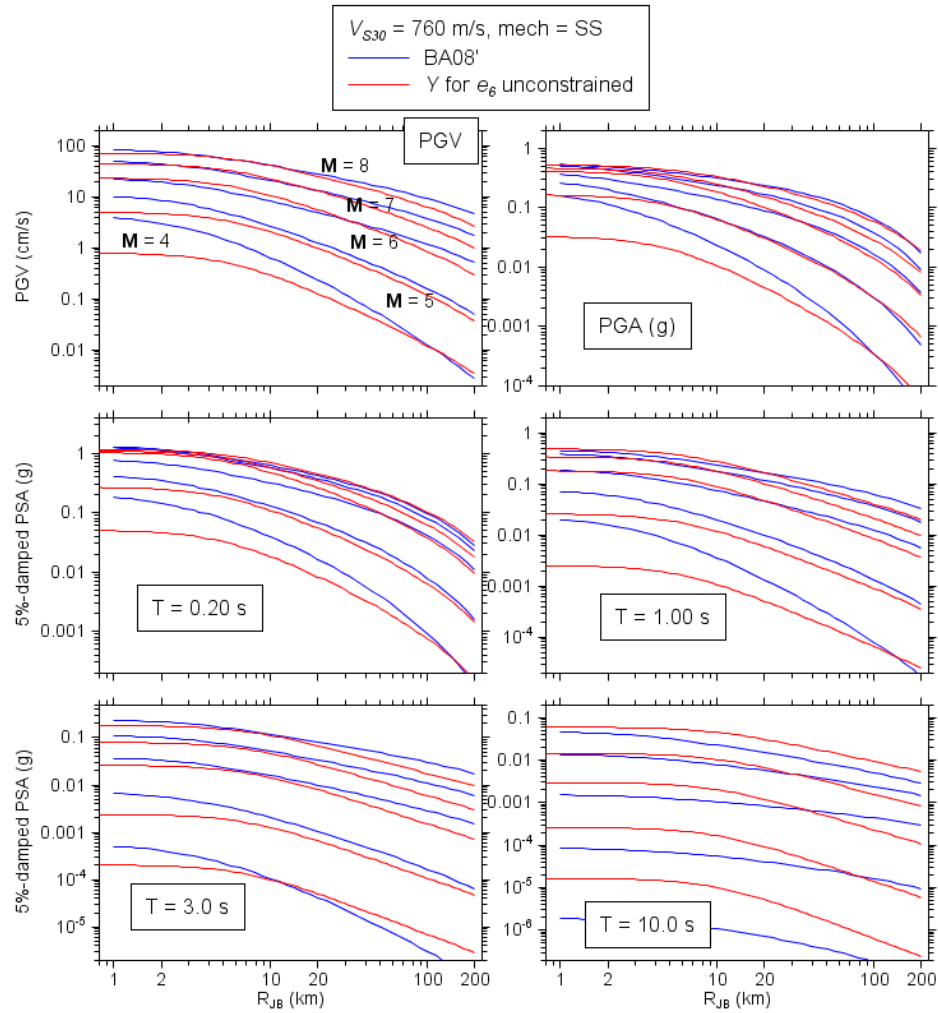
Figure 6.44. Comparison of median trends of proposed GMPE as compared to BA08', as a function of distance. The BA08' values have been adjusted to RotD50 using the ratios RotD50/GMRotI50 in Boore (2010) (maximum adjustment of 1.06 for T=10 s).

Figure 6.45 compares spectra for conditions that are often significant for seismic hazard in the western U.S. – a close-distance **M**6.5 event and a larger-distance **M**8.0 event. For the

M6.5 event the spectra are slightly increased from BA08' across nearly the full range of periods.

For the **M**8.0 event, the spectra are not much changed for $T < 0.5$ sec, are reduced by up to 20-30% for periods between 1 and 3 sec, and are increased beyond approximate 4-5 sec. These trends have been examined carefully and are driven by a number of events with $M > M_h$ that have been added to the database since 2008.
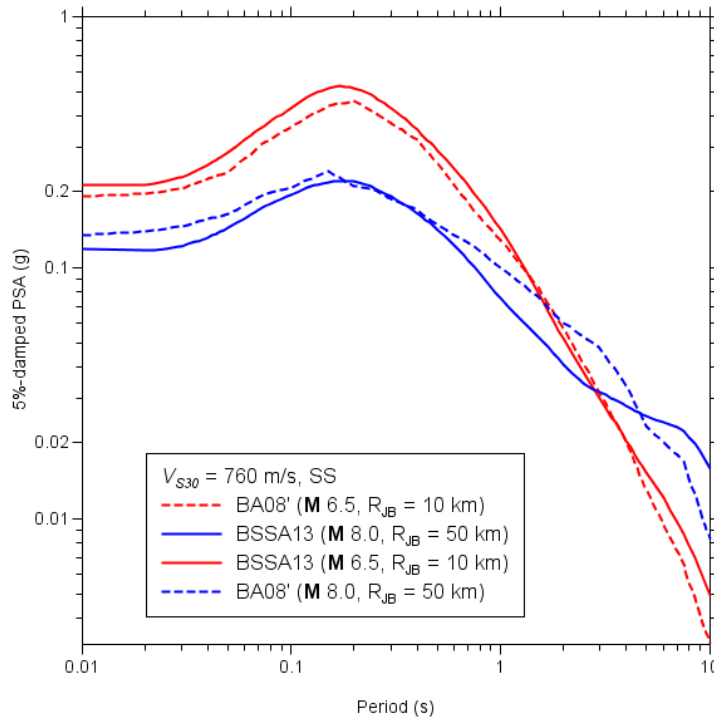
Figure 6.45. Comparison of median PSA of proposed GMPE as compared to BA08' for M6.5 and R$_{JB}$=10 km event and M 8.0 and R$_{JB}$=50 km event. The BA08' values have been adjusted to RotD50 using the ratios RotD50/GMRotI50 in Boore (2010) (maximum adjustment of 1.06 for T=10 s) (Adapted from BEA13).

Figure 6.46 compares standard deviation terms in the present study to those obtained in BA08'. The total standard deviations (σ) from the present study for $M \geq 5.5$, $R_{jb} \leq 80$ km, and $V_{s30} > 300$ m/s are generally comparable to those in BA08', being somewhat higher near $T = 0.1$ sec and lower for $T > 5$ sec. The figure also shows the substantial increase in σ for $M \leq 4.5$

events in the present study, and the relatively dominant effect of within-event variability (ϕ) as compared to between-event variability (τ).
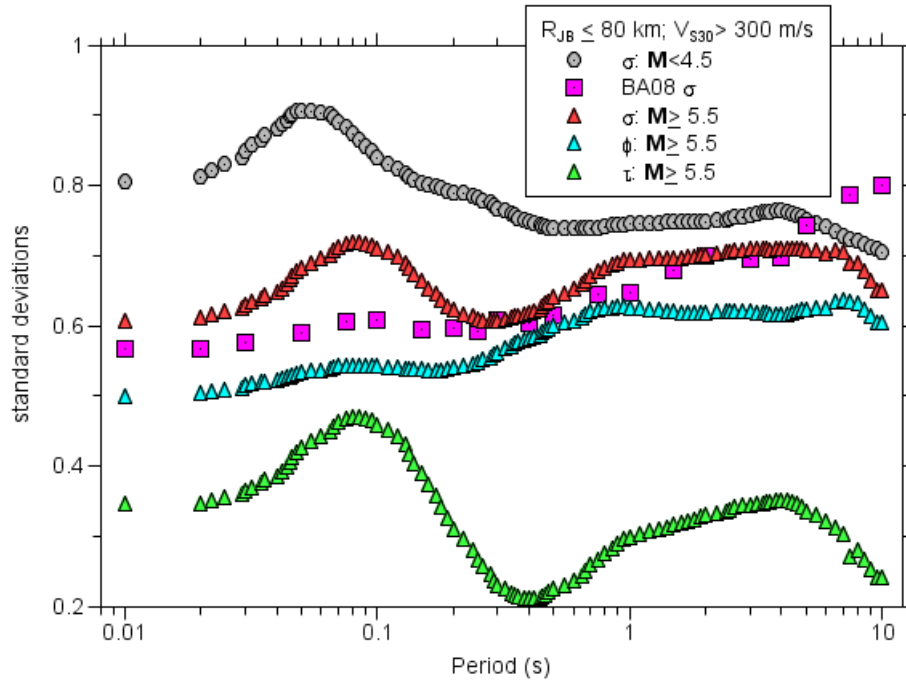
Figure 6.46.   **Comparison of standard deviation terms in proposed GMPE as compared to BA08'** **(Adapted from BEA13).**

6.9   CONCLUSIONS

We have presented a set of ground-motion prediction equations that we believe are the simplest formulation demanded by the NGA-West 2 database used for the regressions. Future versions of the equations might include additional terms if these can be unambiguously supported by data. Data continue to be recorded (our dataset necessarily had to be limited to earthquakes occurring before 2012), and these new data could potentially support the inclusion of more predictor variables. Nevertheless, we think that our equations will be useful, in spite of

the simplified analysis: many predictor variables not included in our equations may be unavailable for use in general seismic hazard analysis applications.

There are a few areas where refinements to the equations are likely over time. One such area of inquiry concerns regional variability of site effects. As noted previously, the regional variability in the site amplification model found by our analysis was not as large as expected, based particularly on the known tendency of Japanese sites to have peak responses at high frequencies. We intend to further investigate the implications of our current findings in relation to other studies (Ghofrani et al., 2013; Stewart et al., 2013). We also intend to evaluate our equations further with respect to directivity and hanging wall effects.

In conclusion, the new relations developed here are a significant improvement over BA08', and provide a demonstrably reliable description of recorded ground-motion amplitudes for shallow crustal earthquakes in active tectonic regions over a wide range of magnitudes, distances, and site conditions.

7   CONCLUSIONS

7.1   SCOPE OF THE RESEARCH

This dissertation combines four multi-disciplinary research studies. The common objective of these studies is to find effective ways to improve the inadequate understanding in accurate ground motion characterization for the use of engineering design purposes.

As described in Chapter 1, ground motions are highly influenced by source, path and site effects. In the first project, I ran the stochastic part of the simulation routine. In the light of the lessons learned from prior work, we focused on removing the too-fast distance attenuation and standard deviation bias by increasing the quality factor and adding randomness to the Fourier spectra. In second project, I started the analysis by comparing the original (2008) NGA site factors to NEHRP site factors to investigate the discrepancies. This work was presented in Chapter 3. Once the misfit was confirmed by analyses, I started to enhance the NGA-West 2 site database to have a more comprehensive data set for further analysis and regressions. Using this data set, I developed a nonlinear site amplification model and proposed new NEHRP site factors for the next updating cycle. This model is then used in a GMPE (BEA13) which I developed in collaboration with others in the group. The studies that are conducted and

outlined here improved the lack in the understanding of ground motion characterization for seismic applications.

7.2   RESEARCH FINDINGS

7.2.1 Calibration of Ground Motion Simulations Findings

As described in Chapter 2, previous validation studies of the hybrid procedure of Graves and Pitarka (2010) that was performed by Star et al., 2011 revealed that high-frequency IMs from this methodology attenuate faster with distance and have lower intra-event dispersion than the median predictions of empirical ground motion prediction equations developed through the NGA project. Although this discrepancy can be attributed to the simulations, GMPEs or both, we considered the fact that the attenuation of high-frequency *IMs* in the NGA models is well constrained up to approximately 100 km for magnitudes between approximately 5.5 and 7.5 and the various models are reasonably consistent (Abrahamson et al. 2008) which in turn relates to the amount of data available to constrain those portions of the empirical models. Thus, we understand this as a paucity in the simulations. We attributed this deficiency mostly to (1) source related terms such as fault dimensions, slip distribution, rupture velocity, etc. and (2) path related terms such as anelastic attenuation, scattering effects, number of ray paths and crustal damping. Our findings after applying the updated parameterization show that:

1) Regarding distance attenuation discrepancy, we have seen the most substantial changes by calibrating the crustal damping and number of ray paths,

2) Ground motions simulated with the increased the quality (increasing the parameter "a" in the frequency-independent portion of the Q model from 25 to 57) exhibit significantly

reduced distance attenuation bias at large distances and revised dispersion terms are more compatible with those from empirical models but remain lower at large distances (e.g., > 100 km),

3) Introducing random site-to-site variations to the Fourier amplitudes using a magnitude dependent log-normal standard deviation (0.45 for $M \leq 6.5$, 0.35 for **M**7.25, 0 for **M**8.0) raised the the intra-event standard deviations of response spectral accelerations to levels consistent with NGA GMPEs in terms of both their overall level and their variation with period,

4) For the **M**8.0 simulations, dispersions from the simulated motions fall-off with distance and are well below those from GMPEs beyond about 10-20 km.

7.2.2 Nonlinear Site Amplification Findings

The site factors incorporated into GMPEs differ from those in the building code, which are presented by BSSC (2009) (typically referred to as NEHRP *Provisions*) (e.g., Huang et al., 2010). These differences create practical difficulties because of caps imposed by regulatory agencies on the levels of ground motion from site specific analysis relative to those developed from prescriptive code procedures. Below are our findings:

1) The NGA and NEHRP site factors are consistent in certain respects (e.g., the scaling of linear site amplification with V_{s30}), but have discrepancies in linear site amplification (applicable for rock PGA $\leq 0.1g$) for site Classes B to E and in the levels of nonlinearity for Classes C and D. The amount of these discrepancies ranges from up to 50% for Class E to amounts ranging from about 0 to 20% for Classes B-D.

2) A major cause of the weak motion amplification misfit is that the NEHRP factors are normalized relative to a reference site condition of V_{ref} = 1050 m/sec (i.e., the equations behind the tabulated factors reach unity at this velocity), whereas their current application is relative to V_{s30} = 760 m/sec. When re-normalized to V_{s30} = 760 m/sec, the NEHRP factors are much closer to NGA factors (especially for Class D), although misfits remain for Classes B, C, and E.

3) The levels of nonlinearity in the NEHRP factors are generally stronger than recent simulation-based models as well as empirically-based models. We find that the nonlinearity in F_a and F_v from recent simulation-based work (WEA08) is smaller than the nonlinearity in the NEHRP factors (Dobry et al. 2000). Those reduced levels of nonlinearity are consistent with trends from empirical ground motion data.

4) Levels of nonlinearity evaluated empirically were found to generally be similar to those implied by a simulation-based model (KEA13).

5) When regional anelastic attenuation effects are considered in the data analysis and the data is extended to large distances, regional site response effects are relatively modest. We found that presence of such trends is sensitive to data selection criteria. When a relatively short cut-off distance is used to minimize anelastic attenuation effects (less than approximately 80 km), regional effects are much stronger, especially for Japanese data at short periods. The nonlinearity in site amplification does not show strong evidence of regional variability. Regional variations are less significant at mid- and long-periods. When data from greater distances were considered (up to approximately 400 km) with appropriate corrections for regional variations in anelastic attenuation, regional variations in V_{s30}-scaling are diminished to the point that the proposed site amplification model (in BEA13) does not include a regional term.

7.2.3 Ground Motion Prediction Equations Findings

The complexity and sophistication of GMPEs has evolved over time as ground-motion databases and associated metadata concerning source and site conditions has grown. The larger and more comprehensive the available database, the greater the resolving power of empirical regression techniques to sort out the many effects that control ground motions. The GMPE presented in Chapter 6 builds on the GMPEs of Boore and Atkinson (2008). Some major changes have been made to BA08 GMPE. Our findings are listed below:

1) The updated version of the site database and accordingly, the NGA-West 2 strong ground motion database provided more robust estimates of the site parameters used in GMPEs and enables us to improve the resolving power of empirical regression techniques to sort out the many effects that control ground motions.

2) We investigated the effects of the distinction between mainshock and aftershock motions; the influence of depth to top of rupture; basin depth effects; and regional variations of site effects and anelastic distance attenuation. Among these, only basin depth and regional apparent anelastic attenuation were found to be statistically significant.

3) We found that over the magnitude range of engineering interest (M > 5) the empirical equations are unbiased with respect to source depth, as represented by either depth to top-of-rupture or hypocentral depth. Hence, a depth term is not introduced.

4) We observed that there is regional differences in apparent anelastic attenuation, the base-case GMPEs are unbiased for data from California and Taiwan, but other regions exhibit faster (Italy and Japan) or slower (China and Turkey) attenuation rates for which adjustment factors are introduced.

5) Residuals trends with $\delta \hat{z}_1$ for Japan is found to be strongest, particularly for negative values of $\delta \hat{z}_1$, whereas trends are the weakest for California. The levels of maximum mean amplification for positive $\delta \hat{z}_1$ are relatively consistent across regions, being approximately 0.5 to 0.75 (in natural log units) at long periods.

6) The between-event component has increasing trends with M with most of the change occurring between magnitudes of approximately 4.5 to 5.5.

7) The within-event component has variable trends with M for different spectral periods (decreases for short periods, increases for long period), increases with distance for $R_{jb} > 80$ km, and is reduced for soft soil sites.

7.3   RECOMMENDATIONS FOR FUTURE RESEARCH

Some items that remain to be investigated in further future studies are listed below:

1) The shorter wavelength features, such as high frequency anelasticity and scattering, are less well constrained, and may require further refinement through ongoing calibration and validation studies.

2) We acknowledge that the dispersion adjustments in the current study were achieved through a simple process of Fourier amplitude randomization. It would be desirable to achieve additional dispersion through variations of physical parameters associated with the source and path models. For example, a more detailed and rigorous exploration of path scattering effects could be used to develop a path-randomization operator that might possibly explain the observed distance dependence of dispersion in the current simulations.

3) The modifications developed here are being implemented in the SCEC broadband simulation platform for general use. These modifications are specific to the Graves and Pitarka (2010) simulation procedure. We recommend similar validation and calibration exercises be carried out for other simulation platforms.

4) Due to the source characterization, intra event standard deviation is expected to be low for ShakeOut event. This part of the model is not validated and would be interesting to see the results of it in a future study.

5) The topic of site amplification in GMPEs would benefit from additional research. One general area of inquiry would be on the use of site parameters other than V_{s30} to improve site amplification functions (e.g., depth and site period). Such parameters may well be able to explain some of the unresolved questions related to regional variations in site terms, which almost certainly are associated with between-region variations in geologic conditions.

6) Current simulation-based modeling techniques are not able to provide a theoretical justification for the nonlinearity that is observed empirically (e.g., at 3.0 sec period). Further data analysis will also help to clarify whether those observations are robust.

7) There will always be an element of epistemic uncertainty in site response. Additional research is needed to define methodologies to better capture the range of viable models for site amplification at long periods, including possible nonlinear effects.

8) As noted in this dissertation, the regional variability in the site amplification model found by our analysis was not as large as expected, based particularly the known tendency of Japanese sites to have peak responses at high frequencies. We intend to further investigate the implications of our current findings in relation to other studies. We also intend to evaluate our

equations further with respect to both the data and the other NGA GMPEs, to more fully

understand their relative constraints and limitations.

APPENDIX: GMPE COEFFICIENTS TABLES

BEA13	Magnitude Scaling								Distance Scaling					
Period (sec)	e_0	e_1	e_2	e_3	e_4	e_5	e_6	M_h	c_1	c_2	c_3	M_{ref}	R_{ref} (km)	h (km)
-1	5.037	5.078	4.849	5.033	1.073	-0.1536	0.2252	6.2	-1.243	0.1489	-0.00344	4.5	1	5.3
0	0.4473	0.4856	0.2459	0.4539	1.431	0.05053	-0.1662	5.5	-1.134	0.1917	-0.00809	4.5	1	4.5
0.01	0.4534	0.4916	0.2519	0.4599	1.421	0.04932	-0.1659	5.5	-1.134	0.1916	-0.00809	4.5	1	4.5
0.02	0.48598	0.52359	0.29707	0.48875	1.4331	0.053388	-0.16561	5.5	-1.1394	0.18962	-0.00807	4.5	1	4.5
0.022	0.49866	0.53647	0.31347	0.49973	1.4336	0.054888	-0.1652	5.5	-1.1405	0.18924	-0.0081	4.5	1	4.5
0.025	0.52283	0.5613	0.34426	0.51999	1.4328	0.057529	-0.16499	5.5	-1.1419	0.18875	-0.00815	4.5	1	4.5
0.029	0.55949	0.59923	0.39146	0.54995	1.4279	0.060732	-0.16632	5.5	-1.1423	0.18844	-0.00829	4.5	1	4.5
0.03	0.56916	0.6092	0.40391	0.55783	1.4261	0.061444	-0.1669	5.5	-1.1421	0.18842	-0.00834	4.5	1	4.49
0.032	0.58802	0.62875	0.42788	0.5733	1.4227	0.062806	-0.16813	5.5	-1.1412	0.1884	-0.00845	4.5	1	4.45
0.035	0.61636	0.65818	0.46252	0.59704	1.4174	0.064559	-0.17015	5.5	-1.1388	0.18839	-0.00864	4.5	1	4.4
0.036	0.62554	0.66772	0.47338	0.60496	1.4158	0.065028	-0.17083	5.5	-1.1378	0.18837	-0.00872	4.5	1	4.38
0.04	0.66281	0.70604	0.51532	0.63828	1.409	0.066183	-0.17357	5.5	-1.1324	0.18816	-0.00903	4.5	1	4.32
0.042	0.68087	0.72443	0.53445	0.65505	1.4059	0.066438	-0.17485	5.5	-1.1292	0.18797	-0.0092	4.5	1	4.29
0.044	0.69882	0.74277	0.55282	0.67225	1.4033	0.066663	-0.17619	5.5	-1.1259	0.18775	-0.00936	4.5	1	4.27
0.045	0.70822	0.75232	0.56222	0.68139	1.4021	0.066774	-0.17693	5.5	-1.1242	0.18764	-0.00944	4.5	1	4.25
0.046	0.71779	0.76202	0.57166	0.69076	1.4009	0.066891	-0.17769	5.5	-1.1224	0.18752	-0.00952	4.5	1	4.24
0.048	0.73574	0.78015	0.58888	0.70854	1.3991	0.067127	-0.1792	5.5	-1.1192	0.1873	-0.00968	4.5	1	4.22

0.05	0.75436	0.79905	0.60652	0.72726	1.3974	0.067357	-0.18082	5.5	-1.1159	0.18709	-0.00982	4.5	1	4.2
0.055	0.7996	0.8445	0.6477	0.7737	1.3947	0.067797	-0.1848	5.5	-1.1082	0.18655	-0.01012	4.5	1	4.15
0.06	0.84394	0.88884	0.68562	0.82067	1.3954	0.068591	-0.18858	5.5	-1.1009	0.18582	-0.01033	4.5	1	4.11
0.065	0.88655	0.93116	0.71941	0.86724	1.4004	0.070127	-0.19176	5.5	-1.0942	0.18485	-0.01048	4.5	1	4.08
0.067	0.9027	0.94711	0.73171	0.88526	1.4032	0.070895	-0.19291	5.5	-1.0918	0.18442	-0.01052	4.5	1	4.07
0.07	0.92652	0.97057	0.7494	0.91227	1.4082	0.072075	-0.19451	5.5	-1.0884	0.18369	-0.01056	4.5	1	4.06
0.075	0.96447	1.0077	0.77678	0.9563	1.4174	0.073549	-0.19665	5.5	-1.0831	0.18225	-0.01058	4.5	1	4.04
0.08	1.0003	1.0426	0.80161	0.99818	1.4261	0.073735	-0.19816	5.5	-1.0785	0.18052	-0.01056	4.5	1	4.02
0.085	1.034	1.0755	0.82423	1.0379	1.4322	0.07194	-0.19902	5.51	-1.0745	0.17856	-0.01051	4.5	1	4.03
0.09	1.0666	1.1076	0.84591	1.0762	1.435	0.068097	-0.19929	5.52	-1.0709	0.17643	-0.01042	4.5	1	4.07
0.095	1.0981	1.1385	0.86703	1.1127	1.4339	0.062327	-0.199	5.53	-1.0678	0.1742	-0.01032	4.5	1	4.1
0.1	1.1268	1.1669	0.8871	1.1454	1.4293	0.055231	-0.19838	5.54	-1.0652	0.17203	-0.0102	4.5	1	4.13
0.11	1.1785	1.2179	0.92702	1.203	1.411	0.037389	-0.19601	5.57	-1.0607	0.1677	-0.00996	4.5	1	4.19
0.12	1.223	1.2621	0.96616	1.2502	1.3831	0.016373	-0.19265	5.62	-1.0572	0.16352	-0.00972	4.5	1	4.24
0.13	1.2596	1.2986	1.0031	1.2869	1.3497	-0.00516	-0.18898	5.66	-1.0549	0.15982	-0.00948	4.5	1	4.29
0.133	1.2692	1.3082	1.0135	1.2961	1.3395	-0.01135	-0.18792	5.67	-1.0545	0.15882	-0.0094	4.5	1	4.3
0.14	1.2883	1.327	1.036	1.3137	1.3162	-0.02471	-0.18566	5.7	-1.0537	0.15672	-0.00923	4.5	1	4.34
0.15	1.3095	1.3481	1.0648	1.3324	1.2844	-0.04207	-0.18234	5.74	-1.0532	0.15401	-0.00898	4.5	1	4.39
0.16	1.3235	1.3615	1.0876	1.3437	1.2541	-0.05759	-0.17853	5.78	-1.0533	0.15158	-0.00873	4.5	1	4.44
0.17	1.3306	1.3679	1.104	1.3487	1.2244	-0.07186	-0.17421	5.82	-1.0541	0.14948	-0.00847	4.5	1	4.49
0.18	1.3327	1.3689	1.1149	1.3492	1.1941	-0.08564	-0.16939	5.85	-1.0556	0.14768	-0.00822	4.5	1	4.53
0.19	1.3307	1.3656	1.1208	1.3463	1.1635	-0.09888	-0.16404	5.89	-1.0579	0.14616	-0.00797	4.5	1	4.57
0.2	1.3255	1.359	1.122	1.3414	1.1349	-0.11096	-0.15852	5.92	-1.0607	0.14489	-0.00772	4.5	1	4.61
0.22	1.3091	1.3394	1.1133	1.3281	1.0823	-0.133	-0.14704	5.97	-1.067	0.14263	-0.00722	4.5	1	4.68
0.24	1.2881	1.315	1.0945	1.3132	1.0366	-0.15299	-0.13445	6.03	-1.0737	0.14035	-0.00675	4.5	1	4.75
0.25	1.2766	1.3017	1.0828	1.3052	1.0166	-0.16213	-0.12784	6.05	-1.0773	0.13925	-0.00652	4.5	1	4.78

0.26	1.2651	1.2886	1.071	1.2972	0.99932	-0.17041	-0.12115	6.07	-1.0808	0.13818	-0.00629	4.5	1	4.82
0.28	1.2429	1.2635	1.0476	1.2815	0.97282	-0.18463	-0.10714	6.11	-1.0879	0.13604	-0.00587	4.5	1	4.88
0.29	1.2324	1.2517	1.0363	1.2736	0.96348	-0.19057	-0.10011	6.12	-1.0913	0.13499	-0.00567	4.5	1	4.9
0.3	1.2217	1.2401	1.0246	1.2653	0.95676	-0.1959	-0.09286	6.14	-1.0948	0.13388	-0.00548	4.5	1	4.93
0.32	1.2007	1.2177	1.0011	1.2479	0.95004	-0.20454	-0.07892	6.16	-1.1013	0.13179	-0.00512	4.5	1	4.98
0.34	1.179	1.1955	0.97677	1.2286	0.94956	-0.21134	-0.06513	6.18	-1.1074	0.12984	-0.00481	4.5	1	5.03
0.35	1.1674	1.1836	0.9638	1.2177	0.95077	-0.21446	-0.05792	6.18	-1.1105	0.1289	-0.00466	4.5	1	5.06
0.36	1.1558	1.172	0.9512	1.2066	0.95278	-0.21716	-0.05104	6.19	-1.1133	0.12806	-0.00453	4.5	1	5.08
0.38	1.1305	1.1468	0.9244	1.1816	0.95899	-0.22214	-0.03676	6.19	-1.119	0.12647	-0.00428	4.5	1	5.12
0.4	1.1046	1.1214	0.89765	1.1552	0.96766	-0.22608	-0.02319	6.2	-1.1243	0.12512	-0.00405	4.5	1	5.16
0.42	1.0782	1.0955	0.87067	1.1276	0.97862	-0.22924	-0.01042	6.2	-1.1291	0.12389	-0.00385	4.5	1	5.2
0.44	1.0515	1.0697	0.84355	1.0995	0.99144	-0.23166	0.001168	6.2	-1.1337	0.12278	-0.00367	4.5	1	5.24
0.45	1.0376	1.0562	0.82941	1.0847	0.99876	-0.23263	0.006589	6.2	-1.1359	0.12227	-0.00359	4.5	1	5.25
0.46	1.0234	1.0426	0.81509	1.0696	1.0064	-0.2335	0.011871	6.2	-1.1381	0.12177	-0.00351	4.5	1	5.27
0.48	0.99719	1.0172	0.7886	1.0415	1.0215	-0.23464	0.020767	6.2	-1.142	0.12093	-0.00336	4.5	1	5.3
0.5	0.96991	0.99106	0.7615	1.012	1.0384	-0.23522	0.029119	6.2	-1.1459	0.12015	-0.00322	4.5	1	5.34
0.55	0.9048	0.9283	0.6984	0.9417	1.0833	-0.23449	0.046932	6.2	-1.1543	0.11847	-0.0029	4.5	1	5.41
0.6	0.84165	0.86715	0.63875	0.87351	1.1336	-0.23128	0.062667	6.2	-1.1615	0.11671	-0.00261	4.5	1	5.48
0.65	0.78181	0.80876	0.58231	0.80948	1.1861	-0.22666	0.077997	6.2	-1.1676	0.11465	-0.00236	4.5	1	5.53
0.667	0.76262	0.78994	0.56422	0.78916	1.2035	-0.22497	0.083058	6.2	-1.1694	0.11394	-0.00228	4.5	1	5.54
0.7	0.72513	0.75302	0.52878	0.74985	1.2375	-0.22143	0.093185	6.2	-1.1728	0.11253	-0.00213	4.5	1	5.56
0.75	0.66903	0.69737	0.47523	0.69173	1.2871	-0.21591	0.10829	6.2	-1.1777	0.11054	-0.00193	4.5	1	5.6
0.8	0.61346	0.64196	0.42173	0.63519	1.3341	-0.21047	0.12256	6.2	-1.1819	0.10873	-0.00175	4.5	1	5.63
0.85	0.55853	0.58698	0.36813	0.57969	1.378	-0.20528	0.13608	6.2	-1.1854	0.10709	-0.0016	4.5	1	5.66
0.9	0.50296	0.53136	0.31376	0.52361	1.4208	-0.20011	0.14983	6.2	-1.1884	0.10548	-0.00146	4.5	1	5.69
0.95	0.44701	0.47541	0.25919	0.46706	1.4623	-0.1949	0.16432	6.2	-1.1909	0.10389	-0.00133	4.5	1	5.72

1	0.3932	0.4218	0.207	0.4124	1.5004	-0.18983	0.17895	6.2	-1.193	0.10248	-0.00121	4.5	1	5.74
1.1	0.28484	0.31374	0.10182	0.30209	1.569	-0.18001	0.21042	6.2	-1.1966	0.10016	-0.00099	4.5	1	5.82
1.2	0.1734	0.20259	-0.0062	0.18866	1.6282	-0.1709	0.2441	6.2	-1.1996	0.098482	-0.0008	4.5	1	5.92
1.3	0.06152	0.09106	-0.11345	0.07433	1.6794	-0.16233	0.27799	6.2	-1.2018	0.097375	-0.00064	4.5	1	6.01
1.4	-0.04575	-0.0157	-0.2155	-0.03607	1.7239	-0.15413	0.30956	6.2	-1.2039	0.096743	-0.00049	4.5	1	6.1
1.5	-0.14954	-0.11866	-0.3138	-0.1437	1.7622	-0.1467	0.33896	6.2	-1.2063	0.096445	-0.00037	4.5	1	6.18
1.6	-0.2486	-0.21672	-0.40682	-0.24708	1.7955	-0.13997	0.36616	6.2	-1.2086	0.096338	-0.00026	4.5	1	6.26
1.7	-0.34145	-0.3084	-0.49295	-0.34465	1.8259	-0.13361	0.39065	6.2	-1.2106	0.096254	-0.00017	4.5	1	6.33
1.8	-0.42975	-0.39558	-0.57388	-0.43818	1.8564	-0.12686	0.41244	6.2	-1.2123	0.096207	-9.9E-05	4.5	1	6.4
1.9	-0.51276	-0.47731	-0.64899	-0.52682	1.8868	-0.11959	0.43151	6.2	-1.2141	0.096255	-4.2E-05	4.5	1	6.48
2	-0.58669	-0.55003	-0.71466	-0.60658	1.9152	-0.11237	0.44788	6.2	-1.2159	0.096361	0	4.5	1	6.54
2.2	-0.72143	-0.6822	-0.83003	-0.75402	1.9681	-0.09802	0.48024	6.2	-1.219	0.096497	0	4.5	1	6.66
2.4	-0.8481	-0.8069	-0.9326	-0.8941	2.017	-0.08377	0.51873	6.2	-1.2202	0.096198	0	4.5	1	6.73
2.5	-0.90966	-0.86765	-0.98228	-0.96187	2.0406	-0.07631	0.53883	6.2	-1.2201	0.096106	0	4.5	1	6.77
2.6	-0.96863	-0.92577	-1.0313	-1.0266	2.0628	-0.06893	0.5581	6.2	-1.2198	0.096136	0	4.5	1	6.81
2.8	-1.0817	-1.0367	-1.1301	-1.1495	2.1014	-0.05523	0.59394	6.2	-1.2189	0.096667	0	4.5	1	6.87
3	-1.1898	-1.142	-1.23	-1.2664	2.1323	-0.04332	0.62694	6.2	-1.2179	0.097638	0	4.5	1	6.93
3.2	-1.2914	-1.2406	-1.3255	-1.376	2.1545	-0.03444	0.65811	6.2	-1.2169	0.098649	-2.3E-05	4.5	1	6.99
3.4	-1.386	-1.3322	-1.415	-1.4786	2.1704	-0.02789	0.68755	6.2	-1.216	0.099553	-0.00004	4.5	1	7.08
3.5	-1.4332	-1.3778	-1.4599	-1.5297	2.1775	-0.025	0.70216	6.2	-1.2156	0.099989	-4.5E-05	4.5	1	7.12
3.6	-1.4762	-1.4193	-1.5014	-1.5764	2.1834	-0.02258	0.71523	6.2	-1.2156	0.10043	-4.9E-05	4.5	1	7.16
3.8	-1.5617	-1.5014	-1.5865	-1.6685	2.1938	-0.01836	0.74028	6.2	-1.2158	0.10142	-5.3E-05	4.5	1	7.24
4	-1.6388	-1.5748	-1.6673	-1.7516	2.204	-0.01464	0.76303	6.2	-1.2162	0.10218	-5.2E-05	4.5	1	7.32
4.2	-1.7116	-1.6439	-1.7451	-1.829	2.2123	-0.01225	0.78552	6.2	-1.2165	0.10269	-4.7E-05	4.5	1	7.39
4.4	-1.7798	-1.7089	-1.8192	-1.9011	2.2181	-0.01146	0.80792	6.2	-1.2169	0.10304	-3.9E-05	4.5	1	7.46
4.6	-1.8469	-1.7731	-1.8923	-1.9712	2.223	-0.01176	0.83126	6.2	-1.2175	0.10324	-2.7E-05	4.5	1	7.52

4.8	-1.9063	-1.8303	-1.9573	-2.0326	2.2268	-0.01288	0.8524	6.2	-1.2182	0.10337	-1.4E-05	4.5	1	7.64
5	-1.966	-1.8882	-2.0245	-2.0928	2.2299	-0.01486	0.87314	6.2	-1.2189	0.10353	0	4.5	1	7.78
5.5	-2.1051	-2.0232	-2.1908	-2.2288	2.2389	-0.0195	0.91466	6.2	-1.2204	0.1046	0	4.5	1	8.07
6	-2.2421	-2.1563	-2.3659	-2.3579	2.2377	-0.02638	0.9487	6.2	-1.2232	0.1075	0	4.5	1	8.48
6.5	-2.3686	-2.2785	-2.5322	-2.477	2.215	-0.03951	0.97643	6.2	-1.2299	0.11231	0	4.5	1	8.9
7	-2.4827	-2.3881	-2.6818	-2.5854	2.172	-0.05914	0.99757	6.2	-1.2408	0.11853	0	4.5	1	9.2
7.5	-2.5865	-2.4874	-2.8176	-2.6854	2.1187	-0.08161	1.0121	6.2	-1.2543	0.12507	0	4.5	1	9.48
8	-2.6861	-2.5829	-2.9438	-2.7823	2.0613	-0.10382	1.0232	6.2	-1.2688	0.13146	0	4.5	1	9.57
8.5	-2.782	-2.6752	-3.0597	-2.8776	2.0084	-0.12114	1.0335	6.2	-1.2839	0.13742	0	4.5	1	9.62
9	-2.8792	-2.7687	-3.1713	-2.9759	1.9605	-0.13407	1.0453	6.2	-1.2989	0.14294	0	4.5	1	9.66
9.5	-2.9769	-2.8634	-3.2785	-3.076	1.9189	-0.14364	1.0567	6.2	-1.313	0.14781	0	4.5	1	9.66
10	-3.0702	-2.9537	-3.3776	-3.1726	1.8837	-0.15096	1.0651	6.2	-1.3253	0.15183	0	4.5	1	9.66

BEA13	Anelastic attenuation			Linear site term			Nonlinear site term				Basin depth	
Period (sec)	Δc_3 (globalCATW)	Δc_3 (ChinaTurkey)	Δc_3 (ItalyJapan)	c	V_c (m/s)	V_{ref} (m/s)	f_1	f_3	f_4	f_5	f_6 (1/km)	f_7
-1	0.00000	0.00435	-0.00033	-0.8050	950.00	760	0	0.1	-0.1000	-0.00844	-9.9	-9.9
0	0.00000	0.00286	-0.00255	-0.5150	925.00	760	0	0.1	-0.1500	-0.00701	-9.9	-9.9
0.01	0.00000	0.00282	-0.00244	-0.5257	930.00	760	0	0.1	-0.1483	-0.00701	-9.9	-9.9
0.02	0.00000	0.00278	-0.00234	-0.5362	967.50	760	0	0.1	-0.1471	-0.00728	-9.9	-9.9
0.022	0.00000	0.00276	-0.00229	-0.5403	964.23	760	0	0.1	-0.1477	-0.00732	-9.9	-9.9
0.025	0.00000	0.00275	-0.00225	-0.5410	961.65	760	0	0.1	-0.1496	-0.00736	-9.9	-9.9
0.029	0.00000	0.00276	-0.00221	-0.5391	959.61	760	0	0.1	-0.1525	-0.00737	-9.9	-9.9

0.03	0.00000	0.00276	-0.00217	-0.5399	959.71	760	0	0.1	-0.1549	-0.00735	-9.9	-9.9
0.032	0.00000	0.00277	-0.00212	-0.5394	956.83	760	0	0.1	-0.1574	-0.00731	-9.9	-9.9
0.035	0.00000	0.00278	-0.00210	-0.5358	955.39	760	0	0.1	-0.1607	-0.00721	-9.9	-9.9
0.036	0.00000	0.00280	-0.00207	-0.5315	954.35	760	0	0.1	-0.1641	-0.00717	-9.9	-9.9
0.04	0.00000	0.00282	-0.00205	-0.5264	953.91	760	0	0.1	-0.1678	-0.00698	-9.9	-9.9
0.042	0.00000	0.00285	-0.00203	-0.5209	954.10	760	0	0.1	-0.1715	-0.00687	-9.9	-9.9
0.044	0.00000	0.00287	-0.00202	-0.5142	955.15	760	0	0.1	-0.1760	-0.00677	-9.9	-9.9
0.045	0.00000	0.00290	-0.00200	-0.5067	957.18	760	0	0.1	-0.1810	-0.00672	-9.9	-9.9
0.046	0.00000	0.00292	-0.00199	-0.4991	960.17	760	0	0.1	-0.1862	-0.00667	-9.9	-9.9
0.048	0.00000	0.00294	-0.00199	-0.4916	963.44	760	0	0.1	-0.1915	-0.00656	-9.9	-9.9
0.05	0.00000	0.00296	-0.00199	-0.4850	967.06	760	0	0.1	-0.1963	-0.00647	-9.9	-9.9
0.055	0.00000	0.00296	-0.00200	-0.4788	970.75	760	0	0.1	-0.2014	-0.00625	-9.9	-9.9
0.06	0.00000	0.00297	-0.00202	-0.4735	973.97	760	0	0.1	-0.2066	-0.00607	-9.9	-9.9
0.065	0.00000	0.00297	-0.00204	-0.4687	976.38	760	0	0.1	-0.2120	-0.00593	-9.9	-9.9
0.067	0.00000	0.00297	-0.00208	-0.4646	977.78	760	0	0.1	-0.2176	-0.00588	-9.9	-9.9
0.07	0.00000	0.00296	-0.00211	-0.4616	978.02	760	0	0.1	-0.2232	-0.00582	-9.9	-9.9
0.075	0.00000	0.00296	-0.00216	-0.4598	977.23	760	0	0.1	-0.2287	-0.00573	-9.9	-9.9
0.08	0.00000	0.00294	-0.00221	-0.4601	974.98	760	0	0.1	-0.2337	-0.00567	-9.9	-9.9
0.085	0.00000	0.00293	-0.00227	-0.4620	972.16	760	0	0.1	-0.2382	-0.00563	-9.9	-9.9
0.09	0.00000	0.00291	-0.00233	-0.4652	969.48	760	0	0.1	-0.2421	-0.00561	-9.9	-9.9
0.095	0.00000	0.00290	-0.00238	-0.4688	966.90	760	0	0.1	-0.2458	-0.00560	-9.9	-9.9
0.1	0.00000	0.00288	-0.00244	-0.4732	964.90	760	0	0.1	-0.2492	-0.00560	-9.9	-9.9
0.11	0.00000	0.00286	-0.00249	-0.4787	963.89	760	0	0.1	-0.2519	-0.00562	-9.9	-9.9
0.12	0.00000	0.00285	-0.00254	-0.4853	964.03	760	0	0.1	-0.2540	-0.00567	-9.9	-9.9
0.13	0.00000	0.00283	-0.00258	-0.4931	965.34	760	0	0.1	-0.2556	-0.00572	-9.9	-9.9
0.133	0.00000	0.00282	-0.00263	-0.5022	967.71	760	0	0.1	-0.2566	-0.00574	-9.9	-9.9

0.14	0.00000	0.00280	-0.00267	-0.5126	970.89	760	0	0.1	-0.2571	-0.00578	-9.9	-9.9
0.15	0.00000	0.00279	-0.00271	-0.5244	974.53	760	0	0.1	-0.2571	-0.00585	-9.9	-9.9
0.16	0.00000	0.00276	-0.00275	-0.5392	977.78	760	0	0.1	-0.2562	-0.00591	-9.9	-9.9
0.17	0.00000	0.00273	-0.00280	-0.5569	979.37	760	0	0.1	-0.2544	-0.00597	-9.9	-9.9
0.18	0.00000	0.00270	-0.00285	-0.5758	979.38	760	0	0.1	-0.2522	-0.00602	-9.9	-9.9
0.19	0.00000	0.00266	-0.00291	-0.5962	978.42	760	0	0.1	-0.2497	-0.00608	-9.9	-9.9
0.2	0.00000	0.00261	-0.00297	-0.6192	975.61	760	0	0.1	-0.2466	-0.00614	-9.9	-9.9
0.22	0.00000	0.00256	-0.00303	-0.6426	971.31	760	0	0.1	-0.2432	-0.00626	-9.9	-9.9
0.24	0.00000	0.00251	-0.00308	-0.6658	965.97	760	0	0.1	-0.2396	-0.00638	-9.9	-9.9
0.25	0.00000	0.00244	-0.00314	-0.6897	960.05	760	0	0.1	-0.2357	-0.00644	-9.9	-9.9
0.26	0.00000	0.00238	-0.00319	-0.7133	954.24	760	0	0.1	-0.2315	-0.00650	-9.9	-9.9
0.28	0.00000	0.00231	-0.00324	-0.7356	948.77	760	0	0.1	-0.2274	-0.00660	-9.9	-9.9
0.29	0.00000	0.00225	-0.00327	-0.7567	943.90	760	0	0.1	-0.2232	-0.00665	-9.9	-9.9
0.3	0.00000	0.00220	-0.00330	-0.7749	940.75	760	0	0.1	-0.2191	-0.00670	-9.9	-9.9
0.32	0.00000	0.00215	-0.00330	-0.7902	939.61	760	0	0.1	-0.2152	-0.00680	-9.9	-9.9
0.34	0.00000	0.00212	-0.00330	-0.8048	939.66	760	0	0.1	-0.2112	-0.00689	-9.9	-9.9
0.35	0.00000	0.00210	-0.00329	-0.8186	940.74	760	0	0.1	-0.2070	-0.00693	-9.9	-9.9
0.36	0.00000	0.00210	-0.00327	-0.8298	943.02	760	0	0.1	-0.2033	-0.00697	-9.9	-9.9
0.38	0.00000	0.00210	-0.00324	-0.8401	945.83	760	0	0.1	-0.1996	-0.00705	-9.9	-9.9
0.4	0.00000	0.00211	-0.00321	-0.8501	949.18	760	0	0.1	-0.1958	-0.00713	-9.9	-9.9
0.42	0.00000	0.00213	-0.00318	-0.8590	952.96	760	0	0.1	-0.1922	-0.00719	-9.9	-9.9
0.44	0.00000	0.00216	-0.00313	-0.8685	957.31	760	0	0.1	-0.1884	-0.00726	-9.9	-9.9
0.45	0.00000	0.00220	-0.00308	-0.8790	962.25	760	0	0.1	-0.1840	-0.00729	-9.9	-9.9
0.46	0.00000	0.00225	-0.00302	-0.8903	967.61	760	0	0.1	-0.1793	-0.00732	-9.9	-9.9
0.48	0.00000	0.00230	-0.00296	-0.9011	972.54	760	0	0.1	-0.1749	-0.00738	-9.9	-9.9
0.5	0.00000	0.00235	-0.00291	-0.9118	977.09	760	0	0.1	-0.1704	-0.00744	-9.9	-9.9

0.55	0.00000	0.00240	-0.00285	-0.9227	981.13	760	0	0.1	-0.1658	-0.00758	-9.9	-9.9
0.6	0.00000	0.00245	-0.00279	-0.9338	984.26	760	0	0.1	-0.1610	-0.00773	-9.9	-9.9
0.65	0.00000	0.00251	-0.00273	-0.9453	986.32	760	0	0.1	-0.1558	-0.00787	0.006	0.004
0.667	0.00000	0.00257	-0.00266	-0.9573	987.12	760	0	0.1	-0.1503	-0.00792	0.026	0.017
0.7	0.00000	0.00263	-0.00260	-0.9692	986.52	760	0	0.1	-0.1446	-0.00800	0.055	0.036
0.75	0.00000	0.00269	-0.00253	-0.9811	984.70	760	0	0.1	-0.1387	-0.00812	0.092	0.059
0.8	0.00000	0.00275	-0.00246	-0.9924	981.17	760	0	0.1	-0.1325	-0.00822	0.140	0.088
0.85	0.00000	0.00280	-0.00238	-1.0033	976.97	760	0	0.1	-0.1262	-0.00830	0.195	0.120
0.9	0.00000	0.00284	-0.00229	-1.0139	972.90	760	0	0.1	-0.1197	-0.00836	0.252	0.152
0.95	0.00000	0.00288	-0.00220	-1.0250	969.79	760	0	0.1	-0.1126	-0.00841	0.309	0.181
1	0.00000	0.00292	-0.00209	-1.0361	967.51	760	0	0.1	-0.1052	-0.00844	0.367	0.208
1.1	0.00000	0.00295	-0.00198	-1.0467	965.94	760	0	0.1	-0.0977	-0.00847	0.425	0.233
1.2	0.00000	0.00298	-0.00186	-1.0565	965.20	760	0	0.1	-0.0902	-0.00842	0.481	0.256
1.3	0.00000	0.00301	-0.00175	-1.0655	965.38	760	0	0.1	-0.0827	-0.00829	0.536	0.276
1.4	0.00000	0.00303	-0.00163	-1.0736	966.44	760	0	0.1	-0.0753	-0.00806	0.588	0.294
1.5	0.00000	0.00304	-0.00152	-1.0808	968.24	760	0	0.1	-0.0679	-0.00771	0.638	0.309
1.6	0.00000	0.00304	-0.00141	-1.0867	969.94	760	0	0.1	-0.0604	-0.00723	0.689	0.324
1.7	0.00000	0.00303	-0.00132	-1.0904	971.24	760	0	0.1	-0.0534	-0.00666	0.736	0.337
1.8	0.00000	0.00300	-0.00125	-1.0923	971.65	760	0	0.1	-0.0470	-0.00603	0.780	0.350
1.9	0.00000	0.00297	-0.00120	-1.0925	970.45	760	0	0.1	-0.0414	-0.00540	0.824	0.364
2	0.00000	0.00292	-0.00117	-1.0908	966.44	760	0	0.1	-0.0361	-0.00479	0.871	0.382
2.2	0.00000	0.00287	-0.00116	-1.0872	959.61	760	0	0.1	-0.0314	-0.00378	0.920	0.404
2.4	0.00000	0.00281	-0.00115	-1.0819	950.34	760	0	0.1	-0.0271	-0.00302	0.969	0.427
2.5	0.00000	0.00276	-0.00116	-1.0753	939.03	760	0	0.1	-0.0231	-0.00272	1.017	0.451
2.6	0.00000	0.00271	-0.00117	-1.0682	926.85	760	0	0.1	-0.0196	-0.00246	1.060	0.474
2.8	0.00000	0.00266	-0.00118	-1.0605	914.07	760	0	0.1	-0.0165	-0.00208	1.099	0.495

3	0.00000	0.00262	-0.00119	-1.0521	900.07	760	0	0.1	-0.0136	-0.00183	1.135	0.516
3.2	0.00000	0.00259	-0.00119	-1.0435	885.63	760	0	0.1	-0.0112	-0.00167	1.164	0.534
3.4	0.00000	0.00258	-0.00119	-1.0350	871.15	760	0	0.1	-0.0093	-0.00158	1.188	0.551
3.5	0.00000	0.00257	-0.00117	-1.0265	856.21	760	0	0.1	-0.0075	-0.00155	1.211	0.570
3.6	0.00000	0.00257	-0.00115	-1.0180	840.97	760	0	0.1	-0.0058	-0.00154	1.234	0.589
3.8	0.00000	0.00259	-0.00112	-1.0101	826.47	760	0	0.1	-0.0044	-0.00152	1.253	0.609
4	0.00000	0.00261	-0.00108	-1.0028	812.92	760	0	0.1	-0.0032	-0.00152	1.271	0.629
4.2	0.00000	0.00262	-0.00102	-0.9949	799.72	760	0	0.1	-0.0023	-0.00152	1.287	0.652
4.4	0.00000	0.00262	-0.00095	-0.9859	787.55	760	0	0.1	-0.0016	-0.00150	1.300	0.674
4.6	0.00000	0.00262	-0.00084	-0.9748	776.05	760	0	0.1	-0.0010	-0.00148	1.312	0.697
4.8	0.00000	0.00262	-0.00072	-0.9613	765.55	760	0	0.1	-0.0006	-0.00146	1.323	0.719
5	0.00000	0.00260	-0.00057	-0.9456	756.97	760	0	0.1	-0.0003	-0.00144	1.329	0.738
5.5	0.00000	0.00259	-0.00041	-0.9273	735.74	760	0	0.1	-0.0001	-0.00140	1.345	0.778
6	0.00000	0.00258	-0.00023	-0.9063	728.14	760	0	0.1	0.0000	-0.00138	1.350	0.803
6.5	0.00000	0.00259	-0.00004	-0.8822	726.30	760	0	0.1	0.0000	-0.00137	1.349	0.815
7	0.00000	0.00260	0.00017	-0.8551	728.24	760	0	0.1	0.0000	-0.00137	1.342	0.816
7.5	0.00000	0.00260	0.00038	-0.8249	731.96	760	0	0.1	-0.0001	-0.00137	1.329	0.809
8	0.00000	0.00263	0.00072	-0.7990	735.81	760	0	0.1	0.0001	-0.00137	1.308	0.795
8.5	0.00000	0.00267	0.00094	-0.7620	739.50	760	0	0.1	0.0001	-0.00137	1.282	0.777
9	0.00000	0.00276	0.00113	-0.7230	743.07	760	0	0.1	0.0001	-0.00137	1.252	0.754
9.5	0.00000	0.00289	0.00131	-0.6840	746.55	760	0	0.1	0.0001	-0.00136	1.218	0.729
10	0.00000	0.00303	0.00149	-0.6440	750.00	760	0	0.1	0.0000	-0.00136	1.183	0.703

BEA13	Aleatory Uncertainty									
Period (sec)	R_1 (km)	R_2 (km)	$\Delta\phi_R$	$\Delta\phi_V$	V_1 (m/s)	V_2 (m/s)	ϕ_1	ϕ_2	τ_1	τ_2
-1	105.00	272.00	0.082	0.068	225	300	0.644	0.552	0.401	0.346
0	110.00	270.00	0.100	0.084	225	300	0.695	0.495	0.398	0.348
0.01	111.67	270.00	0.096	0.079	225	300	0.698	0.499	0.402	0.345
0.02	113.10	270.00	0.092	0.079	225	300	0.702	0.502	0.409	0.346
0.022	113.37	270.00	0.088	0.080	225	300	0.707	0.505	0.418	0.349
0.025	113.07	270.00	0.086	0.081	225	300	0.711	0.508	0.427	0.354
0.029	112.36	270.00	0.084	0.081	225	300	0.716	0.510	0.436	0.359
0.03	112.13	270.00	0.081	0.082	225	300	0.721	0.514	0.445	0.364
0.032	111.65	270.00	0.078	0.082	225	300	0.726	0.516	0.454	0.369
0.035	110.64	270.00	0.077	0.083	225	300	0.730	0.518	0.462	0.374
0.036	109.53	270.00	0.075	0.083	225	300	0.734	0.520	0.470	0.379
0.04	108.28	270.00	0.073	0.084	225	300	0.738	0.521	0.478	0.384
0.042	106.99	270.00	0.072	0.083	225	300	0.742	0.523	0.484	0.390
0.044	105.41	270.00	0.070	0.083	225	300	0.745	0.525	0.490	0.397
0.045	103.61	270.00	0.069	0.082	225	300	0.748	0.527	0.496	0.405
0.046	101.70	270.00	0.067	0.081	225	300	0.750	0.529	0.499	0.412
0.048	99.76	270.00	0.065	0.079	225	300	0.752	0.530	0.502	0.419
0.05	97.93	270.00	0.063	0.077	225	300	0.753	0.532	0.503	0.426
0.055	96.03	270.00	0.062	0.075	225	300	0.753	0.534	0.502	0.434
0.06	94.10	270.01	0.061	0.073	225	300	0.753	0.536	0.499	0.441
0.065	92.08	270.02	0.061	0.070	225	300	0.752	0.538	0.495	0.448
0.067	90.01	270.02	0.061	0.067	225	300	0.750	0.540	0.489	0.455

0.07	87.97	270.03	0.062	0.064	225	300	0.748	0.541	0.483	0.461
0.075	85.99	270.04	0.064	0.062	225	300	0.745	0.542	0.474	0.466
0.08	84.23	270.05	0.067	0.060	225	300	0.741	0.543	0.464	0.468
0.085	82.74	270.06	0.072	0.058	225	300	0.737	0.543	0.452	0.468
0.09	81.54	270.07	0.076	0.057	225	300	0.734	0.542	0.440	0.466
0.095	80.46	270.08	0.082	0.057	225	300	0.731	0.542	0.428	0.464
0.1	79.59	270.09	0.087	0.057	225	300	0.728	0.541	0.415	0.458
0.11	79.05	270.11	0.093	0.059	225	300	0.726	0.540	0.403	0.451
0.12	78.85	270.13	0.099	0.061	225	300	0.724	0.539	0.392	0.441
0.13	78.99	270.15	0.104	0.063	225	300	0.723	0.538	0.381	0.430
0.133	79.47	270.15	0.110	0.066	225	300	0.722	0.538	0.371	0.417
0.14	80.26	270.16	0.115	0.069	225	300	0.721	0.537	0.362	0.403
0.15	81.33	270.16	0.120	0.072	225	300	0.720	0.537	0.354	0.388
0.16	82.86	270.16	0.125	0.076	225	300	0.720	0.536	0.349	0.372
0.17	84.72	270.14	0.128	0.079	225	300	0.718	0.536	0.346	0.357
0.18	86.67	270.11	0.131	0.081	225	300	0.717	0.536	0.344	0.341
0.19	88.73	270.06	0.134	0.084	225	300	0.714	0.537	0.343	0.324
0.2	90.91	270.00	0.136	0.086	225	300	0.711	0.539	0.344	0.309
0.22	93.04	269.83	0.138	0.087	225	300	0.708	0.541	0.345	0.294
0.24	95.08	269.59	0.140	0.088	225	300	0.703	0.544	0.347	0.280
0.25	97.04	269.45	0.141	0.089	225	300	0.698	0.547	0.350	0.266
0.26	98.87	269.30	0.141	0.090	225	300	0.693	0.550	0.353	0.255
0.28	100.53	268.96	0.140	0.091	225	300	0.687	0.554	0.357	0.244
0.29	102.01	268.78	0.139	0.092	225	300	0.681	0.557	0.360	0.236
0.3	103.15	268.59	0.138	0.093	225	300	0.675	0.561	0.363	0.229
0.32	104.00	268.20	0.135	0.094	225	300	0.670	0.566	0.366	0.223

0.34	104.70	267.79	0.133	0.094	225	300	0.664	0.570	0.369	0.218
0.35	105.26	267.58	0.130	0.095	225	300	0.658	0.573	0.372	0.215
0.36	105.61	267.37	0.128	0.095	225	300	0.653	0.576	0.375	0.212
0.38	105.87	266.95	0.125	0.095	225	300	0.648	0.578	0.378	0.210
0.4	106.02	266.54	0.122	0.095	225	300	0.643	0.580	0.381	0.210
0.42	106.03	266.16	0.120	0.094	225	300	0.638	0.583	0.384	0.210
0.44	105.92	265.80	0.117	0.093	225	300	0.634	0.585	0.388	0.211
0.45	105.79	265.64	0.115	0.092	225	300	0.629	0.589	0.393	0.213
0.46	105.69	265.48	0.113	0.091	225	300	0.624	0.592	0.398	0.216
0.48	105.59	265.21	0.111	0.089	225	300	0.619	0.595	0.404	0.219
0.5	105.54	265.00	0.109	0.088	225	300	0.615	0.599	0.410	0.224
0.55	105.61	264.74	0.108	0.086	225	300	0.610	0.603	0.417	0.229
0.6	105.83	264.83	0.106	0.085	225	300	0.605	0.607	0.424	0.235
0.65	106.20	265.20	0.105	0.083	225	300	0.599	0.611	0.431	0.243
0.667	106.75	265.38	0.103	0.082	225	300	0.593	0.615	0.440	0.250
0.7	107.48	265.78	0.102	0.081	225	300	0.587	0.619	0.448	0.258
0.75	108.39	266.51	0.100	0.080	225	300	0.581	0.622	0.457	0.266
0.8	109.62	267.32	0.099	0.079	225	300	0.576	0.624	0.466	0.274
0.85	111.08	268.14	0.099	0.079	225	300	0.570	0.625	0.475	0.281
0.9	112.71	268.90	0.098	0.078	225	300	0.564	0.626	0.483	0.288
0.95	114.50	269.55	0.098	0.078	225	300	0.558	0.626	0.491	0.294
1	116.39	270.00	0.098	0.078	225	300	0.553	0.625	0.498	0.298
1.1	118.30	270.18	0.099	0.078	225	300	0.548	0.624	0.505	0.302
1.2	120.19	269.42	0.100	0.077	225	300	0.543	0.623	0.511	0.306
1.3	122.01	267.82	0.101	0.077	225	300	0.539	0.622	0.516	0.309
1.4	123.75	265.45	0.102	0.077	225	300	0.535	0.620	0.521	0.312

1.5	125.38	262.41	0.104	0.076	225	300	0.532	0.619	0.525	0.315
1.6	126.90	258.78	0.105	0.075	225	300	0.529	0.618	0.528	0.318
1.7	128.14	254.66	0.106	0.074	225	300	0.527	0.618	0.530	0.321
1.8	129.11	250.11	0.106	0.072	225	300	0.526	0.618	0.531	0.323
1.9	129.86	245.25	0.106	0.071	225	300	0.526	0.618	0.532	0.326
2	130.37	240.14	0.105	0.069	225	300	0.526	0.618	0.532	0.329
2.2	130.67	229.55	0.103	0.066	225	300	0.527	0.619	0.533	0.332
2.4	130.81	219.05	0.100	0.064	225	300	0.528	0.619	0.533	0.335
2.5	130.81	214.04	0.097	0.061	225	300	0.530	0.619	0.534	0.337
2.6	130.72	209.32	0.094	0.058	225	300	0.531	0.620	0.535	0.340
2.8	130.57	201.08	0.091	0.056	225	300	0.532	0.619	0.536	0.342
3	130.36	195.00	0.088	0.053	225	300	0.534	0.619	0.537	0.344
3.2	130.13	191.61	0.084	0.050	225	300	0.535	0.618	0.538	0.345
3.4	129.90	190.73	0.081	0.047	225	300	0.535	0.618	0.540	0.346
3.5	129.71	191.11	0.078	0.045	225	300	0.536	0.617	0.541	0.347
3.6	129.56	191.98	0.075	0.042	225	300	0.536	0.616	0.542	0.348
3.8	129.49	195.01	0.072	0.039	225	300	0.536	0.616	0.543	0.349
4	129.49	199.45	0.070	0.036	225	300	0.536	0.616	0.543	0.349
4.2	129.57	204.93	0.068	0.034	225	300	0.535	0.616	0.542	0.349
4.4	129.71	211.09	0.066	0.033	225	300	0.534	0.617	0.540	0.347
4.6	129.87	217.56	0.064	0.032	225	300	0.533	0.619	0.538	0.345
4.8	130.05	223.99	0.063	0.032	225	300	0.531	0.621	0.535	0.341
5	130.22	230.00	0.061	0.032	225	300	0.528	0.622	0.532	0.335
5.5	130.39	241.86	0.060	0.031	225	300	0.526	0.624	0.528	0.329
6	130.53	249.34	0.059	0.031	225	300	0.524	0.625	0.524	0.321
6.5	130.63	252.94	0.059	0.032	225	300	0.520	0.634	0.517	0.312

7	130.70	253.12	0.059	0.033	225	300	0.515	0.636	0.514	0.302
7.5	130.72	250.39	0.058	0.034	225	300	0.512	0.634	0.511	0.270
8	130.87	245.23	0.059	0.033	225	300	0.510	0.630	0.507	0.278
8.5	130.71	238.13	0.059	0.031	225	300	0.509	0.622	0.503	0.265
9	130.50	229.56	0.060	0.028	225	300	0.509	0.613	0.498	0.252
9.5	130.26	220.02	0.060	0.025	225	300	0.509	0.604	0.492	0.239
10	130.00	210.00	0.060	0.025	225	300	0.510	0.604	0.487	0.239

REFERENCES

Aagaard, B. T., Brocher, T. M., Dolenc, D., Dreger, D., Graves, R. W., Harmsen, S., Hartzell, S., Larsen, S., McCandless, K., Nilsson, S., Petersson, N. A., Rodgers, A., Sjögreen, B., and Zoback, M. L. (2008). "Ground Motion Modeling of the 1906 San Francisco Earthquake II: Ground Motion Estimates for the 1906 Earthquake and Scenario Events," *Bull. Seism. Soc. Am.*, **98**(2), 1012–1046, doi 10.1785/0120060410.

Abrahamson, N.A., and Youngs, R.R. (1992). "A Stable Algorithm For Regression Analyses Using the Random Effects Model," *Bull. Seism. Soc. Am.*, **82**: 505–510.

Abrahamson, N. A. and Silva, W.J. (2008). "Summary of the Abrahamson and Silva NGA Ground Motion Relations," *Earthq. Spectra*, **24**, 67-97.

Abrahamson, N. A., Atkinson, G. M., Boore, D. M., Bozorgnia, Y., Campbell, K. W., Chiou, BS-J, Idriss, I. M., Silva, W. J., and Youngs, R. R. (2008). "Comparisons of the NGA Ground-Motion Relations," *Earthq. Spectra*, **24**. 45-66.

Abrahamson, N.A., Silva, W.J., Kamai, R. (2013). "Update of the AS08 Ground-Motion Prediction Equations Based on the NGA-West 2 Data Set," *PEER Report 2013/04*, Pacific Earthquake Engineering Research Center, University of California, Berkeley, CA.

Afacan, K.B., Brandenberg, S.J., Stewart, J.P. (2013). "Centrifuge Modeling Studies of Site Response in Soft Clay Over Wide Strain Range," *J. Geotech. & Geoenv. Engrg.*, ASCE. (Accepted).

Algermissen S.T., Perkins D.M. (1976). "A Probabilistic Estimate of Maximum Ground Acceleration in the Contiguous United States," *U.S. Geological Survey,* USGS Open File Report **76**-416.

Allen, T. I. and Wald, D. J. (2009). "On the Use of High-Resolution Topographic Data as a Proxy for Seismic Site Conditions (V_{S30})," *Bull. Seism. Soc. Am.,* Vol. **99**, No. 2A, pp. 935-943.

Ameri, G., Gallovič, F., Pacor, F., and Emolo, A. (2009). "Uncertainties in Strong Ground Motion Prediction with Finite-Fault Synthetic Seismograms: An Application to the 1984 M5.7 Gubbio, Central Italy, Earthquake," *Bull. Seism. Soc. Am.,* **99**, 647–663.

Ancheta, T. D., Stewart, J.P., and Abramhamson, N.A. (2011). "Engineering Characterization of Earthquake Ground Motion Coherency and Amplitude Variability," Proc. 4th International Symposium on Effects of Surface Geology on Seismic Motion, *IASPEI / IAEE,* August 23–26, 2011, University of California Santa Barbara.

Ancheta T.D., Darragh R.B., Stewart J.P., Seyhan E., Silva W.J., Chiou B.S.-J., Wooddell K.E., Graves R.W., Kottke A.R., Boore D.M., Kishida T., Donahue J.L. (2013). "PEER NGA-West 2 Database," *PEER Report 2013/03*, Pacific Earthquake Engineering Research Center, University of California, Berkeley, CA.

Anderson, J.G., and Hough, S.E. (1984). "A Model for the Shape of the Fourier Amplitude Spectrum of Acceleration at High Frequencies," *Bull. Seism. Soc. Am.,* **74**, 1969–1993.

Anderson, J., Kawase, H., Biasi, G. and Brune, J. (2013). "Ground motions in the Fukushima Hamadori, Japan, normal faulting earthquake," *Bull. Seismol. Soc. Am.*, **113**, in press.

Atkinson, G. M., (1993). "Earthquake Source Spectra in Eastern North America," *Bull. Seismol. Soc. Am.* **83**, 1778-1798.

Atkinson, G. M., and Casey, R. (2003). "A Comparison of Ground Motions from the 2001 M6.8 In-Slab Earthquakes in Cascadia and Japan," *Bull. Seismol. Soc. Am.,* **93**, 1823-1831.

Atkinson, G. M. and Morrison, M., (2009). "Regional Variability in Ground Motion Amplitudes Along the West Coast of North America," *Bull. Seismol. Soc. Am. ,* **99**, 2393 - 2409.

Atkinson, G. M., and Boore, D. M. (2011). "Modifications to Existing Ground-Motion Prediction Equations in Light of New Data," *Bull. Seismol. Soc. Am.*, **101,** 1121-1135.

Beresnev, I.A., and Atkinson, G. M. (1997). "Modeling Finite-Fault Radiation from the ω_n Spectrum," *Bull. Seism. Soc. Am.,* **87**, 67–84.

Bielak, J., Graves, R.W., Olsen, K.B., Taborda, R., Ramirez-Guzman, L., Day, S.M., Ely, G.P., Roten, D., Jordan, T.H., Maechling, P.J., Urbanic, J., Cui, Y.F., Juve, G. (2010). "The ShakeOut Earthquake Scenario: Verification of Three Simulation Sets," *Geophy. J. International,* **180**, 375-404.

Bommer, J. J., Douglas, J. and Strasser, F.O. (2003). "Style-of-faulting in Ground-Motion Prediction Equations," *Bull. Earthquake Engineering,* **1**, 171–203.

Boore, D.M. (1983). "Stochastic Simulation of High-Frequency Ground Motions Based on Seismological Models of the Radiated Spectra," *Bull. Seism. Soc. Am.,* **73**, 1865-1894.

Boore, D.M. and Atkinson, G.M. (1989). "Spectral Scaling of the 1985-1988 Nahanni, Northwest Territories, Earthquakes," *Bull. Seism. Soc. Am.,* **79**, 1736-1761.

Boore, D. M. and W. B. Joyner (1997). "Site Amplifications for Generic Rock Sites," *Bull. Seism. Soc. Am.,* **87**, 327–341.

Boore, D. M., Joyner, W. B., and Fumal, T. E. (1997). "Equations for Estimating Horizontal Response Spectra and Peak Acceleration from Western North American Earthquakes: A Summary of Recent Work (with 2005 Erratum)," *Seismol. Res. Letters,* **68**, 128-153.

Boore, D. M. (2004). "Estimating V_{s30} for NEHRP Site Classes From Shallow Velocity Models (depths < 30 m)," *Bull. Seism. Soc. Am.,* **94**, 591—597.

Boore, D.M. and Asten, M.W. (2005). "Comparisons of Shear-Wave Slowness in the Santa Clara Valley, California, Using Blind Interpretations of Data from Invasive and Noninvasive Methods," *Bull. Seism. Soc. Am.,* **98**, 1983-2003.

Boore, D. M., Watson-Lamprey, J., and Abrahamson, N.A. (2006). "GMRotD and GMRotI: Orientation-Independent Measures of Ground Motion," *Bull. Seism. Soc. Am.,* **94**(6A), 1502–1511.

Boore, D. M., and G. M. Atkinson (2008). "Ground-Motion Prediction Equations for the Average Horizontal Component of PGA, PGV, and 5%-damped PSA at Spectral Periods Between 0.01 s and 10.0 s," *Earthquake Spectra.* **24**, 99–138.

Boore, D.M. (2009). "Comparing Stochastic Point-Source and Finite-Source Ground-Motion Simulations: SMSIM and EXSIM," *Bull. Seism. Soc. Am.,* **99**, 3202-3216.

Boore, D. M. (2010). "Orientation-Independent, Nongeometric-Mean Measures of Seismic Intensity from Two Horizontal Components of Motion," *Bull. Seism. Soc. Am.,* **100**, 1830-1835.

Boore, D. M., Thompson, E.M., and Cadet, H. (2011). "Regional Correlations of V_{s30} And Velocities Averaged over Depths Less than and Greater than 30 m. *Bull. Seism. Soc. Am.,* **101**(6), 3046–3059.

270

Boore D.M., Stewart J.P., Seyhan E., and Atkinson G.M. (2013). "NGA-West 2 Equations for Predicting Response Spectral Accelerations for Shallow Crustal Earthquakes," *PEER Report 2013/05*, Pacific Earthquake Engineering Research Center, University of California, Berkeley, CA.

Borcherdt R.D., Glassmoyer G. (1994). "Influences of Local Geology on Strong and Weak Ground Motions Recorded in the San Francisco Bay Region and Their Implications for Site-Specific Building-Code Provisions," U.S. Geological Survey, T*he Loma Prieta, California Earthquake of October 17, 1989—Strong Ground Motion, USGS U. S. Professional Paper 1551-A, A77-A108.*

Borcherdt R.D. (1994a). "Simplified Site Classes and Empirical Amplification Factors for Site Dependent Code Provisions," *Proceedings, 1992 NCEER/SEAOC/BSSC Workshop on Site Response During Earthquakes and Seismic Code Provisions*, Los Angeles, California, G.R. Martin (ed.), *Research Special Publication NCEER-94-SP01*, National Center for Earthquake Engineering Research, Buffalo, NY.

Borcherdt R.D. (1994b). "Estimates of Site-Dependent Response Spectra for Design (Methodology and Justification)," *Earthq. Spectra*, **10**, 617-653.

Borcherdt, R.D. (2002). "Empirical Evidence for Acceleration-Dependent Amplification Factors," *Bull. Seism. Soc. Am.,* **92**(2), 761–782.

Borcherdt, R.D., and Fumal, T.E. (2002). "Shear-wave Velocity Compilation for Northridge Strong-Motion Recording Sites," *U.S. Geological Survey Open File Report* 2002-107.

Brown, L.T., Diehl, J.G., and Nigbor, R.L. (2000). "A Simplified Procedure to Measure Average Shear Wave Velocity to a Depth of 30 Meters (V_{S30})," *Proc. 12th World Conf. Eqk. Eng.*, Paper 677.

BSSC (1994). "NEHRP Recommended Provisions for Seismic Regulations for New Buildings, Part 1 – Provisions," FEMA 222a, Federal Emergency management Agency

BSSC (1995). "NEHRP Recommended Provisions for Seismic Regulations for New Buildings," Building Seismic Safety Council, 1994 ed., Vol. 1 (Provisions) and Vol. 2 (Commentary), Federal Emergency Management Agency, *FEMA 222A Report*, Washington, DC.

BSSC (1998). "NEHRP Recommended Provisions for Seismic Regulations for New Buildings and Other Structures," 1997 edition, Federal Emergency Management Agency, *FEMA 303 Report*, Washington, DC.

BSSC (2003). "NEHRP Recommended Provisions for Seismic Regulations for New Buildings and Other Structures," Part 1 (Provisions) and Part 2 (Commentary), Federal Emergency Management Agency, Washington D.C.

BSSC (2009). "NEHRP Recommended Seismic Provisions for New Buildings and Other Structures," Part 1 (Provisions) and Part 2 (Commentary), FEMA P-750, Washington D.C.

Cadet, H., and Duval, A.-M. (2009). "A Shear Wave Velocity Study Based on the Kik-Net Borehole Data: A Short Note," *Seismological. Research Letters*. **80**, 440–445.

Campbell, K.W., and Bozorgnia, Y. (2008). "NGA Ground Motion Model for the Geometric Mean Horizontal Component of PGA, PGV, PGD and 5% Damped Linear Elastic Response Spectra for Periods Ranging From 0.01 to 10 s," *Earthquake Spectra*, **24**, 139–171.

Campbell, K.W. (2009). "Estimates of Shear-Wave Q And κ_0 for Unconsolidated and Semiconsolidated Sediments in Eastern North America," *Bull. Seism. Soc. Am.,* **99**, 2365–2392.

Campbell K.W., and Bozorgnia Y. (2013). "NGA-West2 Campbell-Bozorgnia Ground Motion Model for the Horizontal Components of PGA, PGV, and 5%-Damped Elastic Pseudo-Acceleration Response Spectra for Periods Ranging From 0.01 to 10 sec," *PEER Report 2013/06*, Pacific Earthquake Engineering Research Center, University of California, Berkeley, CA.

Cauzzi, C., and Faccioli, E. (2008). "Broadband (0.05 to 20 s) Prediction of Displacement Response Spectra Based on Worldwide Digital Records," *J. Seismology*, **12**, 453–475.

Chiou, B.S.-J., Darragh, R., Dregor, D., and Silva, W.J. (2008). "NGA Project Strong-Motion Database," *Earthquake Spectra*, **24** (1), 23-44.

Chiou, B.S.-J., and Youngs, R. R., (2008a). "An NGA Model for the Average Horizontal Component of Peak Ground Motion and Response Spectra*," Earthquake Spectra,* **24**, 173 - 216.

Chiou, B. Youngs, R., Abrahamson, N.A., and Addo, K. (2010). "Ground-Motion Attenuation Model for Small-to-Moderate Shallow Crustal Earthquakes in California and Its Implications on Regionalization of Ground-Motion Prediction Models," *Earthquake Spectra,* **26**:4, 907-926.

Chiou, BS-J., and Youngs, R.R. (2012). "Updating the Chiou and Youngs NGA Model: Regionalization of Anelastic Attenuation," *Proc. 15th World Conf. on Earthquake Eng*., Sept 24-28, 2012, Lisbon, Portugal.

Chiou, B.S-J., and Youngs, R.R. (2013). "Update of the Chiou and Youngs NGA Ground Motion Model for Average Horizontal Component of Peak Ground Motion and Response Spectra," *PEER Report 2013/05*, Pacific Earthquake Engineering Research Center, University of California, Berkeley, CA.

Choi Y., Stewart J.P. (2005). "Nonlinear Site Amplification as Function of 30 m Shear Wave Velocity," *Earthq. Spectra,* **21**: 1-30.

Choi, Y., Stewart, J.P., and Graves, R.W. (2005). "Empirical Model for Basin Effects that Accounts for Basin Depth and Source Location," *Bull. Seismol. Soc. Am.*, **95**, 1412-1427.

Conte, J.P., and Peng, B.F. (1997). "Fully Nonstationary Analytical Earthquake Ground-Motion Model," *J. Eng. Mech.,* **12**, 15–24.

Day, S. M., Graves, R., Bielak, J., Dreger, D., Larsen, S., Olsen, K.B., Pitarka, A., and Ramirez-Guzman, L. (2008). "Model for Basin Effects on Long-Period Response Spectra in Southern California," *Earthquake Spectra*, **24**, 257–277.

Dobry R., Martin G.M., Parra E., and Bhattacharya A., (1994). "Development of Site-Dependent Ratios of Elastic Response Spectra (RRS) and Site Categories for Building Seismic Codes," *Proceedings, 1992 NCEER/SEAOC/BSSC Workshop on Site Response During Earthquakes and Seismic Code Provisions*, Los Angeles, California, G.R. Martin (ed.), *Research Special Publication NCEER-94-SP01*, National Center for Earthquake Engineering Research, Buffalo, NY.

Dobry R., Borcherdt R.D., Crouse C.B., Idriss I.M., Joyner W.B., Martin G.R., Power M.S., Rinne E.E., and Seed R.B. (2000). "New Site Coefficients and Site Classification System Used in Recent Building Seismic Code Provisions," (1994/1997 NEHRP and 1997 UBC), *Earthq. Spectra*, **16**: 41−68.

Electrical Power Research Institute, EPRI (1993). "Guidelines for Determining Design Basis Ground Motions," Electrical Power Research Institute, *Rpt. No. EPRI TR-102293*, Palo Alto, CA.

Douglas, J. (2003). "Earthquake Ground Motion Estimation Using Strong-Motion Records: A Review of Equations for the Estimation of Peak Ground Acceleration and Response Spectral Ordinates," *Earth-Science Reviews*, **61**, (1–2), 43–104.

Douglas, J., Gehl, P., Bonilla, L. F., Scotti, O., Régnier, J. Duval, A.-M., and Bertrand, E. (2009). "Making the Most of Available Site Information for Empirical Ground-Motion Prediction," *Bull. Seismol. Soc. Am.* **99**, 1502–1520.

Douglas, J. and Halldórsson, B. (2010). "On the Use of Aftershocks When Deriving Ground-Motion Prediction Equations," *Proceedings of the 9th U.S. National and 10th Canadian Conference on Earthquake*, July 25-29, 2010, Toronto, Ontario, Canada, Paper No 220, 10 pp.

Douglas, J. and Jousset, P. (2011). "Modeling the Difference in Ground-Motion Magnitude-Scaling in Small and Large Earthquakes," *Seismol. Res. Letters*, **82**, 504–508.

Fatehi, A., and Herrmann, R.B. (2008). "High-Frequency Ground-Motion Scaling in the Pacific Northwest and in Northern and Central California," *Bull. Seism. Soc. Am.,* **98**, 709–721.

Field, E.H. (2000). "A Modified Ground Motion Attenuation Relationship for Southern California that Accounts for Detailed Site Classification and a Basin Depth Effect," *Bull. Seismol. Soc. Am.*, **90**, S209-S221.

Fletcher, J., Boatwright, J., Haar, L., Hanks, T., and McGarr, A. (1984). "Source Parameters for Aftershocks of the Oroville, California, Earthquake," *Bull. Seismol. Soc. Am.*, **74**, 1101–1123.

Frankel, A. (1993). "Three-Dimensional Simulations Of Ground Motions in the San Bernardino Valley, California, for Hypothetical Earthquakes on the San Andreas Fault," *Bull. Seism. Soc. Am.,* **83**, 1020–1041.

Frankel, A. (1995). "Simulating Strong Motions of Large Earthquakes Using Recordings of Small Earthquakes: The Loma Prieta Mainshock as a Test Case," *Bull. Seism. Soc. Am.,* **85**, 1144–1160.

Frankel A., Mueller C., Barnhard T., Perkins D., Leyendecker E.V., Dickman N., Hanson S., and Hopper M. (1996). "National Seismic Hazard Maps: Documentation June 1996," U.S. Geological Survey, *USGS Open* File Report 96-532, Denver, CO.

Frankel, A. (2009). "A Constant Stress-Drop Model for Producing Broadband Synthetic Seismograms: Comparison with the Next Generation Attenuation Relations," *Bull. Seism. Soc. Am.,* **99**, 664–680.

Fumal, T.E. and Tinsley, J.C. (1985). "Mapping Shear-Wave Velocities of Near-Surface Geologic Materials," In: J.I. Ziony (ed.), Evaluating Earthquake Hazards in the Los Angeles Region-An Earth-Science Perspective. U.S. Geological Survey Professional Paper. 1360, 101-126.

Ghofrani, H., Atkinson, G.M., and Goda, K. (2013). "Implications of the 2011 M9.0 Tohoku Japan Earthquake for the Treatment of Site Effects in Large Earthquakes," *Bull. Earthquake Eng.*, **11**, 171–203.

Goulet, C.A. and Stewart, J.P. (2009) "Pitfalls of Deterministic Application of Nonlinear Site Factors in Probabilistic Assessment of Ground Motions." *Earthq. Spectra,* **25**, 541.

Graves, R.W., Aagaard, B.T., Hudnut, K.W., Star, L.M., Stewart, J.P., and Jordan, T.H. (2008). "Broadband Simulations for M_w 7.8 Southern San Andreas Earthquakes: Ground Motion Sensitivity to Rupture Speed," *Geophys. Res. Lett.,* **35**, L22302, doi:10.1029/2008GL035750.

Graves, R.W. and Pitarka, A. (2010). "Broadband Ground-Motion Simulation Using a Hybrid Approach," *Bull. Seism. Soc. Am.,* **100**(5A), 2095–2123

Graves, R.W., Aagaard, B.T., and Hudnut, K.W. (2011). "The ShakeOut Earthquake Source and Ground Motion Simulations," *Earthq. Spectra,* **27**, 273-291.

Guatteri, M., Mai, P.M., and Beroza, G.C. (2004). "A Pseudo-Dynamic Approximation to Dynamic Rupture Models for Strong Ground Motion Prediction," *Bull. Seism. Soc. Am.,* **94**, 2051-2063.

Harmsen, S and Frankel, A. (2001). "Geographic Deaggregation of Seismic Hazard In the United States," *Bull. Seism. Soc. Am.,* **83**, 13-26.

Hartzell, S., Harmsen, S., Frankel, A., and Larsen, S. (1999). "Calculation of Broadband Time Histories of Ground Motion: Comparison of Methods and Validation Using Strong-Ground Motion from the 1994 Northridge Earthquake," *Bull. Seism. Soc. Am.,* **89**, 1484-1504.

Hartzell, S., Guatteri, M., Mai, P.M., Liu, P-C and Fisk, M. (2005). "Calculation of Broadband Time Histories of Ground Motion, Part II: Kinematic and Dynamic Modeling using Theoretical Green's Functions and Comparison with the 1994 Northridge Earthquake," *Bull. Seismol. Soc. Am.*, **95**, 614–645.

Huang Y.N., Whittaker A.S., and Luco N. (2010). "NEHRP Site Amplification Factors and the NGA Relationships," *Earthq. Spectra*, **26**: 583–593.

Idriss I.M. (2008). "An NGA Empirical Model for Estimating the Horizontal Spectral Values Generated by Shallow Crustal Earthquakes," *Earthq. Spectra*, **24**: 217–242.

Idriss I.M. (2013). "NGA-West2 Model for Estimating Average Horizontal Values of Pseudo-Absolute Spectral Accelerations Generated by Crustal Earthquakes," *PEER Report 2013/08*, Pacific Earthquake Engineering Research Center, University of California, Berkeley, CA.

Iwahashi, J. and Pike, R.J. (2007). "Automated Classifications of Topography from DEMs by an Unsupervised Nested-Means Algorithm and a Three-Part Geometric Signature," *Geomorphology,* **86**:3-4,409-440.

Johnston, A. C., Coppersmith, K. J., Kanter, L. R., and Cornell, C. A. (1994). "The Earthquakes of Stable Continental Regions," *Technical Report TR-102261-VI,* Electric Power Research Institute (EPRI), Palo Alto, CA.

Joyner, W.B., and Fumal, T. . (1984). "Use of Measured Shear-Wave Velocity for Predicting Geologic Site Effects on Strong Ground Motion," *Proc. Eighth World Conf. on Earthquake Eng. (San Francisco)* **2**, 777-783.

Joyner, W.B. and Fumal, T.E. (1985). "Predictive Mapping of Earthquake Ground Motion," in *Evaluating Earthquake Hazards in the Los Angeles Region*, J. I. Ziony, Editor *U.S. Geol. Surv. Profess. Paper 1360*, 203-220.

Joyner, W.B., and Boore, D.M. (1993). "Methods for Regression Analysis of Strong-Motion Data," *Bull. Seismol. Soc. Am.*, **83,** 469-487.

Joyner, W.B., and Boore, D.M. (1994). "Errata: Methods for Regression Analysis of Strong-Motion Data," *Bull. Seismol. Soc. Am.*, **84**, 955-956.

Kamai R., Abrahamson N.A., Silva W.J. (2013). "Nonlinear Horizontal Site Response for the NGA-West 2 Project, "*PEER Report 2013/12*, Pacific Earthquake Engineering Research Center, Berkeley, CA.

Kanno, T., Narita, A., Morikawa, N., Fujiwara, H., and Fukushima, Y. (2006). "A New Attenuation Relation for Strong Ground Motion in JAPAN BASEd on Recorded Data," *Bull. Seismol. Soc. Am.*, **96**, 879–89.

Kinoshita, S. (1998). "Kyoshin-net (K-NET)," *Seismological Research. Letters*, **69**, 309–332.

Kottke, A. (2011). "Selection of Wenchuan Stations Based on Geology," Unpublished internal PEER white paper, November 11, 2011.

Kwok A.O., Stewart J.P. (2006). "Evaluation of the Effectiveness of Theoretical 1D Amplification Factors for Earthquake Ground-Motion Prediction," *Bull. Seism. Soc. Am.*, **96**: 1422–1436.

Lee, Y., and Anderson, J.G. (2000). "Potential for Improving Ground-Motion Relations in Southern California by Incorporating Various Site Parameters," *Bull. Seismol. Soc. Am.*, **90**, S170–S186.

Lee, C.T., Cheng, C.T., Liao, C.W., and Tsai, Y.B. (2001). "Site Classification of Taiwan Freefield Strong-Motion Stations," *Bull. Seismol. Soc. Am.*, **91**(5), 1283–1297.

Lin, G., Thurber, C.H., Zhang, H., Hauksson, E., Shearer, P.M., Waldhauser, F., Brocher, T.M. and Hardebeck, J. (2010). A California statewide three-dimensional seismic velocity model from both absolute and differential times *Bulletin of the Seismological Society of America* 100 (1), 225 - 240.

Liu, H., and Helmberger, D.V. (1985). "The 23:19 Aftershock of the October 1979 Imperial Valley Earthquake: More Evidence for an Asperity," *Bull. Seism. Soc. Am.,* **75**, 689-708.

Liu, P., Archuleta, R.J., and Hartzell, S.H. (2006). "Prediction of Broadband Ground-Motion Time Histories: Hybrid Low/High- Frequency Method with Correlated Random Source Parameters," *Bull. Seism. Soc. Am.,* **96**, 2118-2130.

Mai, P.M., Imperatori, W., and Olsen, K.B. (2010). "Hybrid Broadband Ground-Motion Simulations: Combining Long-Period Deterministic Synthetics with High-Frequency Multiple S-to-S Backscattering," *Bull. Seism. Soc. Am.,* **100**, 2124–2142.

Mena, B., Mai, P.M., Olsen, K.B., Purvance, M.D., and Brune, J.N. (2010). "Hybrid Broadband Ground-Motion Simulation Using Scattering Green's Functions: Application to Large-Magnitude Events," *Bull. Seism. Soc. Am.,* **100**, 2143–2162.

Martirosyan, A., Dutta, U., Biswas, U., Papageorgiou, N., and Combellick, R. (2002). "Determination of site response in Anchorage, Alaska, on the basis of spectral ratio methods," *Earthq. Spectra*, **18**(1), 85–104.

Martin G.M. (ed.) (1994). "Proceedings, 1992 NCEER/SEAOC/BSSC Workshop on Site Response During Earthquakes and Seismic Code Provisions," Los Angeles, California, G.R. Martin (ed.), *Research Special Publication NCEER-94-SP01*, National Center for Earthquake Engineering Research, Buffalo, NY.

Matsuoka, M., Wakamatsu, K., Fujimoto, F. and Midorikawa, S. (2006). "Average Shear-Wave Velocity Mapping Using Japan engineering Geomorphologic Classification Map," *Journal of Structural Mechanics and Earthquake Engineering*, **23**:1, 57s–68s.

Moss, R.E.S. (2008). "Quantifying Measurement Uncertainty of Thirty-Meter Shear-Wave Velocity," *Bull. Seism. Soc. Am.,* **98**:3, 1399–1411.

Okada, Y., Kasahara, K., Hori, S., Obara, K., Sekiguchi, S., Fujiwara, H. and Yamamoto, A. (2004). "Recent Progress of Seismic Observation Networks in Japan-Hi-net, F-net, K-NET and KiK-net," *Earth Planets Space,* **56**:xv–xxviii.

Olsen, K.B., Day, S.M., Minster, J.B., Cui, Y., Chourasia, A., Okaya, D., Maechling, P., and Jordan,T. (2008). "TeraShake2: "Simulation of M_w 7.7 Earthquakes on the Southern San Andreas with Spontaneous Rupture Description," *Bull. Seism. Soc. Am.,* **98**, 1162–1185.

Olsen, K.B., Day, S.B., Dalguer, L.A., Mayhew, J., Cui, Y., Zhu, J., Cruz-Atienza, V.M., Roten, D., Maechling, P., Jordan, T.H., Okaya, D., and Chourasia, A. (2009). "ShakeOut-D: Ground Motion Estimates Using an Ensemble of Large Earthquakes on the Southern San Andreas Fault with Spontaneous Rupture Propagation," *Geophys. Res. Lett.,* **36**, L04303, doi:10.1029/2008GL036832.

Olsen, K.B., and Mayhew, J.E. (2010). "Goodness-of-fit Criteria for Broadband Synthetic Seismograms, with Application to the 2008 M_w 5.4 Chino Hills, California, Earthquake," *Seism. Res. Ltrs.,* **81**, 715-723.

Pacific Gas and Electric Company, PG&E (2011). "Evaluation of Shear Wave Velocity at the DCPP ISFSI," GeoSciences Department, Calculation Document. Document No. GEO.DCPP.10.02.

Pinheiro, H., Bates, D., DebRoy, S., Sarkar, D., and the R Development Core Team (2013). "NLME: Linear and Nonlinear Mixed Effects Models," *R package* version 3.1-108.

Porter, K.A., Jones, L., Cox, D., Goltz, J., Hudnut, K.W., Mileti, D., Perry, S., Ponti, D., Reichle, M., Scawthorn, C.R., Seligson, H.A., Shoaf, K.I., and Wein, A. (2011). "The ShakeOut Scenario: a Hypothetical M_w7.8 Earthquake on the Southern San Andreas Fault," *Earthq. Spectra*, **27**, 2, 239–261.

Power, M., Chiou, B., Abrahamson, N., Bozorgnia, Y., Shantz, T., and Roblee, C., (2008). "An Overview of the NGA Project," *Earthq. Spectra*, **24**, 3 - 21.

Pulido, N., and Dalguer, L.A. (2009). "Estimation of the High-Frequency Radiation of the 2000 Tottori (Japan) Earthquake Based on a Dynamic Model of Fault Rupture: Application to the Strong Ground Motion Simulation," *Bull. Seism. Soc. Am.,* **99**, 2305–2322.

Raoof, M., Herrmann, R.B., and Malagnini, L. (1999). "Attenuation and Excitation of Three-Component Ground Motion in Southern California," *Bull. Seism. Soc. Am.*, **89**, 888–902.

Rezaeian, S., and Der Kiureghian, A. (2008). "A Stochastic Ground Motion Model with Separable Temporal and Spectral Nonstationarities," Eqk Engin & Struct. Dyn., 37, 1565–1584.

Ripperger, J., Mai, P.M., and Ampuero, J.P. (2008). "Variability of Near-Field Ground-Motion from Dynamic Earthquake Rupture Simulation," *Bull. Seism. Soc. Am.,* **98**, 1207-1228.

Sandikkaya M.A., Yilmaz, M.T., Bakir, B.S., and Yilmaz, O. (2010). "Site Classification of Turkish National Strong-Motion Stations," *Journal of Seismology*, **14**:543–563. DOI 10.1007/s10950-009-9182-y.

Scasserra, G., Stewart, J.P., Bazzurro, P., Lanzo, G., and Mollaioli, F. (2009). "A Comparison of NGA Ground-Motion Prediction Equations to Italian Data," *Bull. Seismol. Soc. Am.,* **99**, 2961-2978.

Schmedes, J., Archuleta, R.J., and Lavalle, D. (2010). "Correlation of Earthquake Source Parameters Inferred from Dynamic Rupture Simulations," *J. Geophys. Res.,* **115**, doi:10.1029/2009JB006689.

Seed H.B., and Idriss, I.M. (1970). "Soil Moduli and Moduli Damping Factors for Dynamic Response Analysis," *Report No. UCB/EERC-70/10*, Earthquake Engineering Research Center, University of California, Berkeley, CA.

Seed H.B. Wong, R.T., Idriss I.M., and Tokimatsu K. (1984). "Moduli and Damping Factors for Dynamic Analyses of Cohesionless Soils," *Report No. UCB/EERC/84-14*, Earthquake Engineering Research Center, University of California, Berkeley, CA.

Seed R.B., Dickenson S.E., and Mok, C.M. (1994) "Site Effects on Strong Shaking and Seismic Risk; Recent Developments for Seismic Design Codes and Practice," Proceedings, ASCE Structures Congress, 12: 573–578.

Seyhan E., and Stewart J.P. (2012). "Site Response in NEHRP Provisions and NGA Models," in: *Geotechnical Engineering State of the Art and Practice: Volume of Keynote Lectures from GeoCongress 2012,* Oakland, CA, ASCE *Geotechnical Special Publication No. 226*, K. Rollins and D. Zekkos (eds.), pp. 359–379.

Silva, W.J., and Darragh, R.B. (1995). "Engineering Characterization of Earthquake Strong Ground Motion Recorded at Rock Sites," Report TR-102261, Electric Power Research Institute, Palo Alto, CA.

Silva W.J., and Lee K. (1987). "WES RASCAL Code for Synthesizing Earthquake Ground Motions, State-of-the Art for Assessing Earthquake Hazards in the United States," Report 24, U.S. Army Engineers Waterways Experiment Station, Misc. Paper S-73-1.

Silva, W.J., Li, S., Darragh, R., and Gregor, N. (1999). "Surface Geology Based Strong Motion Amplification Factors for the San Francisco Bay and Los Angeles Areas," Report to Pacific Earthquake Engineering Research Center.

Spudich, P., Fletcher, J.B., Hellweg, M., Boatwright, J., Sullivan, C., Joyner, W.B., Hanks, T.C., Boore, D.M., McGarr, A., Baker, L.M., and Lindh, A.G. (1997). "SEA96 -- A New Predictive Relation for Earthquake Ground Motions in Extensional Tectonic Regimes," *Seismological Research Letters,* **68**, 190-198.

Spudich, P., Joyner, W.B., Lindh, A.G., Boore, D.M., Margaris, B.M., and Fletcher, J.B. (1999). "SEA99 -- A Revised Ground Motion Prediction Relation for Use in extensional Tectonic Regimes," *Bull. Seismol. Soc. Am.,* **89**, 1156-1170.

Star, LM, JP Stewart, and RW Graves (2011). Comparison of ground motions from hybrid simulations to NGA prediction equations, Earthquake Spectra. 27, 333-350.

Steidl, J. H. (2000). "Site Response in Southern California for Probabilistic Seismic Hazard Analysis," *Bull. Seism. Soc. Am.,* **90**, S149-S169.

Stewart, J. P. (2000). "Variations between Foundation-Level and Free-Field Earthquake Ground Motions," *Earthq. Spectra*, **16**, 511-532.

Stewart J.P., Chiou, BS.-J., Bray, J.D., Somerville, P.G., Graves, R.W., Abrahamson, N.A. (2001). "Ground Motion Evaluation Procedures for Performance Based Design," *Report No. PEER-2001/09*, Pacific Earthquake Engineering Research Center, Berkeley, CA, 229 pgs.

Stewart, J.P., Lanzo, G., Pagliaroli, A., Scasserra, G., DiCapua, G., Peppolini, S., Darragh, R. and Gregor, N. (2012). "Ground Motion Recordings from the M_w 6.3 2009 L'Aquila Earthquake in Italy and their Engineering implications," *Earthq. Spectra*, **28:1**, 317-345.

Stewart, J.P., Seyhan, E., Boore, D.M., Campbell, K.W., Erdik, M., and Silva, W.J. (2012). "Site effects in Parametric Ground Motion Models for the GEM-PEER Global GMPEs Project," Proc. 15th World Conf. Earthquake Engineering, Lisbon.

Stewart J.P., Midorikawa S., Graves R.W., Khodaverdi K., Miura H. Bozorgnia Y., Campbell K.W. (2013). "Implications of M_w 9.0 Tohoku-oki Japan earthquake for Ground Motion Scaling with Source, Path, and Site Parameters," *Earthq. Spectra*, **29** (S1): S1-21.

Stewart, J.P., Seyhan, E., and Graves, R.W. (2011). "Calibration of Semi-Stochastic Procedure for Simulating High Frequency Ground Motions," PEER Report 2011/09, Pacific Earthquake Engineering Research Center, UC Berkeley

Stewart, J. P., and Seyhan, E. (2013). "Semi-empirical Nonlinear Site Amplification and Its Application in NEHRP Site Factors," *PEER Report 2013.xx*, Pacific Earthquake Engineering Research Center, Berkeley, California.

Stidham, C., Antolik, M., Dreger, D.S., Larsen, S., and Ramanowicz, B. (1999). "Three-Dimensional Structure Influences on the Strong Motion Wavefield of the 1989 Loma Prieta Earthquake," *Bull. Seism. Soc. Am.,* **89**, 1184-1202.

Thompson, E.M., Baise, L.G., Tanaka, Y., and Kayen, R.E. (2012). "A Taxonomy of Site Response Complexity," *Soil Dynamics and Earthquake Engineering*, **41**, 32-43.

Vucetic M., and Dobry R. (1991). "Effect of Soil Plasticity on Cyclic Response," *J. Geotech. Eng.*, **117**(1): 89-107.

Wakamatsu, K., Kubo, S., Matsuoka, M., Hasegawa, K. & Sugiura, M. (2005). "Japan Engineering Geomorphologic Classification Map with CD-ROM Database," *University of Tokyo Press, Tokyo.* (in Japanese with English abstract and manual)

Wakamatsu, K. and Matsuoka, M. (2006). "Development of the 7.5-Arc-Second Engineering Geomorphologic Classification Database and its Application to Seismic Microzoning," *Bulletin of Earthquake Research Institute*, The University of Tokyo, Vol.**81**, pp.317-324.

Wald, D. J., and Allen, T.I. (2007). "Topographic Slope as a Proxy for Seismic Site Conditions and Amplification," *Bull. Seism. Soc. Am.,* **97**, 1379–1395.

Walling M., Silva W.J., and Abrahamson N.A. (2008). "Nonlinear Site Amplification Factors for Constraining the NGA Models," *Earthq. Spectra*, **24**: 243–255.

Wills, C.J. and Clahan, K.B. (2006). "Developing a Map of Geologically Defined Site-Condition Categories for California," *Bull. Seism. Soc. Am.,* **96**, 1483-1501.

Wills, C.J. and Gutierrez, C. (2008). "Investigation of Geographic Rules for Improving Site-Conditions Mapping," *Calif. Geo. Sur. Final Tech. Rept.,* 20 pp. (Award No. 07HQGR0061).

Wooddell, K. E., and Abrahamson, N. A. (2012). "New Earthquake Classification Scheme for Mainshocks and Aftershocks in the NGA-West 2 Ground Motion Prediction equAtions (GMPEs)," *Proc. 15th World Conf. on Earthquake Eng.*, Sept 24-28, 2012, Lisbon, Portugal.

Xu, J., Bielak, J., Ghattas, O., and Wang, J. (2003). "Three-Dimensional Nonlinear Seismic Ground Motion Modeling in Basins," *Physics of the Earth and Planetary Interiors*, **137**, 81–95.

Yong, A., Hough, S.E., Iwahashi, J. and Braverman, A. (2012). "Terrain-Based Site Conditions Map of California with Implications for the Contiguous United States," *Bull. Seism. Soc. Am.,* **102**, 114-128.

Yong, A., Martin, A., Stokoe, K., and Diehl, J. (2013), "ARRA-funded V_{s30} Measurements at California and Central-Eastern U.S. Strong Motion Stations," U.S. Geol. Surv. Open-File Rept. (in review).

Zeng, Y., Anderson, J.G., and Yu, G. (1994). "A Composite Source Model for Computing Realistic Synthetics Strong Ground Motions," *Geophys. Res. Lett.,* **21**, 725-728.